

## Abstract

# Optical Diagnostics Applied to Quantitative Characterization of Coflow Laminar Diffusion Flames in Microgravity and Normal Gravity

Davide Giassi

2017

Building on the work previously done in our laboratory, this dissertation extends the use of well-established optical techniques and introduces newly developed ones for the quantification of coflow laminar diffusion flame physical and chemical properties, as well as for the characterization of reactive and non-reactive flows.

Single-photon and two-photon laser-induced fluorescence was used to quantify and map the two-dimensional distributions of nitric oxide and carbon monoxide concentrations in steady and time-varying nitrogen-diluted methane flames.

The signal-to-noise ratio of flame temperature and soot volume fraction results was improved with the adaptation and use of high dynamic range imaging. This new approach was successfully applied to normal gravity and microgravity coflow diffusion flames and allowed for a more complete use of partially saturated images that populate microgravity image databases. The use of high dynamic range and time-resolved averaging was investigated and successfully extended to the measurements of reactive and non-reactive unsteady flows using Rayleigh scattering, with the aim of increasing the result's signal-to-noise ratio.

As part of an ongoing research on microgravity flames and a collaboration with NASA, a consumer camera was used for the quantitative evaluation of  $CH^*$  concentration in normal and microgravity coflow flames and, thanks to complementing numerical results,  $CH^*$  chemiluminescence was related to flame heat release rate.

Nitrogen-diluted methane flames were investigated as a function of ambient pressure and fuel dilution, and the results compared with numerical predictions, as a way to validate computational models applied to highly diluted and heavily sooty flames.

Demosaicing algorithms were implemented for the improvement of image spatial resolution and measurement accuracy, and their application tested for the analysis of the *Advanced Combustion via Microgravity Experiments* (ACME) campaign's images. The flight and ground units of the ACME coflow burners were fully characterized in normal gravity, and the ACME imaging system was calibrated to be used for quantitative imaging experiments.

**Optical Diagnostics Applied to  
Quantitative Characterization of Coflow  
Laminar Diffusion Flames in Microgravity  
and Normal Gravity**

A Dissertation  
Presented to the Faculty of the Graduate School  
of  
Yale University  
in Candidacy for the Degree of  
Doctor of Philosophy

by  
Davide Giassi

Dissertation Director: Professor Marshall B. Long

May, 2017

Copyright © 2017 by Davide Giassi

All rights reserved.

# Acknowledgements

I would like to express my most sincere gratitude to Professor Marshall Long, my advisor, for guiding me academically and professionally during my time at Yale. His deep and broad scientific knowledge has and always will be a great source of inspiration. I would also like to thank my committee members, Professor Mitchell Smooke and Professor Alessandro Gomez, for their valuable contributions and suggestions over the course of my graduate studies. I am also very grateful to Professor Derek Dunn-Rankin for kindly accepting to be my external reader.

Many thanks to my lab mates, Dr. Bin Ma and Dr. Nathan Kempema, as well as collaborators Dr. Luca Tosatto, Dr. Su Cao, Dr. Lorenzo Figura, Dr. Beth Anne Bennett, and Mr. Dhrubajyoti Das. The interactions and discussions we had over the years were instrumental to the completion of this dissertation.

Thank you to Dr. Dennis Stocker, for the collaboration between Yale and NASA that allowed me to be part of microgravity projects and experiments, as well as to Mr. Nicholas Bernardo and Mr. David Johnson at Yale for sharing their expertise with all the machining-related projects.

I would like to thank my parents, Giampiero and Tiziana, as well as my sisters, Marianna and Giulia; without them and their support I would not have been able to achieve this prestigious goal.

And finally, my deepest gratitude goes to my wife, Caroline, for completing my life with her love and invaluable friendship.

# Contents

<b>Acknowledgements</b>	<b>iii</b>
<b>List of Figures</b>	<b>viii</b>
<b>List of Tables</b>	<b>xix</b>
<b>1 Introduction</b>	<b>1</b>
<b>2 Experimental hardware and optical diagnostics</b>	<b>7</b>
2.1 Yale coflow burner . . . . .	7
2.2 Luminosity-based techniques . . . . .	9
2.2.1 Color ratio pyrometry . . . . .	9
2.2.2 Soot volume fraction . . . . .	15
2.2.3 Thin filament pyrometry . . . . .	15
2.2.4 Chemiluminescence . . . . .	18
2.2.5 Absolute light intensity calibration . . . . .	19
2.3 Laser-based techniques . . . . .	21
2.3.1 Laser-induced fluorescence . . . . .	21
2.3.2 Two-photon laser-induced fluorescence . . . . .	24
2.3.3 Rayleigh scattering . . . . .	27
<b>3 Minor species characterization using laser-induced fluorescence</b>	<b>31</b>

3.1	Nitric oxide LIF . . . . .	34
3.1.1	Experimental setup . . . . .	34
3.1.2	Diagnostic considerations . . . . .	37
3.1.3	Results and discussion . . . . .	48
3.2	Carbon monoxide LIF . . . . .	54
3.2.1	Experimental setup . . . . .	54
3.2.2	Diagnostic considerations . . . . .	56
3.2.3	Results and discussion . . . . .	66
3.3	Conclusions . . . . .	82
<b>4</b>	<b>High dynamic range imaging applied to combustion diagnostics</b>	<b>83</b>
4.1	Application of HDR imaging to color ratio pyrometry . . . . .	85
4.2	HDR algorithms . . . . .	92
4.3	Detector characterization and pixel crosstalk . . . . .	99
4.4	Improvements in signal-to-noise ratio . . . . .	103
4.5	Examples of HDR imaging applications . . . . .	107
4.5.1	Thin filament pyrometry . . . . .	107
4.5.2	Soot pyrometry . . . . .	112
4.5.3	Microgravity flames . . . . .	117
4.6	Conclusions . . . . .	120
<b>5</b>	<b>Time-resolved image averaging and high dynamic range imaging applied to laser flow diagnostics</b>	<b>122</b>
5.1	Time-resolved image averaging . . . . .	123
5.1.1	Experimental setup . . . . .	124
5.1.2	Detector and image intensifier characterization . . . . .	129
5.1.3	Results . . . . .	133
5.2	High dynamic range imaging . . . . .	140

5.2.1	Experimental setup . . . . .	141
5.2.2	Results . . . . .	144
5.3	Conclusions . . . . .	147
<b>6</b>	<b>Measurements of <math>CH^*</math> concentration in microgravity and normal gravity laminar coflow diffusion flames</b>	<b>149</b>
6.1	Experimental setup . . . . .	151
6.2	Imaging and spectral considerations . . . . .	156
6.3	SLICE computational model . . . . .	162
6.4	$CH^*$ concentration diagnostics . . . . .	162
6.5	Results . . . . .	166
6.6	Conclusions . . . . .	176
<b>7</b>	<b>Nitrogen-diluted methane flames under moderate pressure</b>	<b>177</b>
7.1	Experimental setup . . . . .	178
7.2	Results and discussion . . . . .	180
<b>8</b>	<b>Demosaicing algorithms for the improvement of spatial resolution and accuracy in color ratio pyrometry</b>	<b>194</b>
8.1	Demosaicing algorithms . . . . .	195
8.2	Experimental setup . . . . .	198
8.3	Results . . . . .	199
8.4	Conclusions . . . . .	207
<b>9</b>	<b>ACME experiments</b>	<b>208</b>
9.1	Burner design . . . . .	208
9.2	CLD burner flow velocity profiles . . . . .	214
9.2.1	Hot wire setup and calibration . . . . .	216
9.2.2	Results . . . . .	218

9.3	Detector characterization and calibration . . . . .	223
9.4	Normal gravity flames . . . . .	229
9.4.1	Examples of quantitative measurements applied to normal gravity ACME flames . . . . .	234
<b>10</b>	<b>Conclusions</b>	<b>238</b>
<b>A</b>	<b>ACME CLD burner velocity profiles</b>	<b>242</b>
A.1	Flight unit . . . . .	243
A.2	Ground unit . . . . .	253
<b>B</b>	<b>ACME CLD flames</b>	<b>258</b>
	<b>Bibliography</b>	<b>269</b>

# List of Figures

2.1	Schematic of the Yale coflow laminar diffusion flame burner . . . . .	8
2.2	Spectral response of the Nikon D300s color filter array, and transmissivity of a 1 mm BG7 Schott color filter. . . . .	11
2.3	Spectral response of the Prosilica GC-1380-CH color filter array, and transmissivity of a coated 2 mm BG7 Schott color filter. . . . .	12
2.4	(Top) soot lookup tables evaluated for the Nikon D300s using the 1 mm BG7 color filter, and (bottom) for the Prosilica GC-1380CH using the coated 2 mm BG7 color filter. . . . .	13
2.5	Type-S thermocouple lookup table evaluated for the Prosilica GC-1380CH using an uncoated 2 mm BG7 color filter. . . . .	17
2.6	Two-level energy level diagram for the description of laser-induced fluorescence. . . . .	22
2.7	Four-level energy level diagram for the description of two-photon laser-induced fluorescence. . . . .	24
3.1	Centerline fuel velocity modulations investigated for the forced flames, with the five measured phases identified by the letters A, B, C, D, and E. . . . .	35
3.2	Schematic representation of the experimental setup used for the measurement of <i>NO</i> LIF. . . . .	35
3.3	Overlap between measured <i>NO</i> excitation spectrum (blue curve) and simulated one (red curve). The $Q(18)$ green line identifies the transition selected for the LIF excitation. . . . .	38
3.4	Experimental setup for the spectrally-resolved measurement of <i>NO</i> laser-induced fluorescence. . . . .	39
3.5	Radially resolved <i>NO</i> emission spectrum as collected through a Nikon FF-52 UV filter. . . . .	40
3.6	<i>NO</i> emission spectrum as collected through a Nikon FF-52 UV filter, for a fixed radial coordinate. . . . .	41
3.7	Simulated normalized <i>NO</i> LIF signal for the 65% methane flame: the white dashed line identifies the section along which the results of Fig. 3.8 are plotted. . . . .	42
3.8	Comparison between normalized simulated and measured fluorescence, evaluated considering the contribution of different emission bands, plotted along the section defined in Fig. 3.7. . . . .	43

3.9	<i>NO</i> laser-induced fluorescence signal as function of laser energy. The inset highlights the linear fluorescence regime. . . . .	44
3.10	Quenching cross sections of the most relevant <i>NO</i> collisional partners as function of temperature. . . . .	45
3.11	(a) Computed temperature, (b) Boltzmann population fraction, and (c) quenching rate used for the evaluation of Eq. 2.22. . . . .	46
3.12	Resonant (left) and off-resonant (right) <i>NO</i> laser-induced fluorescence signals for the steady 65% methane flame. . . . .	47
3.13	Computed (left) and measured (right) <i>NO</i> laser-induced fluorescence signals for the steady 65% methane flame. . . . .	48
3.14	Comparison between the measured and computed centerline fluorescence intensities for the steady 65% methane flame. The result from [4] is reported as well. . . . .	49
3.15	a) Measured temperature, (b) Boltzmann population fraction, (c) quenching rate, and (d) <i>NO</i> mole fraction. . . . .	50
3.16	Measured <i>NO</i> laser-induced fluorescence signal for the time-varying 65% methane flame - steady result and five phases of the (top) 30% and (bottom) 50% modulation. . . . .	52
3.17	Measured <i>CH*</i> chemiluminescence for the time-varying 65% methane flame - five phases of the 50% modulation. . . . .	53
3.18	Schematic representation of the experimental setup used for the measurement of <i>NO</i> LIF . . . . .	55
3.19	Total <i>CO</i> population fraction as function of three rotational quantum numbers <i>J</i> . . . . .	57
3.20	Overlap between measured <i>CO</i> excitation spectrum (blue curve) and simulated one (red curve). The green line identifies the wavelength selected for the LIF excitation. . . . .	58
3.21	Overlap of the broadened transitions (modelled as Lorentzians) with the laser pulse. . . . .	59
3.22	Transition's contribution as function of the rotational quantum number <i>J</i> . . . . .	60
3.23	<i>CO</i> emission spectrum plotted along with one of the <i>C</i> <sub>2</sub> <sup>*</sup> band and interference filter spectral collection region. . . . .	61
3.24	In-flame <i>CO</i> emission spectrum. (Top) off-resonant signals and spectral position of <i>C</i> <sub>2</sub> <sup>*</sup> Swan bands; (bottom) resonant signal and spectral position of the <i>CO</i> bands with respect to <i>C</i> <sub>2</sub> <sup>*</sup> ones and collection region. . . . .	62
3.25	Quenching cross sections of the most relevant <i>CO</i> collisional partners, as function of temperature. . . . .	63
3.26	(a) Computed temperature, (b) Boltzmann population fraction, (c) quenching rate, and (d) photoionization rate used for the evaluation of Eq. 2.27. . . . .	64
3.27	Relation between <i>CO</i> laser-induced fluorescence and laser energy. . . . .	65
3.28	Computed (left) and measured (right) <i>CO</i> laser-induced fluorescence signals for the steady 65% methane flame. . . . .	66

3.29	Fluorescence intensity cross section along the centerline and at three different heights above the burner: comparison between measured and simulated results. . . . .	67
3.30	(a) Measured temperature, (b) Boltzmann population fraction, and (c) quenching rate. . . . .	68
3.31	Computed (left), fluorescence-derived (center), and Raman-derived (right) CO mole fraction. . . . .	69
3.32	Fluorescence intensity cross section along the centerline and at three different heights above the burner: influence of the quenching correction. . . . .	70
3.33	(Top) measured and (bottom) computed <i>CO</i> laser-induced fluorescence signal for the time-varying 65% methane flame - steady result and five phases of the 30% modulation. . . . .	71
3.34	(Top) computed temperature and (bottom) computed Boltzmann population fraction for the steady and 30% modulation flame. . . . .	72
3.35	(Top) computed quenching rate and (bottom) photoionization rate for the steady and 30% modulation flame. . . . .	73
3.36	Fluorescence intensity along the flame centerline for the time-varying flame shown in Fig. 3.33. . . . .	74
3.37	(Top) measured and (bottom) computed <i>CO</i> laser-induced fluorescence signal for the time-varying 65% methane flame - steady result and five phases of the 50% modulation. . . . .	76
3.38	(Top) computed temperature and (bottom) computed Boltzmann population fraction for the steady and 50% modulation flame. . . . .	77
3.39	(Top) computed quenching rate and (bottom) photoionization rate for the steady and 50% modulation flame. . . . .	78
3.40	Fluorescence intensity along the flame centerline for the time-varying flame shown in Fig. 3.37. . . . .	79
3.41	<i>CO</i> fluorescence cross section of laser sheet intensity acquired during three different measurements. . . . .	81
4.1	Normalized LED temporal response, as measured by a photomultiplier.	87
4.2	LED linearity, as measured by integrating the voltages shown in Fig. 4.1. . . . .	87
4.3	Detector response of the red channel as a function of LED pulse length for the three selected cameras. The linear LED response, as measured by the photomultiplier, is shown by the solid line. . . . .	88
4.4	Detector response of the green channel as a function of LED pulse length for the three selected cameras. The linear LED response, as measured by the photomultiplier, is shown by the solid line. . . . .	89
4.5	Reciprocity curves of the red, green, and blue channels for the Nikon D300s determined from LED measurements. . . . .	90
4.6	Reciprocity curves of the red, green, and blue channels for the Nikon D70 determined from LED measurements. . . . .	90

4.7	Reciprocity curves of the red, green, and blue channels for the Prosilica GC-1380CH determined from LED measurements. . . . .	91
4.8	Difference between nominal and real exposure values for the DSLR camera Nikon D300s. . . . .	92
4.9	Five target images with increasing exposure times, cropped to select a strip in which vertical intensity gradients are minimal. The image sequence was used to obtain the camera response function of the D300s using the Debevec algorithm. Pixels with one or more saturated color channels are shown in yellow. . . . .	96
4.10	Comparison between red channel reciprocity curves as determined from LED measurements (markers) and Debevec algorithm (lines). . . . .	97
4.11	Comparison between green channel reciprocity curves as determined from LED measurements (markers) and Debevec algorithm (lines). . . . .	97
4.12	Spatial distribution of the red, green, and blue pixels on a Bayer pattern CFA. . . . .	100
4.13	Prosilica reciprocity results determined from the LED measurement, showing the effect of red pixel crosstalk on the bottom pixels of the green channel. . . . .	102
4.14	SNR as a function of normalized signal for the D300s red and green color channels; LDR image (top) and HDR image (bottom). . . . .	104
4.15	SNR variation for a fixed (top) and variable (bottom) number of frames from the blue channel of the D300s. . . . .	106
4.16	LDR and HDR TFP-derived temperature; D300s (left) and Prosilica (right). . . . .	109
4.17	LDR and HDR TFP-derived temperature (left) and SNR map (right) for the 65% methane flame evaluated with the D300s. . . . .	110
4.18	Conventional fiber image . . . . .	111
4.19	Defocused fiber image . . . . .	111
4.20	LDR and “defocused” TFP-derived temperature for the 65% methane flame evaluated with the D300s. . . . .	112
4.21	SNR map of the RGB channels in an image of a 40% ethylene flame taken with the D300s; contour plots highlight the SNR values in low intensity regions. . . . .	113
4.22	SNR map of the RGB channels in an image of a 40% ethylene flame taken with the Prosilica camera; contour plots highlight the SNR values in low intensity regions. . . . .	113
4.23	Number of averaged frames in the HDR image reconstruction - Nikon D300s. . . . .	114
4.24	Number of averaged frames in the HDR image reconstruction - Prosilica GC1380-CH. . . . .	115
4.25	HDR normalized intensity as a function of the LDR one - D300s (top) and Prosilica (bottom). . . . .	116
4.26	SNR map of the RGB channels in an image of a 40% ethylene flame taken with the D300s, comparing conventional averaging and HDR imaging. . . . .	117

4.27	Comparison between LDR- and HDR-derived temperature, in Kelvin, (left) and soot volume fraction (right). 100 % $CH_4$ flame, fuel velocity 72 cm/s, air coflow velocity 40 cm/s, 1.6 mm nozzle. . . . .	118
4.28	Comparison between LDR- and HDR-derived temperature, in Kelvin, (left) and soot volume fraction (right). 100 % $CH_4$ flame, fuel velocity 314 cm/s, air coflow velocity 5 cm/s, 1.6 mm nozzle. . . . .	119
5.1	Schematic drawing of the experimental set up, showing the detector, the collection optics, the burner, and the laser sheet forming optics. . . . .	125
5.2	Normalized phosphor temporal decay, shown for decreasing light intensity, when compared to the image intensifier gate and Sensicam exposures. . . . .	127
5.3	(a) Sensicam linearity as determined by LED measurements. Solid and empty markers identify the first and second frames of the interline-transfer CCD, respectively. (b) Image intensifier linearity as determined by photomultiplier measurements. . . . .	130
5.4	(a) Average counts evaluated from Rayleigh scattering images of dichlorodifluoromethane, divided by the neutral density filter transmittance, and (b) SNR of those images as function of the image intensifier gain. The error bars identify the standard deviation over 10 measurements. . . . .	132
5.5	(a) Rayleigh signal, in arbitrary units and corrected for laser sheet non-uniformities, and (b) SNR distribution of the conventional Rayleigh image for the steady methane/air partially premixed flame. The dashed lines define a region over which axial averaging was performed to plot the curves shown in Fig. 5.7, while the blue square pointed by the arrow shows the size of the interrogation region used for the SNR evaluation, as explained in Section 5.1.2. . . . .	134
5.6	(a) Rayleigh signal, in arbitrary units and corrected for laser sheet non-uniformities, and (b) SNR distribution of the averaged Rayleigh image for the steady methane/air partially premixed flame. The dashed lines define a region over which axial averaging was performed to plot the curves shown in Fig. 5.7 . . . . .	135
5.7	(a) Comparison between the axially averaged Rayleigh counts and (b) the axially averaged SNR, for the steady partially premixed methane/air flame. . . . .	137
5.8	(a) Rayleigh signal, in arbitrary units and corrected for laser sheet non-uniformities, and (b) SNR distribution of the conventional Rayleigh images for the turbulent methane/air partially premixed flame ( $Re \sim 4000$ ). . . . .	138
5.9	(a) Rayleigh signal, in arbitrary units and corrected for laser sheet non-uniformities, and (b) SNR distribution of the averaged Rayleigh images for the turbulent methane/air partially premixed flame ( $Re \sim 4000$ ). . . . .	139
5.10	Schematic diagram of the experimental set-up used for the HDR planar Rayleigh scattering imaging. . . . .	141

5.11	(a) HDR image of Rayleigh intensity, in arbitrary units, from a Freon-12 jet injected into air (corrected for laser sheet non uniformities); the white line identifies the separation between the saturated (left) and unsaturated areas (right) of the raw Freon-12 Rayleigh image. (b) SNR distributions for the HDR, (c) LDR, and (d) conventionally-averaged image. The solid black lines define a region over which the axial averaging was performed to plot the curves shown in Fig. 5.12b.	145
5.12	(a) Comparison between the axially averaged Rayleigh counts and (b) the axially averaged SNR.	146
5.13	HDR normalized pixel intensity as function of the LDR one.	147
6.1	Photograph (left) and schematic representation (right) of the SLICE coflow burner.	152
6.2	Two-dimensional chemiluminescence intensity comparison between Nikon D300s blue channel (left half) and 430 nm interference filter signal (right half). Each chemiluminescent signal was normalized with respect to its maximum. The horizontal dashed lines are axial locations that are the focus of analysis in Section 6.2.	154
6.3	(a) Spectral transmissivity of the Nikon D300s blue channel and a 430 nm interference filter, each normalized with respect to its maximum. (b) Normalized flame and simulated $CH^*$ spectrum showing the spectral location of relevant flame emitting species.	156
6.4	Influence of lens $f$ -number on the Abel-inverted two-dimensional chemiluminescence of the reference nitrogen-diluted 65% methane flame. Each image was normalized with respect to its maximum value.	157
6.5	(a) Flame spectrum, normalized to the maximum, as a function of the radial coordinate (7.5 mm above the burner) for the reference nitrogen-diluted 65% methane flame introduced in Section 6.1. (b) Radial chemiluminescence profiles, normalized with respect to their maximum values, obtained by integrating over the spectral regions of the 430 nm and blue filters.	159
6.6	Comparison between the radial chemiluminescence, as collected by the blue channel (left half), and 430 nm interference filter (right half). The three curves identify the axial locations defined in Fig. 6.2, and each is normalized with respect to its maximum.	161
6.7	Variation of the normalized peak $CH^*$ concentration when evaluating $CH_{em}$ in the range 1500 K - 2000 K.	164
6.8	Line-of-sight luminosity of a representative microgravity partially sooty flame (40% $CH_4$ , 60% $N_2$ , 17 cm/s and 89 cm/s for coflow and fuel velocity, respectively) as collected by the (a) blue and (b) green channels. (c) Soot luminosity as determined by the subtraction between the green and blue channels. (d) Flames blue signal free of soot interference. Each image was normalized with respect to its maximum.	165

6.9	Two-dimensional $CH^*$ mole fraction of the reference nitrogen-diluted 65% methane flame (left half) as compared to the result from [111] (right half). . . . .	167
6.10	Two-dimensional $CH^*$ mole fraction for the nitrogen-diluted methane flames from sequence <b>A</b> of Table 1 (40% $CH_4$ , 60% $N_2$ , coflow velocity, labeled C, of 17 cm/s, fuel velocities, labeled F, between 17 cm/s and 89 cm/s). The 0 g result is on the left half of each plot, and the 1 g result is on the right half. . . . .	169
6.11	Variation of the peak $CH^*$ concentration for the flame sequences <b>A</b> , <b>B</b> , and <b>C</b> of Table 6.1. The coflow and fuel velocities are summarized in each plot. . . . .	170
6.12	Integrated $CH^*$ concentration in a cross section and integrated heat release rate (each normalized with respect to its minimum normal gravity value), for the flame sequences <b>A</b> , <b>B</b> , and <b>C</b> of Table 1. The coflow and fuel velocities are summarized in each plot. . . . .	171
6.13	Comparison between normalized two-dimensional $CH^*$ concentration (left half) and computed two-dimensional heat release rate (right half) for two of the flames from sequence <b>A</b> (40% $CH_4$ , 60% $N_2$ , coflow velocity of 17 cm/s and fuel velocities of 25 and 50 cm/s). Microgravity and normal gravity results are shown in the two leftmost and the two rightmost images, respectively. . . . .	173
6.14	(a) Radially integrated $CH^*$ , (b) radially integrated $CH$ , and (c) radially integrated heat release rate of a representative SLICE flame from sequence <b>A</b> (40% $CH_4$ , 60% $N_2$ , coflow velocity of 17 cm/s, fuel velocity of 25 cm/s.) Solid lines identify microgravity results, while dashed lines identify normal gravity ones. Each curve is normalized with respect to its maximum. . . . .	174
6.15	Variation of the computed peak heat release rate for the flame sequences <b>A</b> , <b>B</b> , and <b>C</b> of Table 6.1. The coflow and fuel velocities are summarized in each plot. . . . .	175
7.1	Decrease of average flow velocity as a function of increasing chamber pressure. . . . .	179
7.2	(Top) Normalized flame luminosity, (center) soot temperature, in Kelvin, and (bottom) soot volume fraction for the 50% methane flame as a function of pressure (in atm). . . . .	181
7.3	(Top) Normalized flame luminosity, (center) soot temperature, in Kelvin, and (bottom) soot volume fraction for the 55% methane flame as a function of pressure (in atm). . . . .	182
7.4	(Top) Normalized flame luminosity, (center) soot temperature, in Kelvin, and (bottom) soot volume fraction for the 60% methane flame as a function of pressure (in atm). . . . .	183
7.5	(Top) Normalized flame luminosity, (center) soot temperature, in Kelvin, and (bottom) soot volume fraction for the 65% methane flame as a function of pressure (in atm). . . . .	184

7.6	(Top) Soot temperature, in Kelvin, and (bottom) soot volume fraction for the $CH^*$ -subtracted 50% methane flame as a function of pressure (in atm). . . . .	186
7.7	(Top) Soot temperature, in Kelvin, and (bottom) soot volume fraction for the $CH^*$ -subtracted 55% methane flame as a function of pressure (in atm). . . . .	187
7.8	(Top) Soot temperature, in Kelvin, and (bottom) soot volume fraction for the $CH^*$ -subtracted 60% methane flame as a function of pressure (in atm). . . . .	188
7.9	(Top) Soot temperature, in Kelvin, and (bottom) soot volume fraction for the $CH^*$ -subtracted 65% methane flame as a function of pressure (in atm). . . . .	189
7.10	Peak centerline soot temperature, in Kelvin, for a subset of the four tested nitrogen-diluted methane flames as a function of pressure. . .	191
7.11	Peak centerline soot volume fraction for the four tested nitrogen-diluted methane flames as a function of pressure. . . . .	191
7.12	Computed peak centerline soot temperature, in Kelvin, for the four nitrogen-diluted methane flames as a function of pressure. Solid lines refer to results that include a soot model. . . . .	192
7.13	Computed peak centerline soot volume fraction for the four nitrogen-diluted methane flames as a function of pressure. . . . .	192
8.1	Sequence to convert a raw image into a demosaiced one (image courtesy of skyandtelescope.com). . . . .	195
8.2	General pixel coordinates used for the formulation of demosaicing algorithms. . . . .	196
8.3	(a) Soot temperature, in Kelvin, for the reference $C_2H_4$ flame evaluated with the Nikon D300s, and (b) normalized radial gradients intensity. Soot temperature evaluated considering the (c) B/G and (d) B/G* ratios with the Prosilica. Soot temperature evaluated after implementation of (e) bilinear interpolation and (f) Malvar algorithm. . . . .	200
8.4	Ratios between non-demosaiced and demosaiced Prosilica temperature results: (a) bilinear interpolation and (b) Malvar algorithm. . . . .	202
8.5	Temperature maps' SNR, calculated with the Prosilica. (a) non-demosaiced result, (b) bilinear interpolation, and (c) Malvar algorithm. . . . .	203
8.6	Abel-inverted blue profiles collected with the Prosilica and with a raw image magnification of 44 pixel/mm: (a) non demosaiced result, (b) bilinear interpolation, and (c) Malvar algorithm. The white dashed line identifies the section chosen to plot the results of Fig. 8.9. . . .	204
8.7	Abel-inverted blue profiles collected with the Prosilica and with a raw image magnification of 34 pixel/mm: (a) non demosaiced result, (b) bilinear interpolation, and (c) Malvar algorithm. . . . .	205
8.8	Abel-inverted blue profiles collected with the Prosilica and with a raw image magnification of 20 pixel/mm: (a) non demosaiced result, (b) bilinear interpolation, and (c) Malvar algorithm. . . . .	205

8.9	Normalized radial intensities, along the direction identified by the dashed line of Fig. 8.6a, of the Abel-inverted blue profiles shown in Figs. 8.6 to 8.8. . . . .	206
9.1	Yale prototype of the ACME CLD burner. . . . .	209
9.2	CNC-machined brass plate used to replace the conventional honeycomb in the 25.4 mm (1") coflow burner. . . . .	210
9.3	Comparison between velocity profiles measured at different HAB. . . . .	211
9.4	Version of the ACME CLD burner built by ZIN Technologies. . . . .	212
9.5	Comparison between peak flame luminosity (top), and flame length (bottom), for flames lit in an air-filled and nitrogen-filled pressure chamber. . . . .	213
9.6	Top view of the ACME CLD burner with the hot wire scanning directions identified by the blue, red, green, and orange arrows. The teal arrow identifies the ACME camera viewing direction. . . . .	214
9.7	Calibration curve of the hot wire probe used for the measurements of the CLD burner flow profiles. . . . .	217
9.8	(Left) velocity profiles as determined from hot wire measurements and (right) symmetry plots - 10 cm/s matched flow velocities. . . . .	219
9.9	(Left) velocity profiles as determined from hot wire measurements and (right) symmetry plots - 30 cm/s matched flow velocities. . . . .	219
9.10	(Left) velocity profiles as determined from hot wire measurements and (right) symmetry plots - 50 cm/s matched flow velocities. . . . .	219
9.11	Original (left) and final (right) CLD burner coflow internal components. . . . .	220
9.12	50% methane flames selected for the verification of flame symmetry: the solid white lines identify the flame bases, while the dashed lines are the $\pm 0.5$ mm variations. Flow velocity shown at the bottom of each flame. . . . .	222
9.13	Drawing of the ACME imaging system, showing the camera, lens, and optical filter barrel. . . . .	223
9.14	Spectral response of the Prosilica GC1380-CH, BG7 coated color filter, and turning mirror. . . . .	224
9.15	Geometry and optical path of the ACME color camera. . . . .	225
9.16	Pt thermocouple lookup table: comparison between experimental color ratios and numerically-derived curves. The error bars identify the standard deviation over 10 samples. . . . .	227
9.17	Calibration constants as determined from thermocouple measurements. . . . .	228
9.18	Expected decrease of the average flow velocity as a consequence of pressure increase. . . . .	230
9.19	Expected CIR relative pressure increase as a function of time and flow rates. . . . .	230
9.20	Normalized flame luminosity of nitrogen-diluted methane flames lit on the flight (top) and ground units of the CLD flame burner (bottom). . . . .	234

9.21	Soot temperature evaluated as a function of pressure for the 100% ethylene flames: 35 cm/s (left) and 20 cm/s average flow velocities (right), as measured at atmospheric pressure. . . . .	235
9.22	Soot volume fraction evaluated as a function of pressure for the 100% ethylene flames: 35 cm/s (left) and 20 cm/s average flow velocities (right), as measured at atmospheric pressure. . . . .	236
9.23	$CH^*$ mole fraction, as a function of pressure, for a 100% (top), 80% (center), and 50% (bottom) nitrogen-diluted methane flame. Flow velocity equal to 10 cm/s, as measured at atmospheric pressure. . . .	237
A.1	(Left) velocity profiles as determined from hot wire measurements and (right) symmetry plots - 10 cm/s matched flow velocities. (Top) 0.5 mm, (middle) 5 mm, (bottom) 10 mm HAB. . . . .	243
A.2	(Left) velocity profiles as determined from hot wire measurements and (right) symmetry plots - 20 cm/s matched flow velocities. (Top) 0.5 mm, (middle) 5 mm, (bottom) 10 mm HAB. . . . .	244
A.3	(Left) velocity profiles as determined from hot wire measurements and (right) symmetry plots - 30 cm/s matched flow velocities. (Top) 0.5 mm, (middle) 5 mm, (bottom) 10 mm HAB. . . . .	245
A.4	(Left) velocity profiles as determined from hot wire measurements and (right) symmetry plots - 40 cm/s matched flow velocities. (Top) 0.5 mm, (middle) 5 mm, (bottom) 10 mm HAB. . . . .	246
A.5	(Left) velocity profiles as determined from hot wire measurements and (right) symmetry plots - 50 cm/s matched flow velocities. (Top) 0.5 mm, (middle) 5 mm, (bottom) 10 mm HAB. . . . .	247
A.6	(Left) velocity profiles as determined from hot wire measurements and (right) symmetry plots - 0 and 10 cm/s for fuel and coflow velocities, respectively. . . . .	248
A.7	(Left) velocity profiles as determined from hot wire measurements and (right) symmetry plots - 0 and 20 cm/s for fuel and coflow velocities, respectively. . . . .	248
A.8	(Left) velocity profiles as determined from hot wire measurements and (right) symmetry plots - 0 and 30 cm/s for fuel and coflow velocities, respectively. . . . .	248
A.9	(Left) velocity profiles as determined from hot wire measurements and (right) symmetry plots - 0 and 40 cm/s for fuel and coflow velocities, respectively. . . . .	249
A.10	(Left) velocity profiles as determined from hot wire measurements and (right) symmetry plots - 0 and 50 cm/s for fuel and coflow velocities, respectively. . . . .	249
A.11	(Left) velocity profiles as determined from hot wire measurements and (right) symmetry plots - 10 and 30 cm/s for fuel and coflow velocities, respectively. . . . .	249

A.12 (Left) velocity profiles as determined from hot wire measurements and (right) symmetry plots - 10 and 50 cm/s for fuel and coflow velocities, respectively. . . . .	250
A.13 (Left) velocity profiles as determined from hot wire measurements and (right) symmetry plots - 30 and 10 cm/s for fuel and coflow velocities, respectively. . . . .	250
A.14 (Left) velocity profiles as determined from hot wire measurements and (right) symmetry plots - 30 and 50 cm/s for fuel and coflow velocities, respectively. . . . .	250
A.15 (Left) velocity profiles as determined from hot wire measurements and (right) symmetry plots - 50 and 10 cm/s for fuel and coflow velocities, respectively. . . . .	251
A.16 (Left) velocity profiles as determined from hot wire measurements and (right) symmetry plots - 50 and 30 cm/s for fuel and coflow velocities, respectively. . . . .	251
A.17 Turbulence results. In each subplots, the top figure shows the flow velocity, while the bottom figure shows the maximum percent deviation with respect to the average velocity. The error bars are evaluated as $\pm \sigma$ . . . . .	252
A.18 (Left) velocity profiles as determined from hot wire measurements and (right) symmetry plots - 10 cm/s matched flow velocities. (Top) 0.5 mm, (middle) 5 mm, (bottom) 10 mm HAB. . . . .	253
A.19 (Left) velocity profiles as determined from hot wire measurements and (right) symmetry plots - 20 cm/s matched flow velocities. (Top) 0.5 mm, (middle) 5 mm, (bottom) 10 mm HAB. . . . .	254
A.20 (Left) velocity profiles as determined from hot wire measurements and (right) symmetry plots - 30 cm/s matched flow velocities. (Top) 0.5 mm, (middle) 5 mm, (bottom) 10 mm HAB. . . . .	255
A.21 (Left) velocity profiles as determined from hot wire measurements and (right) symmetry plots - 40 cm/s matched flow velocities. (Top) 0.5 mm, (middle) 5 mm, (bottom) 10 mm HAB. . . . .	256
A.22 (Left) velocity profiles as determined from hot wire measurements and (right) symmetry plots - 50 cm/s matched flow velocities. (Top) 0.5 mm, (middle) 5 mm, (bottom) 10 mm HAB. . . . .	257

# List of Tables

4.1	Cases analyzed for the evaluation of SNR sensitivity. . . . .	105
6.1	Summary of the flow conditions and camera settings of the normal gravity and microgravity image sequences considered in this chapter. . . . .	153
B.1	Nitrogen-diluted ACME $CH_4$ flames: 50 cm/s flow velocities. . . . .	259
B.2	Nitrogen-diluted ACME $CH_4$ flames: 45 cm/s flow velocities. . . . .	259
B.3	Nitrogen-diluted ACME $CH_4$ flames: 40 cm/s flow velocities. . . . .	260
B.4	Nitrogen-diluted ACME $CH_4$ flames: 35 cm/s flow velocities. . . . .	260
B.5	Nitrogen-diluted ACME $CH_4$ flames: 30 cm/s flow velocities. . . . .	261
B.6	Nitrogen-diluted ACME $CH_4$ flames: 25 cm/s flow velocities. . . . .	261
B.7	Nitrogen-diluted ACME $CH_4$ flames: 20 cm/s flow velocities. . . . .	262
B.8	Nitrogen-diluted ACME $CH_4$ flames: 15 cm/s flow velocities. . . . .	262
B.9	Nitrogen-diluted ACME $CH_4$ flames: 10 cm/s flow velocities. . . . .	262
B.10	Nitrogen-diluted ACME $CH_4$ flames: 10 cm/s and 30 cm/s fuel and coflow velocities, respectively. . . . .	263
B.11	Nitrogen-diluted ACME $CH_4$ flames: 10 cm/s and 50 cm/s fuel and coflow velocities, respectively. . . . .	263
B.12	Nitrogen-diluted ACME $CH_4$ flames: 30 cm/s and 10 cm/s fuel and coflow velocities, respectively. . . . .	264
B.13	Nitrogen-diluted ACME $CH_4$ flames: 30 cm/s and 50 cm/s fuel and coflow velocities, respectively. . . . .	264
B.14	Nitrogen-diluted ACME $CH_4$ flames: 50 cm/s and 10 cm/s fuel and coflow velocities, respectively. . . . .	265
B.15	Nitrogen-diluted ACME $CH_4$ flames: 50 cm/s and 30 cm/s fuel and coflow velocities, respectively. . . . .	265
B.16	Nitrogen-diluted ACME $C_2H_4$ flames: 35 cm/s flow velocities. . . . .	266
B.17	Nitrogen-diluted ACME $C_2H_4$ flames: 30 cm/s flow velocities. . . . .	266
B.18	Nitrogen-diluted ACME $C_2H_4$ flames: 25 cm/s flow velocities. . . . .	267
B.19	Nitrogen-diluted ACME $C_2H_4$ flames: 20 cm/s flow velocities. . . . .	267
B.20	Nitrogen-diluted ACME $C_2H_4$ flames: 15 cm/s flow velocities. . . . .	268
B.21	Nitrogen-diluted ACME $C_2H_4$ flames: 10 cm/s flow velocities. . . . .	268

# Chapter 1

## Introduction

Optical diagnostic techniques are a powerful scientific tool that can be used to investigate and quantify important physical and chemical properties in a wide variety of combustion systems. Their application can range from the study of idealized laboratory-scale diffusion flames, to the characterization of full-scale industrial combustors. Combustion and oil-based energy, despite the long-term issues with fossil fuel availability, as well as health and global warming problems related to combustion-derived pollutants and emissions, still play a fundamental role in our society as we transition towards more ecological and renewable energy sources [1]. Increasing emission regulations require modern combustion systems to be efficient to minimize harmful and unwanted combustion byproducts (soot, carbon monoxide,  $NO_x$ , etc). A deep understanding of the physics and chemistry involved in the production of these byproducts is therefore required if technological advances in combustion devices are to be achieved. From this standpoint, fundamental research can provide insight into combustion processes. The analysis of relatively simple reactive flows allows for an accurate experimental quantification of chemical species and temperature that can be replicated by, and used to validate, numerical simulations and chemical models. Numerical simulations have, in fact, gained increasing importance due to their ability

to not only speed up the development of new technologies and concepts, but also guide the design of better and targeted experiments.

The Yale combustion research group led by Professor Long, in collaboration with the numerical group led by Professor Smooke, has been focusing on the experimental study and characterization of coflow laminar diffusion (CLD) flames and on the validation of numerically-derived results through experimental observations and measurements. A reference coflow burner was designed to facilitate comparisons between experiments and simulations, and target nitrogen-diluted methane and ethylene flames were selected as test cases for this systematic analysis. Previous students were involved with the measurement of temperature and major/minor species concentrations in both non-sooty steady methane flames [2], and sooty ethylene flames [3,4]. Soot and major species measurements in time-varying flames [3,4] extended the examination to the wider range of interactions between chemistry and flow field that unsteady phenomena can provide. Additionally, in collaboration with NASA, our team performed experiments on CLD flames in normal gravity and microgravity, and investigated flame structure, radical species chemiluminescence [5], as well as soot temperature and soot volume fraction [6]. Because current computational models are still not able to fully predict flames at the extremes of fuel concentration (both highly diluted and sooty flames), microgravity has the advantage of providing an easier environment in which to test and refine those models. Microgravity's lack of buoyancy simplifies the flow field and the results' interpretation; moreover, highly-diluted flame conditions, which are not sustained in normal gravity, can be created and stabilized in microgravity.

In combustion experiments, laser-based imaging diagnostics are among the most accurate techniques. They can provide quantitative, nonintrusive measurements of chemical species concentration, gas density, and temperature with a high degree of spatial and temporal resolution. However, in microgravity, practical limitations

restrict the available optical diagnostics to emission-based ones such as pyrometry and chemiluminescence. New approaches and tactics must therefore be envisioned to maximize the scientific return when employing these simple and relatively limited techniques. The spectral characterization of consumer digital single-lens reflex (DSLR) cameras, along with the development of alternative approaches for absolute light calibrations [7], proved very valuable during the NASA *Structure and Liftoff in Combustion Experiments* (SLICE) campaign. From the collected images, our team extracted not only flame structure information, but also quantitative data regarding  $CH^*$  concentration, soot temperature, and soot volume fraction. Numerical data was also available and complemented the experimental results by providing further insight into soot formation and flame behavior in microgravity [8].

Building on the work already done in our laboratory and outlined in the previous paragraphs, my dissertation research began with extending the chemical species database of the Yale target flames, continued with developing and implementing new imaging approaches for the improvement of images' signal-to-noise ratio (SNR), and concluded with doing preparatory work for the NASA *Advanced Combustion via Microgravity Experiments* (ACME) campaign. Specifically, this dissertation is organized as follows:

Chapter 2 describes the Yale coflow burner and the main diagnostics implemented throughout this thesis. Emission-based imaging techniques such as color ratio pyrometry and chemiluminescence are complemented by the description of how to perform absolute light intensity calibration and obtain quantitative values of soot volume fraction and species concentrations. The theoretical background of laser diagnostics, such as laser-induced fluorescence and Rayleigh scattering, is presented as well.

In Chapter 3, nitric oxide and carbon monoxide concentrations are measured in steady and time-varying nitrogen-diluted methane flames with an imaging approach that returned results with improved SNR. Diffusion flames produce these chemical

species in very low concentrations and sensitive techniques, such as single- and two-photon laser-induced fluorescence, are required in order to accurately measure them. When possible, a comparison was done between the measured and the simulated fluorescence signal, rather than the measured and the computed species mole fraction in order to achieve a better SNR. The study of these combustion byproducts is important from an environmental and health point of view: nitric oxide is in fact responsible for photochemical smog and ozone depletion, and carbon monoxide is a toxic pollutant. Understanding how these species are formed, and the best approaches to reducing them in practical combustion systems, is still one of the major goals of today's research.

Chapter 4 introduces the concept of high dynamic range (HDR) imaging and applies it to the quantitative measurements of flame temperature (using thin filament pyrometry), and soot temperature and volume fraction (using color ratio pyrometry), in selected coflow laminar diffusion flames. Due to enhanced residence times, microgravity flames tend to be sootier, and thus more luminous, than their normal gravity counterparts. When collecting images in microgravity for the SLICE campaign, this increased luminosity caused hundreds of images to be partially saturated and, in turn, made them not immediately usable for quantitative measurements. To overcome this limitation, HDR imaging was tested and applied to the quantitative analysis of these partially saturated images. After proper characterization of the detector's linearity and reciprocity, a simplified HDR algorithm was implemented and was able to return results with an improved SNR while allowing for a more complete use of the SLICE image database.

In Chapter 5, as a way to improve the signal-to-noise ratio in time-resolved laser-based experiments, the HDR approach is extended and applied to the imaging of an unsteady jet of dichlorofluoromethane injected in air, using Rayleigh scattering. The ability of interline transfer CCD cameras to collect two consecutive frames with

very short temporal separation, combined with the use of a dual-laser system with different energies, allowed for partial image saturation to be induced in one of the two camera frames, and an HDR image with improved SNR to be reconstructed.

Additionally, a novel image read-out approach is presented and its application to turbulent reactive flows demonstrated using Rayleigh scattering. By exploiting the temporal decay characteristics of image intensifiers, and by timing the relative delay between intensifier's gate and laser pulse, the phosphor screen's emitted light was distributed over the two sequential frames of an interline transfer CCD camera and used to reconstruct a two-image average that showed improved SNR.

In Chapter 6, the non-sooty blue flames from the SLICE image database are analyzed to assess the color camera's blue signal's ability to accurately sample the  $CH^*$  radical chemiluminescence. A spectral characterization of the camera, along with the spectral analysis of a well-known nitrogen-diluted methane flame, allowed for a calibration of the detector so that absolute concentration of  $CH^*$  could be evaluated in selected normal and microgravity CLD flames. Additionally, a comparison with numerical results allowed for the study of the relationship of  $CH^*$  chemiluminescence to the local and total flame heat release rate.

In Chapter 7, selected nitrogen-diluted methane flames are investigated as a function of pressure and fuel dilution, and the experimental findings are compared to the numerical predictions as a way to verify the chemical models. As mentioned above, current computational models are in fact not able to fully predict CLD flames at the extremes of fuel concentration (i.e. highly diluted, or heavily sooty flames). This prompted the joint experimental/numerical study on the effects that those parameters have on the structure and sooting behavior of coflow diffusion flames.

In Chapter 8, the implementation of demosaicing algorithms for the post-processing of the ACME camera's color images is demonstrated to maintain the original full spatial resolution when the raw images are decoded into the three color channels. This,

moreover, helped preserving the correct image intensity gradients, and techniques based on color ratios were able to return more accurate results (i.e. color ratio pyrometry).

Chapter 9 presents the preliminary work done for the characterization of the flight and ground units of the ACME CLD burners. The burner velocity profiles are measured using hot-wire anemometry, and flame images are collected as a function of flow rates, fuel dilution, and pressure to build the normal gravity image database. The ACME imaging system is spectrally characterized and an absolute light intensity calibration is performed using a heated S-type thermocouple.

Finally, Chapter 10 provides some concluding remarks and suggestions for future research.

# Chapter 2

## Experimental hardware and optical diagnostics

This chapter introduces the Yale coflow laminar diffusion flame burner that is used for the study of the Yale target flames, and describes the main optical diagnostic techniques that have been employed throughout this thesis.

### 2.1 Yale coflow burner

The standard sooty and non-sooty flames that have become a target for both experiments and computational investigations at the Yale *Center for Laser Diagnostics* are axisymmetric nitrogen-diluted laminar coflow diffusion flames. The sooty ethylene flames have fuel concentrations of 80%, 60%, 40%, and 32%, with  $N_2$  balance, by volume. The non-sooty methane flame has a fuel concentration of 65%, with  $N_2$  balance, by volume. The burner on which these flames are lit is shown in Fig. 2.1; it has an axisymmetric structure with an inner stainless steel fuel tube with a 4 mm I.D. surrounded by a 75 mm I.D. air coflow. The length of the fuel tube is such that a parabolic velocity profile is established at the outlet, while the coflow velocity has a plug profile. A 1/32" cell honeycomb, placed at the burner exit and flush with the

fuel tube, ensures the straightness and symmetry of the coflow. The average flow velocities of 35 cm/s, for both fuel mixture and oxidizer, are such that the resulting non-sooty flame is lifted  $\sim 2$  mm from the burner surface avoiding any unwanted heat transfer to the fuel tube.

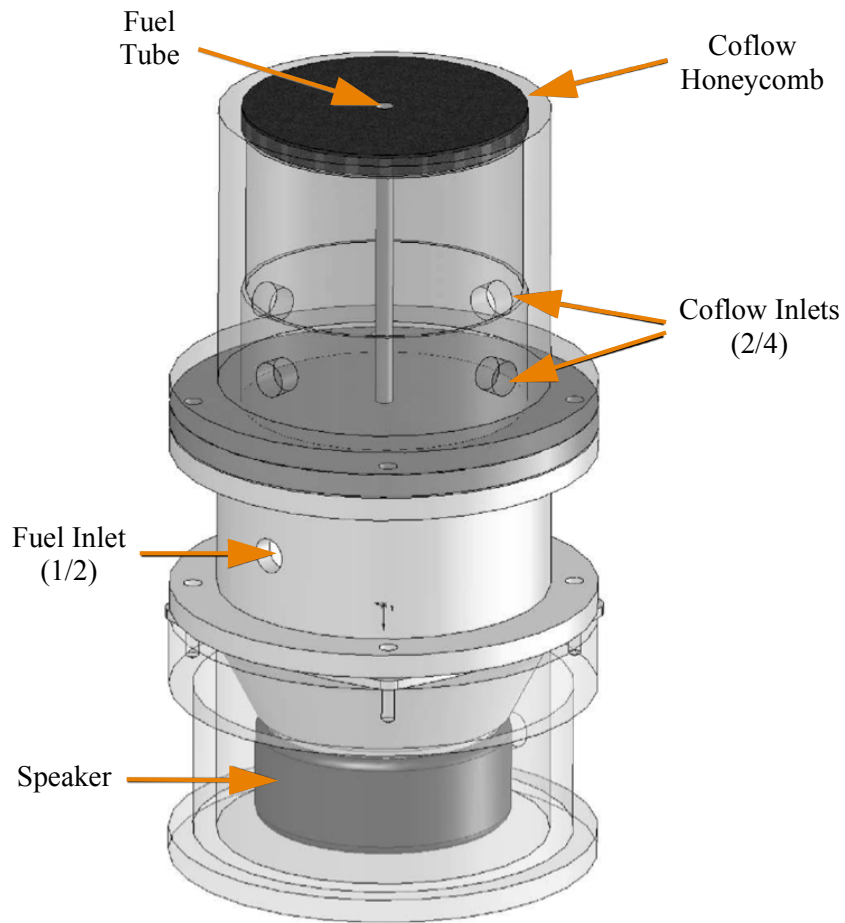


Figure 2.1: Schematic of the Yale coflow laminar diffusion flame burner

The addition of an inert gas to the fuel mixture (nitrogen) serves the purpose of reducing the overall flame temperature and varying the soot load; for the methane flame case the soot is reduced to only a faint tip, so that laser diagnostics such as Rayleigh scattering can be implemented without the detector-damaging problems of elastic scattering from soot particles. The burner has been specifically designed to

facilitate the comparison between experimental results and numerical simulation; the well known flow characteristics - velocity profiles, and the assumption that the burner surface is at room temperature, for the lifted case - are in fact the boundary conditions of the numerical simulations (recent work done in our lab has shown that the constant temperature assumption is not valid for the attached sooty flames [9]). The axisymmetric structure of the flames allows for a reduction of the problem unknowns, since the simulation can be performed only along the two-dimensional flame cross-section. The creation of forced, time-varying flames can be accomplished with a speaker that is placed in the fuel plenum; by driving the speaker with a sinusoidal input (out of a function generator) it is possible to create modulated and periodic fuel velocity profiles.

## 2.2 Luminosity-based techniques

### 2.2.1 Color ratio pyrometry

Pyrometry is a technique capable of inferring the temperature of a body from its emitted radiation. A body's radiance  $I$ , in fact, depends on the temperature according to Planck's law:

$$I(\lambda, T) = \epsilon(\lambda) \frac{2\pi hc^2}{\lambda^5 (e^{\frac{hc}{\lambda kT}} - 1)}. \quad (2.1)$$

Here,  $\epsilon(\lambda)$  is the body wavelength emissivity dependence,  $h$  the Planck's constant,  $c$  the speed of light, and  $k$  the Boltzmann constant.

Soot is made up of carbon-based particles that are formed during combustion processes from species such as acetylene ( $C_2H_2$ ) and polycyclic aromatic hydrocarbons (PAHs) and their radiation is responsible for the orange color of some flames; at typical flame temperatures soot that is produced in the flame emits in the visible region,

allowing the majority of scientific and consumer detectors to be used as imaging pyrometers. The signal measured by a detector,  $S_F$ , can be related to the intensity of radiation, integrated over the detector's detection wavelengths, and it is proportional to the exposure time  $\tau$  as in Eq. 2.2:

$$S_F = \tau \int_{\lambda_1}^{\lambda_2} \epsilon(\lambda)\eta(\lambda) \frac{2\pi hc^2}{\lambda^5 (e^{\frac{hc}{\lambda kT}} - 1)} d\lambda. \quad (2.2)$$

Here  $\eta(\lambda)$  accounts for the efficiency of the detector, as well as for the transmittance of the collection optics and geometric factors;  $\lambda_1$  and  $\lambda_2$  are the extremes of the detection bandwidth which, for detectors sensitive to the visible spectrum, are usually 400 *nm* and 700 *nm*.

In conventional color ratio pyrometry the radiation signal is collected through two different narrowband filters (with a filter's FWHM smaller than the spacing between the central wavelengths of the two filters) so that each filter's transmissivity  $\eta(\lambda)$  can be considered constant and Eq. 2.2 simplified [10, 11]. The resulting implicit relation can then be iteratively solved for the temperature once the characterization of the detection system is known. An alternative approach, introduced by [12] and extensively used in our research group for the evaluation of soot temperature, relies on the use of the broadband color filter array (CFA) that already equips a color camera in place of the aforementioned narrowband filters. By measuring the spectral response of each color filter  $\eta_{F_i}(\lambda)$  the integral in Eq. 2.2 can be computed numerically as a function of temperature and, if the emissivity  $\epsilon(\lambda)$  is known, the ratio between two color signals can be evaluated using Eq. 2.3:

$$\frac{S_{F_1}}{S_{F_2}} = \frac{\int_{\lambda_1}^{\lambda_2} \eta_{F_1}(\lambda) \frac{\epsilon(\lambda)}{\lambda^5 (e^{\frac{hc}{\lambda kT}} - 1)} d\lambda}{\int_{\lambda_1}^{\lambda_2} \eta_{F_2}(\lambda) \frac{\epsilon(\lambda)}{\lambda^5 (e^{\frac{hc}{\lambda kT}} - 1)} d\lambda}. \quad (2.3)$$

When numerically evaluated, Eq. 2.3 will produce a lookup table that can be used to estimate a temperature value after a color ratio is known. Figs. 2.2 and 2.3 show the measured spectral response of the CFA of two selected color detectors: the Nikon D300s (used in the microgravity SLICE campaign - see Chapters 4 and 6) and the Prosilica GC-1380CH (selected for the microgravity ACME campaign - see Chapters 4 and 9). Superimposed is the transmissivity of a BG7 color filter which is used to reduce the strong red component emitted by sooty flames and balance the response of the three color channels as a way to improve the signal-to-noise ratio of the measurement. The SLICE imaging setup relied on a 2 mm thick BG color filter (whose response mimics the one of a 1 mm BG7 Schott filter), while the ACME setup is equipped with a coated 2 mm Schott filter.

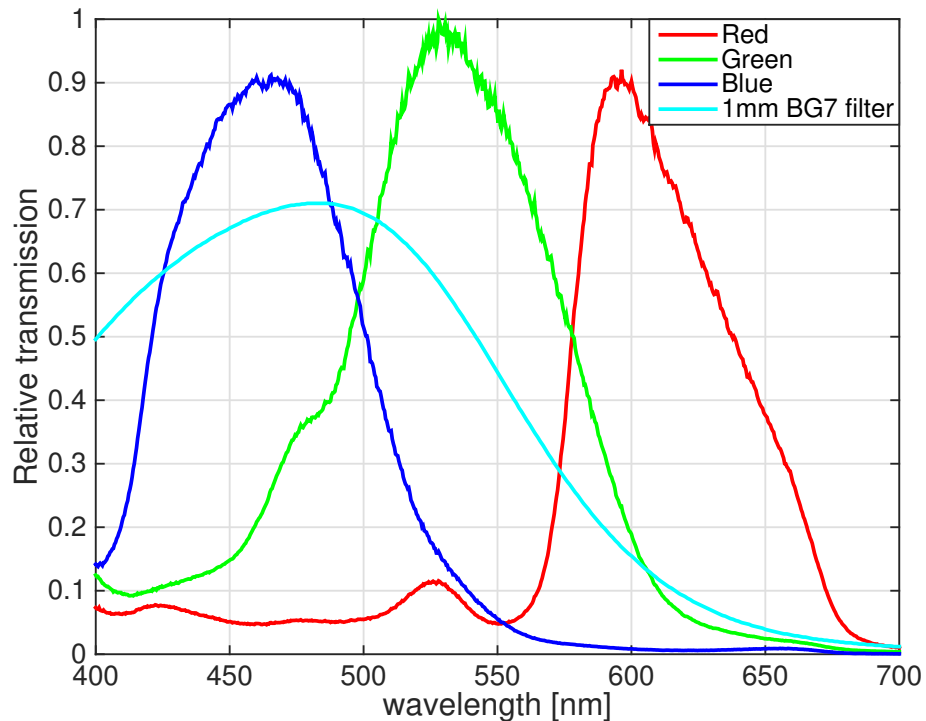


Figure 2.2: Spectral response of the Nikon D300s color filter array, and transmissivity of a 1 mm BG7 Schott color filter.

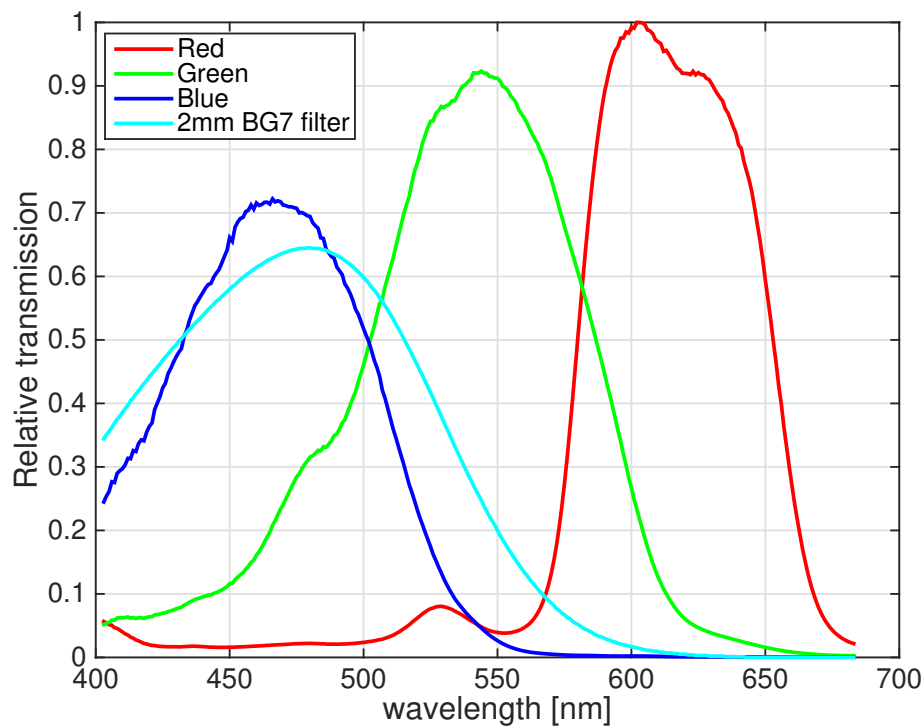


Figure 2.3: Spectral response of the Prosilica GC-1380-CH color filter array, and transmissivity of a coated 2 mm BG7 Schott color filter.

Figure 2.4 shows the lookup tables evaluated for the measurement of soot temperature, using the Nikon D300s and the Prosilica GC-1380CH responses, respectively. Since the CFAs are equipped with three different color filters to make up the so-called “Bayer pattern” (red, green, blue), three color ratios will be able to provide temperature information.

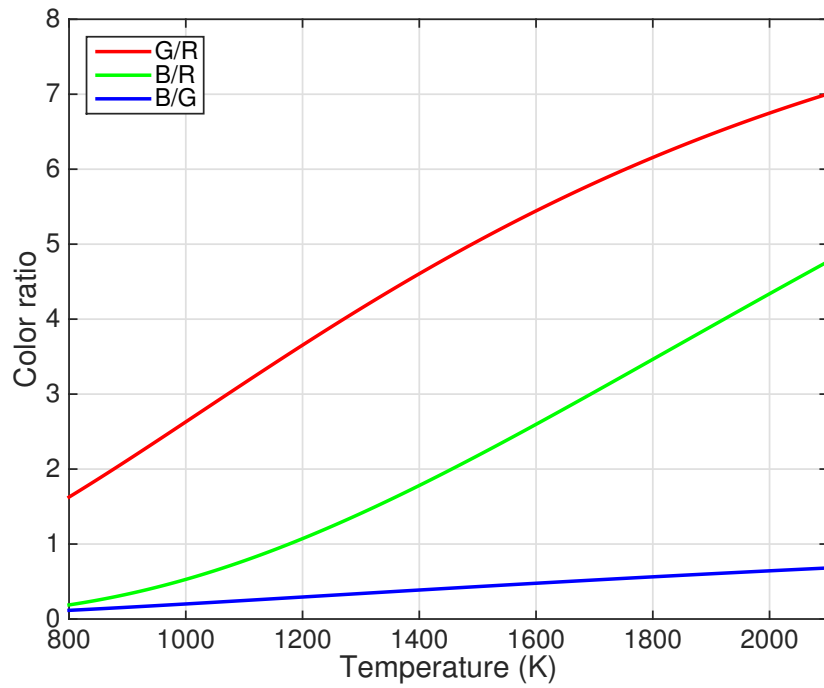
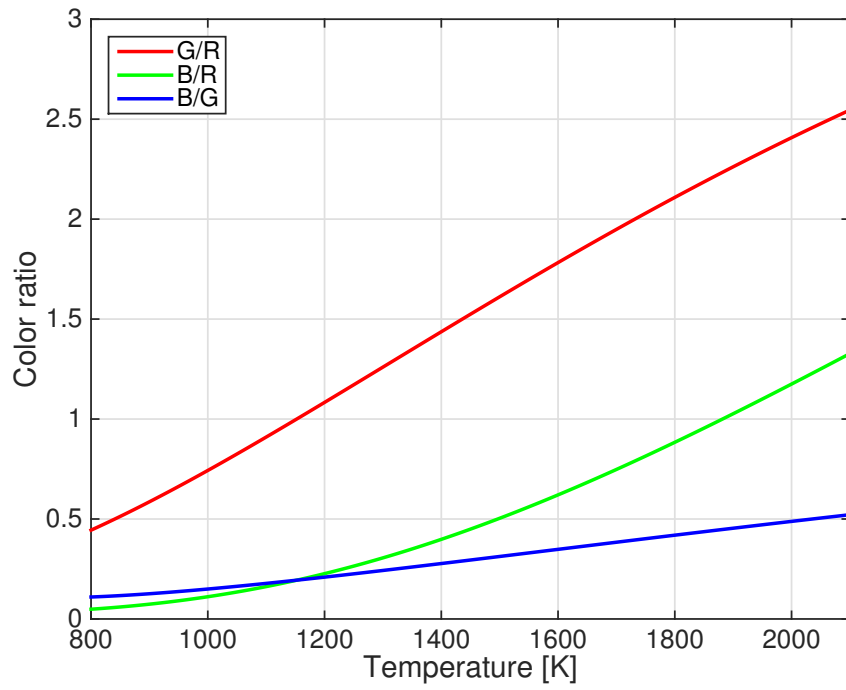


Figure 2.4: (Top) soot lookup tables evaluated for the Nikon D300s using the 1 mm BG7 color filter, and (bottom) for the Prosilica GC-1380CH using the coated 2 mm BG7 color filter.

In terms of soot emissivity, the wavelength dependence is assumed to be proportional to  $\lambda^{-1.38}$ , following the work and soot refractive index measurements performed by [13]. The assumption that a constant dispersion exponent ( $\alpha = 1.38$ ) can be used to describe soot emissivity is, however, known to be an approximation. Such value, in fact, is spatially dependent and varies depending on soot properties and age [14, 15]. It was shown that, by measuring the two-dimensional distribution of the dispersion exponent using multi-angle light scattering (MALS) and spectrally-resolved line of sight attenuation (spec-LOSA), flame temperature could vary up to  $\pm 60$  K (higher on the flame wings, and lower at the base of the flame centerline, when compared to measurements performed with a constant  $\alpha = 1.38$ ). Therefore, a more accurate way to perform pyrometry measurements would rely on information from two-dimensional  $\alpha$  maps, but since these distributions are generally unknown until specific measurements are done (particularly for not-well characterized flames such as the microgravity ones introduced in later chapters), a constant  $\alpha$  value (equal to 1.38) will be used throughout this thesis.

The soot incandescence collected and imaged onto a detector is always path-integrated over the depth of the flame but, thanks to the axisymmetric structure of the flames studied in our laboratory, a mathematical deconvolution process can be used to retrieve the cross-sectional intensity. Axisymmetric flame deconvolution is governed by Abel's equation, under the assumption that the collected rays are parallel, and relates the path-integrated intensity,  $P(x)$ , to the cross-sectional one,  $F(r)$ , as in Eq. 2.4 [16]:

$$F(r) = -\frac{1}{\pi} \int_x^R \frac{P'(x)}{\sqrt{x^2 - r^2}} dx, \quad (2.4)$$

where  $P'(x) = dP/dx$ . Among the various deconvolution methods available [17], the three-point Abel inversion will be used throughout this thesis because of its robustness

and its being less prone to noise. Deconvolution procedures, in fact, rely on the solution of an ill-posed problem and have the tendency of returning a noisy result as the radius approaches zero, particularly if the signal-to-noise ratio along the axis of symmetry is already low [18].

### 2.2.2 Soot volume fraction

Once the soot temperature is determined, the evaluation of the soot volume fraction is straightforward if an absolute light intensity calibration is available. The soot volume fraction  $f_v$  can be determined by employing the relation provided by [19] and reported in Eq. 2.5:

$$f_v = -\frac{\lambda_s}{K_{ext}L} \ln \left\{ 1 - \epsilon_L(\lambda, T_L) \frac{\tau_s S_s}{\tau_L S_L} \cdot \exp \left[ -\frac{hc}{k\lambda_s} \left( \frac{1}{T_L} - \frac{1}{T_s} \right) \right] \right\}. \quad (2.5)$$

$K_{ext}$  is the non-dimensional extinction coefficient (assumed to be = 8.6 [20]),  $L$  is the pixel size,  $\epsilon_L(\lambda, T_L)$  the emissivity of the calibration source,  $\tau$  is the exposure time,  $S$  the counts recorded by the detector, and  $T$  the temperature. The subscripts  $s$  and  $L$  correspond to the **S**oot and calibrated **L**ight source, respectively.  $\lambda_s$  is the effective color filter wavelength, defined as the wavelength corresponding to the maximum value of the product between camera filter response and the blackbody intensity evaluated at the temperature  $T$ .

### 2.2.3 Thin filament pyrometry

In flames where a radiating body like soot is not present, pyrometry-based temperature measurements can be performed by employing the thin filament approach [21–23]: a SiC fiber ( $\sim 15 \mu m$  in diameter) is stretched across the flame and its radiation imaged with a color camera; the fiber surface temperature can then be evaluated using the color ratio approach outlined in Section 2.2.1 and the appropriate lookup

table. The fiber is assumed to behave like a gray body, with a constant emissivity of 0.88 [21]. The flame gas temperature,  $T_g$ , can be inferred afterwards by performing a “radiation correction”; the fiber temperature  $T_f$ , in fact, is related to the balance between the convective heat transfer from the gas phase and the radiative losses into the ambient (the conductive contribution along the fiber filament is assumed to be negligible). This balance is expressed as:

$$\dot{Q} = h(T_g - T_f) - \epsilon_F \sigma (T_f^4 - T_g^4). \quad (2.6)$$

Here  $h$  is the convective heat transfer coefficient,  $\epsilon_F$  the fiber emissivity, and  $\sigma$  is the Stefan-Boltzmann constant. Assuming equilibrium ( $\dot{Q} = 0$ ), Eq. 2.6 can be rewritten as:

$$T_g = \frac{\epsilon \sigma (T_f^4 - T_g^4)}{h} + T_f. \quad (2.7)$$

The heat transfer coefficient  $h$  is related to the flow properties and can be evaluated from Eq. 2.8:

$$h = \frac{Nu \cdot k_{gas}}{d_f}. \quad (2.8)$$

Here  $k_{gas}$  is the gas thermal conductivity,  $d_f$  the fiber diameter, and the Nusselt number,  $Nu$ , is determined based on the Reynolds number as follows:  $Nu = C \cdot Re^m$  (with  $C = 0.8$ ,  $m = 0.28$  for  $0.09 < Re < 1$ , and  $C = 0.795$ ,  $m = 0.384$  for  $1 < Re < 35$ ) [24].

## Lookup table verification

The accuracy of the lookup tables such as the ones shown in Fig. 2.4 (and as an extension the accuracy of the measured detector response) can be assessed through a procedure that involves the imaging of objects that are heated to a well defined temperature and whose spectral emissivity is known. In general, blackbody furnaces or heated *Pt* thermocouples [7, 22] can be used for such verifications: images of

the cavity of a blackbody (or the heated thermocouple junction) are taken with the detector, the ratios are evaluated from the red, green, and blue (RGB) channels (if the detector is a color camera) and they are compared to the analytical solution returned by Eq. 2.3. Fig 2.5 shows, as an example, the calibration of the Prosilica GC1380-CH lookup table using a heated type-S thermocouple: the markers identify the measured color ratios evaluated from the thermocouple junction images (and with a temperature that was self measured by the thermocouple itself), while the solid lines are the analytical solution of Eq. 2.3.

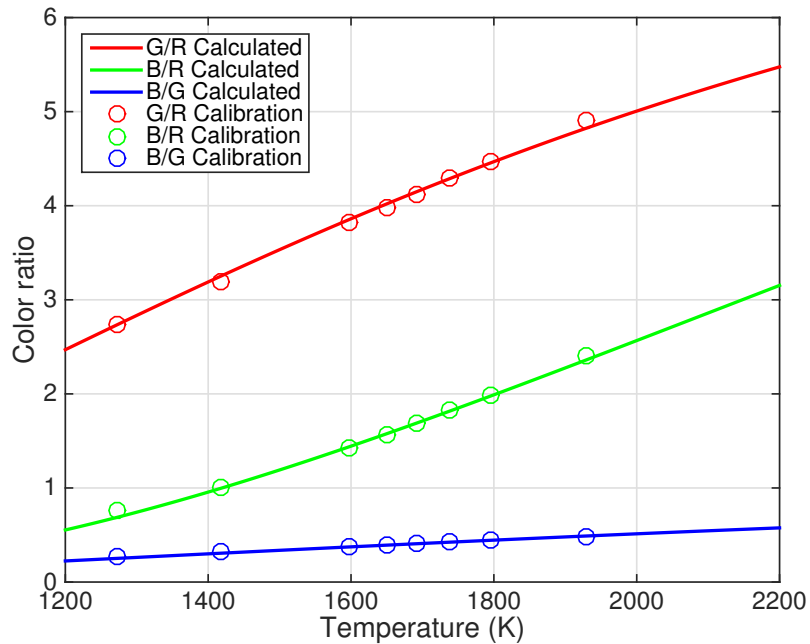


Figure 2.5: Type-S thermocouple lookup table evaluated for the Prosilica GC-1380CH using an uncoated 2 mm BG7 color filter.

The spectral emissivity of the Platinum type-S thermocouple has been characterized in our lab by a previous student [22] and found equal to  $\epsilon_{tc} = 1.067 \cdot 10^{-6} \cdot \lambda^2 - 1.5375 \cdot 10^{-3} \cdot \lambda + 0.8581$ . Typically, to match the calculated and the measured ratios, the transmission of the individual colors of a camera’s CFA is increased/decreased by few percent, and it is assumed that the adjustments needed to match the blackbody or thermocouple lookup tables are the same required for the soot ones.

The advantages of the blackbody calibration, over the thermocouple, are the more temporally stable temperatures that can be achieved and the larger area that can be imaged with the detector; the thermocouple, on the other hand, is relatively inexpensive, compact, and can be heated to a higher temperature that is closer to the range where soot temperature is generally measured ( $\sim 1900/2000$  K against  $\sim 1450$  K for the blackbody).

## 2.2.4 Chemiluminescence

Chemiluminescence is the spontaneous emission of a photon that happens during the relaxation of a molecule  $M$  from an electronically-excited state to a stable ground state:



In Eq. 2.9,  $M^*$  identifies the excited molecule,  $h$  is the Planck’s constant, and  $\nu = c/\lambda$  is the photon frequency;  $h\nu$  represents the photon energy which, being solely related to the energy levels of the transition, is a unique “fingerprint” for a specific molecule. Chemiluminescent species are one of the main sources of flame luminosity ( $CH^*$ , for example, is responsible for the blue appearance of premixed or diluted flames), and are often considered useful markers to identify flame structure and flame heat release rate [25–29]. From a diagnostics standpoint, during the spontaneous emission process that the excited radicals undergo, the number density of the emitted photons  $N^*$  can

be related to the signal collected by a detector  $S_{em}$  according to

$$S_{em} = \frac{1}{4\pi} A_{21} \tau V_{em} N^* K \gamma. \quad (2.10)$$

In the above equation,  $A_{21}$  is the Einstein  $A$  coefficient,  $\tau$  the detector's exposure time, and  $V_{em}$  the pixel volume.  $K$  is a constant that accounts for the solid collection angle and detector efficiency. It provides a relation between recorded counts and the absolute number of emitted photons and is determined from an absolute light intensity calibration (see Section 2.2.5) [30].  $\gamma$  represents the energy transmitted by a photon through the collection optics and is defined as

$$\gamma = \int_{\lambda_1}^{\lambda_2} \eta(\lambda) \frac{hc}{\lambda} N_{em}(\lambda) d\lambda. \quad (2.11)$$

Here  $\eta$  accounts for the spectral sensitivity of the detector as well as the transmissivity of any optical filters,  $h$  is again the Planck's constant,  $c$  is the speed of light, and  $N_{em}$  is the normalized chemiluminescent spectral emission of the particular chemiluminescent species. The latter can be numerically obtained using a spectral simulation software, such as LIFBASE [31], once the temperature of the reaction zone, where such radical species exist, is known (from measurements or simulations).

## 2.2.5 Absolute light intensity calibration

Quantitative measurements like the determination of soot volume fraction (Section 2.2.2), or the evaluation of the concentration of a radical species (Section 2.2.4), require an absolute light intensity calibration to relate the counts recorded by a detector to the actual number of photons hitting the pixels. This counts/photons relationship is affected by numerous factors that change depending on the specifics of the acquisition setup, such as the collection solid angle, the lens  $f$ -number, the transmissivity of the optical filters, and the spectral sensitivity of the detector. An absolute light

intensity calibration is generally performed using a light source with a known spectral radiance so that a relation between the measured counts and emitted photons can be established. Traditional calibration sources are blackbody furnaces or tungsten lamps (which are expensive and require frequent re-calibrations). Less complex and less expensive alternatives are heated SiC fibers and thermocouples [7, 22, 23]; the latter can be used in smaller volumes, but they have their own advantages and disadvantages as well: SiC fibers, for example, allow the measurement of their temperature using color ratio pyrometry (therefore not requiring any extra equipment), but are affected by a large uncertainty in the self measured temperature ( $\sim 30K$ ) which translates into a greater uncertainty in the calibration constant [23]. Thermocouples are more accurate in their temperature readings, but require additional voltage-acquisition instrumentation.

With reference to Eq. 2.10, the calibration constant  $K$  is determined by using

$$K = \frac{C}{\tau \int_{\lambda_1}^{\lambda_2} \eta(\lambda)\epsilon(\lambda)I_{BB}(\lambda, T)d\lambda} \quad (2.12)$$

where  $C$  is an average of the recorded counts,  $\eta$  once again accounts for the transmissivity of the detector and any optical filters,  $\epsilon$  is the emissivity of the calibration source, and  $I_{BB}$  is the blackbody radiation evaluated at the temperature  $T$  of the calibration source. When employing SiC fibers or thermocouples, as is the case with the intensity calibrations performed in this work, the value of the parameter  $C$  was determined by summing the pixel counts along the radial direction of the filament, and averaging them along the axial direction, in a region where the axially recorded counts were seen to be relatively constant.

## 2.3 Laser-based techniques

### 2.3.1 Laser-induced fluorescence

Fluorescence is the spontaneous emission of radiation from an upper energy level, which has been excited by an external source, to a ground state. In laser-induced fluorescence (LIF) the excitation is provided by photons from a laser, which has the advantage of being able to provide highly spatial, temporal and spectrally selective excitation [32]. LIF is both a resonant and inelastic process, involving energy exchange between the incoming photons and the molecule; for this reason, the fluorescence emission will tend to have a lower energy with an emission that will be red-shifted with respect to the excitation wavelength. Because of the resonant nature of the process, the excited molecule's cross section can be relatively large, allowing species sensitivity down to the parts per million; thus, LIF is typically employed to measure and monitor minor chemical species that are hard to detect with other techniques such as Raman scattering.

The LIF treatment reported in the next paragraphs will follow the discussion presented in [32]. In the first approximation, the simplest system that can be used to mathematically describe LIF is a two-level energy model, like the one shown in Fig. 2.6. Despite being simple, this model is an accurate enough representation of the fluorescent behavior of diatomic molecules such as *NO*, *CH*, and *OH*.

With reference to Fig. 2.6, levels 1 and 2 represent specific ro-vibrational states within the pair of ground and excited electronic states; the upper level population, level 2, is related to the lower level population through the radiative rate coefficients of stimulated absorption and emission  $b_{12}$  and  $b_{21}$ , the Einstein rate coefficient for spontaneous emission  $A_{21}$ , the collisional quenching rate constant  $Q_{21}$ , the photoionization rate constant  $W_{2i}$ , and a predissociation rate constant  $P$ . The predissociation and quenching are non-radiative processes and do not involve any emission or ab-

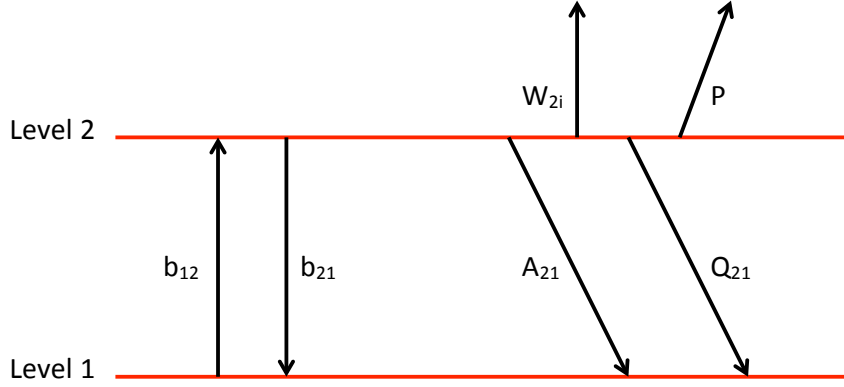


Figure 2.6: Two-level energy level diagram for the description of laser-induced fluorescence.

sorption of photons. The rate coefficients for stimulated absorption/emission  $b_{ij}$  are related to the Einstein rate coefficient of stimulated absorption/emission  $B_{ij}$  by

$$b_{ij} = \frac{B_{ij}I_\nu}{c} \quad (2.13)$$

where  $I_\nu$  is the laser irradiance per unit frequency ( $\frac{W}{cm^2s}$ ), and  $c$  is the speed of light.

The rate equations of the state population densities  $N$  can be written as:

$$\frac{dN_1}{dt} = -N_1b_{12} + N_2(b_{21} + A_{21} + Q_{21}) \quad (2.14)$$

$$\frac{dN_2}{dt} = N_1b_{12} - N_2(b_{21} + A_{21} + Q_{21} + P + W_{2i}). \quad (2.15)$$

In the case of moderate laser energies, predissociation and photoionization can be considered negligible; therefore, by adding Eqs. 2.14 and 2.15, one obtains:

$$\frac{dN_1}{dt} + \frac{dN_2}{dt} = \frac{d}{dt}(N_1 + N_2) = 0. \quad (2.16)$$

This results in:

$$N_1 + N_2 = constant. \quad (2.17)$$

A common approximation assumes that the system can be considered in steady state and that  $N_1 \approx N_1^0$ ; the superscript 0 identifies the population level prior to any laser excitation. Hence, Eqs. 2.14 and 2.15 are equal to 0, and Eq. 2.15 can be rewritten as:

$$N_2 = N_1^0 \frac{B_{12}}{B_{12} + B_{21}} \frac{1}{1 + \frac{I_{sat}^\nu}{I_\nu}}, \quad (2.18)$$

where  $I_{sat}^\nu$  is the saturation spectral irradiance defined as:

$$I_{sat}^\nu = \frac{A_{21} + Q_{21}}{B_{12} + B_{21}} c. \quad (2.19)$$

As in Eq. 2.20, the fluorescence emission  $F$  is proportional to the upper level population,  $N_2$ , and the Einstein rate coefficient for spontaneous emission,  $A_{21}$ :

$$F = \alpha A_{21} N_2. \quad (2.20)$$

Here,  $\alpha$  is a constant that takes into account the geometry of the collection optics as well as the camera gain. By substituting Eq. 2.18 into 2.20, the fluorescence signal can be written as:

$$F = \alpha N_1^0 \frac{B_{12}}{B_{12} + B_{21}} \frac{A_{21}}{1 + \frac{I_{sat}^\nu}{I_\nu}}. \quad (2.21)$$

In the case of “linear fluorescence” (which is valid for low excitation radiances),  $I_\nu \ll I_{sat}^\nu$ , and 2.21 becomes:

$$F = \alpha N_1^0 B_{12} I_\nu \frac{A_{21}}{A_{21} + Q_{21}}. \quad (2.22)$$

This formulation will be used in Section 3.1 to describe the fluorescence behavior of the molecule  $NO$ .

### 2.3.2 Two-photon laser-induced fluorescence

Several molecules that are relevant to combustion processes have absorptions close to- or in the deep UV spectral region; this region presents a very strong absorption and any excitation wavelength generated in this range would not be able to propagate in a gaseous environment (thus the term vacuum UV). Multi-photon excitation allows access to these transitions via the simultaneous absorption of two or more photons. Following the model presented in [33], and extended in [34], the single-wavelength two-photon LIF model that will be relevant to the measurement of carbon monoxide described in Section 3.2 is presented in the following paragraphs. The mathematical treatment relies on a four-level energy diagram like the one depicted in Fig. 2.7.

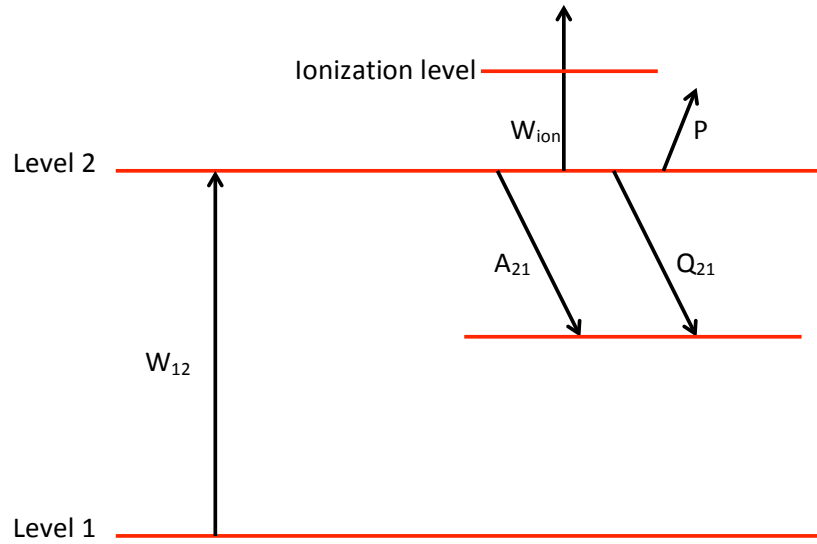


Figure 2.7: Four-level energy level diagram for the description of two-photon laser-induced fluorescence.

Similarly to what was introduced for the single-photon fluorescence case, the upper level population, level 2, is related to the lower level population by the rate coefficients for two-photon absorption  $W_{12}$ , quenching  $Q_{21}$ , spontaneous emission  $A_{21}$  and

photoionization  $W_{ion}$  through the equation

$$\frac{dN_2}{dt} = N_1W_{12} - N_2(A_{21} + Q_{21} + W_{ion}). \quad (2.23)$$

Under the assumption of both steady state and a sufficiently small rate coefficient of stimulated absorption  $W_{12}$  (such that  $N_1 \approx N_1^0$ ), the equation simplifies to:

$$N_2 = \left( \frac{W_{12}}{A_{21} + Q_{21} + W_{ion}} \right) N_1^0. \quad (2.24)$$

For linearly polarized light the rate coefficient for two-photon absorption  $W_{12}$  can be expressed in terms of a two-photon cross section  $\sigma$  [ $cm^4$ ]:

$$W_{12} = (\sigma I^2)/(h\nu_L)^2. \quad (2.25)$$

In this equation,  $I$  is the laser irradiance (whose quadratic dependence is now the result of the simultaneous absorption of two photons),  $h$  is the Planck constant, and  $\nu_L$  is the excitation frequency. Given the laser energy used in the measurements of Section 3.2, the ionization rate was not considered negligible and its contribution was expressed in terms of a photoionization cross section  $\sigma_{ion}$  [35]. The ionization rate is expressed here as:

$$W_{ion} = (\sigma_{ion}I)/(h\nu_L). \quad (2.26)$$

Once again, the fluorescence signal will be proportional to  $A_{21}N_2$  and, by combining Eq. 2.20 with Eqs. 2.24 - 2.26, one can obtain a final relation for the two-photon fluorescence signal:

$$F = \alpha N_1^0 I^2 \frac{A_{21}}{A_{21} + Q_{21} + W_{ion}}. \quad (2.27)$$

## Boltzmann correction

The fraction of molecules in a particular energy level  $j$  can be related to the total number density by employing the Boltzmann distribution evaluated at the local flame temperature. This can be expressed as

$$N_j = N_{tot}f_j, \quad (2.28)$$

where  $N_{tot}$  is the total number density and  $f_j$  is the population fraction of the state  $j$ . As shown in Eq. 2.29, the fraction  $f$  of molecules in the level  $j$  includes the contributions from the rotational and vibrational population distributions,  $f_J$  and  $f_V$ :

$$f_j = f_J f_V = (2J + 1) \frac{B}{k_b T} e^{\left(-\frac{B}{k_b T} J(J+1)\right)} e^{\left(-\frac{Vhc\omega_e}{k_b T}\right)} \left(1 - e^{-\frac{hc\omega_e}{k_b T}}\right). \quad (2.29)$$

The rotational fraction  $f_J$  derives from the modeling of the molecule as a rigid rotor, with  $B$  being the rotational constant [36] and  $J$  the rotational quantum number.  $(2J + 1)$  is the degeneracy of the partition function in state  $J$ . The vibrational fraction,  $f_V$ , is obtained from considering the molecule as an harmonic oscillator, with  $\omega_e$  the spacing between energy levels and  $V$  the vibrational quantum number. The population densities in Eqs. 2.22 and 2.27 can therefore be rewritten, accounting for the Boltzmann correction, in terms of the total number density,  $N_{tot}$ , and the population fraction of the ground state 1,  $f_1$ :

$$N_1^0 = N_{tot}f_1. \quad (2.30)$$

## Quenching correction

The quenching rate  $Q_{21}$ , assuming that the collisional component is the dominant phenomenon, can be estimated considering the number density of the  $i^{th}$  deactivating species  $N_i$  [32], the collisional cross section  $\sigma_i$ , and the relative velocity  $v_i$  between the molecule  $m$  and the collisional partner  $i$ :

$$Q_{21} = \sum_{i=1}^n N_i \sigma_i v_i. \quad (2.31)$$

$v_i$  is a thermally averaged velocity dependent on the temperature, the Boltzmann constant,  $k_b$ , and the reduced mass of the species  $i$  and excited molecule  $m$ ,  $\mu_{i,m}$ :

$$v_i = \left( \frac{8k_b T}{\pi \mu_{i,m}} \right)^{\frac{1}{2}}. \quad (2.32)$$

The collisional cross sections  $\sigma_i$  are highly temperature- and species dependent, and their values, in the temperature range between 293 K and 1031 K, are available in Refs. [37] and [38] for *NO* and *CO*, respectively, along with their most relevant flame species collisional partners.

### 2.3.3 Rayleigh scattering

Rayleigh scattering is a sensitive elastic laser technique based on the interaction between an incoming electromagnetic wave and the molecule's electrons. It relies on the assumption that the excitation wavelength is longer than the molecule size so that the electric field can be considered constant over the spatial displacement of the molecule. Unlike the fluorescence process described in section 2.3.1, Rayleigh scattering does not involve any energy exchange and the scattered light will be at the same wavelength as the excitation. The mathematical treatment used to describe Rayleigh scattering, as presented in [32], stems from the concept of induced dipole

moment of a molecule as seen in Eq. 2.33:

$$\vec{p} = \epsilon_0 \alpha \vec{E}. \quad (2.33)$$

Here  $\epsilon_0$  is the permittivity of free space,  $\alpha$  the molecular polarizability, and  $\vec{E}$  the electric field. The irradiance, the quantity that we can measure, is related to the electric field through:

$$I(r, \theta) = \frac{\epsilon_0 c |E(r, \theta)|^2}{2}, \quad (2.34)$$

whereas the amplitude of the electric field is related to the dipole moment through:

$$E(r, \theta) = \frac{p \omega^4 \sin \theta}{4\pi c^2 \epsilon_0 r}. \quad (2.35)$$

Here  $c$  is the speed of light and  $\omega$  the scattered light frequency. The irradiance from an oscillating dipole, normalized to the unit solid angle, can then be written by combining Eqs. 2.34 and 2.35:

$$I^\Omega(\theta) = \frac{p^2 \omega^4}{32\pi^2 c^3 \epsilon_0} \sin^2 \theta. \quad (2.36)$$

If the electric field has the form  $\vec{E} = \vec{E}_0 \cos(\omega_0 t)$ , and if only the static term of the molecular polarizability  $\alpha_0$  is considered (the time-varying term will be relevant to the Raman scattering emission), then the induced dipole moment becomes:

$$\vec{p} = \epsilon_0 \alpha_0 \vec{E}_0 \cos(\omega_0 t). \quad (2.37)$$

In general,  $\alpha$  is a tensor and the dipole moment will change depending on the molecule orientation with respect to the electric field. Additionally, the random orientation of the molecules will require the scattering model to include some averaging over the molecule orientations. Experimentally, Rayleigh scattered light is collected at  $90^\circ$

with respect to the incident beam with a collected radiant intensity equal to

$$I_{iz}^{\Omega}(90^{\circ}) = n_m \frac{\epsilon_0 \omega^4 \overline{\alpha_{iz}^2} E_z^2}{32\pi^2 c^3}. \quad (2.38)$$

In Eq. 2.38,  $n_m$  is the number of scatterers of type  $m$ ,  $\overline{\alpha_{iz}}$  is the averaged polarizability tensor, and  $i$  can either be  $y$  or  $z$  depending on the detection polarization. However, a more general and commonly used expression is the following:

$$I_{iz}(90^{\circ}) = C_{exp} V N_m I_0 \left( \frac{\partial \sigma_m}{\partial \Omega} \right)_{iz}. \quad (2.39)$$

In this version of the equation,  $C_{exp}$  is an experimental constant that accounts for the efficiency of the collection optics,  $V$  is the volume illuminated by the laser beam,  $N_m$  the number density of the species  $m$ ,  $I_0$  the laser irradiance, and the partial derivative term is defined as a cross section. Eq. 2.39 relates to Eq. 2.38 through the following equivalences:  $I_0 = (c\epsilon_0)/2 * E_z^2$ ;  $n_m = V N_m$ ;  $(\partial \sigma_m / \partial \Omega)_{iz} \propto \omega^4 \overline{\alpha_{iz}^2}$ . The cross section can be related to the index of refraction  $n$  of a material with number density  $N$  thanks to the Lorentz-Lorenz equation:

$$\alpha = \frac{3}{4\pi N} \frac{n^2 - 1}{n^2 + 2}. \quad (2.40)$$

Hence, the polarized Rayleigh cross section written in terms of index of refraction is:

$$\left( \frac{\partial \sigma_m}{\partial \Omega} \right) = \frac{4\pi^2 (n_m - 1)^2}{N_0^2 \lambda^4} = \sigma_m. \quad (2.41)$$

In conclusion, the Rayleigh signal collected by a detector is:

$$S_{Ray} = K I_0 N V \sum_i x_i \sigma_i, \quad (2.42)$$

where  $K$  is the efficiency of the collection optics, and  $x_i$  and  $\sigma_i$  are the mole fraction and Rayleigh cross section of species  $i$ , respectively. Rayleigh scattering can be used to evaluate the temperature of a gas mixture through the dependence of the signal on the number density  $N$  [39]. If the local mixture composition is known, the summation term (known as effective Rayleigh cross-section) can be calculated, and the temperature inferred from the number density using the ideal gas law under the assumption of constant pressure. The Rayleigh scattering technique will be employed in Chapter 5 where it is used as a test-case for the evaluation of the effectiveness of high dynamic range imaging and time-resolved averaging in flow diagnostics.

# Chapter 3

## Minor species characterization using laser-induced fluorescence

Nitric oxide ( $NO$ ) and carbon monoxide ( $CO$ ) are well recognized as critical minor species in combustion processes because of either their relevance to reaction progress or their implication as a toxic pollutants. In combustion the importance of carbon monoxide is well known since the oxidation of  $CO$  to  $CO_2$  is responsible for approximately one third of the total flame heat release [40, 41]; its presence among the products is an indicator of the overall combustion efficiency and it is one of the major pollutants because of its toxicity.  $NO$ , on the other hand, is one of the main contributors to photochemical smog as well as ozone depletion in the stratosphere through the following generalized reaction scheme:



$M$  is a generic third body and  $h\nu$  represents the energy of a photon.  $NO$  itself, at atmospheric pressure, is mainly formed through two major pathways known as *Zeldovich* and *Prompt* mechanisms. The reactions of the Zeldovich mechanism are summarized as follows [42, 43]:



Because of the high activation energies, the above reactions are favored at high temperatures; on the other hand, the Prompt mechanism can progress at lower temperatures and it accounts for the formation of  $NO$  through the reactions of  $N_2$  with  $C$ ,  $CH$ , and  $CH_2$  radicals from the fuel that produce intermediate species such as  $NH$ ,  $HCN$ , or  $H_2CN$  that can ultimately oxidize to form  $NO$  (*Fenimore* pathways [44]). For obvious environmental concerns, practical combustion systems are designed and operated in a way that minimizes the production of both  $NO$  and  $CO$ ; internal combustion engines or gas turbines are operated in an optimized “window” of mixture fraction values (or temperature) in which a balance exists between hot lean reactions (which can favor the complete oxidation of  $CO$  into  $CO_2$  due to the excess of oxygen) and low temperatures, so that the Zeldovich  $NO$  formation mechanism is not triggered. The understanding of the interdependence between  $NO$  and  $CO$ , and the understanding of the critical reactions behind their formations is therefore an important step towards the goal of pollutant reduction.

Previous work focused on the measurement of  $NO$  in the target Yale methane flame comparing the Raman scattering and LIF approaches [2], while [4] investigated the effect and interdependency of temperature and soot formation in the target nitrogen-diluted ethylene flames, as well as the effect that temperature has on the Zeldovich and

Fenimore *NO* formation pathways. Among the various techniques to measure *NO* and *CO* concentration, laser-induced fluorescence has proved itself a very sensitive method for their detection especially since *NO* and *CO* are difficult to measure with Raman scattering because of their relatively low concentration and/or interferences with other species.

This chapter focuses on the quantitative full-field LIF measurements of *NO* and *CO* in the target axisymmetric nitrogen-diluted 65% methane coflow laminar diffusion flame, with the aim of extending the Yale experimental species database [45], and presents results obtained in both steady and time-varying flames. Coflowing time-varying flames offer a much wider range of interactions between the chemistry and the flow field than can be examined under steady-state conditions and are therefore a good case for comparison with numerical models. The complex coupling between chemistry and fluid flow in time-varying laminar flames effectively samples different regimes of temperature, mixture fraction, residence time, strain and scalar dissipation rates than are observed under steady conditions. Joint experimental/computational studies have been undertaken to study these effects and in previous works, [2, 46–49], comparisons have been made between computations and measurements of temperature and major species based on Rayleigh and Raman scattering.

When possible, and as it has been done in previous work [49], a comparison of the results has been made between the measured and computed fluorescence signals. Using calculated values to derive measured signals rather than measuring several quantities to derive a single calculated quantity (e.g. a mole fraction) yields a simpler experiment that can have a higher signal to noise ratio and lower uncertainties. Comparative studies [46–49] on steady and time-varying axisymmetric coflow diffusion flames showed that the numerical model developed at Yale is able to predict both the temperature field and major chemical species distributions with high accuracy. These computed results were used to simulate an expected fluorescence signal, and

the agreement between the measured and calculated signals that was observed in some cases provided confidence in the computational results, the fluorescence model, and the measurement.

## 3.1 Nitric oxide LIF

### 3.1.1 Experimental setup

As already introduced in Section 2.1, the coflow diffusion flame studied burns a mixture of methane and nitrogen (65%  $CH_4$  and 35%  $N_2$  by volume) to reduce soot and its interference with laser scattering to a negligible level. Both the coflow air and the fuel mixture have an average exhaust velocity of 35 cm/s with a flat and a parabolic profile for the coflow and fuel, respectively. The resulting flame is mainly blue with a small, lightly sooting region close to the tip. The flame is lifted 2 mm above the burner to avoid heat transfer to the fuel tube, simplifying the numerical simulations. The fuel tube has a 4 mm inner diameter and it is surrounded by a 74 mm I.D. coflow; a 1/32" size honeycomb is used to stabilize and straighten the air flow. The fuel mixture was set using 2 calibrated Tylan FC-280 flow controllers, while the air coflow was regulated using a Sierra Instruments Smart-Trak mass flow controller. The fuel flow could be driven by a speaker in the fuel plenum to produce a periodic time-varying exit velocity profile. In the present set of experiments the speaker was operated at 20 Hz - a multiple of the 10 Hz laser frequency - and phase-locked measurements were performed after synchronization of all the components. A Stanford Research System DS345 function generator drove the speaker through a signal amplifier. Five phases with different modulations (30% and 50% fuel velocity modulations) were studied and are summarized in Fig. 3.1. The green markers, labeled with the letters A to E, identify the phases at which the phase-locked LIF measurements have been performed.

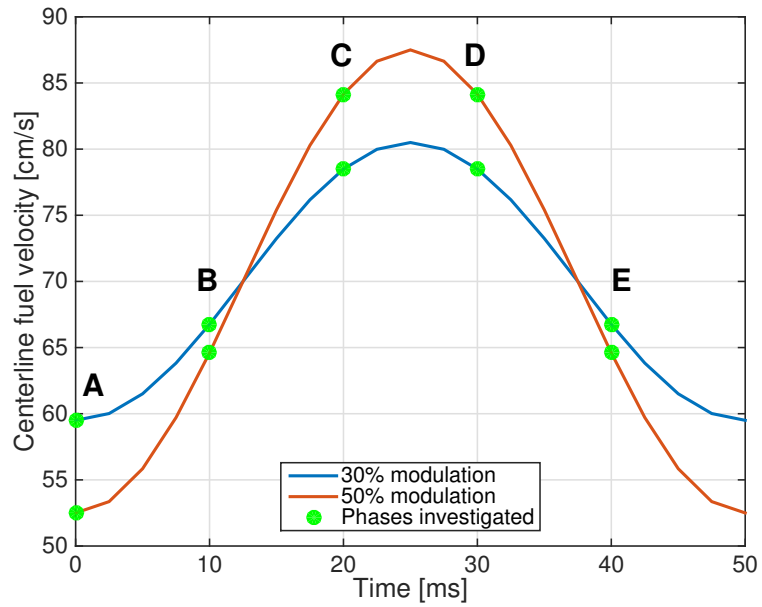


Figure 3.1: Centerline fuel velocity modulations investigated for the forced flames, with the five measured phases identified by the letters A, B, C, D, and E.

A schematic representation of the experimental setup used to measure *NO* fluorescence is shown in Fig. 3.2.

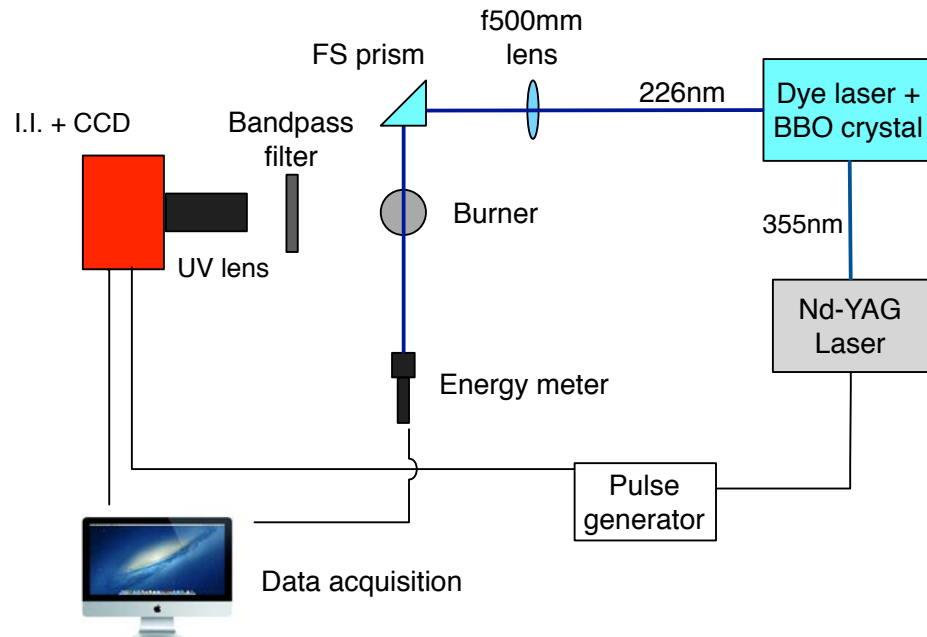


Figure 3.2: Schematic representation of the experimental setup used for the measurement of *NO* LIF.

As a way to replicate the approach utilized by [4], the third harmonic of a pulsed Quanta Ray Pro-250 Nd-YAG laser (10 Hz repetition rate) was used to pump a tunable Sirah Precision Scan dye laser containing a solution of ethanol and Coumarin C450 (0.15 g/L). The output of the dye laser was frequency doubled with a BBO crystal and used to excite the Q branch (0,0) of the  $A^2\Sigma^+ \leftarrow X^2\Pi$  transition near 226 nm. The laser beam was focused to a line using a spherical f-500 mm quartz lens and sent onto the burner through a fused silica prism; the resulting beam size was measured to be 150  $\mu\text{m}$  FWHM.

The  $A^2\Sigma^+ \rightarrow X^2\Pi$  (0,1) to (0,6) transitions were selected as collection bands for the fluorescence emission and the fluorescence was collected through a bandpass Nikon FF-52 UV filter (which reduced the Rayleigh scattered intensity to a minimum while letting the red-shifted fluorescent emission pass) and imaged with a 105 mm UV Nikkor lens onto a Gen II DEP image intensifier gated on for 5  $\mu\text{s}$  (the intensifier gain was set to 8.5 V, equal to 70% of its operative voltage range). The intensifier, which worked also as a fast shutter, was optically coupled to a cooled SBIG STF-8300M camera (3352 x 2532 pixels, 17.96 x 13.52 mm CCD size) using a pair of coupled Nikkor 50 mm lenses. The acquired images were binned 3x3 pixels, and the length projected onto the chip, increased by mounting the UV lens on an extension tube, was equal to 47.3 pixels/mm. A Stanford Research System DG535 pulse/delay generator provided the synchronization between the laser, the camera, and the energy meter (Laser Probe Rm-3700). The latter took into account the energy variation associated with the degradation of the dye solution and the temporal fluctuations of the Nd-YAG laser output. Over the course of the measurement, the average laser energy used was in the range 50 - 180  $\mu\text{J}$  per pulse. The burner assembly was placed on a translation stage driven by a Velmex stepper motor: consequently, data was obtained at different burner heights in a 0.2 mm spaced scan of the flame, which allowed for a two-dimensional reconstruction of the *NO* fluorescence spatial distribution. For

every scan, a line image was the result of an integration over 10 seconds (100 laser pulses). All the phases of the acquisition process were monitored using the software OMA [50], which allowed for a complete interface between image recording, laser energy measuring and burner translation control.

### 3.1.2 Diagnostic considerations

As previously shown in Eq. 2.22, the fluorescence signal depends on the number density of a molecule through the Boltzmann distribution; therefore the knowledge of the precise excited rotational quantum number  $J$  is critical; to simplify the fluorescence modeling, ideally one would like to excite a specific energy level (transition) that is determined by a specific rotational number, and that does not overlap with other allowed transitions. The strength of the transition is another important factor to consider, as well as the possibility that the selected energy level may be a resonant level for other chemical species. LIFBASE [31] is a laser-induced fluorescence simulation software very useful in determining the position of all the transitions of interest. One of the software capabilities is, in fact, the ability of simulating an excitation spectrum and this numerically derived spectrum can be compared with a measured one and used to recognize specific transitions. Figure 3.3 shows the comparison between the LIFBASE derived  $NO$  excitation spectrum (simulated with a temperature  $T = 1800$  K and a spectral resolution of 0.05 Angstrom), and a measured one. The excitation spectrum measurement was performed in a flame (in a region where, from Rayleigh measurements, the temperature was known to be  $\sim 1800$  K) by tuning the dye laser grating and scanning the wavelengths in the region 225.574 - 225.999 nm, with 0.001 nm increments.

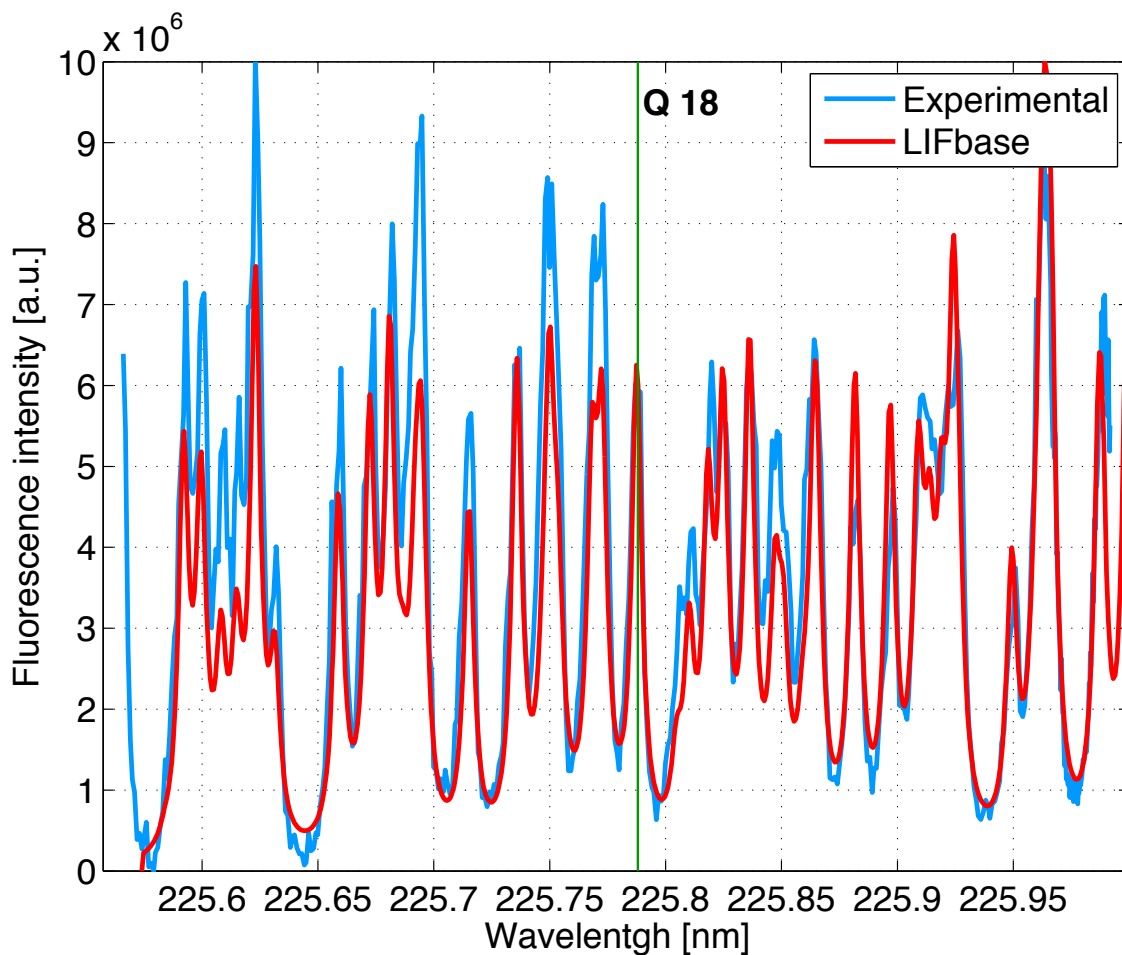


Figure 3.3: Overlap between measured  $NO$  excitation spectrum (blue curve) and simulated one (red curve). The  $Q(18)$  green line identifies the transition selected for the LIF excitation.

Because of an offset in the dye laser grating position, the measured spectrum was shifted 0.0085 nm when compared to the simulated one. After the relative shift was accounted for, the excellent overlap between the two spectra allowed for the recognition of the transition of interest (as marked in Fig. 3.3). For the purpose of this work, the  $Q_1(J=18)$  transition at 225.7880 nm was selected as excitation wavelength since it did not overlap with other allowed transitions, it was relatively strong and well populated at flame temperature and it reduced the possibility of interference from vibrationally hot oxygen [52]. The subtraction of an off-resonant signal at 225.6400 nm accounted for molecular broadband fluorescence, PAH incandescence interferences, as

well as flame luminosity.

The experimental setup described in Section 3.1.1 relies on the direct imaging of *NO* fluorescence, which comprises emission from several emission bands. Previous *NO* LIF measurements [4] relied on the spectrally resolved collection of the fluorescence and the selection of a single emission band (i.e the (0,3) band) thanks to the use of an imaging spectrometer. Since the imaging approach would increase the throughput and the efficiency of the entire collection system, thus the signal-to-noise ratio of the measurement, and simplify the data post-processing, spectrally resolved measurements were initially taken with the setup shown in Fig. 3.4 as a way to assess the feasibility of an imaging approach over the more conventional spectrally-resolved one.

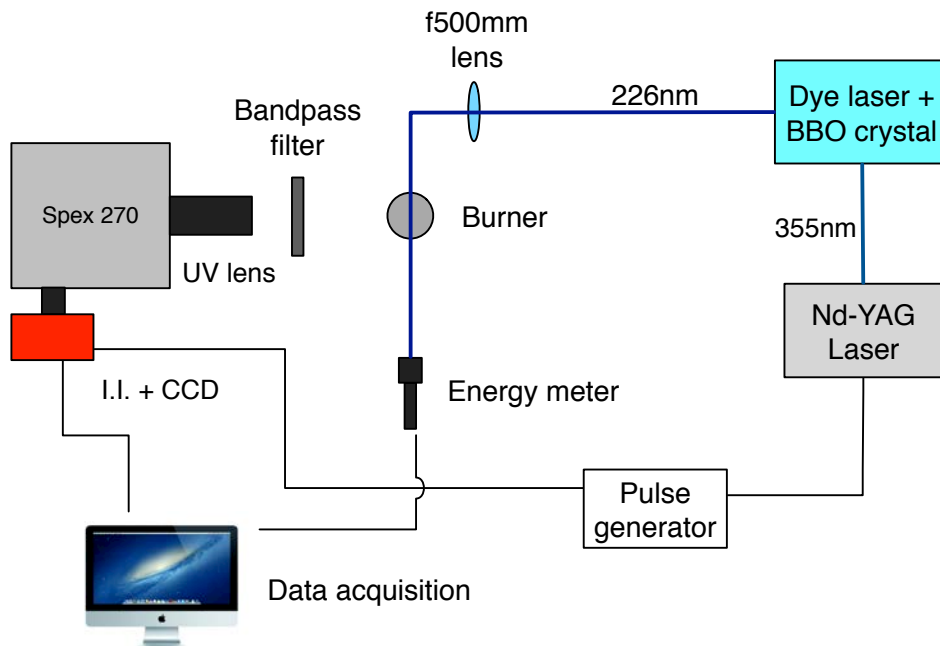


Figure 3.4: Experimental setup for the spectrally-resolved measurement of *NO* laser-induced fluorescence.

In this setup (shown in Fig. 3.4) the fluorescence was collected once again through a bandpass Nikon FF-52 UV filter and imaged with a 105 mm UV Nikkor lens onto the entrance slit of a SPEX 270 imaging spectrometer (300  $\mu\text{m}$  wide, 300 groove/mm grating with a 250 nm blaze angle). The spectrometer output was sent onto a Gen II DEP image intensifier (gated on for 5  $\mu\text{s}$ ), optically coupled to a cooled SBIG STF-8300M camera using a pair of coupled Nikkor 50 mm lenses. A typical in-flame spectrum returned by the spectrometer is shown in Fig. 3.5; the individual emission bands are clearly visible and their fluorescence intensity, taken at a fixed height above the burner, is displayed here as function of wavelength and the radial coordinate (the zero coordinate refers to the flame axis).

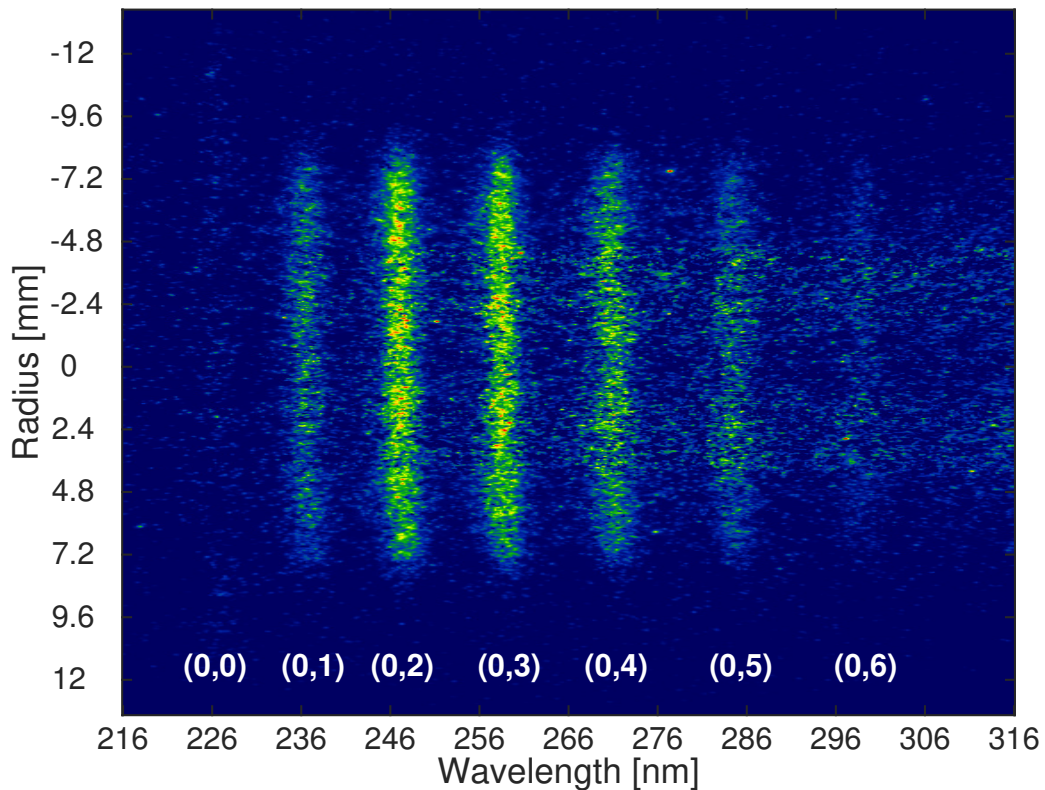


Figure 3.5: Radially resolved  $\text{NO}$  emission spectrum as collected through a Nikon FF-52 UV filter.

A clearer representation of Fig. 3.5 is shown in Fig. 3.6, where the resonant fluorescence emission is plotted as function of wavelength, for a fixed radial coordinate; the blue curve shows the emission bands (0,0) to (0,6) as collected through the FF-52 UV bandpass filter, whereas the red curve represents the fluorescent off-resonant background. Note that, normally, the (0,1) band would be the strongest one but the acquired signal intensity was shaped by the transmittance of the bandpass filter used.

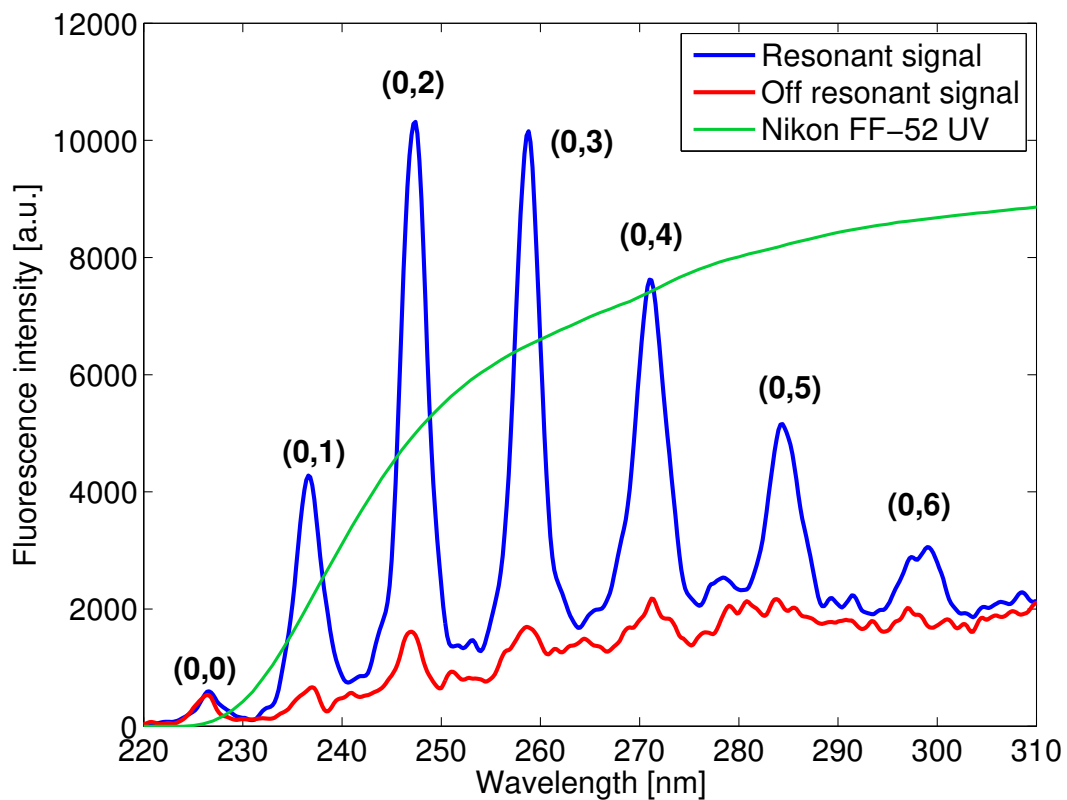


Figure 3.6: *NO* emission spectrum as collected through a Nikon FF-52 UV filter, for a fixed radial coordinate.

The fluorescent intensity is generally evaluated by integrating the signal of a specific emission band over a spectral interrogation region; however, the larger the number of integrated bands, the larger the expected signal-to-noise ratio of the measurement. To verify that the same quantitative result is obtained independently of the selection of emission bands, a comparison between measured and computed fluorescence signals (along the axial section shown by the white dashed line in Fig. 3.7) was made by considering several combinations of spectral interrogation regions. Specifically, results were obtained by spectrally integrating over the (0,1) band, the (0,3) band, the (0,1) to (0,2) bands, and the (0,1) to (0,5) bands, and the results, normalized with respect to the maximum simulated value, are shown in Fig. 3.8.

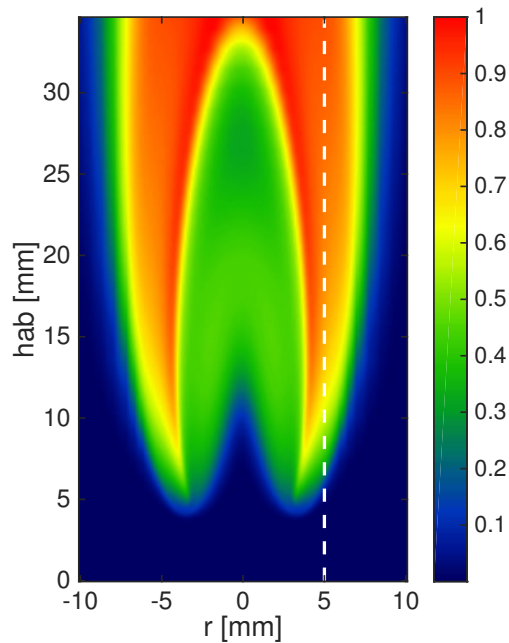


Figure 3.7: Simulated normalized *NO* LIF signal for the 65% methane flame: the white dashed line identifies the section along which the results of Fig. 3.8 are plotted.

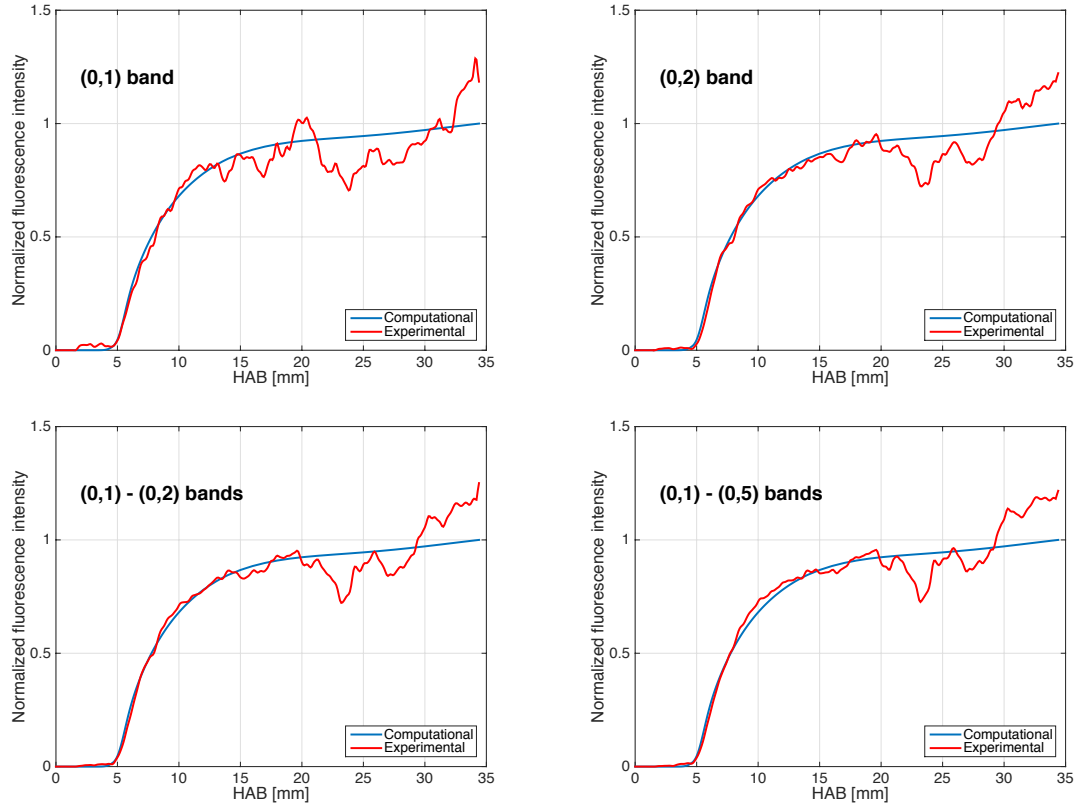


Figure 3.8: Comparison between normalized simulated and measured fluorescence, evaluated considering the contribution of different emission bands, plotted along the section defined in Fig. 3.7.

The average quantitative results returned by the various combination of bands were seen to be equivalent to one another; the selection of the (0,1) band was the case that returned the noisiest result because of its relatively low intensity (see Fig. 3.5); as the selection shifted towards bands with higher signal-to-noise ratio, or towards multiple bands, the final fluorescence displayed an overall improved signal-to-noise ratio. Since the off-resonant signal subtraction was seen to account for the presence of broadband fluorescence in a satisfactory way, it was therefore possible to use all the bands above the (0,0) as the spectral collection region, thus enabling the possibility of a direct imaging of *NO* fluorescence through the aforementioned bandpass filter. The (0,0) band, being coincident with the Rayleigh scattering line, cannot be easily used to derive quantitative results, and therefore was filtered out and not considered.

The fluorescence and quenching models implemented to describe *NO* LIF (see Eq. 2.22) presume that the fluorescence is “linear”; this requires the measurements to be performed below saturation, in a regime where the fluorescence signal scales linearly with the laser intensity. A linearity check was performed by measuring, for a fixed excitation wavelength, the in-flame fluorescence signal of *NO* as a function of the laser output energy. For the analysis, the laser energy was varied from 1 mJ to 70  $\mu\text{J}$  by simply waiting for the dye to degrade over time. As one can see from Fig. 3.9, the signal displayed a linearly behavior for intensities lower than  $\sim 150 \mu\text{J}$  (see inset and blue markers in Fig. 3.9); for this reason, the in-flame *NO* measurements were performed with laser energies lower than this threshold.

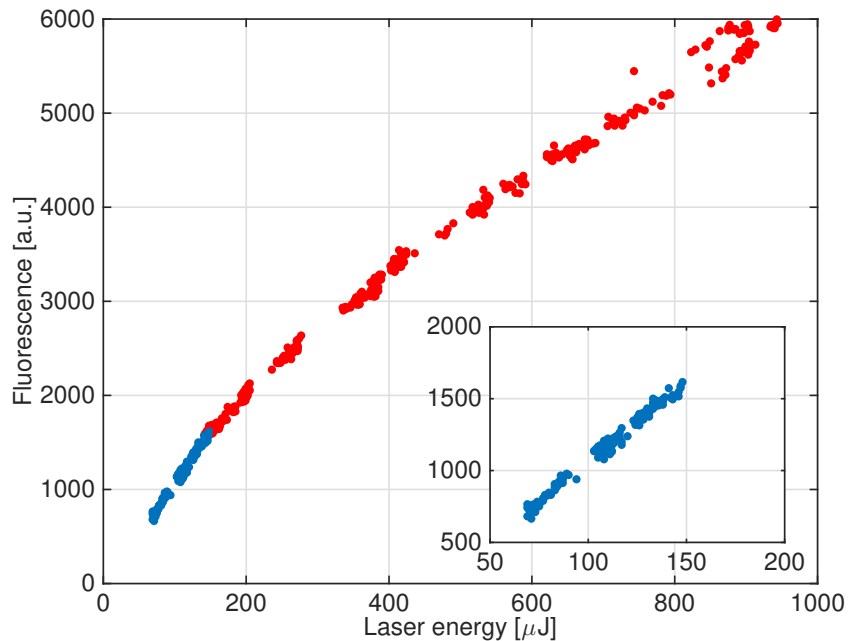


Figure 3.9: *NO* laser-induced fluorescence signal as function of laser energy. The inset highlights the linear fluorescence regime.

The  $NO$  saturation limit has been reported to be  $1.2 * 10^7 W * cm/cm^2$  [53], similar to the highest spectral irradiance recorded in the linear regime that we measured ( $\sim 1.25 * 10^7 W * cm/cm^2$ ). The quenching contribution was evaluated following the relation given in Eq. 2.31 and assuming that the collisional quenching cross sections provided in [37] could be extrapolated up to flame temperatures, as shown in Fig. 3.10.

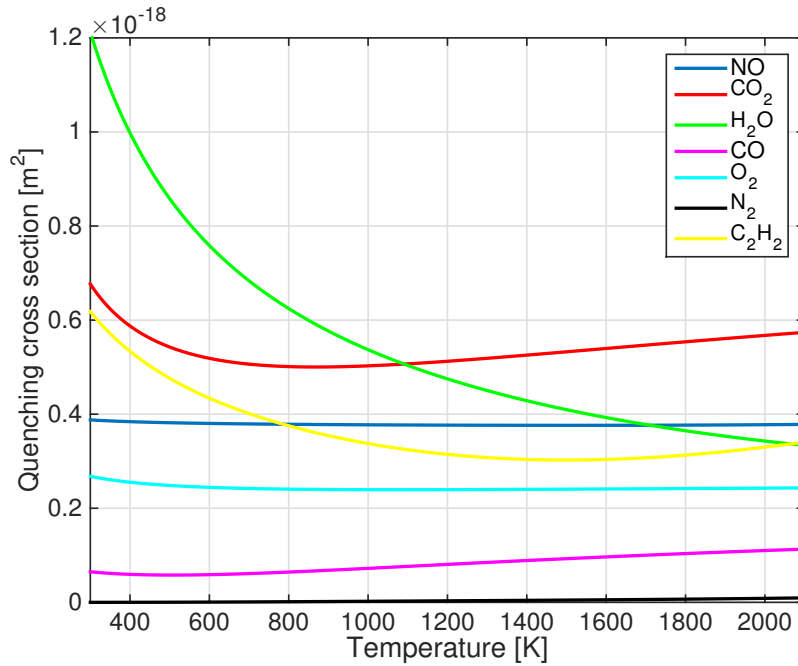


Figure 3.10: Quenching cross sections of the most relevant  $NO$  collisional partners as function of temperature.

The resulting quenching correction is shown in Fig. 3.11 along with the computed temperature used for its evaluation and the Boltzmann population fraction, computed according to Eq. 2.29.

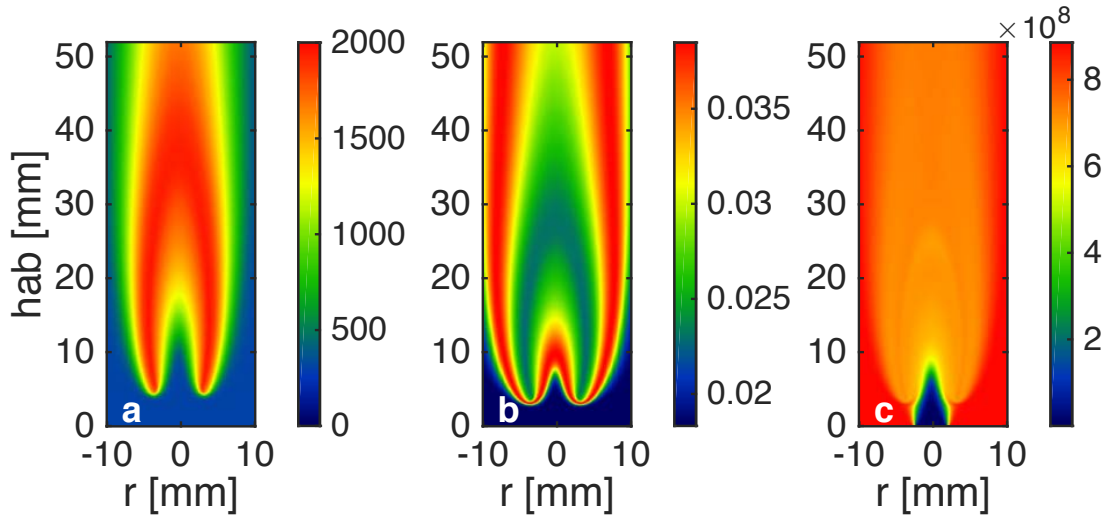


Figure 3.11: (a) Computed temperature, (b) Boltzmann population fraction, and (c) quenching rate used for the evaluation of Eq. 2.22.

The fluorescence derived from a nitrogen-diluted  $NO$  mixture of known composition at room temperature (45.2 ppm of  $NO$  in  $N_2$ , with the addition of 3% of oxygen, by volume) was compared with a simulated fluorescence signal calculated under the same conditions and used to calibrate and determine the experimental constant  $\alpha$  in Eq. 2.22. The addition of  $O_2$  was found to be necessary to control the quenching rate of the mixture; the quenching cross section of  $NO$  by  $N_2$  is small and not very well known [37], whereas  $O_2$  has a larger and better defined cross section that can be exploited to reduce the uncertainties associated with the evaluation of the quenching rate. The final simulated  $NO$  fluorescence signal was then computed using a Matlab script and compared with the measured two-dimensional fluorescence raw signal. The latter was derived by subtracting the off-resonant signal to the resonant one, and by mirroring the image along its symmetry axis to average the two halves as a way to increase the signal-to-noise ratio of the result. An example of raw resonant and off-resonant  $NO$  signals (in arbitrary units) for the steady 65% methane flame is shown in Fig. 3.12.

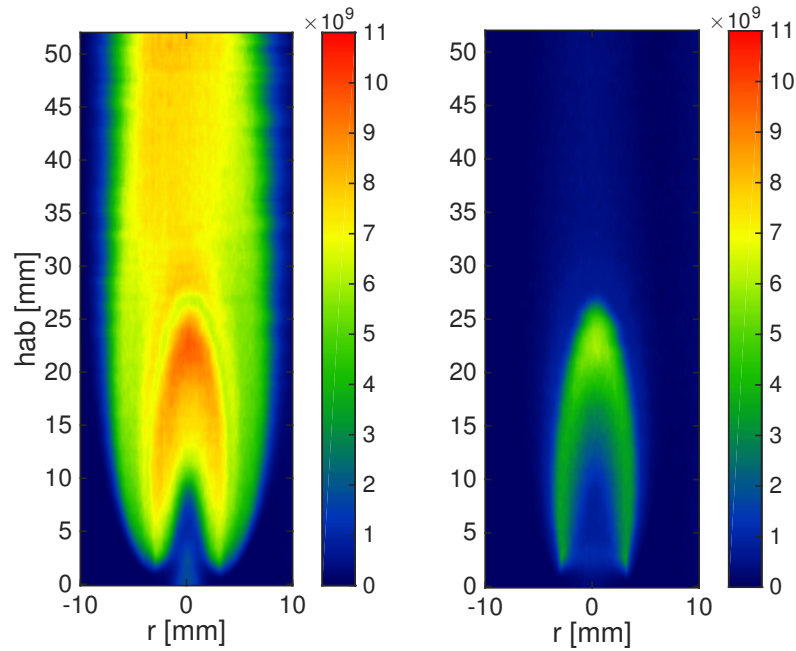


Figure 3.12: Resonant (left) and off-resonant (right) *NO* laser-induced fluorescence signals for the steady 65% methane flame.

### Numerical model

The numerical model implemented for the simulations consisted of an unconfined, axisymmetric, laminar diffusion flame in which a cylindrical fuel stream is surrounded by a coflowing oxidizer jet. The real fuel and coflow velocity profiles have been measured with PIV to ensure that the profiles were parabolic and flat, respectively, and those measurements were used as boundary conditions for the computation. The set of elliptic two-dimensional governing equations - mass, momentum, species and energy - were solved in a vorticity-velocity formulation. The resulting nonlinear equations were solved by a combination of time integration and Newtons method. The computation employed the GRI 3.0 chemical mechanism with 52 species for the steady flame, and a reduced GRI 2.11 mechanism with 31 species for the time-varying one. A more detailed discussion is presented in [49] and [48] for the steady and the time-varying flames, respectively.

### 3.1.3 Results and discussion

#### Steady flame

As mentioned, *NO* fluorescence in the steady 65% flame had already been measured through spectrally resolved measurements and compared to simulations [4]; the first step was therefore the repetition of the steady flame acquisition with the new imaging approach to ensure consistency between the results. Figure 3.13 shows the resulting computed (left) and measured (right) *NO* fluorescence.

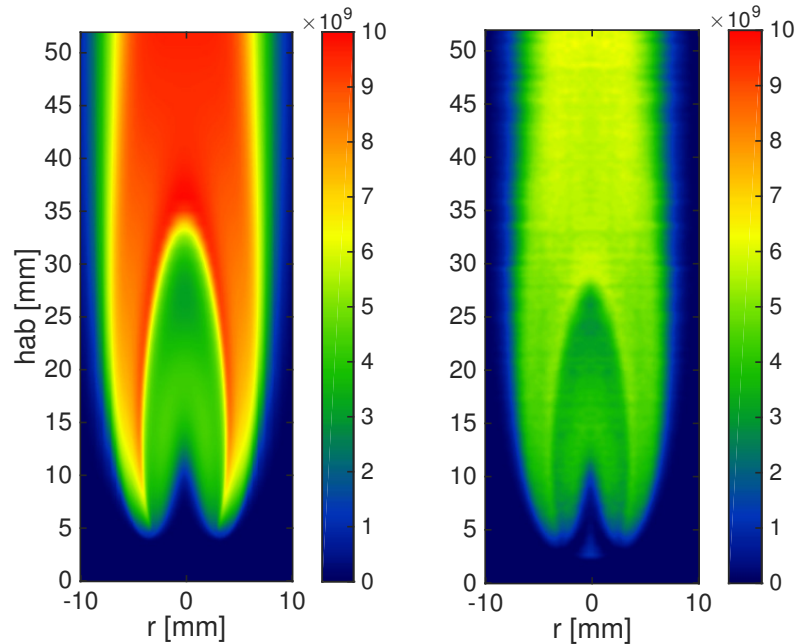


Figure 3.13: Computed (left) and measured (right) *NO* laser-induced fluorescence signals for the steady 65% methane flame.

The absolute fluorescence intensity, between simulation and experiment, showed a noticeable difference, especially along the flame wings and in the plume above the flame. The *NO* fluorescence, on the fuel side, was modeled in a quantitatively reasonable way, whereas its simulation on the oxidizer side overestimated its concentration (the chemical mechanism employed was known to over predict *NO* production by a factor of  $\sim 2.5$  [51]; on the other hand, the GRI 2.11 mechanism was seen to underestimate

*NO* production instead [4]). Despite the disagreement in the absolute signals, the gradients distribution of *NO* on the oxidizer side is still comparable: the *NO* fluorescence peak at the flame front is present in both results (because of the Fenimore *NO* formation as a consequence of the presence of *CH* radicals), and the relative intensity gradients in the wings and plume are correctly reproduced. The current experimental data, along with the numerical simulation discrepancy, was consistent with the findings of [4]. Figure 3.14 shows the fluorescence intensity plotted along the flame centerline, together with the previous results from Connelly.

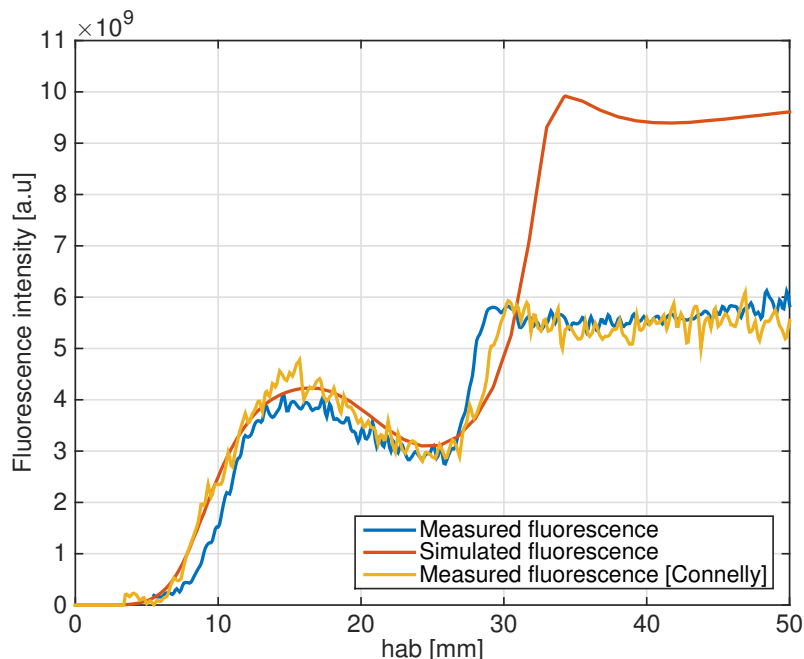


Figure 3.14: Comparison between the measured and computed centerline fluorescence intensities for the steady 65% methane flame. The result from [4] is reported as well.

The overall experimental *NO* distribution was found to be equivalent, with the imaging approach returning the same quantitative information as the spectrally resolved one, but with an improved signal-to-noise ratio. The small differences in flame height between the current and previous experimental results (see blue and orange curves in Fig. 3.14) were attributed to slightly different calibrations of the flow controllers.

The experimentally derived- temperature and major species [47,48] were finally used to evaluate the Boltzmann and quenching corrections and derive a  $NO$  mole fraction value from the acquired fluorescence signal. Figure 3.15 shows those results along with the measured  $NO$  concentration.

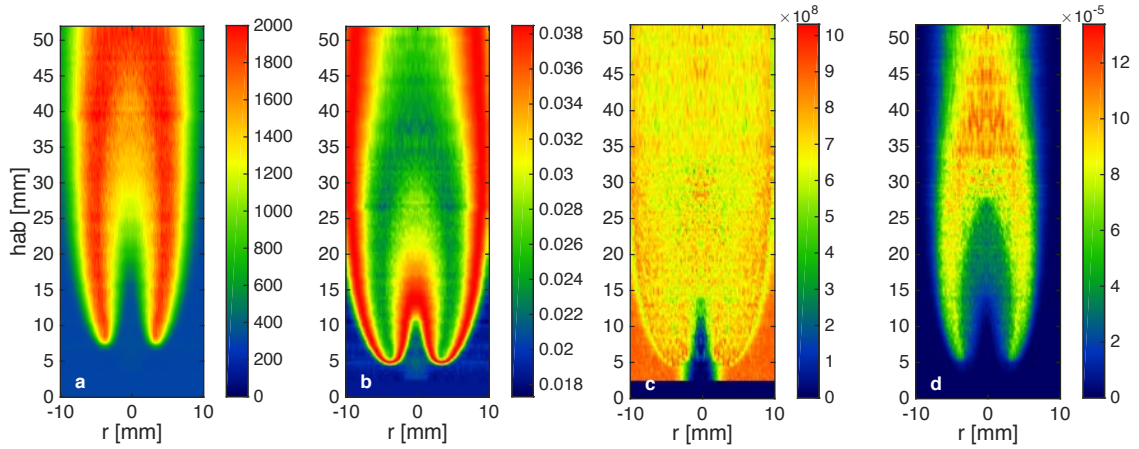


Figure 3.15: a) Measured temperature, (b) Boltzmann population fraction, (c) quenching rate, and (d)  $NO$  mole fraction.

Despite the fluorescent signal having a good signal-to-noise ratio, the final reconstructed  $NO$  mole fraction still had a relatively high noise. This was due to the fact that the quenching rate depended on high-noise Raman measurements of species such as  $CO$ ,  $CO_2$  and  $H_2O$  that negatively affected the smoothness of the quenching correction (see Fig 3.15c).

## Time-varying flame

Figure 3.16 show the results of the measured  $NO$  fluorescence distribution for five different phases of the time-varying flame with a 30% and 50% modulation of the fuel velocity (top and bottom, respectively). For the specific case of the time-varying flames, the chemical model used for the simulation was a “reduced” variant of the GRI 2.11 which did not have any nitrogen-containing species (except  $N_2$ ); therefore a direct comparison between simulated and measured fluorescence was not possible. Such reductions were implemented to decrease the size of the system and reduce the overall computational time (simulated time-varying results are however available for the specific case of  $CO$ , reported in the next section).

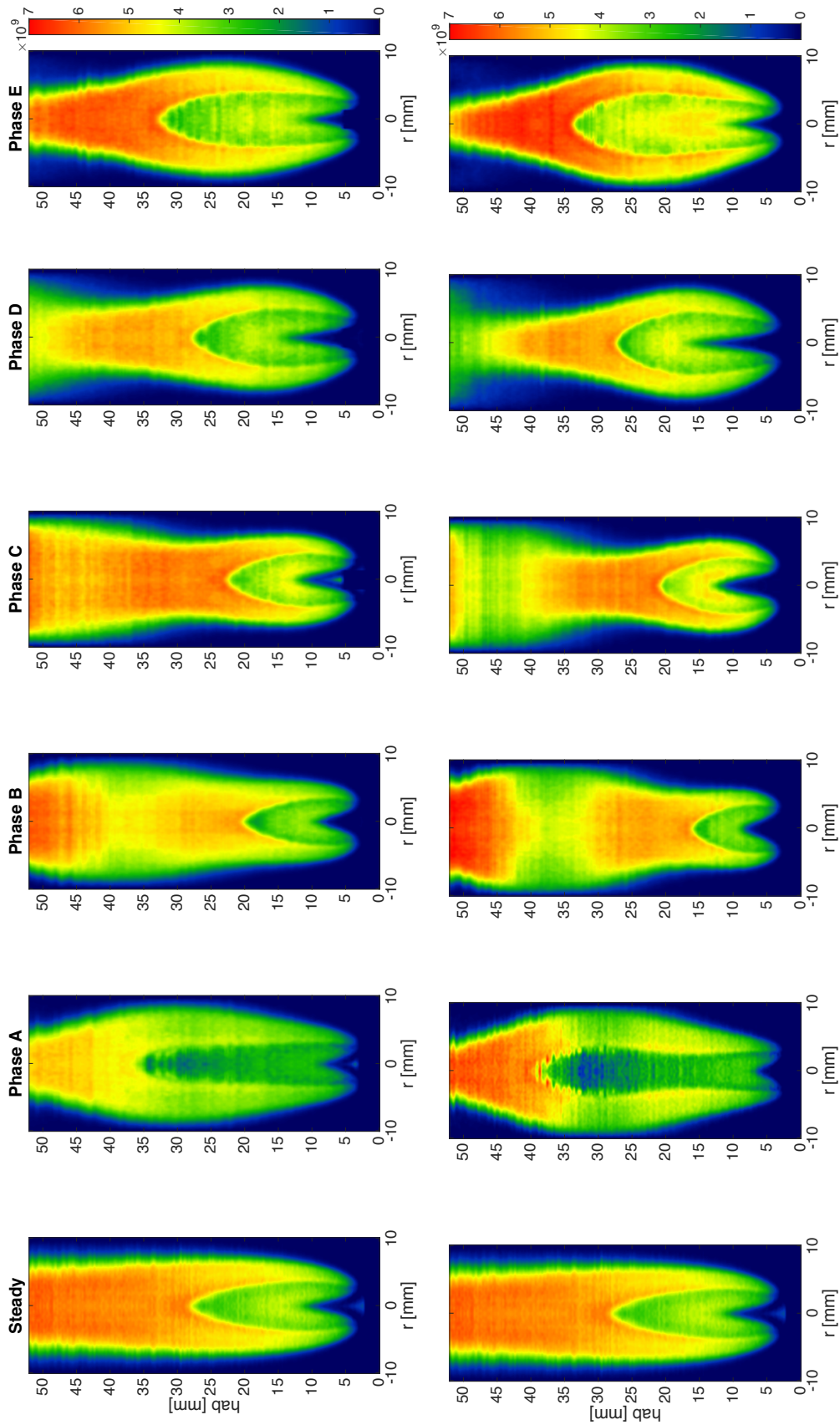


Figure 3.16: Measured  $NO$  laser-induced fluorescence signal for the time-varying 65% methane flame - steady result and five phases of the (top) 30% and (bottom) 50% modulation.

The fluorescence distribution is expected to be somehow smooth and continuous so, in order to remove unrealistic discrete jumps between line measurements taken at progressive heights above the burner, the above images were smoothed along the vertical direction.

When compared to the steady result, the absolute peak fluorescence signal of the time-varying cases did not change significantly; the flame modulation, naturally, induced a spatial redistribution of  $NO$  whose sudden increase, from the fuel to the oxidizer side, tended to follow the position of the peak  $CH^*$  profiles (see the normalized  $CH^*$  distributions in Fig. 3.17), confirming the major role of the Fenimore mechanism on the  $NO$  formation.

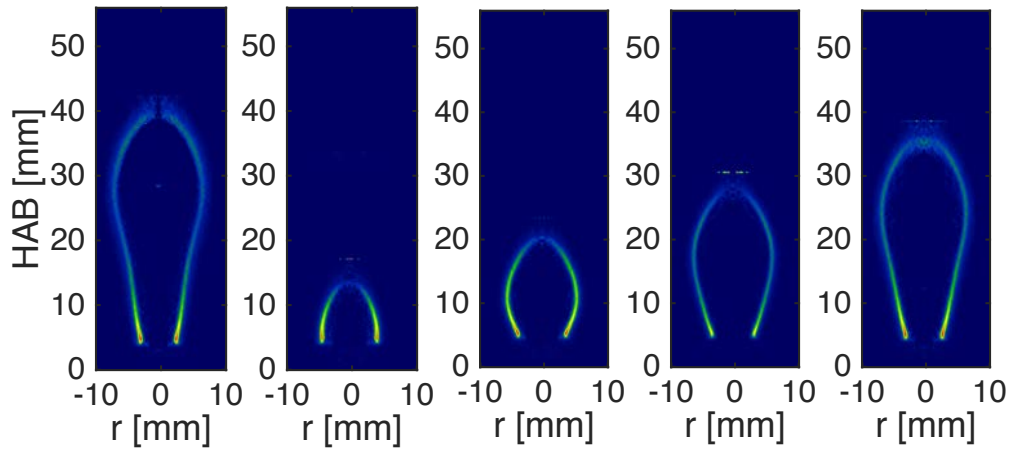


Figure 3.17: Measured  $CH^*$  chemiluminescence for the time-varying 65% methane flame - five phases of the 50% modulation.

Note that the measurements shown in Fig. 3.16 were very sensitive to the relative phase: in the forced flames soot production was facilitated since, at some locations and phases, the residence times increased, favoring soot growth. A small phase mismatch between resonant and off-resonant signals could therefore have introduced unwanted soot-derived luminosity when the two signals were subtracted.

## 3.2 Carbon monoxide LIF

One- and two-dimensional quantitative laser-induced fluorescence (LIF) measurements of  $CO$  concentrations in steady and time-varying hydrocarbon flames have been reported in several studies in the past proving the accuracy, reliability and detection limits of the technique. The majority of the approaches excite the  $B^1\Sigma^+ \leftarrow X^1\Sigma^+$  transition in the Hopfield-Birge system around 230.1 nm using a two-photon process [54–58,137], and rely on the  $B^1\Sigma^+ \rightarrow A^1\Pi^+ (0,1)$  transition as a collection band. To overcome the possible crosstalk of Swan band  $C_2^*$  fluorescence emission in the aforementioned collection region, Linow et al. [59] proposed an alternative scheme that excites the  $C^1\Sigma^+ \leftarrow X^1\Sigma^+$  transition via a two-photon process at 217.5 nm. As an additional and alternative example of  $CO$  measurement, Kirby et al. [60] performed  $CO$  imaging in flames by employing infra-red LIF.

Previous studies have shown that operating at high laser intensity has several advantages other than improving the signal intensity [55, 58]: in a regime where photoionization dominates, in fact, the quenching contribution can be neglected and the fluorescence is seen to scale linearly to the laser energy. In this section, an unpublished model of two-photon  $CO$  LIF developed by Settersten and coworkers (Personal Communication [34]) was partially implemented to take photoionization into account and get as accurate results as possible.

### 3.2.1 Experimental setup

The burner and flame used for the  $CO$  measurements are the same as described in Section 3.1.1 and their description will not be repeated here. Figure 3.18 shows a schematics of the experimental setup used for the  $CO$  LIF measurement.

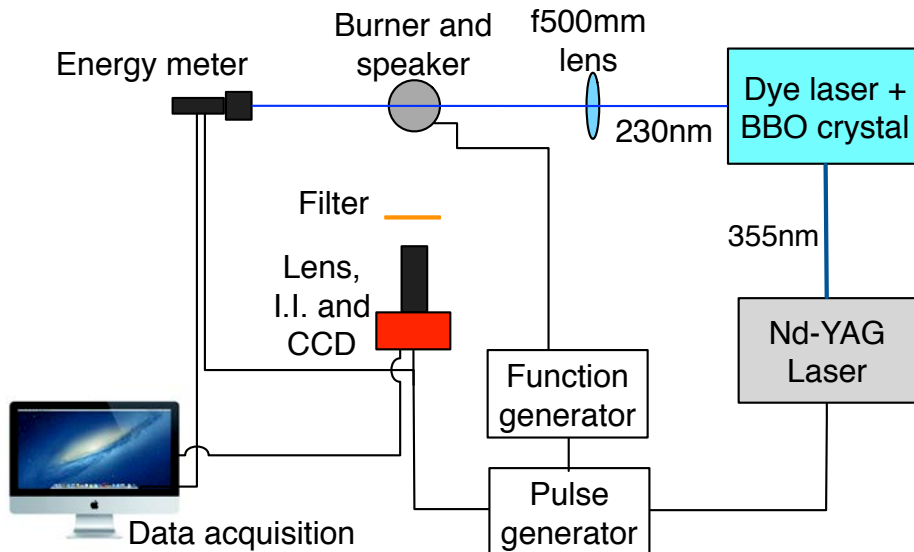


Figure 3.18: Schematic representation of the experimental setup used for the measurement of *NO* LIF

The third harmonic of a pulsed Quanta Ray Pro-250 Nd-YAG laser (10 Hz repetition rate) was used to pump a tunable Sirah Precision Scan dye laser containing a solution of methanol and Coumarin C450 (0.152 g/L). The output of the dye laser was frequency doubled with a BBO crystal and used to excite the Q branch (0,0) of the  $B^1\Sigma^+ \leftarrow X^1\Sigma^+$  transition near 230 nm through a two-photon process. The laser beam (line width of  $\sim 0.5 \text{ cm}^{-1}$ ) was focused to a line above the burner using a spherical f-500 mm quartz lens; the resulting beam size was measured to be  $150 \mu\text{m}$  FWHM. The  $B^1\Sigma^+ \rightarrow A^1\Pi^+$  (0,1) transition was selected as a collection band for the fluorescence emission and it was collected through a 488 nm interference filter (10 nm FWHM bandwidth, tilted  $15^\circ$  to decrease the central wavelength from 488 to 483 nm) and focused with an 85 mm Nikkor lens onto a Gen II DEP image intensifier gated on for  $3 \mu\text{s}$  (the intensifier gain was set to 8.5 V, equal to 70% of its operative voltage range, and the glass lens doubled as a filter for the scattered UV light). The intensifier, which worked also as a fast shutter, was optically coupled to a cooled SBIG STF-8300M camera (3352 x 2532 pixels, 17.96 x 13.52 mm CCD size) using a pair of

Nikkor 50 mm lenses. The magnification achieved, increased by mounting the 85 mm lens on an extension tube, was 200 pixels/mm. A Stanford Research System DG535 pulse/delay generator provided the synchronization between the laser, the camera, the energy meter (Laser Probe Rm-3700) and the function generator that drove the speaker for the fuel velocity modulation (Stanford Research System DS345). The energy meter took into account the energy variation associated with the degradation of the dye solution and the temporal fluctuations of the Nd-YAG laser output. During the experiments, a new dye solution allowed for an hour of measurements before the substitution of the worn-out dye was necessary. During this time the laser energy typically ranged between 1.9 and 1.3 mJ per pulse. The burner assembly was placed on a vertical translation stage driven by a Velmex stepper motor. Consequently, data was obtained at different burner heights in a 0.2 mm spaced scan of the flame, which allowed for a 2D reconstruction of the *CO* fluorescence spatial distribution. For every scan, a “line” image was the result of an integration over 20 seconds (200 laser pulses). As was the case for the *NO* measurements, all the phases of the acquisition process were monitored using the software OMA [50].

### 3.2.2 Diagnostic considerations

As previously shown in Eq. 2.27, the fluorescence signal depends on the number density of a molecule through the Boltzmann distribution, which requires the knowledge of the precise excited rotational quantum number  $J$  for its evaluation. The temperature dependence of the *CO* total population fraction is plotted in Fig. 3.19, according to Eq. 2.29, for three different rotational quantum numbers  $J$  (and for  $V_s = 0$ ) showing how, in the temperature range 1000 - 2000 K, the dependence decreases as the number  $J$  is increased.

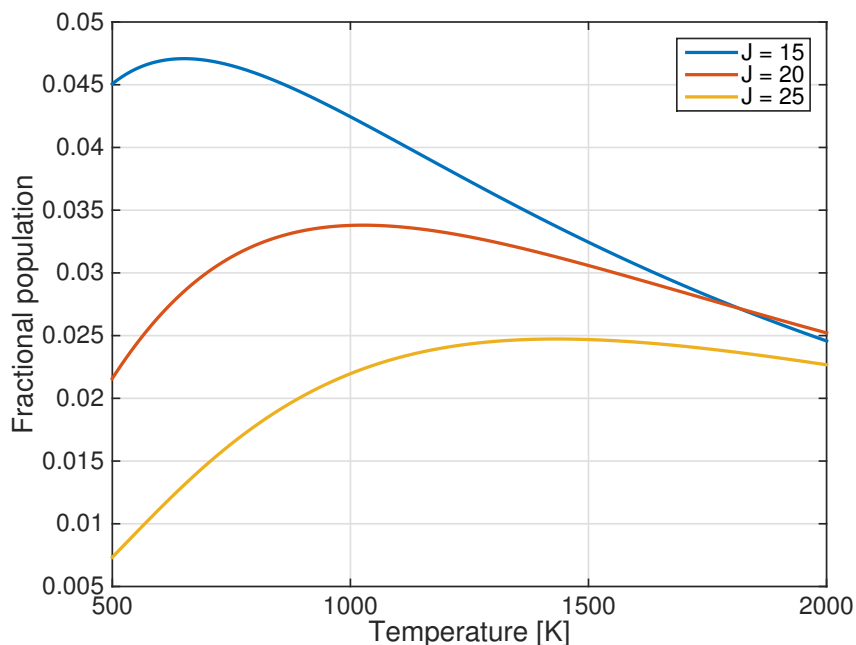


Figure 3.19: Total  $CO$  population fraction as function of three rotational quantum numbers  $J$ .

In the current study,  $J = 25$  was the rotation quantum number selected for the excitation because of its minimal dependence in the range of temperatures relevant to in-flame  $CO$  production ( $\sim 1000 - 2000$  K). This reduced dependence minimized any error related to the temperature evaluation while keeping the signal-to-noise ratio satisfactory.

To relate the selected  $J$  to a specific excitation wavelength an in-flame  $CO$  excitation spectrum was performed in a region where the flame temperature was known from previous Rayleigh measurements [2]. Unlike the case of  $NO$ , LIFBASE does not compute  $CO$  spectra, therefore the simulated spectrum needed for the comparison was computed according to [36,61–63] and it is shown in Fig. 3.20 (assuming a  $T_{flame} = 1200$  K); such comparison allowed for the selection of the 230.008 nm wavelength on the dye laser that excited the rotational quantum number  $J = 25$ . An off-resonant signal at 230.15 nm was taken as a background, and this accounted for molecular broadband fluorescence, incandescence interferences, and flame luminosity.

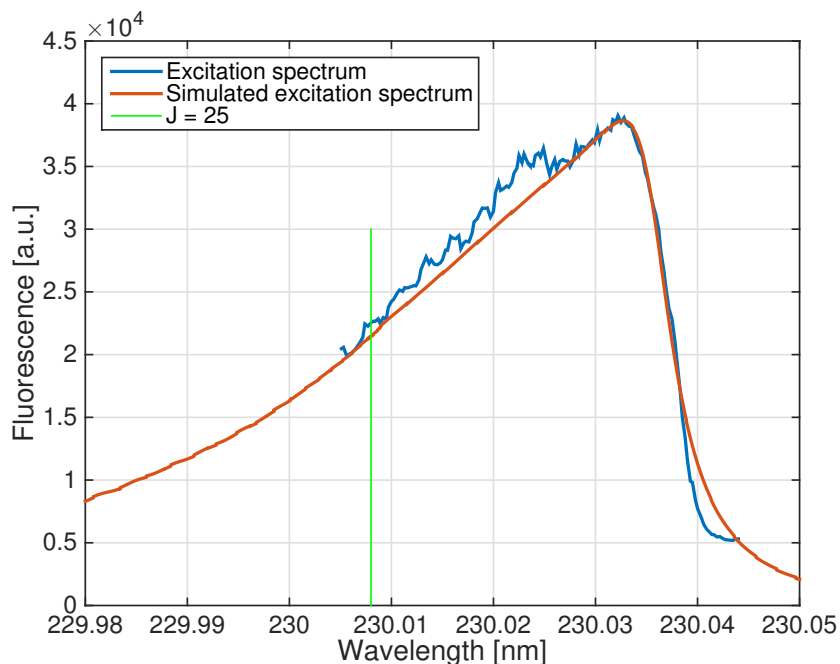


Figure 3.20: Overlap between measured  $CO$  excitation spectrum (blue curve) and simulated one (red curve). The green line identifies the wavelength selected for the LIF excitation.

Additionally, the simulated spectrum allowed for the evaluation of the line spacing between the rotational quantum numbers around  $J = 25$ . In this region the spacing was calculated to be  $\sim 0.6 \text{ cm}^{-1}$ , which is wider than the line width of the laser that was employed; however, Doppler and pressure effects caused the broadening of these lines which in turn lead to a band overlap with a consequent excitation of multiple  $J$  levels. The modeling of the broadening was done assuming Lorentzian distributions with  $1.3 \text{ cm}^{-1}$  FWHM bandwidth, as suggested in [61]. Figure 3.21 plots the broadened lines distribution in the range between  $J = 20$  to  $J = 30$  highlighting the simultaneous excitation of numerous transitions by the laser pulse (shown by the red curve).

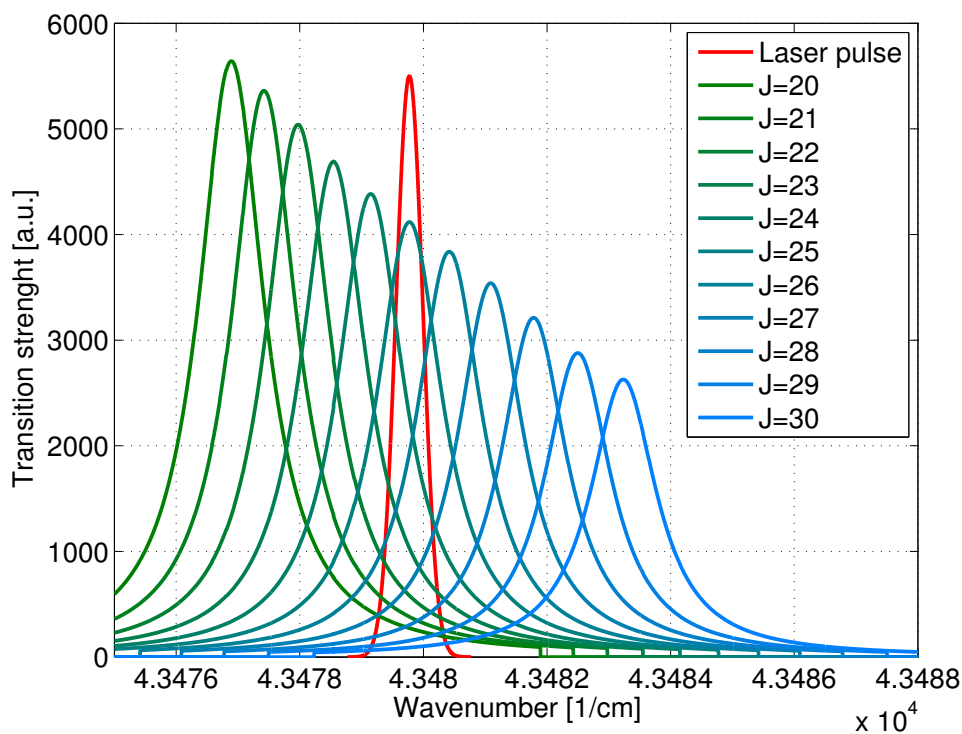


Figure 3.21: Overlap of the broadened transitions (modelled as Lorentzians) with the laser pulse.

To account for the simultaneous excitation of multiple  $J$ s an effective Boltzmann population distribution was evaluated considering a weighted average of all the transitions overlapping with the laser excitation. The relative contribution of the various  $J$ s to the final Boltzmann distribution is summarized in Fig. 3.22; with reference to Fig. 3.21, for each  $J$ , the contribution was evaluated as the ratio between the total area of the Lorentzian, and the area of the region spanned by the  $0.5 \text{ cm}^{-1}$  laser line width.

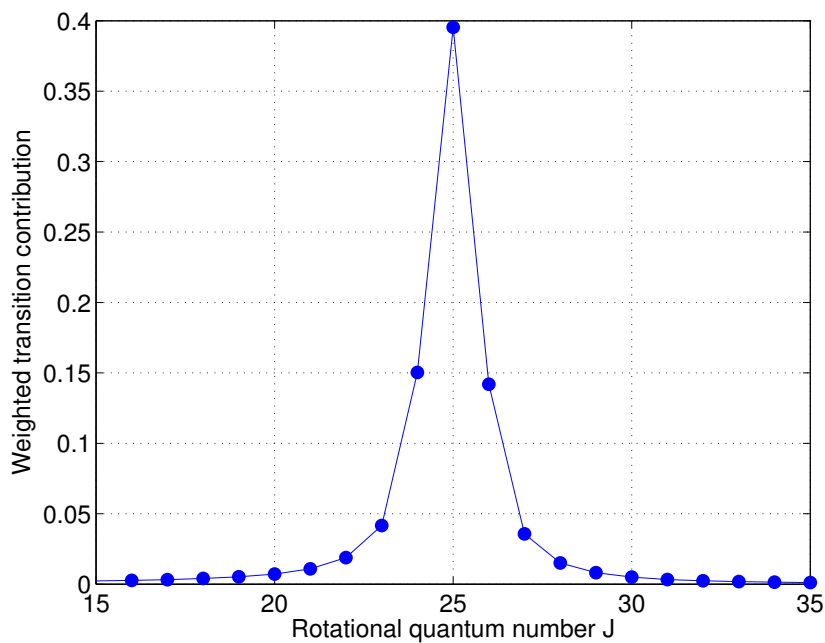


Figure 3.22: Transition's contribution as function of the rotational quantum number  $J$ .

The  $B^1\Sigma^+ \rightarrow A^1\Pi^+$  (0,1) transition that was chosen to collect the fluorescence signal was verified not to overlap with the nearby  $C_2^*$  Swan band emission, whose closest peaks are located around 470 nm ( $C_2^*$  was seen to overlap instead with the (0,2) emission band centered around 518 nm). Figure 3.23 shows a superposition of a  $CO$  emission spectrum (measured at ambient temperature using a calibration gas), the collection region determined by the interference filter (orange curve), and part of the  $C_2^*$  emission that could possibly interfere with the (0,1) band (red curve).

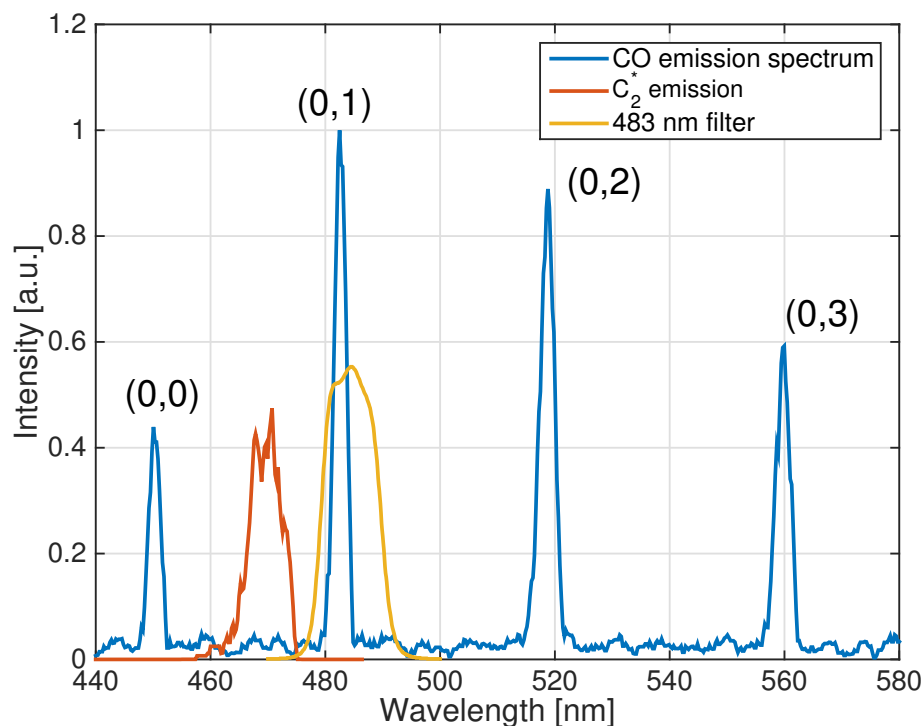


Figure 3.23:  $CO$  emission spectrum plotted along with one of the  $C_2^*$  band and interference filter spectral collection region.

Spectroscopic measurements of in-flame  $CO$  emission have also been performed and are shown in Fig. 3.24. The top plot displays the emission recorded when tuning the laser to several off-resonant frequencies, while the bottom one displays the resonant signals. The off-resonant results clearly revealed the relative position of the  $C_2^*$  bands with respect to the collection region and  $CO$  bands. In the resonant results, despite the poor signal-to-noise ratio, the (0,1) band clearly exhibited a broadening and a blue-shifting when the laser excitation was tuned to higher  $J$ s (higher wavelengths), and it was verified that in the collection region defined by the interference filter  $C_2^*$  overlap was never present, regardless of the excited  $J$ .

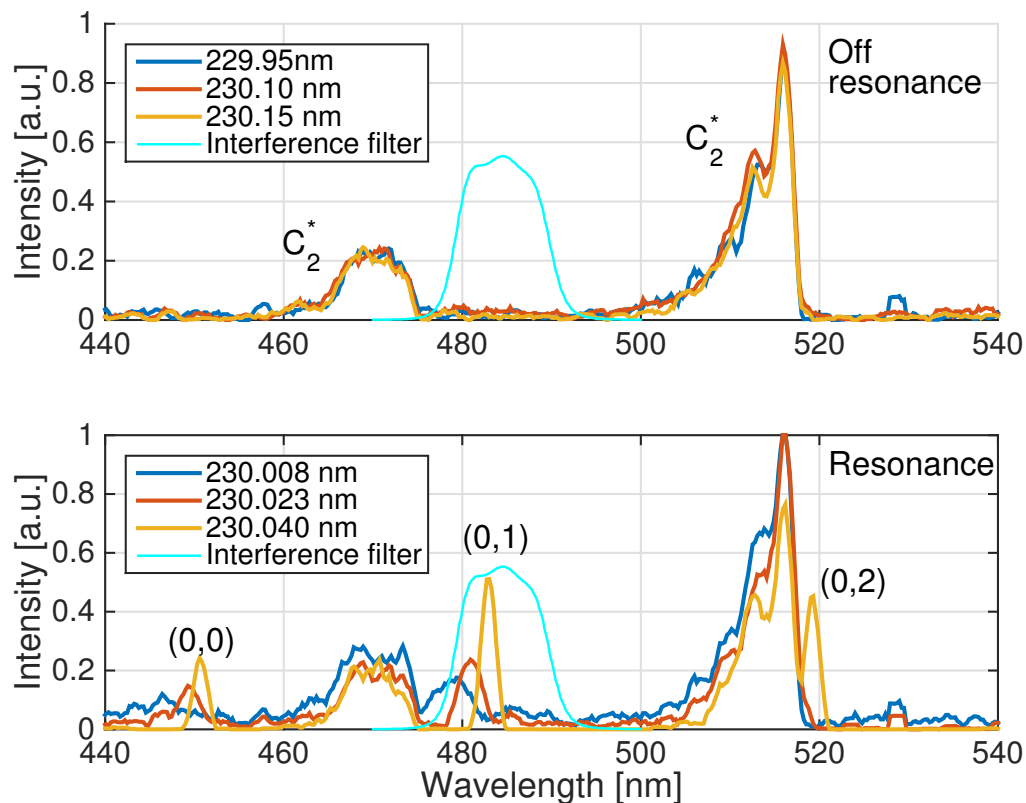


Figure 3.24: In-flame  $CO$  emission spectrum. (Top) off-resonant signals and spectral position of  $C_2^*$  Swan bands; (bottom) resonant signal and spectral position of the  $CO$  bands with respect to  $C_2^*$  ones and collection region.

The numerical model implemented is the same as the one described in Section 3.1.2 and will not be repeated here. The simulation results have undergone multiple validations [2,46–49] giving us confidence about their reliability; thus, the numerically-derived temperature and species distributions were used to determine the Boltzmann and quenching rate corrections through the use of Eqs. 2.29 and 2.31. Despite being a minor contributor, the quenching rate was modeled and implemented in the overall calculation: it was evaluated following the relation given in Eq. 2.31 and assuming that the collisional quenching cross sections provided in [38] could be extrapolated to flame temperatures as well, as shown in Fig. 3.25.

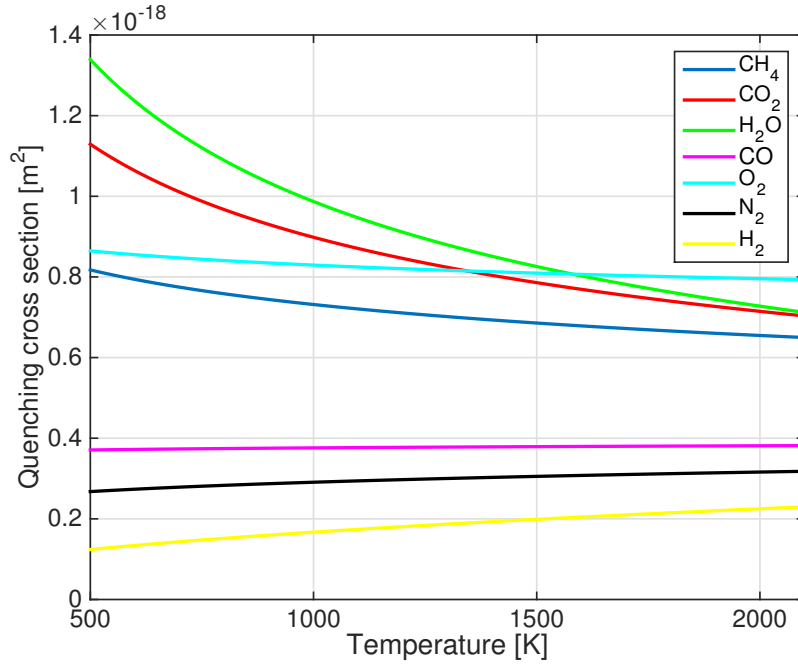


Figure 3.25: Quenching cross sections of the most relevant  $CO$  collisional partners, as function of temperature.

In the flame region the quenching rate value was measured to be on the order of  $\sim 3 \cdot 10^9 \text{ s}^{-1}$ , a value that had to be compared with the photoionization rate in order to verify the accuracy of the photoionization-dominance claim. Because of the high average laser fluences used in this study ( $\sim 8.5 \text{ J/cm}^2$ ), the photoionization effect was indeed significant: its value, in the flame region, was calculated according to [34] to be on the order of  $\sim 10^{10} \text{ s}^{-1}$ . The resulting photoionization rate is shown in Fig. 3.26, along with the computed temperature, Boltzmann, and quenching corrections.

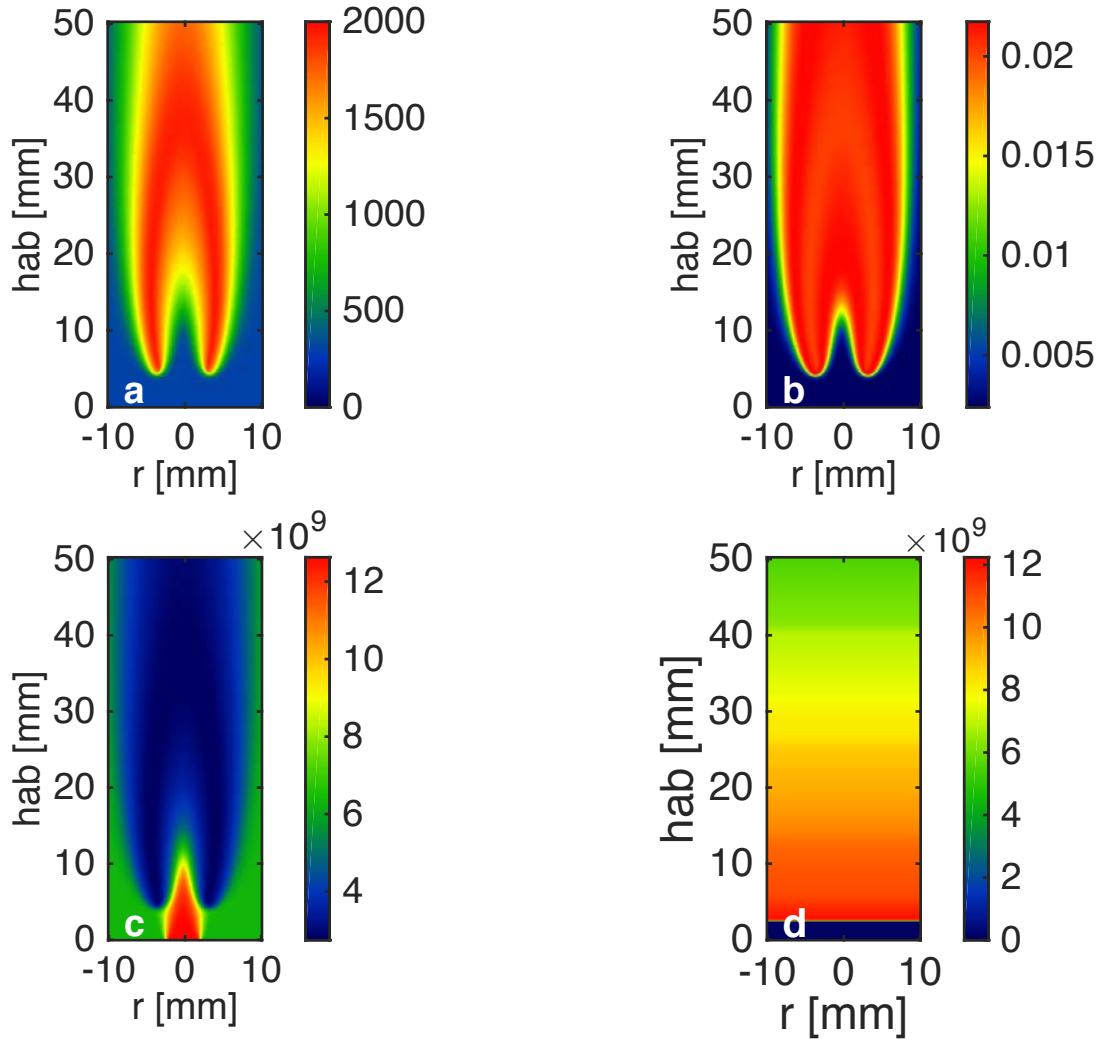


Figure 3.26: (a) Computed temperature, (b) Boltzmann population fraction, (c) quenching rate, and (d) photoionization rate used for the evaluation of Eq. 2.27.

The photoionization rate distribution was seen to be constantly decreasing with the distance from the burner surface; this was due to the temporal degradation of the dye that resulted in lower laser energy output as the measurement was performed (the flame scan was done from the bottom to the top). The denominator of Eq. 2.27 was dominated by the photoionization term yielding an overall nearly linear dependence of the fluorescence signal to the laser intensity; the linearity of the  $CO$  fluorescence was verified by recording LIF resonant emission, measured in flame, as function of

the laser energy (see Fig. 3.27).

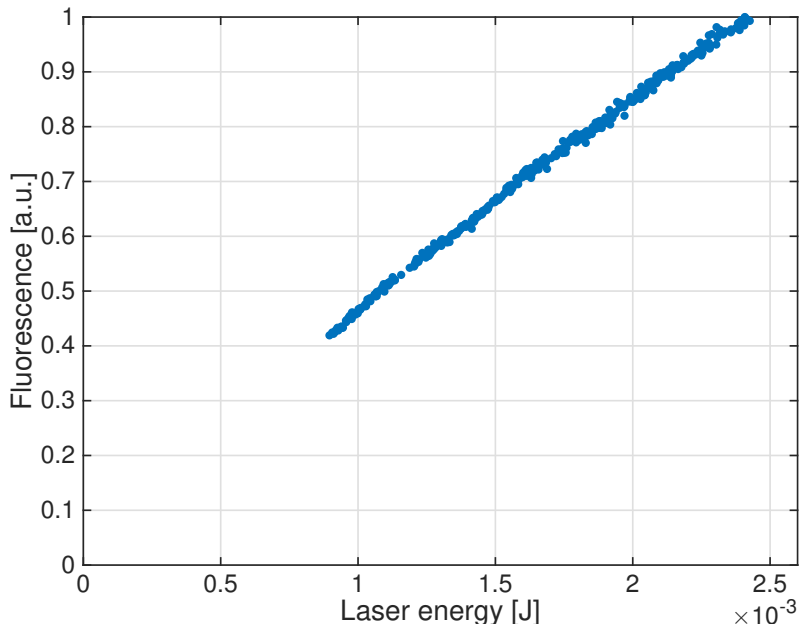


Figure 3.27: Relation between *CO* laser-induced fluorescence and laser energy.

The linear dependence of the fluorescence signal to the laser energy allowed for a shot-to-shot signal correction based on the power meter reading. Note that, if extrapolated, the data points shown in Fig. 3.27 will not intersect the axis origin; this was due to the fact that the data were derived from resonant signals only, and were missing an off-resonant subtraction. Given the absence of any laser-induced fluorescence in the off-resonant signals (as seen in Fig. 3.24) the linear trend shown in Fig. 3.27, therefore the linear behavior of the fluorescence, was believed to be accurate.

The spontaneous emission rate, according to [64], was assumed to be on the order of  $10^7 \text{ s}^{-1}$ ; because of the linear scaling of the fluorescence with the laser intensity, stimulated emission was assumed to be negligible. Production of *CO* from *CO*<sub>2</sub> by photolytic reactions was considered negligible as well; from the good agreement between simulations and Raman scattering measurements, and given the fact that photolytic *CO* production can be most important in lean premixed flames, it was implied that

such contribution was minor for this specific case. The fluorescence derived from a nitrogen-diluted  $CO$  mixture of known composition at room temperature (4%  $CO$ , 96%  $N_2$ , by volume) was compared with a simulated fluorescence signal calculated under the same conditions and finally used to calibrate and determine the experimental constant  $\alpha$  in Eq. 2.27. The final simulated  $CO$  fluorescence signal was then computed using a Matlab script and compared with the measured two-dimensional fluorescence raw signal.

### 3.2.3 Results and discussion

#### Steady flame

As a first step, the calculated and measured  $CO$  fluorescence signals were evaluated for the steady flame case and their comparison is shown in Fig. 3.28 (left and right, respectively).

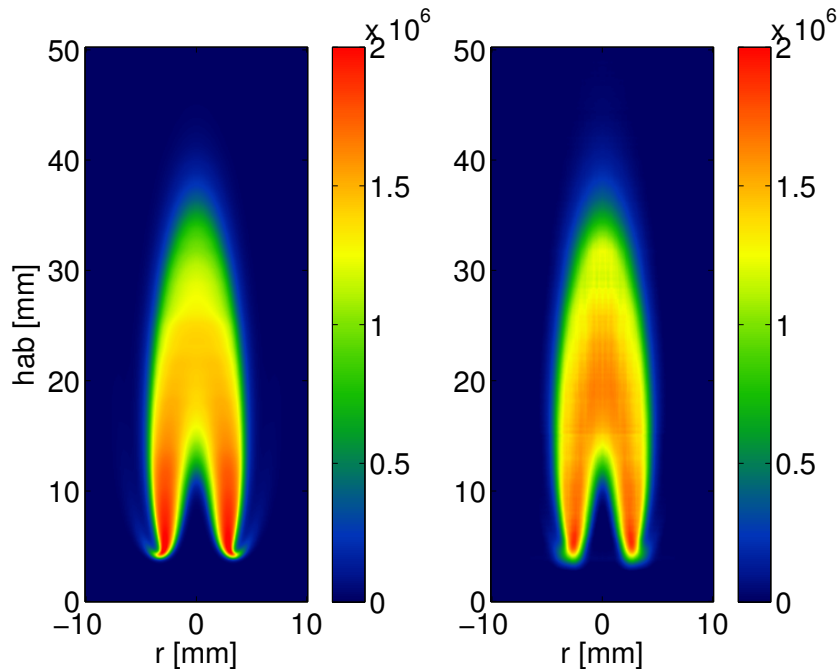


Figure 3.28: Computed (left) and measured (right)  $CO$  laser-induced fluorescence signals for the steady 65% methane flame.

Cross sections of the fluorescence intensity taken along the flame centerline, and along the radius, for three different heights above the burner, are shown in Fig. 3.29.

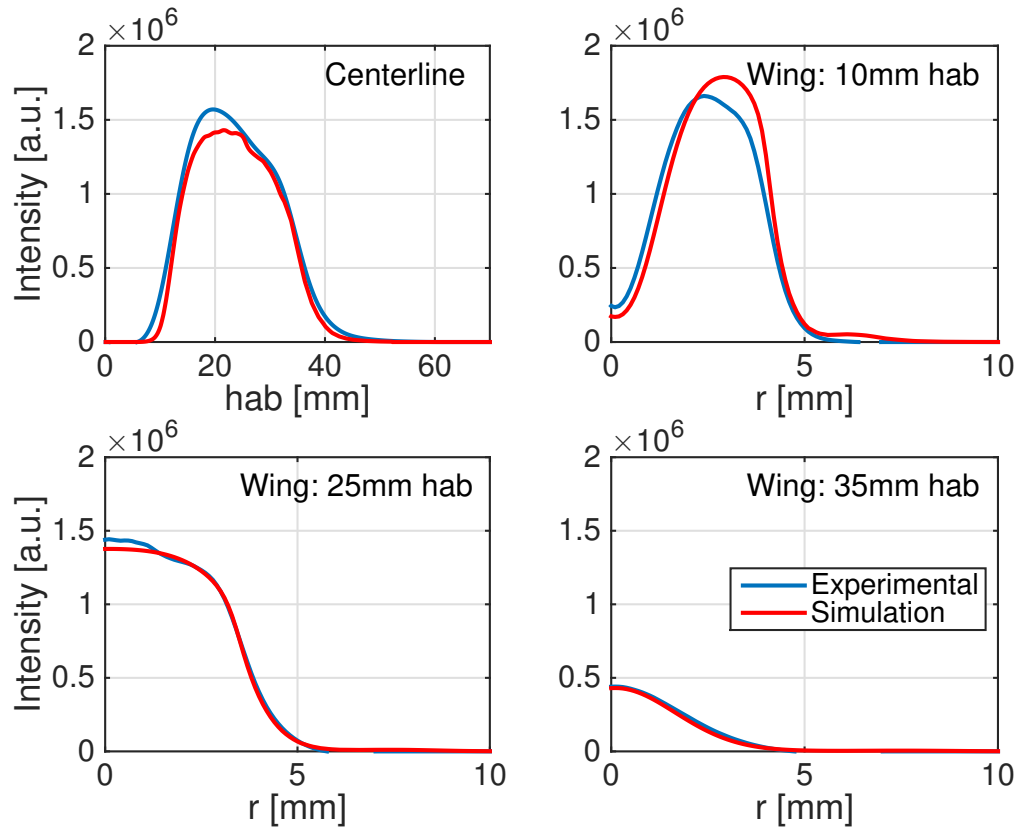


Figure 3.29: Fluorescence intensity cross section along the centerline and at three different heights above the burner: comparison between measured and simulated results.

The agreement is seen to be excellent when considering both the spatial distribution and the overall absolute intensity; the liftoff height and the flame length are correctly predicted as well as the fluorescence intensity gradients. The good agreement provided confidence in both the fluorescence measurement and the modeling itself. Because the major species in this flame were measured separately using Raman scattering, and the temperature was measured with Rayleigh scattering [47, 48], the fluorescence signal could be used to determine the absolute  $CO$  number density by employing Eq. 2.27. The measured temperature and species concentrations were used for the Boltzmann and quenching corrections (see Fig. 3.30), while the recorded laser intensity accounted for the photoionization rate. Figure 3.31 shows the comparison between calculated (left), LIF-derived (center) and Raman-derived (right)  $CO$  mole fractions.

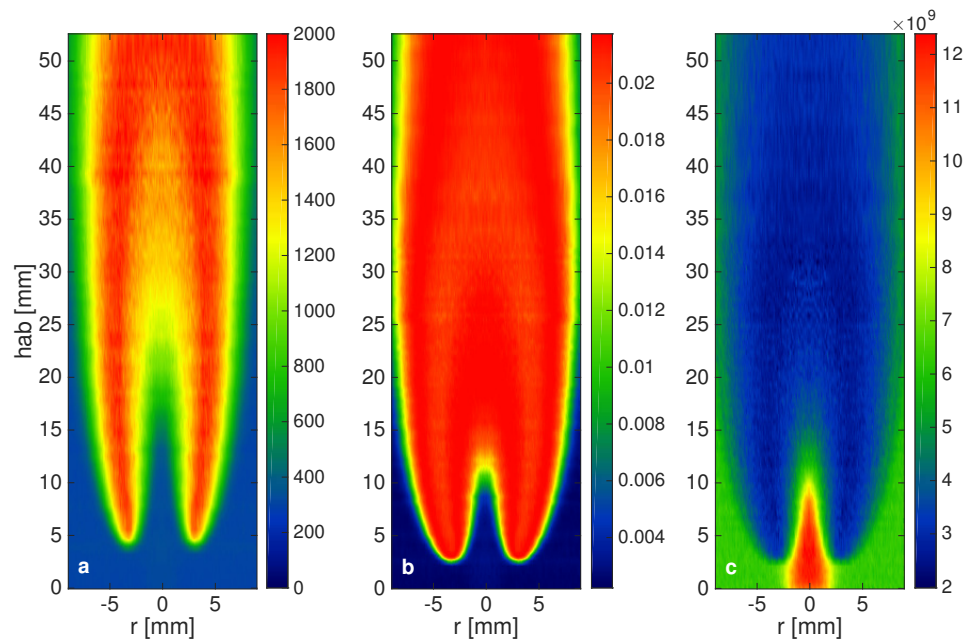


Figure 3.30: (a) Measured temperature, (b) Boltzmann population fraction, and (c) quenching rate.

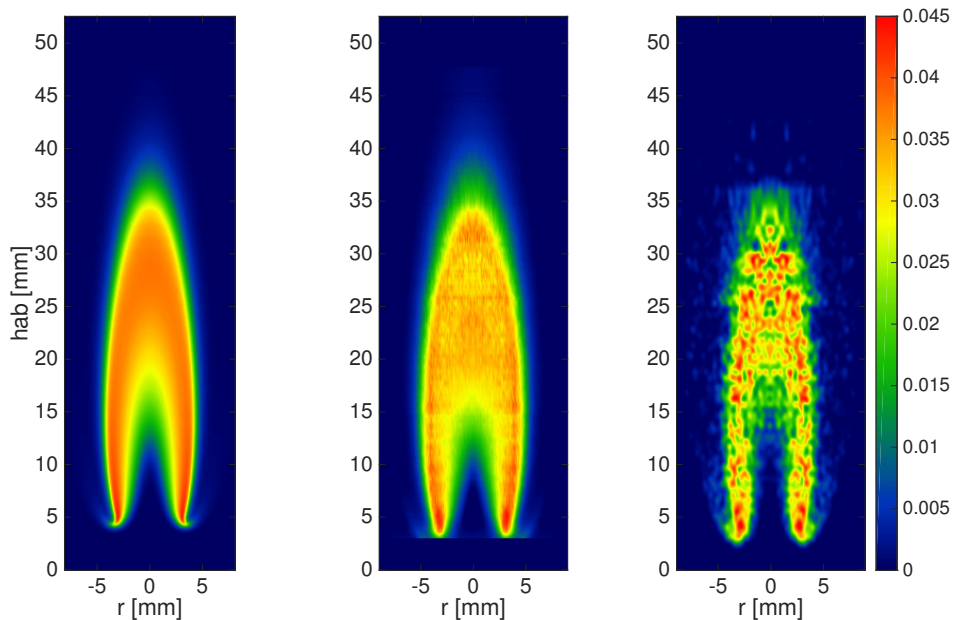


Figure 3.31: Computed (left), fluorescence-derived (center), and Raman-derived (right) CO mole fraction.

The signal-to-noise ratio (SNR) in the measured  $CO$  mole fraction is  $\sim$  five times greater than the previous one measured with Raman scattering. The SNR was evaluated by considering an interrogation region below the tip of the flame where, according to computations, the average  $CO$  mole fraction is roughly constant. In this region the SNR was calculated by dividing the mean pixel values by the RMS. As expected, the SNR for the  $CO$  mole fraction is lower than the fluorescence one, since the experimental measurements contribute to the overall noise. The calculated absolute  $CO$  mole fraction is comparable to the measured value and the absolute intensity and features, like the  $CO$  peak along the flame wings, as well as the overall distribution, are correctly reproduced.

Despite the fact that the quenching rate in the flame region is roughly 33% of the photoionization rate, the justification for neglecting the quenching correction came from the comparison between the fluorescence calculated with and without quenching contribution; as can be seen from the plots in Fig. 3.32 (plots along the centerline and

across the flame for three different heights above the burner) such difference was less than  $\sim 10\%$ .

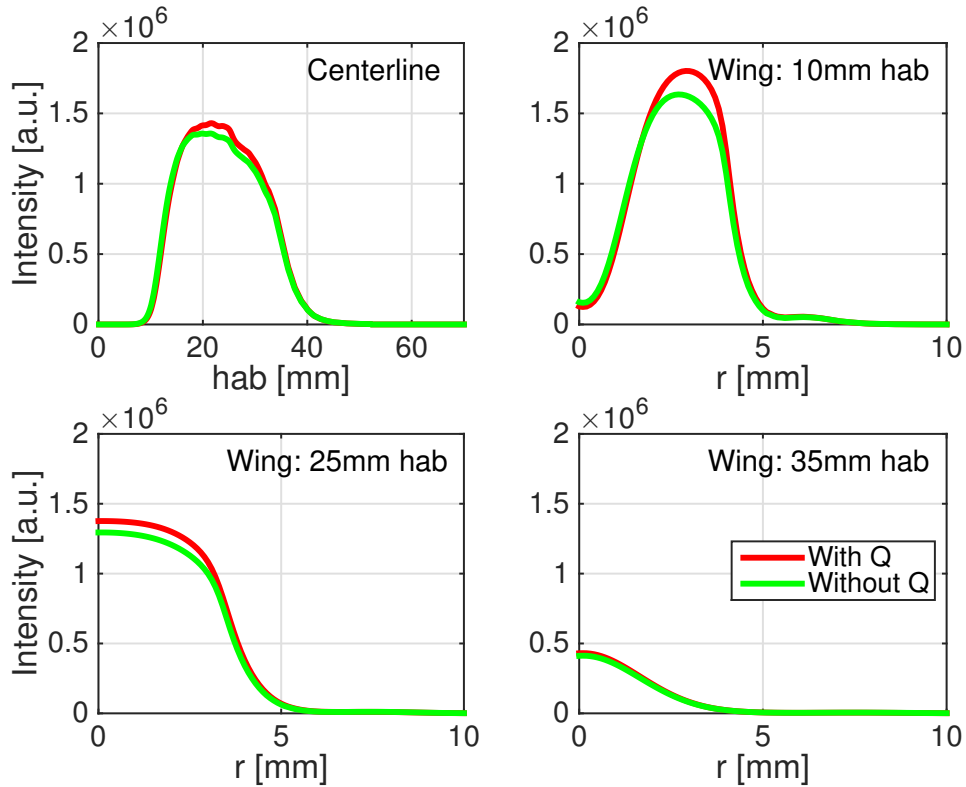


Figure 3.32: Fluorescence intensity cross section along the centerline and at three different heights above the burner: influence of the quenching correction.

### Time-varying flame

Having demonstrated reasonable agreement for the steady flame, the approach was subsequently extended to the time-varying cases. Figure 3.33 show the results for the measured and computed  $CO$  fluorescence distribution at five different phases of the time-varying flame with a 30% modulation of the fuel velocity. Each column represents one of the five phases investigated (except the first one which is the steady result) and the fluorescence signal is shown along with the computed temperature and computed Boltzmann population fraction (Fig. 3.34), and the computed quenching correction and photoionization rate (Fig. 3.35).

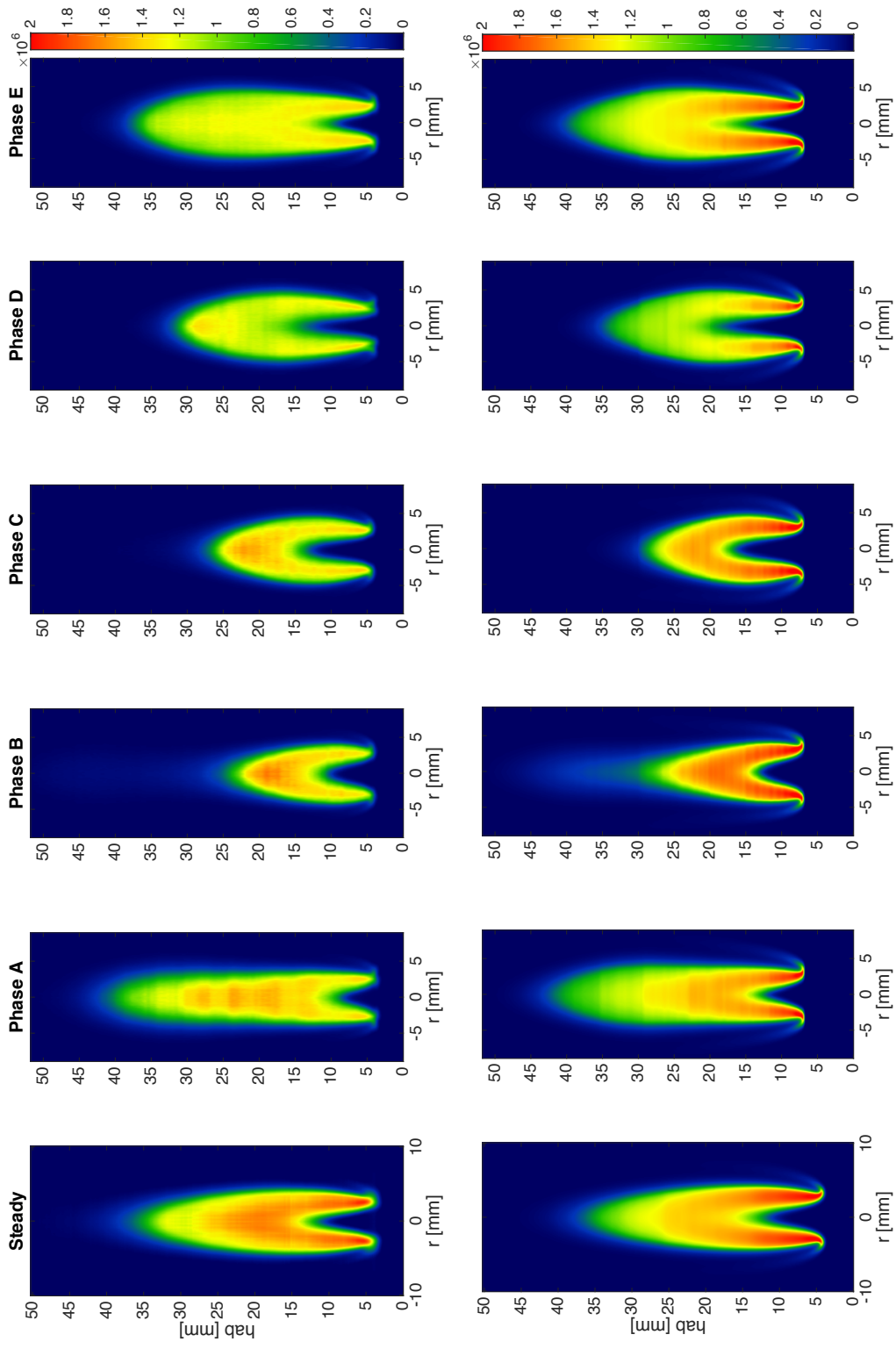


Figure 3.33: (Top) measured and (bottom) computed  $CO$  laser-induced fluorescence signal for the time-varying 65% methane flame - steady result and five phases of the 30% modulation.

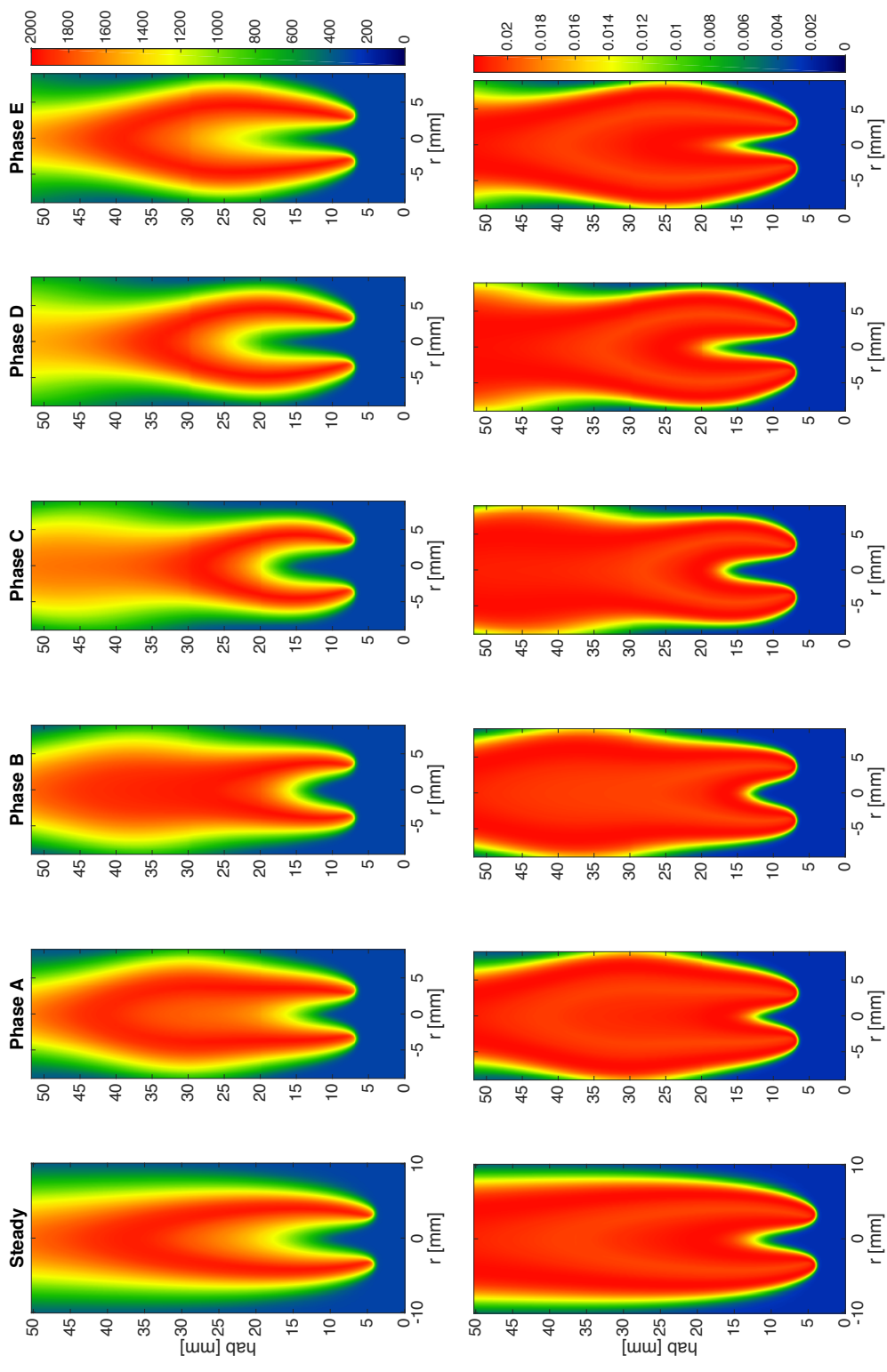


Figure 3.34: (Top) computed temperature and (bottom) computed Boltzmann population fraction for the steady and 30% modulation flame.

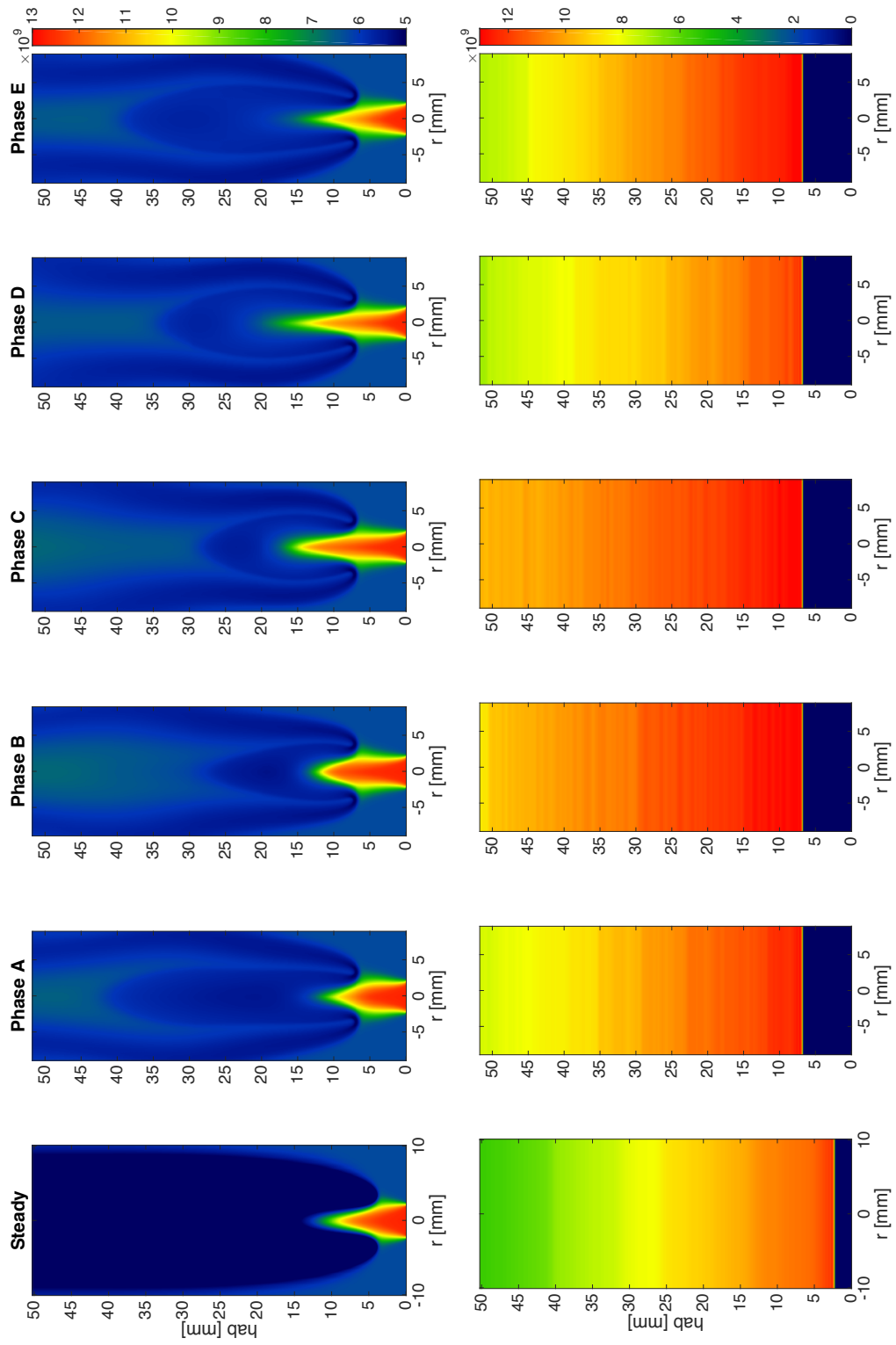


Figure 3.35: (Top) computed quenching rate and (bottom) photoionization rate for the steady and 30% modulation frame.

The plots in Fig. 3.36 compare the fluorescence intensity along the flame centerline for the five phases considered.

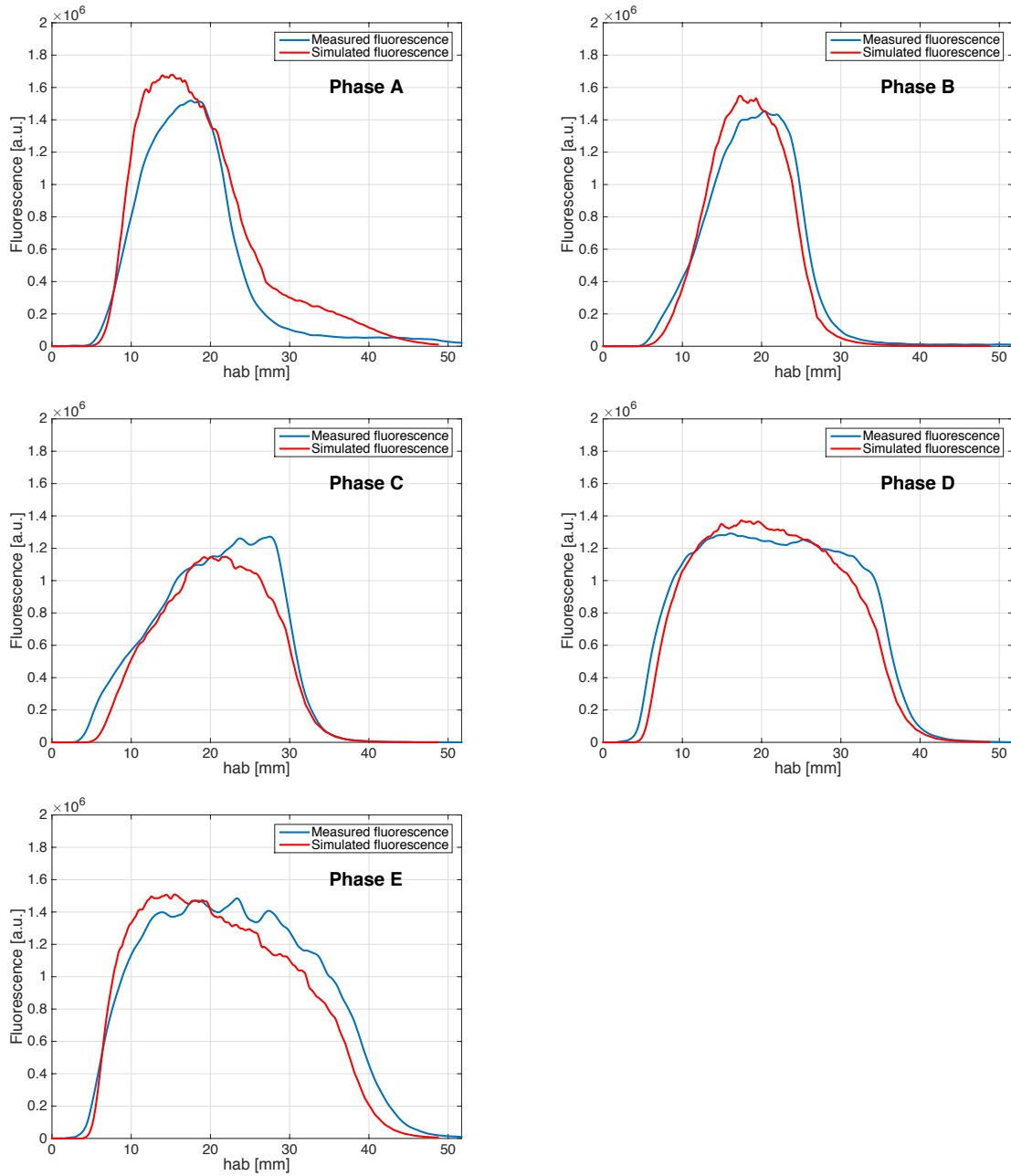


Figure 3.36: Fluorescence intensity along the flame centerline for the time-varying flame shown in Fig. 3.33.

Figure 3.37 show the results for the measured and computed  $CO$  fluorescence distribution at five different phases of the time-varying flame with a 50% modulation of the fuel velocity. Each column represents one of the five phases investigated (except the first one which is the steady result) and the fluorescence signal is shown along with the computed temperature and computed Boltzmann population fraction (Fig. 3.38), and the computed quenching correction and photoionization rate (Fig. 3.39).

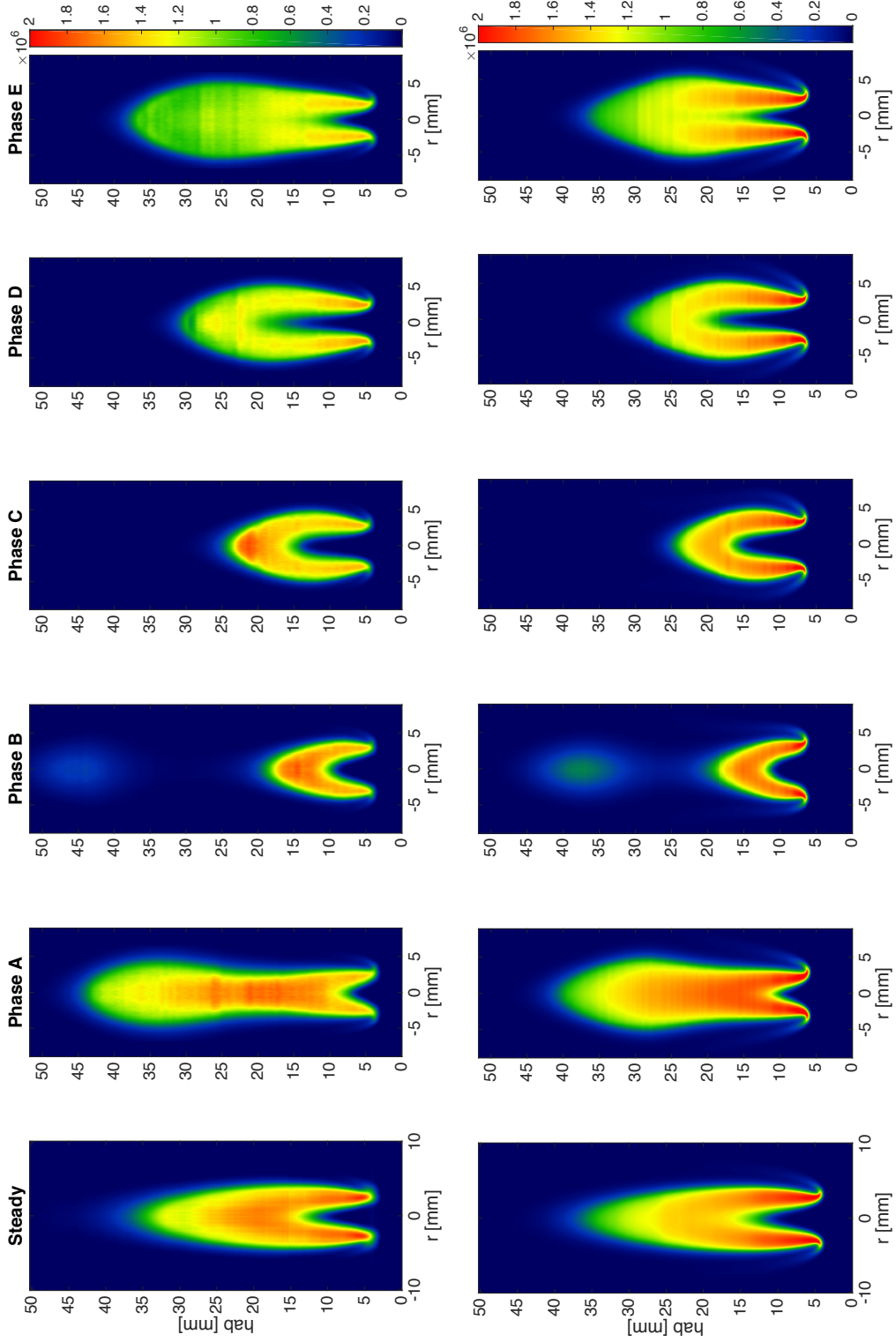


Figure 3.37: (Top) measured and (bottom) computed  $CO$  laser-induced fluorescence signal for the time-varying 65% methane flame - steady result and five phases of the 50% modulation.

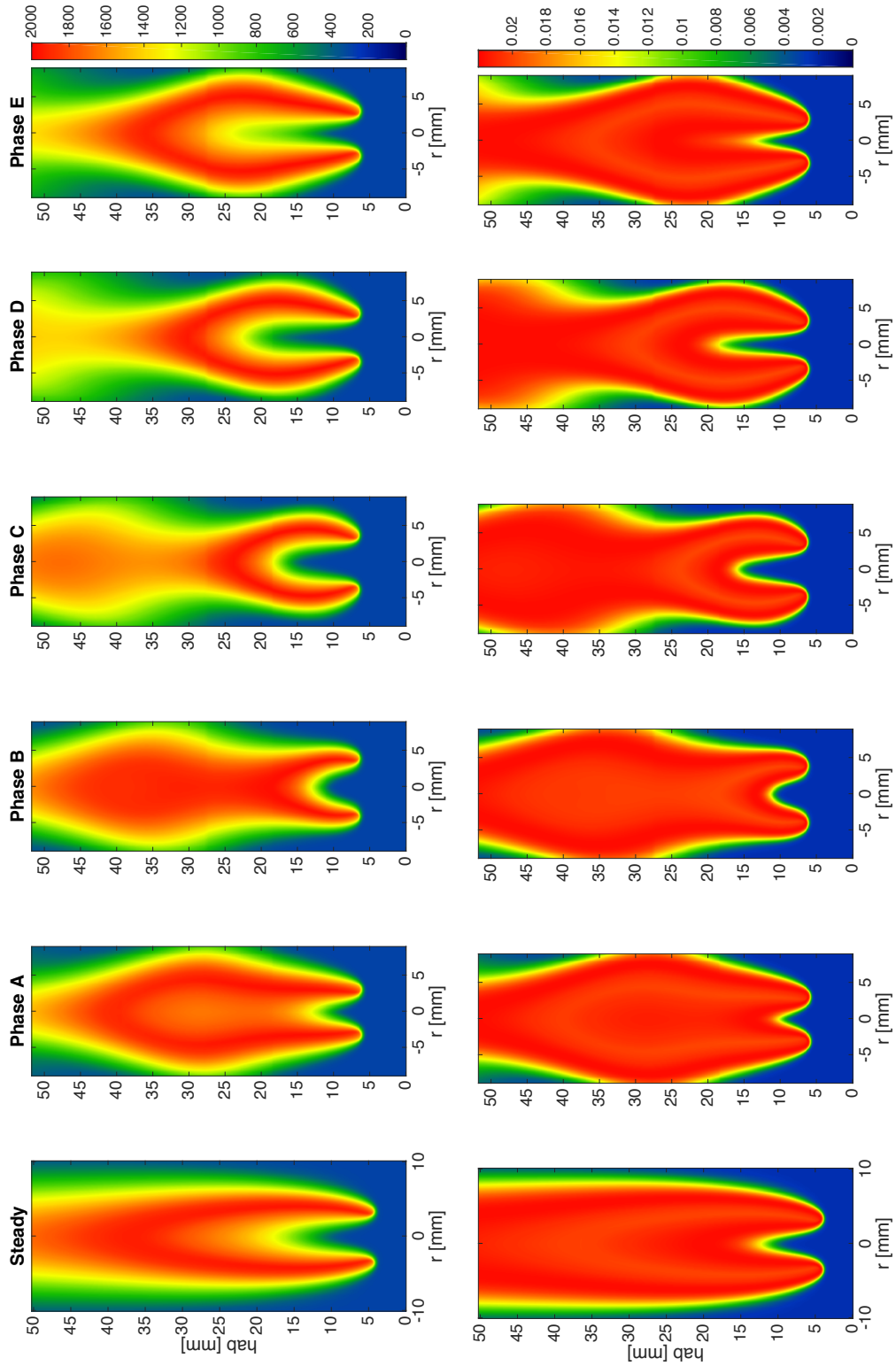


Figure 3.38: (Top) computed temperature and (bottom) computed Boltzmann population fraction for the steady and 50% modulation flame.

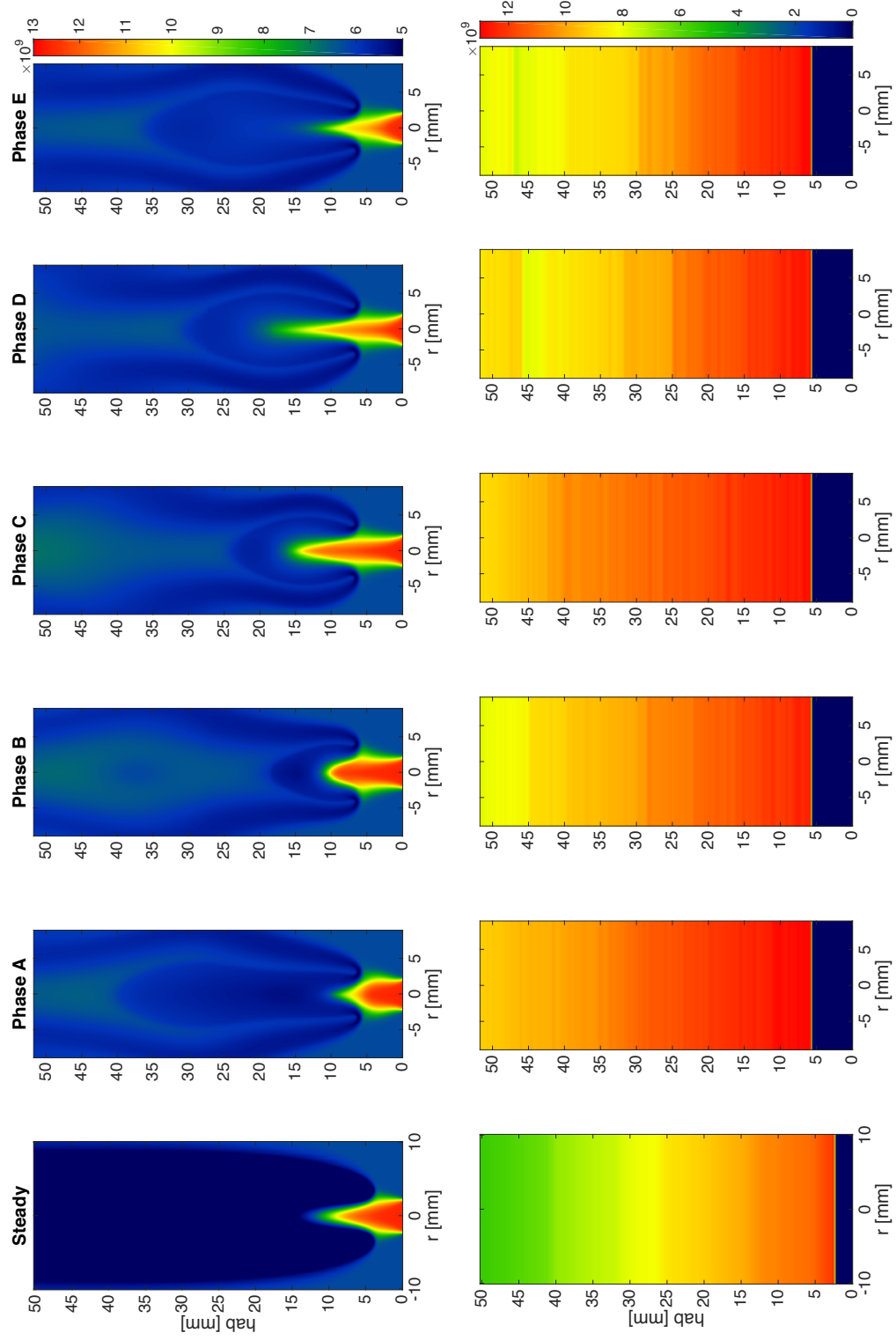


Figure 3.39: (Top) computed quenching rate and (bottom) photoionization rate for the steady and 50% modulation flame.

The plots in Fig. 3.40 compare the fluorescence intensity along the flame centerline for the five phases considered.

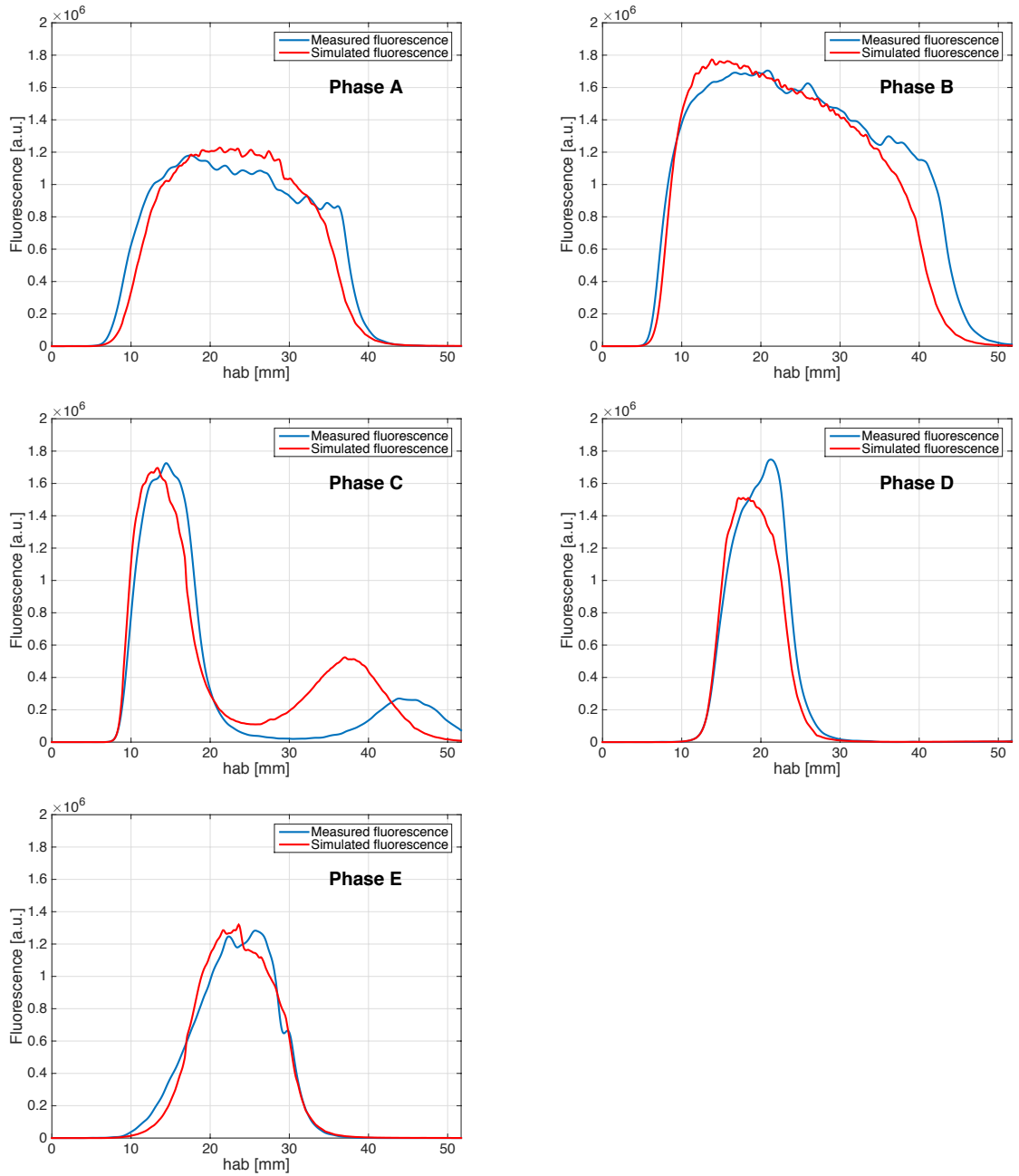


Figure 3.40: Fluorescence intensity along the flame centerline for the time-varying flame shown in Fig. 3.37.

The agreement in the spatial distribution was found to be reasonable despite some variations in the fluorescence signal intensity ( $\sim 15\%$  discrepancy). These measurements, in fact, proved to be quite sensitive to the relative phase: compared to the steady, non-sooting case, the forced flame starts to produce soot since, at some locations and phases, the residence times increase and the growth of soot is favored. A small phase mismatch between resonant and off-resonant signals could therefore have introduced unwanted soot-derived luminosity when the two signals were subtracted. The measurements were also found to be sensitive to changes in the calibration constant: the calibration was performed immediately after the steady flame case and works well for that condition. However, for the remainder of the dataset (ten flames corresponding to five phases of two forcing conditions) the initial calibration was found to be less satisfactory. The calculations have shown that the *CO* fluorescence intensity at the base of the flame is essentially constant regardless of the specific phase. Therefore, a calibration correction was made to ensure phase-to-phase consistency by scaling and matching the intensity at the base of the flames. For future reference, improvements in the intensity accuracy are expected with more frequent and consistent calibrations. In any case, the computations seemed to systematically overestimate the signal on the flame wings, while fluorescence intensity peaks were in some cases present at the flame tip, probably because of soot interference not properly corrected. The uncertainty in the measured steady flame CO mole fraction was estimated to be  $\sim 10\%$ . This value derived from the uncertainties related to the beam spot area evaluation ( $\sim 7\%$ ), photoionization rate ( $\sim 6\%$ ), and calibration constant ( $\sim 3\%$ ). The error is higher for the time-varying case because of the additional uncertainty on the relative phase and calibration, but it hasn't been quantified. The fluorescence-derived *CO* mole fraction for the time-varying flame was not computed; a small phase shift between the LIF measurements and the Raman/Rayleigh ones did not allow for a correct match and solution.

## Imaging considerations

The fluorescence images presented in this chapter were obtained by combining multiple one-dimensional line measurements. A direct and more conventional two-dimensional imaging procedure, however, would improve the quality of the experimental data even more. The overall acquisition time would decrease with two major benefits: first, the shorter the time required to complete the measurement, the lower the dye degradation will be, along with the fluctuation of laser energies associated with it. Second, the closer the calibration procedure is to the actual beginning and end of the measurement, the more accurate will be the quantitative result. Imaging of a 3 mm high laser sheet was tried with minor success: the main problem was not the reduced laser fluence, but the multiple modes generated by the dye laser that produced laser sheets with unsteady and temporally-variable intensity profiles (see Fig. 3.41 where laser sheet intensity cross sections belonging to different measurements are compared). These non repeatable profiles would not allow for a proper laser sheet intensity correction and background subtraction.

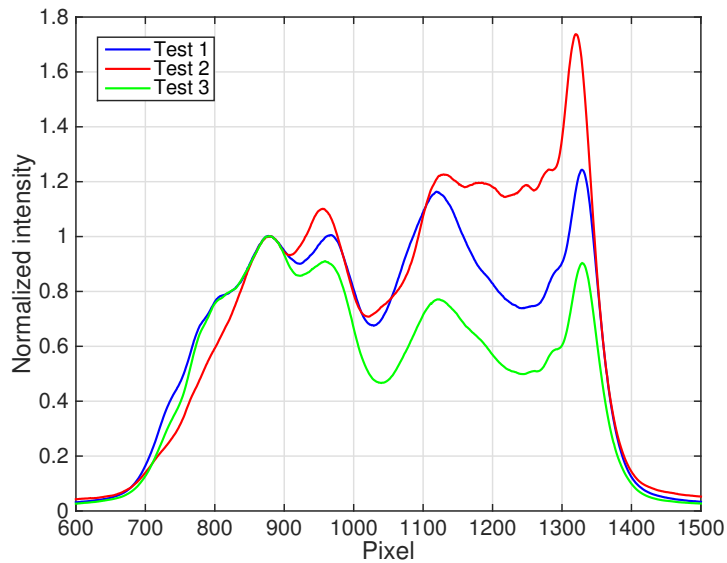


Figure 3.41:  $CO$  fluorescence cross section of laser sheet intensity acquired during three different measurements.

### 3.3 Conclusions

The results obtained and presented in this chapter extended the experimental database of minor species pertaining the target Yale 65% methane flame; the experimental data (fluorescence measurements, photoionization rate, and numerical results) are now available online for the scientific community [45]. The nitric oxide LIF evaluation was simplified by substituting spectrally resolved measurements with more straightforward imaging measurements; the *NO* spatial distribution of the steady flame was complemented with the measurement of *NO* fluorescence in two time-varying flames characterized by different fuel modulation velocities. It was observed that the peak fluorescence increase is related to the spatial positioning of the *CH* radical, and the notion that the Fenimore pathways play a major part in the formation of *NO* in these flames was confirmed.

The carbon monoxide LIF measurements improved the overall signal-to-noise ratio of the previous Raman-based results and confirmed that measurements performed in the photoionization dominant region are indeed a viable approach that can be used to simplify quantitative *CO* measurements; the evaluation of the quenching rate can in theory be avoided and a shot-to-shot intensity correction is possible due to the linearity of the fluorescent signal.

# Chapter 4

## High dynamic range imaging applied to combustion diagnostics

High dynamic range (HDR) imaging is the process of combining several images, with varying degrees of saturation, into a single unsaturated one [65, 66]. The basic ideas have been used in photography for many years and nowadays, with the increased availability and power of digital imaging systems, numerous algorithms have been developed for HDR imaging [67]. These algorithms generally consist of two parts, namely the creation of a high dynamic range image from several exposures, and the so called “tone mapping” to allow HDR images to be displayed on low dynamic range screens or hard copies. While the tone mapping part of HDR algorithms has mainly artistic value, the creation of images with increased dynamic range has useful potential for scientific applications.

The quality of data in quantitative imaging experiments can, in general, be limited by the finite dynamic range of the detection systems and by the limited signal-to-noise ratio (SNR) at low signal levels. This can be particularly problematic when arithmetic operations on several images or color channels must be combined to obtain a desired quantity. If the phenomenon under study is steady, improvements in SNR can be

obtained by signal averaging; however, the HDR approach can be helpful when only a limited number of exposures are possible or available.

One such example is the NASA *Structure and Liftoff in Combustion Experiment* (SLICE) campaign aboard the International Space Station (ISS) [68]. The investigation of the effects of microgravity on laminar coflow diffusion flames was undertaken by taking images of flames under different conditions (i.e., by varying the fuel type and dilution, nozzle dimension, gas velocity) with a commercial digital single-lens reflex (DSLR) camera. As shown in Section 2.2.1, the response of the detector had been spectrally characterized allowing the camera to be used as a two-color imaging pyrometer to derive the soot temperature and soot volume fraction distributions [68]. In microgravity, because of the longer residence times, the soot load in such flames increases compared to normal gravity conditions, and so does the overall luminosity, which resulted in some saturated images. As a consequence of limited fuel supply, the saturated acquisitions could not be repeated with lower exposure times as would be required for conventional signal averaging. HDR processing of these frames, however, can prove useful in retrieving quantitative information that would otherwise be rejected.

Other applications can also be envisioned, and are described in more detail in Chapter 5 of this thesis. In planar imaging of unsteady phenomena, for example, HDR techniques can be applied by using a double-pulsed laser with differing pulse energies and an interpulse separation short enough that two consecutive frames sample the same event. Signal detection using a fast interline-transfer detector to acquire two sequential images with different signal levels could be used to reconstruct an HDR image in which the SNR is comparable in both low and high signal level regions.

While much of the literature on HDR imaging deals with the tone mapping related to the image rendering, this aspect is not relevant for the purpose of quantitative measurements, it has not been investigated, and will not be discussed in this thesis.

Scientific detectors are designed to have a linear response; consumer digital cameras, on the other hand, might behave differently and have built-in capabilities to modify the detector response near the low and high end of the dynamic range, just for rendering purposes. For this reason, HDR algorithms have been developed with the ability to retrieve the camera response function, given a sequence of frames at different exposures, to reconstruct the final HDR image [69, 70].

Application of HDR imaging to scientific measurements has been pursued in various fields including sonar imaging, biology, microscopy, and optics [71–75]. Despite problems related to vignetting, alternative approaches to HDR imaging based on variation of aperture instead of exposure have been investigated and proposed as well [76]. In this chapter, the use of HDR imaging algorithms is presented as a way to improve combustion measurements. It is shown that the HDR approach can help increase the SNR in low intensity regions when a limited number of frames are available, while maintaining the original quantitative information.

## **4.1 Application of HDR imaging to color ratio pyrometry**

Two-color ratio pyrometry is a technique capable of determining the temperature of a radiating body using a digital color camera as an imaging pyrometer. Flame temperature information can be retrieved by measuring the incandescence from soot or a SiC fiber placed in the flame. When the spectral responses of the red, green and blue (RGB) channels of a color filter array (CFA) are measured, and the spectral emissivity of the bodies is known, signal ratios can be calculated as a function of the emitting body temperature. More detailed descriptions are reported in [12, 23] and in Section 2.2.1 of this thesis. Naturally, the method accuracy and its applicability to quantitative measurements rely on the camera having a linear response across the

whole dynamic range; in addition, the camera reciprocity gains relevance when dealing with HDR images, since the data are collected at several exposure times and need to be normalized with respect to a reference exposure. Additionally, for HDR imaging, linearity and reciprocity must also be assessed when some areas of the images are saturated.

Three color cameras suitable for two-color ratio pyrometry that have been used for LDR measurements, and whose extension to HDR imaging will be analyzed in this chapter, consisted of the following:

- Nikon D300s: CMOS sensor, 4288 by 2848 pixels, 23.6 x 15.8 mm<sup>2</sup> sensor size, 14 bit A/D converter (used in the SLICE experimental campaign [68]).
- Nikon D70: CCD sensor, 3002 x 2000 pixels, 23.7 x 15.6 mm<sup>2</sup> sensor size, 12 bit A/D converter (used in a soot pyrometry work [12]).
- Prosilica GigE GC1380CH: CCD progressive sensor, 1360 x 1024 pixels, 8.77 x 6.60 mm<sup>2</sup> sensor size, 12 bit A/D converter (selected for the ACME experimental campaign [77]).

Because of the unique requirements of HDR imaging, separate measurements were performed to determine the linearity and reciprocity of the detectors.

### **Detector linearity**

To assess the detector linearity, the cameras were used to image a LED light source that was lit for varying amounts of time ranging from 25  $\mu$ s to 250 ms. The LED gating was controlled with a pulse generator and the LED rise time was measured to be  $\sim$  250 ns using a Hamamatsu R928 photomultiplier connected to an oscilloscope. Since the rise time was small compared to the shortest gate, this configuration provided a simple and accurate way of producing a linearly increasing intensity. Figure 4.1 shows the normalized temporal response of several LED pulses as recorded by the

photomultiplier. The integrated voltages are then plotted as a function of the pulse length and used to verify the LED linearity, as shown in Fig. 4.2

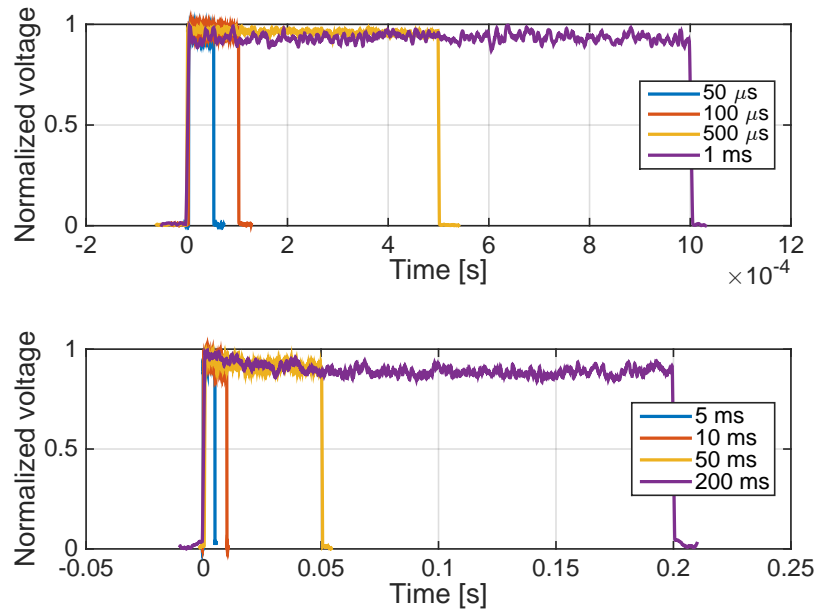


Figure 4.1: Normalized LED temporal response, as measured by a photomultiplier.

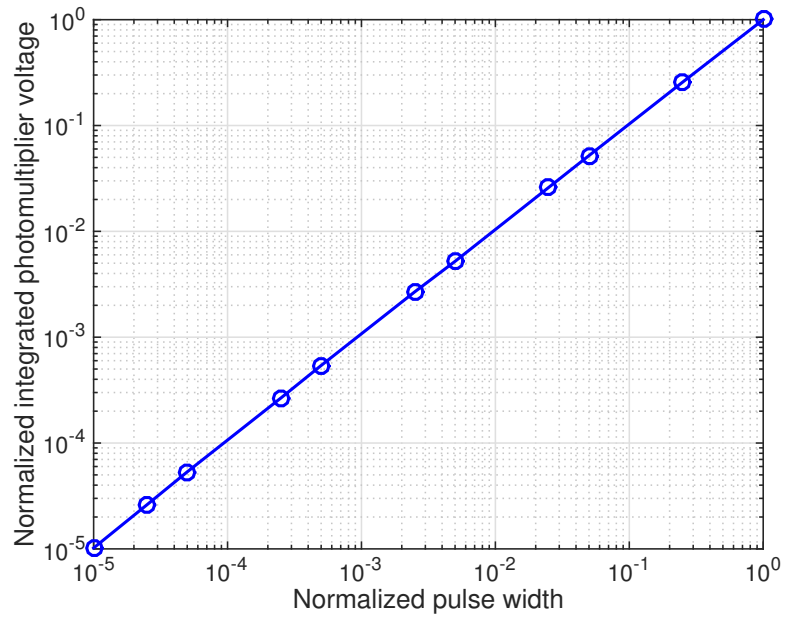


Figure 4.2: LED linearity, as measured by integrating the voltages shown in Fig. 4.1.

A sequence of images for increasing LED gate times was obtained with each detector using a fixed one-second exposure. The signal counts from the red and green channels are plotted as a function of increasing normalized LED pulse lengths in Figs. 4.3 and 4.4, where the counts are an average over a nearly constant intensity region of the detector. The A/D offset was subtracted to the acquired images, and all three detectors showed excellent linearity. Because of the specific color of the LED used for the linearity test (an orange LED), the blue channel results suffered poor signal-to-noise ratios and are not reported here, but they are expected to behave like the red channel.

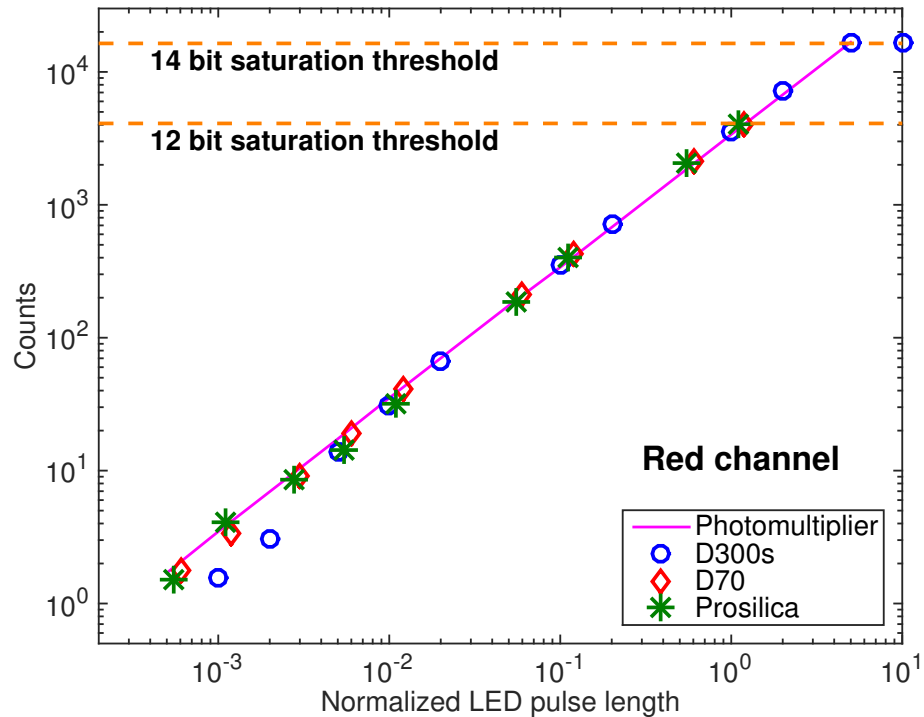


Figure 4.3: Detector response of the red channel as a function of LED pulse length for the three selected cameras. The linear LED response, as measured by the photomultiplier, is shown by the solid line.

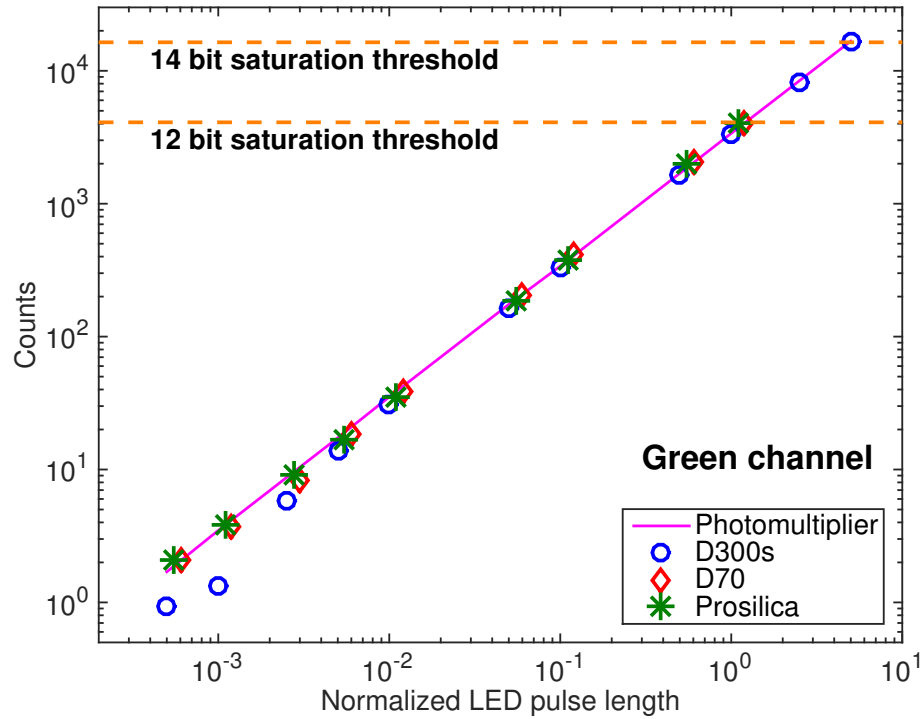


Figure 4.4: Detector response of the green channel as a function of LED pulse length for the three selected cameras. The linear LED response, as measured by the photomultiplier, is shown by the solid line.

### Detector reciprocity

Reciprocity is the ability of a detector to record a signal that is directly proportional to the exposure time. For the evaluation of the reciprocity, a similar setup was used with the LED left in the ON state while each camera recorded images with varying exposure times. Unlike the linearity analysis, the proper background was subtracted from each image, and a white LED coupled to a BG color filter was used instead. Results for the RGB channels of the three detectors are shown as symbols in Figs. 4.5, 4.6, and 4.7.

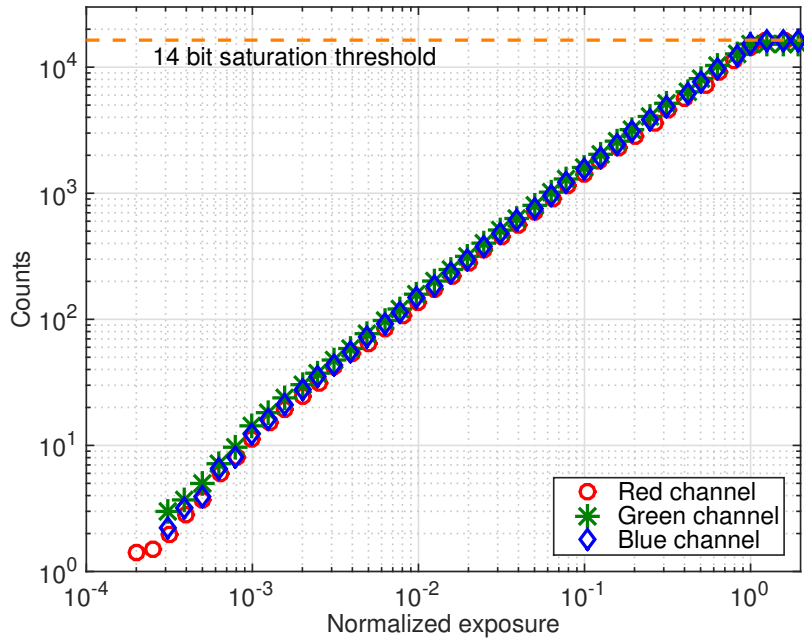


Figure 4.5: Reciprocity curves of the red, green, and blue channels for the Nikon D300s determined from LED measurements.

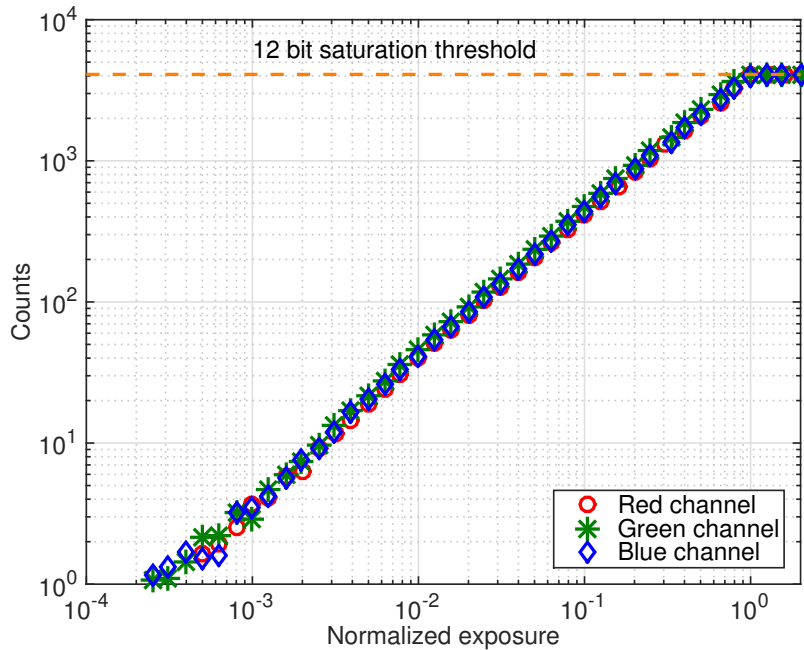


Figure 4.6: Reciprocity curves of the red, green, and blue channels for the Nikon D70 determined from LED measurements.

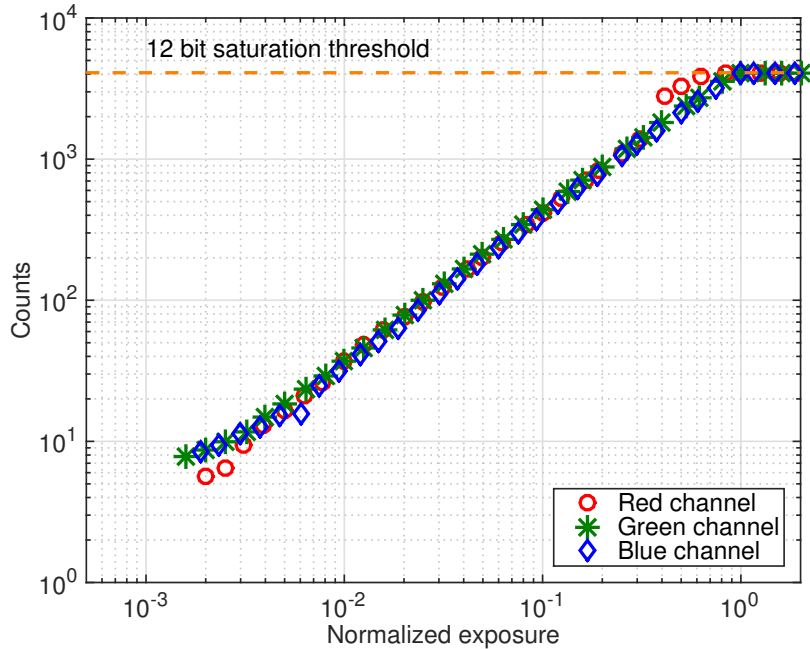


Figure 4.7: Reciprocity curves of the red, green, and blue channels for the Prosilica GC-1380CH determined from LED measurements.

The reciprocity was seen to be excellent for the DSLR cameras, while the Prosilica displayed some nonlinear behavior near the saturation limit that will be discussed in more detail in Section 4.3 (see the deviation of the red markers in Fig. 4.7).

According to [69], modern DSLR cameras with electronically controlled shutters vary the exposure time by powers of two between stops; as a consequence, the correct values for nominal exposures such as 1/250, 1/125, 1/60, 1/30, and 1/15 seconds would be 1/256, 1/128, 1/64, 1/32, and 1/16 seconds, instead. Such difference was captured and verified using the LED-based reciprocity evaluation and it is shown, for the case of the D300s, in Fig. 4.8. The blue circles display the reciprocity results using the nominal values returned by the camera; the green dots show the more realistic and linear result using the corrected values, as suggested by [69]. The red marker are the nominal exposures that deviate from the real ones.

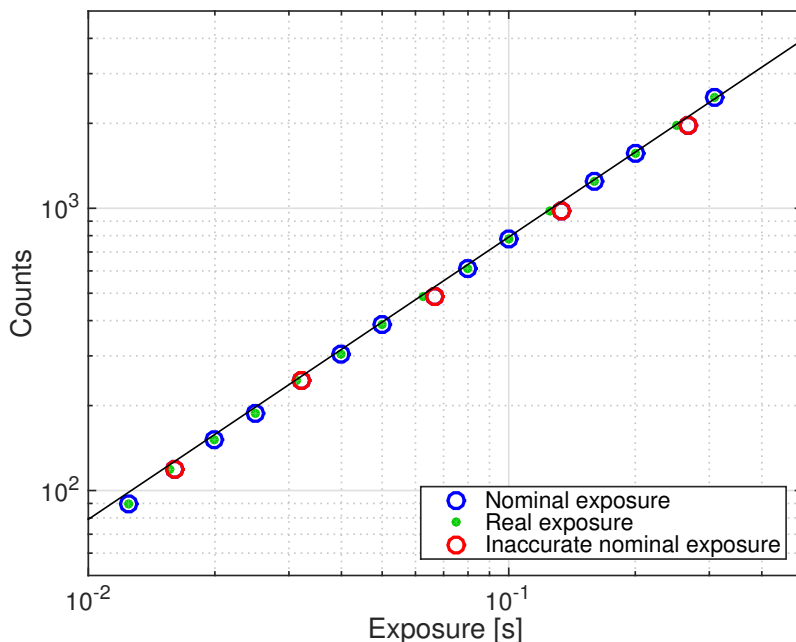


Figure 4.8: Difference between nominal and real exposure values for the DSLR camera Nikon D300s.

## 4.2 HDR algorithms

Historically, HDR algorithms were initially developed to deal with images recorded on film, which has inherent nonlinearities; therefore, the first step of these algorithms was generally that of deriving a camera response function. According to the algorithm developed by Debevec and Malik for static scenes [69], a series of  $P$  images with different exposures is able to sample the camera response curve,  $f$ , which can be represented as

$$Z_{ij} = f(E_i \Delta t_j), \quad (4.1)$$

where  $Z_{ij}$  is the digitized pixel value at pixel  $i$  and exposure  $j$ ,  $E_i$  is the irradiance at pixel  $i$ , and  $\Delta t_j$  is the non-dimensional exposure time for the  $j^{\text{th}}$  exposure. The  $Z_{ij}$  and  $\Delta t_j$  values are known while the response curve,  $f$ , is unknown, but it is assumed to be smooth and monotonic. The irradiance values  $E_i$  are also unknown, but are constant across all  $j$  exposures. The method uses linear optimization techniques to

find a smooth response curve that minimizes an objective function representing the mean squared error. A weight function  $w$  is usually introduced in the algorithm to emphasize the smoothness and fitting in the middle part of the response curve, and to reduce the impact of “blooming artifacts (as a consequence,  $f$  will be less smooth and the fitting will be poorer at the lower and upper extremes of the dynamic range). Once the response curve  $f$  is solved, the high dynamic range irradiance values can be determined from the  $P$  images employing Eq. 4.2:

$$\ln E_i = \frac{\sum_{j=1}^P w(Z_{ij}) [\ln(f(Z_{ij})) - \ln \Delta t_j]}{\sum_{j=1}^P w(Z_{ij})}. \quad (4.2)$$

The script used to evaluate the response curves was implemented in Matlab and it is reported here [69]:

```
function [g, lE]=gsolve (Z,B,l,w,n)
A = zeros (size (Z,1)*size (Z,2)+n+1,n+size (Z,1));
b = zeros (size (A,1),1);}

%% Include the data-fitting equations
k = 1;
for i=1:size (Z,1)}
    for j=1:size (Z,2)}
        wij = w(Z(i,j)+1);
        A(k,Z(i,j)+1) = wij;
        A(k,n+i) = -wij;
        b(k,1) = wij * B(j);
        k=k+1;
    end
end
```

```

%% Fix the curve by setting its middle value to 0 1;
A(k,round(n/2)+1) = 1;
k = k+1;

%% Include the smoothness equations
for i=1:n-2
    A(k,i)=l*w(i+1);
    A(k,i+1)= -2*l*w(i+1);
    A(k,i+2)=l*w(i+1);
    k=k+1;
end

```

```

%% Solve the system using SVD

```

```

x = A\b;
g = x(1:n);
lE = x(n+1:size(x,1));

```

The parameters are defined as follows:  $g$  is the computed camera response function,  $Z$  is the sampled pixel count value of the image,  $lE$  the logarithm of the irradiance of pixel  $Z$ ,  $B$  is the logarithm of the exposure time,  $l$  a coefficient to determine the smoothness of the fitting (chosen to be = 15),  $n$  is the saturation pixel counts that also determines the size of the system (limited to 256), and  $w$  the triangular weight function, defined as:

```

Z_max = 255;
Z_min = 0;
z = [0:1:Z_max];

```

```

for i = 1:Z_max+1
    if z(i) <= 0.5*(Z_max+Z_min)
        w(i) = z(i) - Z_min;
    end
    if z(i) > 0.5*(Z_max+Z_min)
        w(i) = Z_max - z(i);
    end
end
end

```

To obtain the camera response function using the Debevec algorithm a reference target image, with a normalized intensity varying from 0 to 1, was created using the software OMA [16] and displayed on a computer screen. Pictures of the target were then taken with the detectors at various exposure times. Images were slightly defocused to avoid Moire effects from the computer monitor's RGB pixels. In all cases, the shortest exposure did not saturate any color channel while still using a significant portion of the cameras dynamic range. In order to mimic light conditions typically encountered in soot and thin filament pyrometry, the color of the target was chosen in such a way that the RGB response of the detector was comparable to that obtained when a 1 mm thick Schott BG7 color filter is used to image sooty flames. The magnitude of the recorded color channels varied detector by detector (it is related to the spectral response of each camera), but generally the blue and green channels reached saturation before the red one. Figure 4.9 shows an example of five target images with different exposures, taken with the Nikon D300s, and cropped to select a strip in which the vertical intensity gradients are minimal (pixels in which one or more color channels are saturated are highlighted in yellow).



Figure 4.9: Five target images with increasing exposure times, cropped to select a strip in which vertical intensity gradients are minimal. The image sequence was used to obtain the camera response function of the D300s using the Debevec algorithm. Pixels with one or more saturated color channels are shown in yellow.

Image sequences similar to that of Fig. 4.9 were used to derive the camera response function of the three considered detectors using the algorithm developed by Debevec and Malik and employing a triangular weighting function. In each image, several pixels were selected and their intensity, as a function of the exposure time, was evaluated for the determination of the camera response. When possible, the camera settings, ISO and white balance were chosen to minimize any camera software interference on the final raw data. Raw images were decoded using algorithms implemented in the open source code `dcrw` [78], which provided signal counts without additional processing normally done in conversion to other formats such as jpeg. With the DSLR cameras, images were taken with nominal exposure values of 1/60, 1/30, 1/15, 1/8, 1/4, 1/2, 1, 2, 4 seconds and aperture  $f$  1.4, resulting in highly saturated images in the green and blue channels. Generally, in an image sequence, only the first frame was completely unsaturated. As mentioned previously, for the DSLR cameras, the exposure time varied by powers of 2 between stops and the exposure values of 1/64, 1/32, 1/16, 1/8, 1/4, 1/2, 1, 2, 4 seconds were used instead of the values returned by the camera. The resulting response curves were smoother and showed better linearity when employing the latter values. With the Prosilica camera, images were taken with nominal exposure values of 2, 4, 8, 12, 16, milliseconds and aperture  $f$  1.4.

The response curves for the various color channels were processed separately and the Debevec results for the red and green color channels are plotted in Figs. 4.10 and

4.11, along with the LED reciprocity results from Figs. 4.5, 4.6., and 4.7

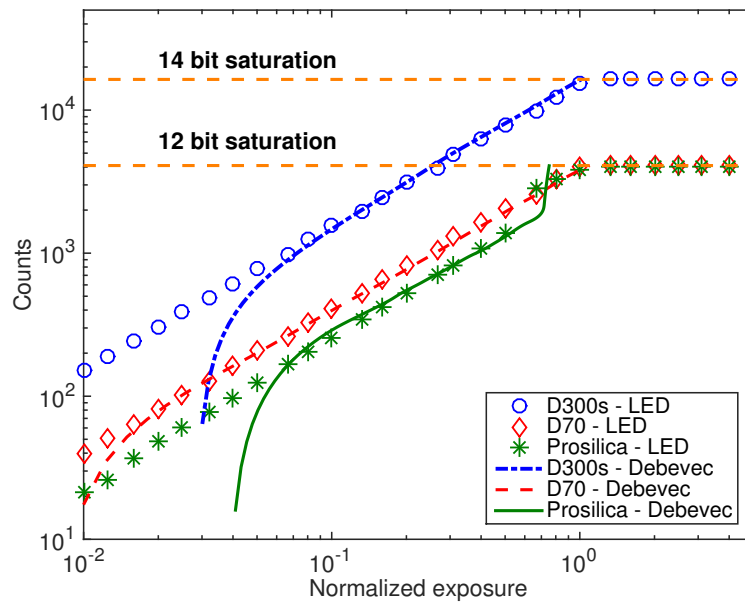


Figure 4.10: Comparison between red channel reciprocity curves as determined from LED measurements (markers) and Debevec algorithm (lines).

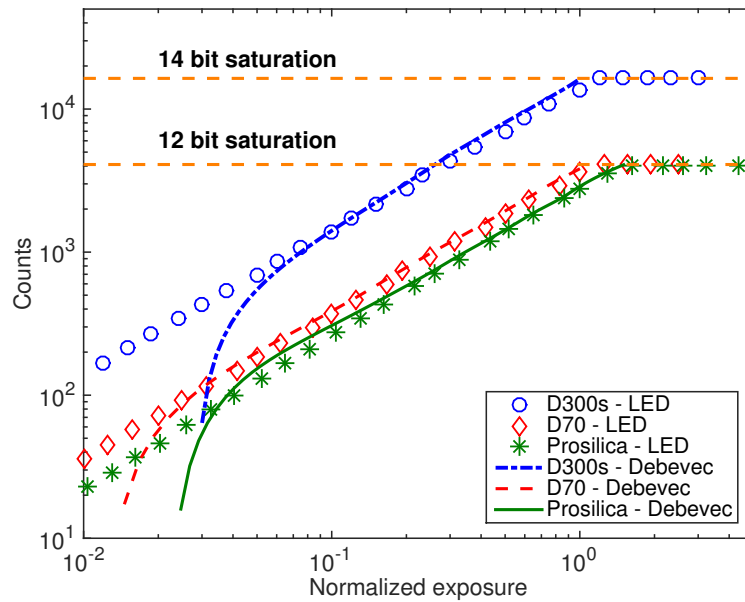


Figure 4.11: Comparison between green channel reciprocity curves as determined from LED measurements (markers) and Debevec algorithm (lines).

The reciprocity curves obtained using the Debevec algorithm were seen to be consistent with that obtained from the LED measurements for the D300s and D70 for all but the bottom 5% of the dynamic range. The Prosilica showed a reasonably good agreement above 7% of the dynamic range up to a certain exposure value, beyond which the red channel (the last one to reach saturation in the current setup) exhibited a nonlinear behavior. Pointing at the differences between the LED-derived and Debevec-derived results, it is important to note that the response curves calculated using the Debevec and Malik algorithm are a result of a mathematical fitting that depends on the pixels selected for the fitting and the chosen weighting function. This function, as mentioned, prioritized the fitting quality along the central part of the dynamic range while disregarding the low and high ends.

As can be seen in Figs. 4.10 and 4.11, the “decay” in the Debevec response curves at low signal levels for each detector is not physically accurate, but a result of the weighting: the real response, in fact, should decrease linearly as the exposure time is reduced. However, the algorithm maintains its utility when capturing nonlinear behaviors induced by chip saturation as is seen in the high signal region of the Prosilica red result.

The verification of linearity and reciprocity of the detectors considered here enabled the implementation of a simple and straightforward HDR algorithm for the image post-processing. For detectors with a high degree of linearity and reciprocity, the  $i^{th}$  pixel value in the final reconstructed HDR image,  $H_i$ , can be evaluated as

$$H_i = \frac{\sum_{j=1}^{R_i} \left( \frac{h_{ij}}{\Delta t_j} \right) \Delta t_1}{R_i}, \quad (4.3)$$

where  $h_{ij}$  is the  $i^{th}$  pixel value in the  $j^{th}$  image of the sequence,  $\Delta t_j$  the exposure value of image  $j$ ,  $\Delta t_1$  a reference exposure value (typically the exposure of the first, unsaturated, image), and  $R_i$  the total number of frames in which the pixel  $h_{ij}$  is

not saturated (the saturation threshold can be chosen to be a specific percent of the full dynamic range and can be optimized depending on the signals, applications or detectors).

Note that all the HDR algorithms rely on the assumption that the objects in the acquired images are steady and do not move frame by frame. In flame measurements this might not always be the case: for example, flame flicker can arise from buoyancy instabilities, mass flow controller jitter, or ambient air movement, yielding an HDR image that shows unphysical features, known as “ghosts”.

### 4.3 Detector characterization and pixel crosstalk

Crosstalk is the unwanted exchange of signals between adjacent pixels and has the effect of reducing both spatial resolution and detector sensitivity, while returning unphysical results. As reported in [79], crosstalk can be explained in terms of:

- Spectral crosstalk: due to imperfect and unbalanced color filters that allow the transmission of unwanted spectral components.
- Optical crosstalk: due to the spatial separation between pixel surface and color filter. Light impinging on the sensor with an angle, and passing through a specific color filter, can hit the surface of adjacent pixels, other than the one right below the specific color filter.
- Electrical crosstalk: due to electron charge transfer from one pixel to adjacent ones.

These effects are more pronounced in detectors with small pixels and high pixel density. Because of the consequences of crosstalk when detectors are used for scientific purposes, several works have focused on its study and characterization, particularly for CMOS sensors. Some approaches relied on the use of micro lenses to illuminate a

single pixel while monitoring the signal in the adjacent ones [79,80]; others exploited a relation between quantum efficiency of the single color channels and the overall quantum efficiency of the chip to derive information about crosstalk [81,82]. Despite being very comprehensive studies, these investigations focused on generic chip performance, and were limited to the dynamic range of the sensors without any extension into the saturation region. For HDR imaging with color cameras, where saturation of some pixels is the norm, it was seen that for some detectors, when one color channel saturates, the electrical crosstalk to an adjacent pixel (and hence another color) could be significant. Because of the Bayer color filter used on many color cameras (see an example in Fig. 4.12), this pixel-to-pixel electrical cross talk not only leads to a decrease in spatial resolution, it results in corruption of color information in the neighborhood of saturated pixels.

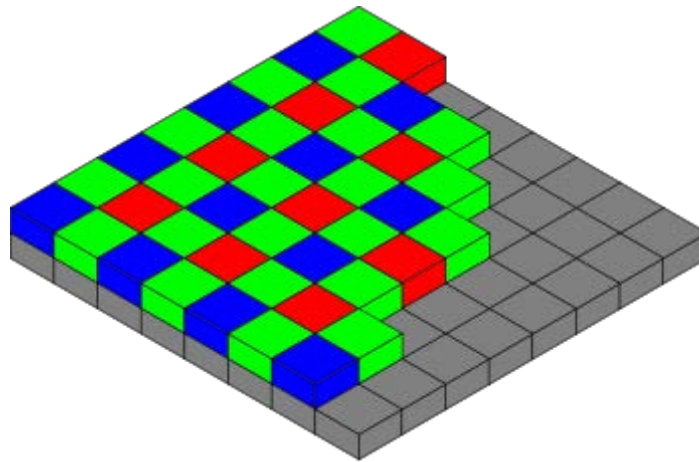


Figure 4.12: Spatial distribution of the red, green, and blue pixels on a Bayer pattern CFA.

The analysis of the occurrence of crosstalk in saturated images can be assessed by acquiring a sequence of images in which the color channel intensities are unbalanced (i. e. one channel saturates before the others); by considering every RGGB pixel cluster in the Bayer pattern, and checking if the reciprocity of the unsaturated neighbors is maintained, one can determine if any crosstalk is present. As a specific example, the reciprocity results shown in Figs. 4.5, 4.6, and 4.7 were derived from an image sequence in which green was the first saturating channel. It was seen that the red reciprocity response for both DSLR cameras, was linear up to the saturation level. On the other hand, the red channel of the Prosilica showed some nonlinear behavior as a consequence of pixel crosstalk: when the green pixels reached the saturation threshold, some electron leakage occurred to the nearby red pixels causing the recorded red intensity to be higher than the supposed linear trend.

It must be clarified that this particular response is not exclusive to the mentioned color channel, since the electronics has no way to discern between colors. Moreover, the Prosilica results from Fig. 4.5 are not conclusive when trying to determine if the chip readout direction has any influence on the crosstalk. Because of the geometric configuration of the Bayer pattern (see Fig. 4.12 and inset in Fig. 4.13) and the presence of two diagonally placed green pixels for every red-blue pair, the green saturation could influence the red pixels regardless of the readout direction. Focusing on the Prosilica response, an additional reciprocity analysis was done by changing the type of LED used in the imaging setup, so that the first saturating channel was the red one. The acquired RGB images were decomposed into 4 color layers instead of the usual 3 (considering, then, two separate green layers for the “side” and “bottom” pixels, with respect to the red one) and the reciprocity results for the red and green channels are shown in Fig. 4.13.

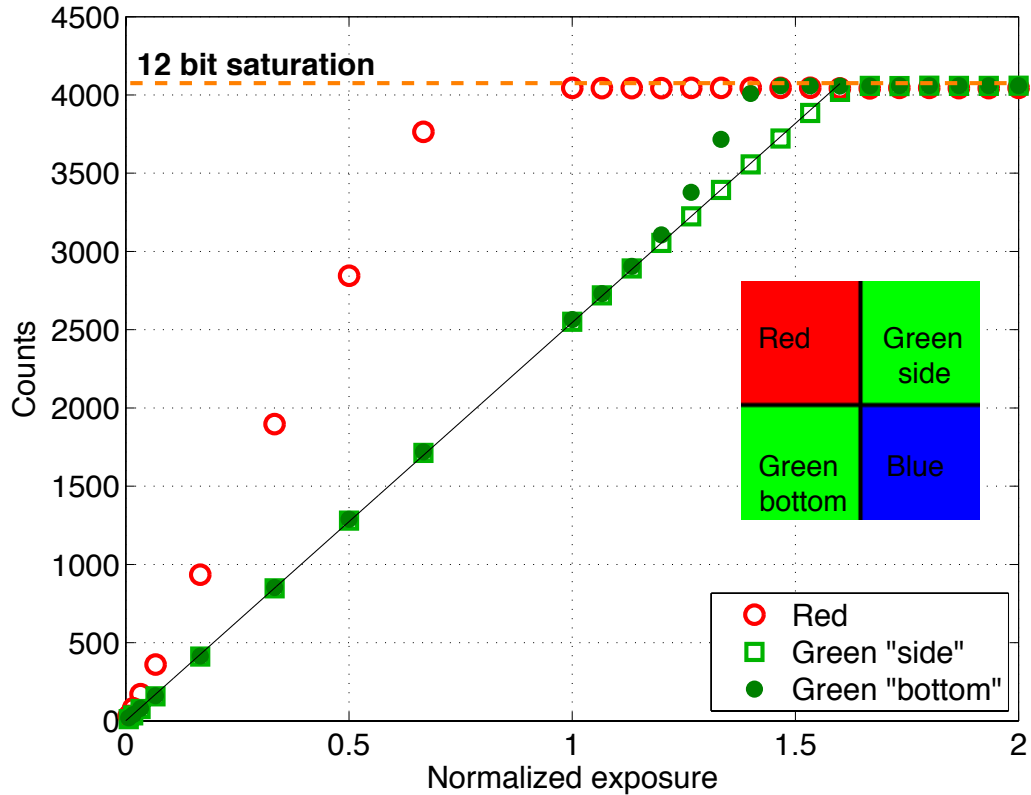


Figure 4.13: Prosilica reciprocity results determined from the LED measurement, showing the effect of red pixel crosstalk on the bottom pixels of the green channel.

The Prosilica CCD readout operates by columns and, as can be inferred from Fig. 4.13, the pixel crosstalk is related to it. It occurs between red and “bottom” green pixels, the ones along the readout direction; after the red channel reaches saturation, the “bottom” green signal deviates from linearity. The “side” green pixels and the blue ones (not shown) are unaffected and scale linearly with the exposure time up to the saturation threshold.

Despite the presence of crosstalk, this particular configuration could still be used for quantitative purposes by simply discarding the information of one of the nonlinear green layers, while retaining the one that is still linear. In soot and thin-filament pyrometry, however, the use of a BG7 color filter is a requisite given by the strong red emission of the considered radiating bodies. The resulting and inevitable green

saturation, then, would make this particular detector not ideal for HDR pyrometry. A possible solution that would help reduce the impact of nonlinear pixels would be to lower the saturation cut-off value when employing Eq. 4.3. By decreasing the value of the saturation threshold it would be possible to still retain information from the partially saturated frames by considering only the RGGB clusters that are not saturated.

From these results, the best quantitative HDR capabilities and linearity characteristics were seen to be detector specific, rather than architecture specific; both the D70 and the Prosilica have CCD sensors, but their response is very different. It therefore appeared that no unique conclusion could be drawn about the relation between nonlinearity and sensor type, and a camera-specific assessment should be performed to evaluate HDR capabilities and limitations. While it may be reasonable to assume that the response will be consistent for a given camera model, evidently differences in how manufacturers design and build devices have consequences on the sensor response when used under partially saturated conditions. Having shown the similarities and differences among the detectors, examples of quantitative measurements that will be introduced in the following sections will be based only on the Nikon D300s and Prosilica GC1380CH, an optimal and a less-than-ideal HDR detector.

## 4.4 Improvements in signal-to-noise ratio

The image sequence from Fig. 4.9, other than the reciprocity analysis, was used to assess the SNR improvement that is achievable with HDR imaging, when compared to the original LDR image. The SNR at each pixel was evaluated by considering a surrounding two-dimensional interrogation region in which the pixel intensity can be considered roughly constant. For this specific example, this region was chosen to have a  $1/e^2$  full width of 7 by 7 pixels. For each pixel, the SNR was calculated by

dividing the average value of the interrogation region by the root mean square of the difference between the region intensity and an “average surface” of the 7 by 7 pixel area, obtained with a two-dimensional smoothing.

Figure 4.14 shows a scatter plot of the SNR of the red, green and blue color channels of the D300s as a function of the normalized intensity, for both LDR (top) and HDR (bottom) images. The HDR image was reconstructed considering a four-image sequence with nominal exposures of 1/60, 1/30, 1/15, and 1/8 seconds.

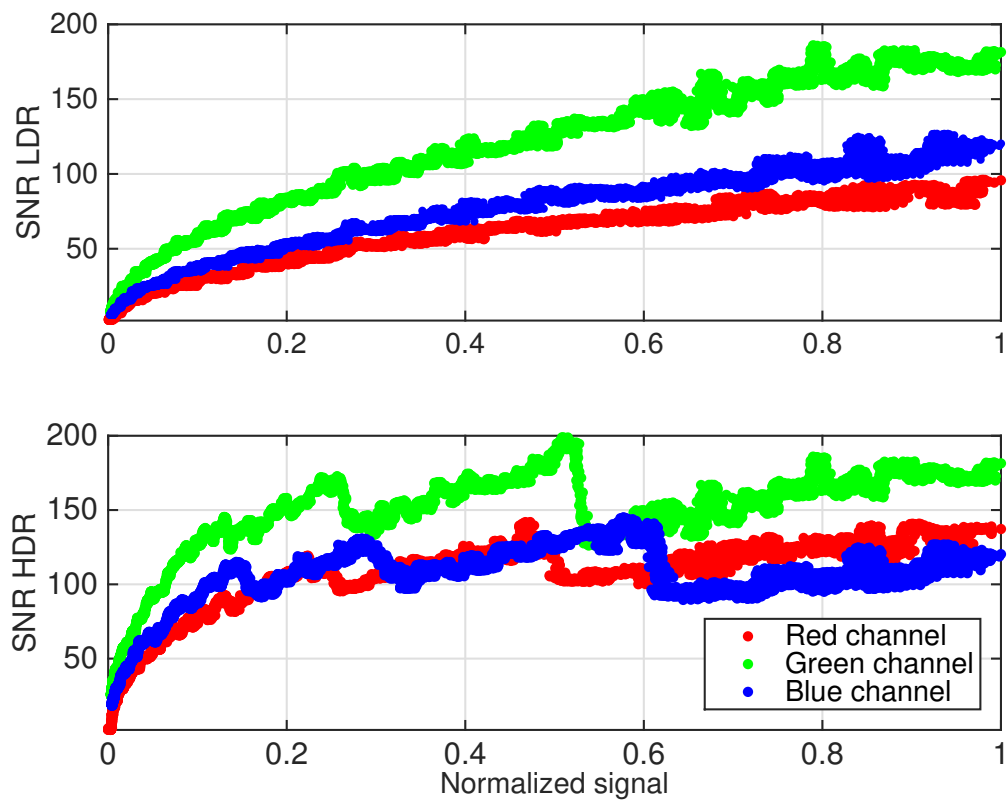


Figure 4.14: SNR as a function of normalized signal for the D300s red and green color channels; LDR image (top) and HDR image (bottom).

Figure 4.14 (bottom) clearly shows the contribution from the four different frames; the discontinuities in the SNR are due to the averaging where multiple frames are combined and the most significant increase, predictably, happens in the low intensity region where all the available frames are averaged. For such pixels, the SNR increased by approximately a factor of two.

Numerous parameters can influence the SNR of a reconstructed HDR image such as the overall number of frames considered, the exposure time increments or the exposure ratio between the unsaturated and most saturated frames. To understand such effects, a parametric study was done by evaluating the SNR as a function of the aforementioned variables. Images from the sequence introduced in Fig. 4.9 were considered for the analysis. The analyzed cases varied either the final exposure time or total number of frames. The combinations are presented in Table 4.1. The “sequence” column relates to the scatter plots in Fig. 4.15 where, to ease the comparison, only the blue channel SNR is displayed.

Number of frames	Nominal exposure (seconds)	Sequence
4	[1/60, 1/4, 2, 4]	a
4	[1/60, 1/15, 1/4, 1]	b
4	[1/60, 1/30, 1/15, 1/8]	c
3	[1/60, 1/30, 1/15]	d
2	[1/60, 1/30]	e

Table 4.1: Cases analyzed for the evaluation of SNR sensitivity.

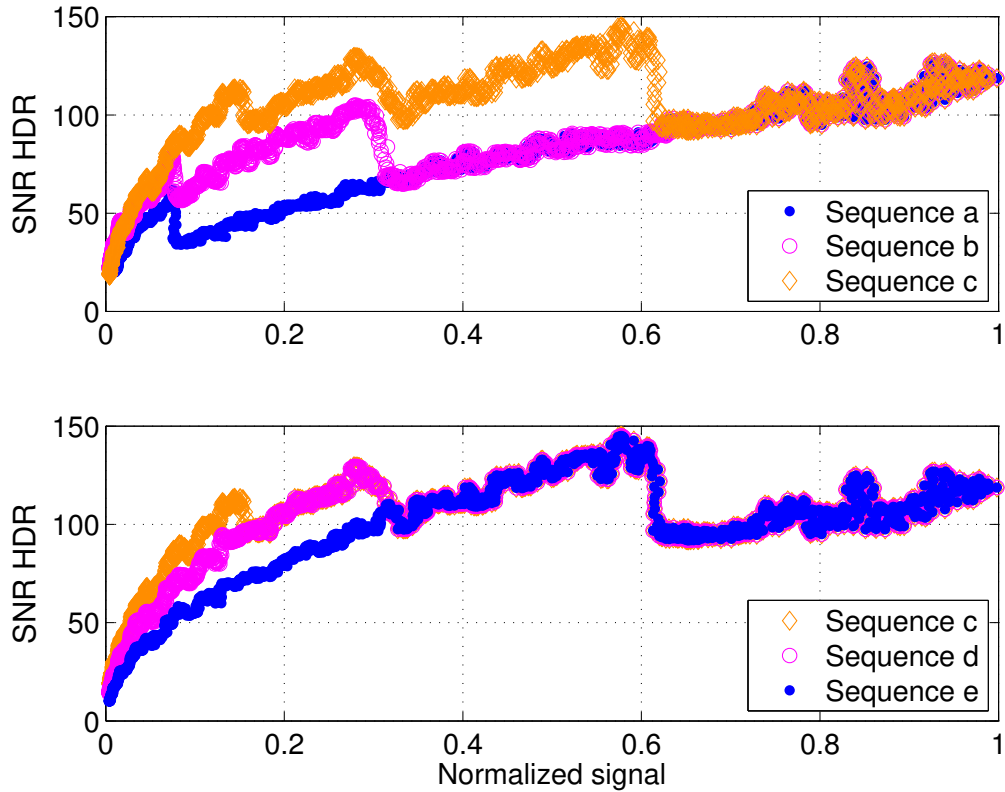


Figure 4.15: SNR variation for a fixed (top) and variable (bottom) number of frames from the blue channel of the D300s.

With reference to Fig. 4.15 (top), it was seen that the larger the difference between the exposure times of the unsaturated and most saturated frame, the lower the sensitivity and SNR in the medium/high intensity region; the effect was less severe in the low intensity areas. Figure 4.15 (bottom) shows how the SNR in the low intensity region increased as the number of frames used for the HDR image reconstruction increased.

In general it is intuitive to state that the best SNR is obtained with a large number of frames and low exposure ratios (between unsaturated and most saturated frames). The latter is related to the fact that, in order to increase the SNR across the whole dynamic range of the detector, intermediate steps (small exposure increments) are desirable to enhance the SNR in between the high and low signal regions. Large

exposure ratios with a low number of frames will only increase the SNR in the low intensity regions neglecting the high and medium ranges. The worst among the studied cases (sequence *a*) shows little effect except at the very lowest signal levels.

## 4.5 Examples of HDR imaging applications

In this section the HDR approach will be tested on thin-filament and soot two-color ratio pyrometry. The first technique was applied to the one-dimensional temperature measurement along a SiC fiber placed in a soot-free flame (the absence of soot is a necessary condition for the reliability of the technique, since soot contamination of the fiber would change its spectral properties). The second technique is a two-dimensional imaging approach that was applied to the measurement of the soot temperature field in a steady diffusion flame.

### 4.5.1 Thin filament pyrometry

For the purpose of the thin filament test, a SiC fiber (Ceramic Grade Nicalon SiC Fiber, manufactured by Nippon Carbon Co., 15  $\mu\text{m}$  diameter) was placed in a laminar coflow diffusion methane flame; the fuel was diluted with nitrogen (65% and 35% in volume, respectively) to decrease the overall soot load and minimize fiber contamination. The temperature measurement was made along the flame diameter at 14 mm above the burner. To evaluate the effectiveness of the approach, both low and high dynamic range images were taken with the Nikon D300s and the Prosilica GC1380CH.

Generally speaking, the best SiC fibers for thin filament pyrometry applications are the ones that can withstand flame temperature for long times, have stable spectral properties and have the smallest diameter in order to interfere with the flow as little as possible. Unfortunately, and depending on the magnification of the imaging

system, the typical fiber dimensions yield an image that spans only few pixels along the fiber radial direction. This, combined with the inherent camera noise, returns measurements with extremely poor SNR. The extreme case scenario, that must be avoided to obtain accurate and meaningful results, would be the imaging of the fiber only on one pixel row. By doing so the resulting green channel value would be the average of a properly illuminated pixel and a non-illuminated pixel (when a raw image is decomposed into the color channels without any demosaicing, the green value is evaluated as an average of the two green pixels in the RGGB cluster). Moreover, depending on the row, either the red or blue channel would not record any signal. Clearly, the effect is less severe in detectors with a high pixel density. A typical way to overcome the problem is to slightly defocus the image without excessively compromising the spatial resolution; by doing so the fiber image can be spread over a larger number of pixels.

Figure 4.16 (left) shows the comparison between the TFP derived temperatures when employing LDR and HDR imaging approaches with the Nikon D300s. The profiles are the average of the three color-ratio-derived temperatures. The high dynamic range sequence was reconstructed considering four frames with successive exposure times increased by a factor of two; the cut-off threshold was set equal to  $\sim 90\%$  of the camera full dynamic range. Similar trends were obtained with the Prosilica, as shown in Fig. 4.16 (right). To be consistent with the Nikon results, the HDR sequence was reconstructed considering the same exposure increments. As can be seen from Fig. 4.16, when compared to the classic low dynamic range approach, the HDR approach returns a smoother temperature profile, particularly in the low temperature/low intensity regions close to the flame axis (below 1600 K).

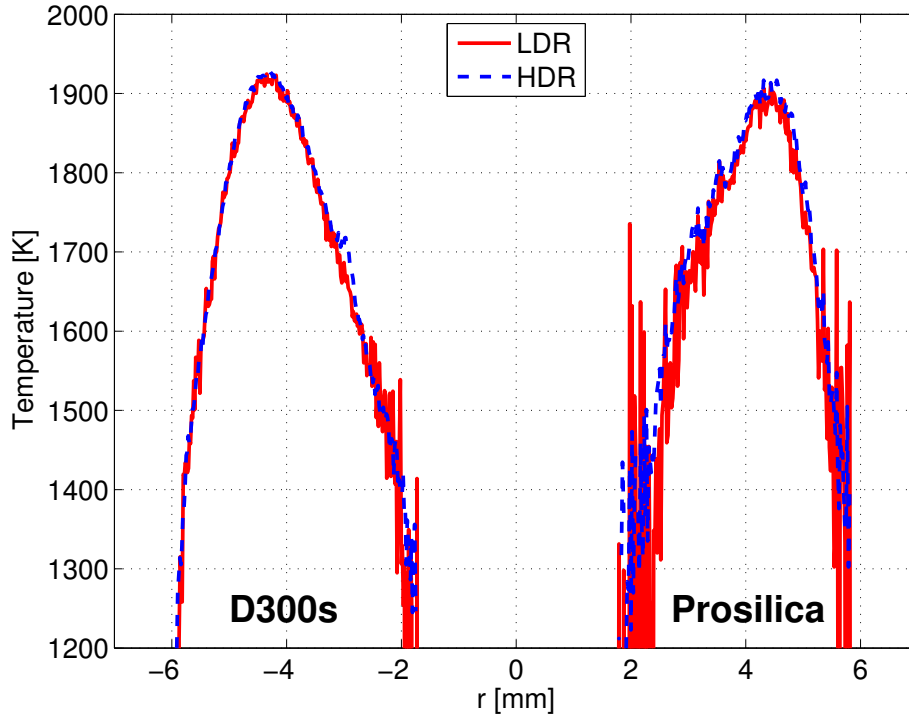


Figure 4.16: LDR and HDR TFP-derived temperature; D300s (left) and Prosilica (right).

The magnifications chosen for the Nikon and Prosilica setup were such that a comparable number of pixels ( $\sim 1200$  for the Prosilica and  $\sim 1400$  for the Nikon) were used to image the fiber along the radial direction. Thus, despite projecting the same area on a comparable number of pixels, the Nikon camera provided an overall better SNR. Moreover, to limit the saturation-related linearity problems that affected the Prosilica, the cut-off threshold for the reconstructed HDR image was lowered to  $\sim 75\%$  of the camera full dynamic range. This resulted in a limited usage of the saturated frames, and in a less-than-optimal SNR improvement in the final HDR image.

Figure 4.17 (left) shows a comparison between the LDR and HDR approaches when applied to a full-flame temperature measurement using thin filament pyrometry and the Nikon D300s. The flame was the same nitrogen-diluted methane flame

described previously in this section and the two-dimensional temperature field was reconstructed by stacking one-dimensional measurements taken every 0.25 mm. From the temperature distribution comparison the differences between LDR and HDR results are not so evident; however, when considering the overall SNR distribution (Fig. 4.17 right), the increase in SNR towards the flame edges (low temperature regions) is clearer. The increased measurement sensitivity introduced by the HDR algorithm allowed for a better-defined temperature field with a smoother transition between flame and background temperature. Note that, because of possible soot deposition on the fiber, temperature values within the  $\pm 2$  mm radius, and above 22 mm above the burner, may not be accurate.

Even though the above example focused on the application of the technique to two-color thin filament pyrometry, the same approach could be used when employing intensity-ratio pyrometry [23]. Since HDR imaging returns an image with higher SNR, particularly in low-signal regions, increased sensitivity in low intensity/temperature areas would be expected as well.

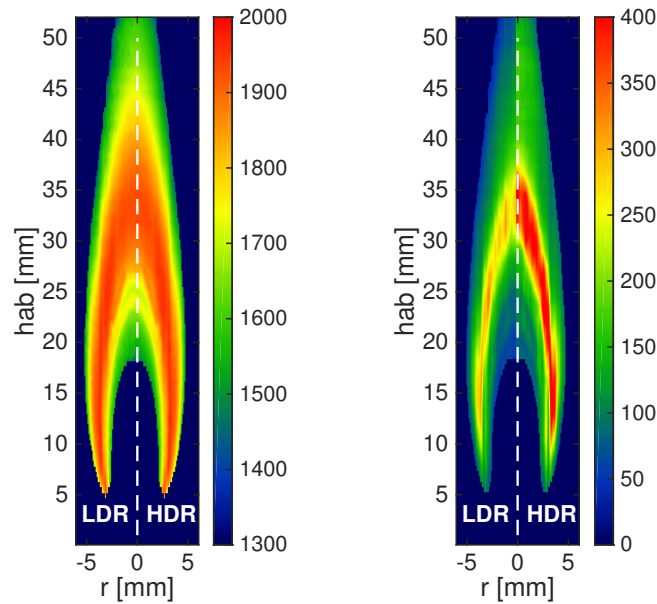


Figure 4.17: LDR and HDR TFP-derived temperature (left) and SNR map (right) for the 65% methane flame evaluated with the D300s.

## Defocused thin filament pyrometry

An alternative way to increase the SNR of a thin filament pyrometry measurement, and to reduce the problem related to the imaging of a sufficient number of pixels, relies on the use of a cylindrical lens to spatially spread the imaged fiber over multiple pixels. A cylindrical 100 mm focal-length lens was used to test this approach: it was positioned in front of the camera lens so that the fiber fell along the focal point of the lens, and the parallel rays generated by the imaging system were collected and imaged onto the detector. Figures 4.18 and 4.19 show the fiber as imaged with the Nikon D300s using a conventional setup and with the addition of the cylindrical lens, respectively.



Figure 4.18: Conventional fiber image



Figure 4.19: Defocused fiber image

Figure 4.20 compares the radial temperature profiles, at the same flame location of Fig. 4.16 showing, this time, the LDR result and the “defocused” one. The defocused result was obtained, like the LDR one, using a single exposure but an increase in SNR was observed across the entire temperature range.

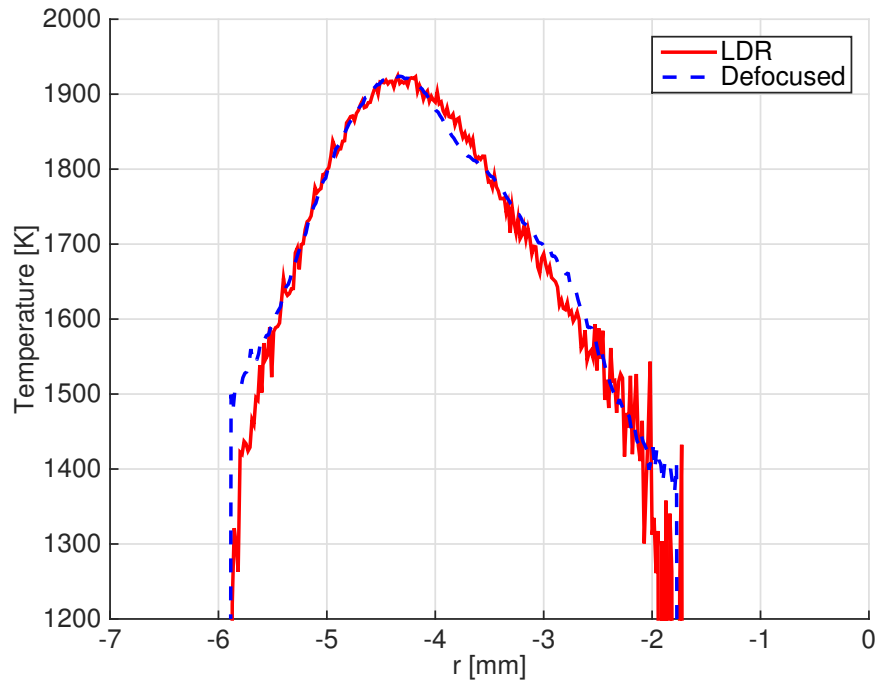


Figure 4.20: LDR and “defocused” TFP-derived temperature for the 65% methane flame evaluated with the D300s.

### 4.5.2 Soot pyrometry

In this section, the SNR of HDR images was evaluated for a flame in which two-dimensional temperature measurements using LDR color-ratio pyrometry have been reported previously [12]. The flame was a nitrogen-diluted coflow ethylene flame (40% ethylene, 60% nitrogen by volume, 35 cm/s average flow velocity of both fuel and oxidizer). Figure 4.21 shows a map of the SNR distribution for the RGB color channels obtained with the Nikon D300s (the SNR was determined at each pixel as described in Section 4.4). Figure 4.22 displays the result obtained with the Prosilica camera, instead. Each color channel figure is split with the left half showing the LDR result and the right half the HDR one; contour plots were added to help highlight the differences in the low SNR regions. The HDR image was reconstructed considering four frames with exposure times of 1/128, 1/64, 1/32, and 1/16 seconds, and 5, 10, 20, and 40 milliseconds for the Nikon and Prosilica, respectively.

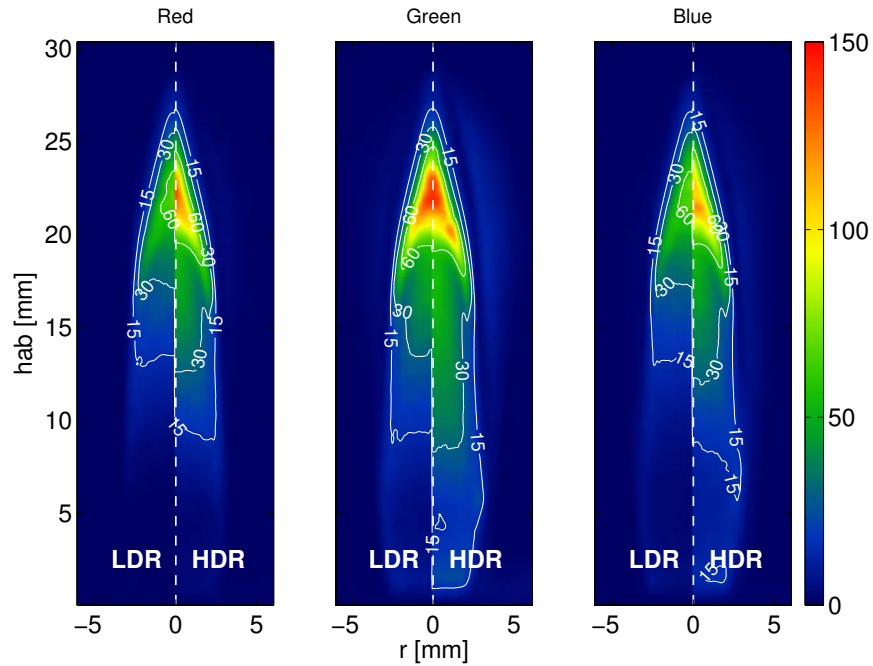


Figure 4.21: SNR map of the RGB channels in an image of a 40% ethylene flame taken with the D300s; contour plots highlight the SNR values in low intensity regions.

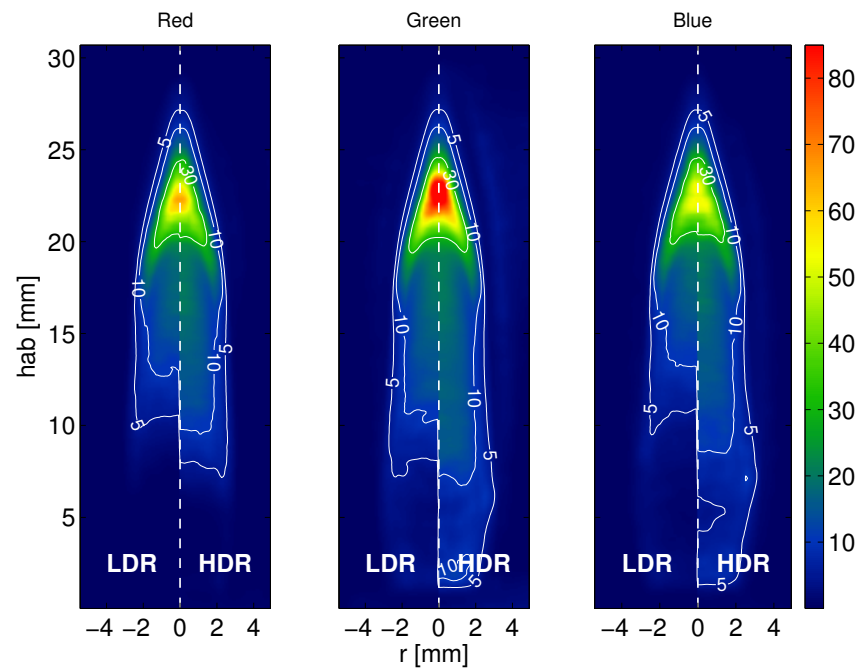


Figure 4.22: SNR map of the RGB channels in an image of a 40% ethylene flame taken with the Prosilica camera; contour plots highlight the SNR values in low intensity regions.

For the Nikon D300s, the HDR algorithm yielded an image that had an overall higher SNR. In the saturating green channel, the major SNR improvements occurred in the low intensity regions, while the red and blue channels showed improvements over the whole image. The SNR map for the Prosilica camera showed a more modest improvement between LDR and HDR results. This was mainly due to the fact that, as already mentioned, the Prosilica cut-off threshold had to be lowered to avoid nonlinearity issues. Figures 4.23 and 4.24 show the number of frames that were averaged when computing the HDR image from the aforementioned sequences. The large SNR improvements for the Nikon red and blue channels (Fig. 4.23) were due to the averaging of at least 3 different frames; the same averaging did not happen in the Prosilica acquisition (Fig. 4.24) and the only SNR improvements were the ones involving the low intensity regions.

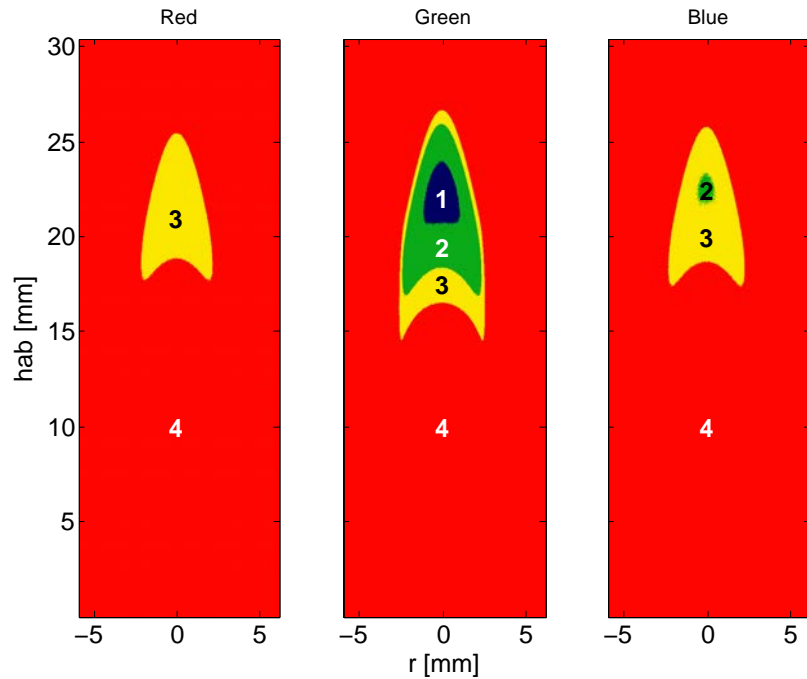


Figure 4.23: Number of averaged frames in the HDR image reconstruction - Nikon D300s.

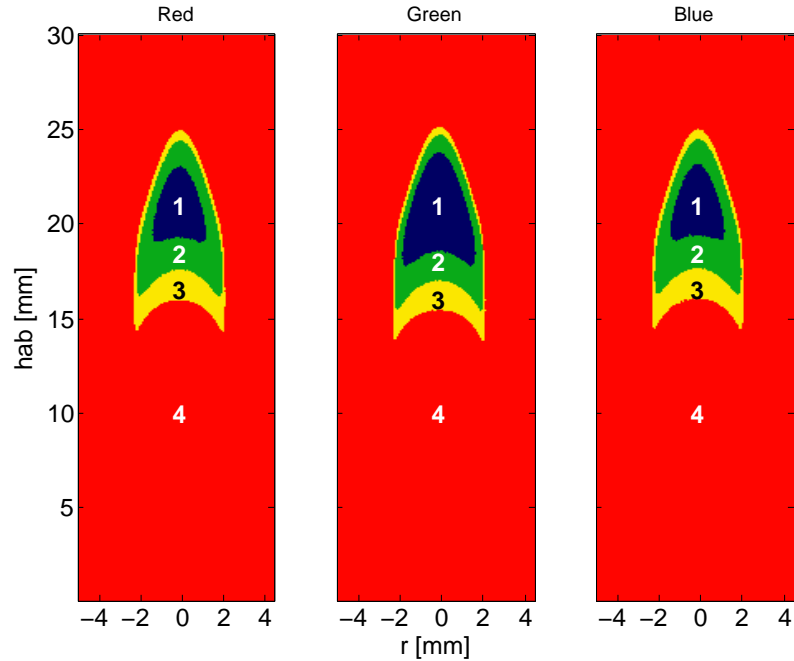


Figure 4.24: Number of averaged frames in the HDR image reconstruction - Prosilica GC1380-CH.

A further verification that the HDR image retained all the information of the LDR one without introducing unwanted and unphysical artifacts was done by plotting the intensity of the HDR pixel as a function of the respective LDR pixel. The ideal result would be a line with slope one and intersecting the axis at the origin. Figure 4.25 shows the aforementioned plots (normalized to the detector full dynamic range) for the 40% ethylene LDR and HDR flame images. Figure 4.25 (top) shows results for the D300s camera, while Fig. 4.25 (bottom) is for the Prosilica. As can be inferred from Fig. 4.25, both HDR results retained the correct information; the small deviations from the theoretical distribution were likely due to both inherent camera noise and minor spatial fluctuations among the frames used to reconstruct the HDR image.

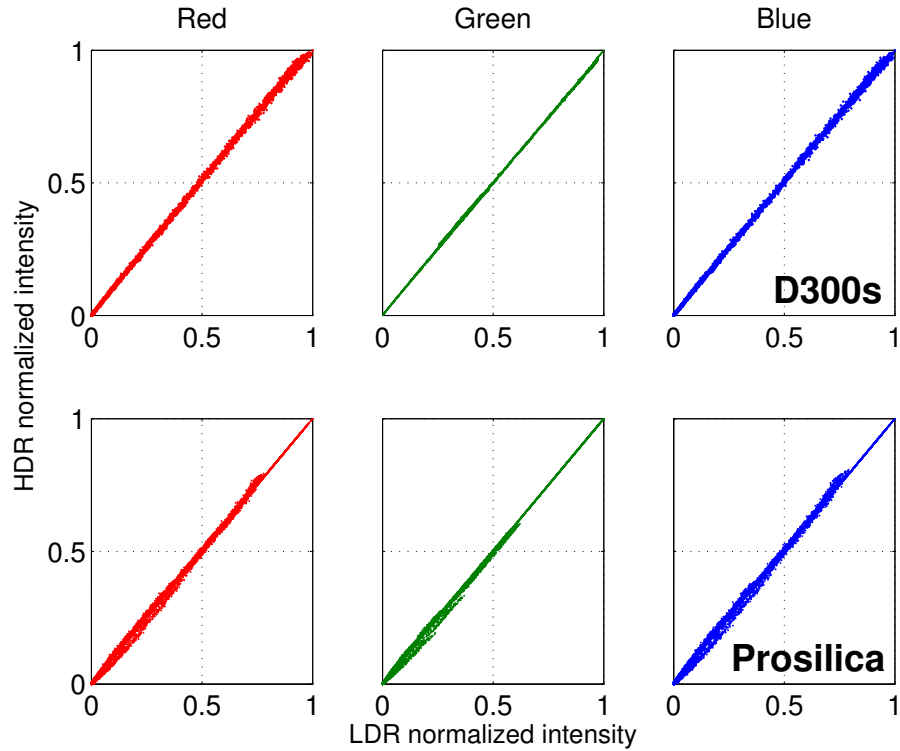


Figure 4.25: HDR normalized intensity as a function of the LDR one - D300s (top) and Prosilica (bottom).

To complete the comparison, Fig. 4.26 shows the SNR map from the D300s for both an HDR image (right half) and an image resulting from a conventional averaging (left half, four frames, 1/128 second exposure time). The maximum SNR value is the same as the one shown in Fig. 4.21, but the color scale was chosen to highlight differences in the low intensity regions, where the HDR images still show a higher SNR.

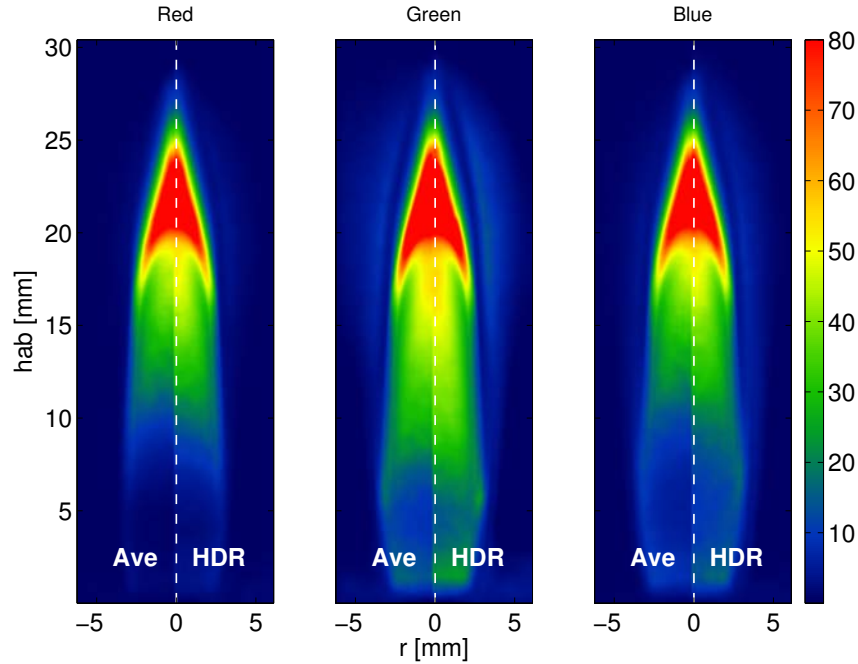


Figure 4.26: SNR map of the RGB channels in an image of a 40% ethylene flame taken with the D300s, comparing conventional averaging and HDR imaging.

### 4.5.3 Microgravity flames

It has been mentioned that HDR imaging is useful when trying to retrieve information from partially saturated frames of steady phenomena; such is the case for images in the SLICE dataset where, because of unknown flame luminosity levels under microgravity conditions, bracketing sequences with varying exposure times were used to capture images of steady microgravity laminar flames. The broad exposure sampling resulted in numerous partially saturated frames that have been mainly unused. As an additional and practical example of the HDR imaging effectiveness, Figs. 4.27 and 4.28 show a comparison between the temperature (left) and soot volume fraction (right) derived from LDR and HDR SLICE images of two representative flames in microgravity; Fig. 4.28 highlights just the region close to the flame tip where the effectiveness of the HDR approach can be observed. The flames consist of 100 % methane coflow diffusion flames (fuel velocity 72 cm/s, air coflow velocity 40 cm/s,

1.6 mm nozzle, and fuel velocity 314 cm/s, air coflow velocity 5 cm/s, 1.6 mm nozzle, respectively). The Nikon D300s was used to take a series of images with nominal exposures of 1/60, 1/40, 1/25, and 1/15 seconds.

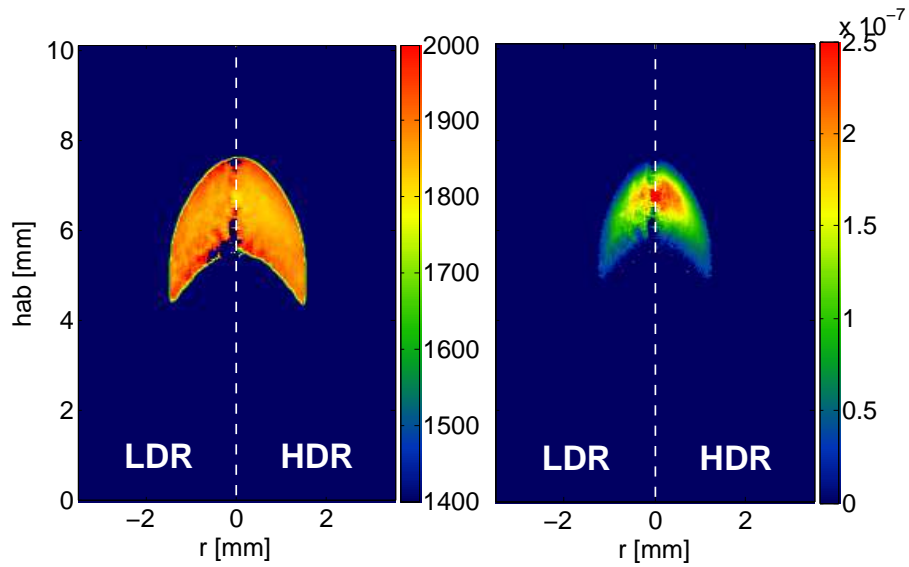


Figure 4.27: Comparison between LDR- and HDR-derived temperature, in Kelvin, (left) and soot volume fraction (right). 100 %  $CH_4$  flame, fuel velocity 72 cm/s, air coflow velocity 40 cm/s, 1.6 mm nozzle.

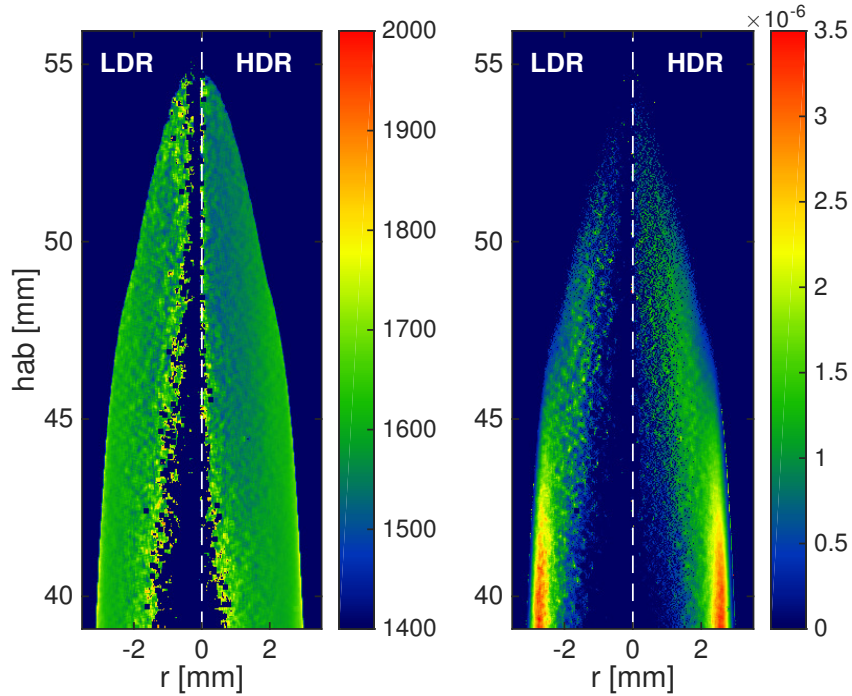


Figure 4.28: Comparison between LDR- and HDR-derived temperature, in Kelvin, (left) and soot volume fraction (right). 100 %  $CH_4$  flame, fuel velocity 314 cm/s, air coflow velocity 5 cm/s, 1.6 mm nozzle.

In order to obtain the cross-sectional temperature distribution shown in Figs. 4.27 and 4.28, the original images were Abel inverted and pairs of color ratios were used with a lookup table to determine the temperature. The temperature, in turn, was used along with the Abel-inverted intensity to determine soot volume fraction. As mentioned in Section 2.2.1 one of the major drawbacks of the Abel inversion is the noise propagation, and this is particularly critical for the region along the centerline. Since the temperature result is generally obtained by averaging the results from the three different color ratios, the low SNR of the LDR red and blue channels (similar to that seen in Fig. 4.21) will influence negatively the final average temperature. The higher SNR across the whole HDR image resulted in less noisy Abel-inverted images that provided better temperature maps. As seen in Figs. 4.27 and 4.28, the biggest difference and improvement in the HDR results was indeed along the centerline, where

the LDR image did not have sufficient sensitivity to properly map the temperature field.

## 4.6 Conclusions

High dynamic range imaging was successfully applied to one and two-dimensional temperature measurements in non-sooty and sooty flames using two-color thin filament and soot pyrometry, respectively. The original HDR algorithm proposed by Debevec and Malik was tested on three selected color cameras and was able to detect nonlinear effects in the response function of one of the detectors operating under partially saturated conditions. However, because the response curves calculated using the Debevec and Malik algorithm are a result of a mathematical fitting that prioritizes the quality of fit in the central part of the dynamic range, the derived response curves were not as accurate as the ones obtained by direct measurement using a pulsed LED.

Verification of the linearity and reciprocity of the detectors allowed the implementation of a simplified HDR imaging algorithm. Furthermore, it revealed the necessity of carefully selecting the detector and the HDR image parameters (particularly the maximum degree of saturation) in order to exploit and optimize the camera HDR performance. Pixel crosstalk has been shown to be a limitation that reduces the detectors HDR potential, particularly for color cameras.

The main motivation for HDR imaging was the improvement in the SNR that could be achieved. SNR analysis showed that a factor-of-two increase could be gained in low pixel count regions. The SNR improvement in the mid and high pixel count regions was less substantial, but could be improved using frame sequences that have small exposure time increments. As the exposure increments get smaller and smaller, HDR imaging tends to approximate conventional averaging.

Application of HDR imaging to one-dimensional thin filament pyrometry mea-

measurements showed that the technique increases the low temperature sensitivity, thus spatially extending the measurable region. Moreover, it was seen that, the less sensitive the detector, the bigger the improvements introduced by the HDR approach.

HDR imaging applied to two-dimensional soot pyrometry confirmed the conclusions obtained in the one-dimensional case. A nitrogen-diluted ethylene diffusion flame was selected to show the SNR improvements gained with the proposed method. It was demonstrated that the quantitative information carried by the HDR image was the same as the LDR one, and it was shown that the differences between the HDR result and conventional averaging were minimal, with HDR imaging providing slightly higher SNR in the low-pixel-count regions.

Finally, the application of HDR imaging to the existing SLICE dataset showed the dual advantages of this new approach. First, partially saturated data that had been unused so far found its way into the quantitative analysis. Second, the Abel-inverted HDR images, that were required to compute temperature and soot volume fraction distributions, had a higher SNR along the centerline, which resulted in better temperature and soot volume fraction measurements.

## Chapter 5

# Time-resolved image averaging and high dynamic range imaging applied to laser flow diagnostics

Laser-based imaging diagnostics such as Rayleigh scattering or laser-induced fluorescence are used extensively for studying reacting and non-reacting flows and can provide quantitative, nonintrusive measurements of chemical species concentration, gas density and/or temperature [32, 83, 84]. As seen in Chapter 4, practical limitations affecting the quality of the collected data might include the finite dynamic range of the detectors and the limited signal-to-noise ratios (SNR) of the measurements; inherent noise sources, such as shot, dark and readout noise can, in fact, adversely affect the measurements [85]. Numerous post-processing denoising techniques have been developed to reduce image noise, albeit with the risk of losing spatial accuracy; recent reviews of existing denoising methods are presented in [86–88]. In some cases, the SNR can be improved by averaging multiple acquisitions or, as shown in Chapter 4, by implementing high dynamic range imaging [89]. This, however, can be problematic in those situations when conventional averaging or phase locked measurements

cannot be implemented, such as with the imaging of turbulent flows. This chapter presents two alternatives that can be used to increase the signal-to-noise ratio in these kind of environments.

## 5.1 Time-resolved image averaging

The scope of this section is to demonstrate a technique that would allow an increase of the SNR in images of unsteady flows, where conventional averaging or the implementation of HDR imaging is in general not possible. Without any additional increase in hardware complexity, the approach could prove valuable in those experimental set-ups already designed for the time-resolved characterization of turbulent flows, in which image intensifiers are used either to increase the intensity of weak signals, or as fast gating devices.

Image intensifiers operate by converting low levels of light into electrons (through a photocatode, via the photoelectric effect), accelerating those electrons with microchannel plates (MCP), amplifying them through secondary cascade emission when the electrons hit the MCP, and finally converting them back into photons when they strike a phosphor screen at the back end of the intensifier. The idea behind the approach presented in this section exploits the inherent behavior of these devices and relies on the finite temporal decay of the phosphor emission. By using the capability of interline transfer CCD cameras to acquire two sequential images with a short interframe temporal separation, it is possible to collect the phosphor-emitted light over the two consecutive frames and use them to perform an averaging that comprises two images. Despite the phosphor temporal decay being relatively slow, thus limiting the measurement repetition rate (in this set of experiments, the intensifier phosphor light reached 5% of its peak value after  $\sim 50 \mu\text{s}$ ), the minimum time scales that are resolvable are still determined by the length of the laser pulse (order of ns).

To prove the validity of the concept and its possible application to real experimental conditions, planar Rayleigh imaging was used to acquire and compare the SNR from two different sets of images of a partially premixed methane/air flame. Data was obtained first using the conventional Rayleigh imaging approach, where the total Rayleigh scattered light is collected in a single image; this result served as a reference and provided a baseline to which the SNR of the new approach could be compared. A second dataset was obtained using the two-image averaging technique. To avoid uncertainties in the interpretation of results associated to the variable nature of the turbulent features, datasets were first collected in a steady flame, and then extended to a turbulent one.

### 5.1.1 Experimental setup

As derived in Section 2.3.3, the Rayleigh signal  $S_{Ray}$  that is collected by a detector can be expressed as

$$S_{Ray} = KE_0NV \sum_i x_i \sigma_i, \quad (5.1)$$

where  $K$  is the efficiency of the collection optics,  $E_0$  the laser single shot energy,  $N$  the number density, and  $V$  the collection volume. In the summation term (called the effective Rayleigh cross section),  $x_i$  and  $\sigma_i$  are the mole fraction and Rayleigh cross section of the  $i^{th}$  chemical species, respectively [39]. Rayleigh scattering can be used to determine species concentration in the case of isothermal mixing or, given information on the effective Rayleigh cross section, for temperature measurements through the inverse relationship with  $N$  [39]. In Rayleigh thermometry, the signal reaches its minimum at the flame front, where the temperature is the highest; the resulting low SNR of this region may be a limitation in the accuracy of such measurement. For this reason Rayleigh scattering was considered as a test case to show if low SNR values could be mitigated with the proposed two-image averaging.

The experimental configuration used to test the applicability of the approach to reactive flows is shown in Fig. 5.1 where an illuminating laser sheet was generated using a sheet-forming telescope and sent into the probe volume where the Rayleigh-scattered light was collected and imaged onto an interline transfer CCD through a Gen III image intensifier.

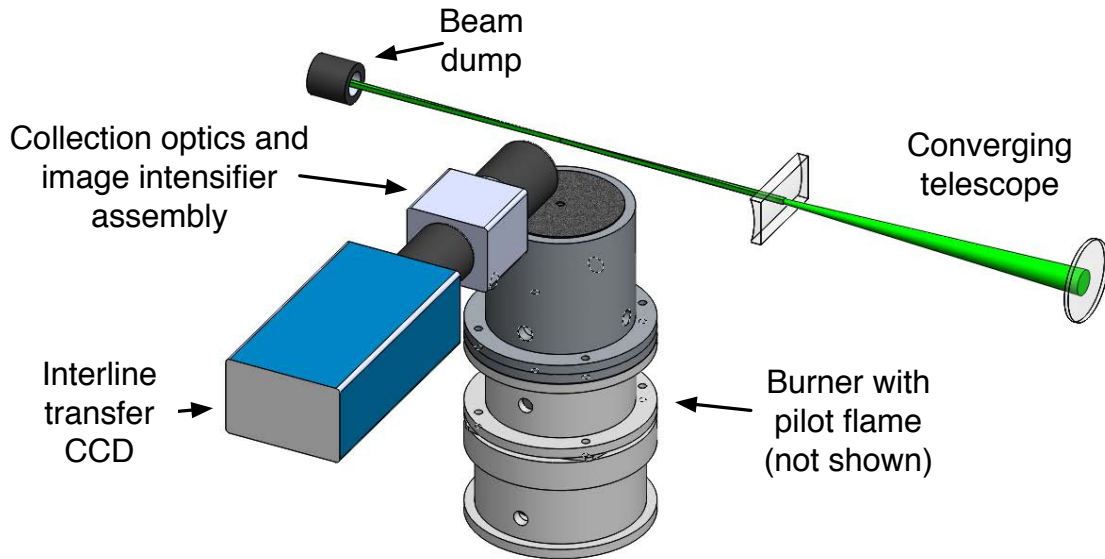


Figure 5.1: Schematic drawing of the experimental set up, showing the detector, the collection optics, the burner, and the laser sheet forming optics.

The second harmonic of a Spectra Physics Pro 250 Nd-YAG laser was focused into a sheet (3.3 mm height,  $\sim 35 \mu\text{m}$  FWHM beam waist thickness as determined by imaging the attenuated laser sheet onto a detector, 350 mJ/pulse, 10 Hz repetition rate, 10 ns pulse length) and sent through a partially premixed methane flame (75% air, 25%  $\text{CH}_4$  by volume, 4 mm and 2 mm nozzle diameter for the steady and turbulent flames, respectively) surrounded by an air coflow (75 mm O.D. diameter, 35 cm/s average velocity). The beam focusing and sheet forming was achieved with a telescope comprising a 300 mm focal length spherical lens and a negative 100 mm focal length concave cylindrical lens. The beam height was decreased from 10 mm to 3.3 mm to match the detector chip size and increase the fluence. The average

velocities of the fuel mixture were 2.6 m/s for the steady flame and 32 m/s for the turbulent flame, resulting in a jet Reynolds number of  $\sim 4000$ . A premixed methane pilot flame, in an arrangement co-annular to the main jet (9.6 mm I.D., 13.3 mm O.D.), was added to the burner to anchor the turbulent flame and avoid blow off. The Rayleigh-scattered light was collected through a pair of Nikkor 50 mm lenses and imaged onto the front faceplate of an ITT Gen III MCP image intensifier (GaAs photocatode, 18 mm diameter, 45 lp/mm, 1  $\mu$ s gate time, P20 phosphor, 5 V to 10 V nominal gain voltage range) using one-to-one magnification. The resulting intensified image was then imaged onto the chip of a cooled Sensicam Interline Transfer CCD (1280 x 512 pixels - when operated in double frame mode, binned 2x2 pixels, 12 bit A/D converter) using an additional pair of Nikkor 50 mm lenses with one-to-one magnification. The measurements were performed at a height above the burner (HAB) centered either at six or twelve diameters downstream for the steady and turbulent flames, respectively. Two Stanford Research DG535 pulse generators synchronized the laser, image intensifier and camera. The intensifier gain voltages were matched to the laser pulse energy and set to 6.5 V and 7 V for the conventional and averaged measurements, respectively, so that the collected images used the same portion of the camera dynamic range without any saturation. The light emitted by the intensifier phosphors was recorded by the interline transfer CCD camera using the double frame option; when operated in this mode, the camera was able to record two consecutive frames with a time separation of 1  $\mu$ s. The exposure could only be set for the first of the two frames, with the exposure of the second image determined by the speed of the CCD readout (measured to be 46.45 ms). For the conventional Rayleigh measurement, the first exposure was set to 50 ms in order for the first frame to collect all the light emitted by the intensifier phosphors. Conversely, for the averaged Rayleigh measurement, the exposure of the first frame was reduced to 30  $\mu$ s so that the integrated collected light, thus the recorded counts, was equally divided between the two

frames.

Figure 5.2 shows the normalized intensity of the phosphor light as function of time, as measured with a photomultiplier, and summarizes the relative delays between laser pulse, intensifier gate and camera exposures for the case of the averaged acquisition. With reference to Fig. 5.2, the 10 ns laser pulse (not shown) is centered at 0  $\mu\text{s}$ , the 1  $\mu\text{s}$  gate time of the image intensifier is shown by the green square wave, while the exposure of the first and second frames of the interline transfer CCD are shown by the red and orange square waves, respectively. Note that the “tail” of the P20 phosphor decay continues up to  $\sim 50$  ms [90,91] and the second frame exposure continues up to 46.45 ms, but they are truncated at 50  $\mu\text{s}$  for ease of visualization.

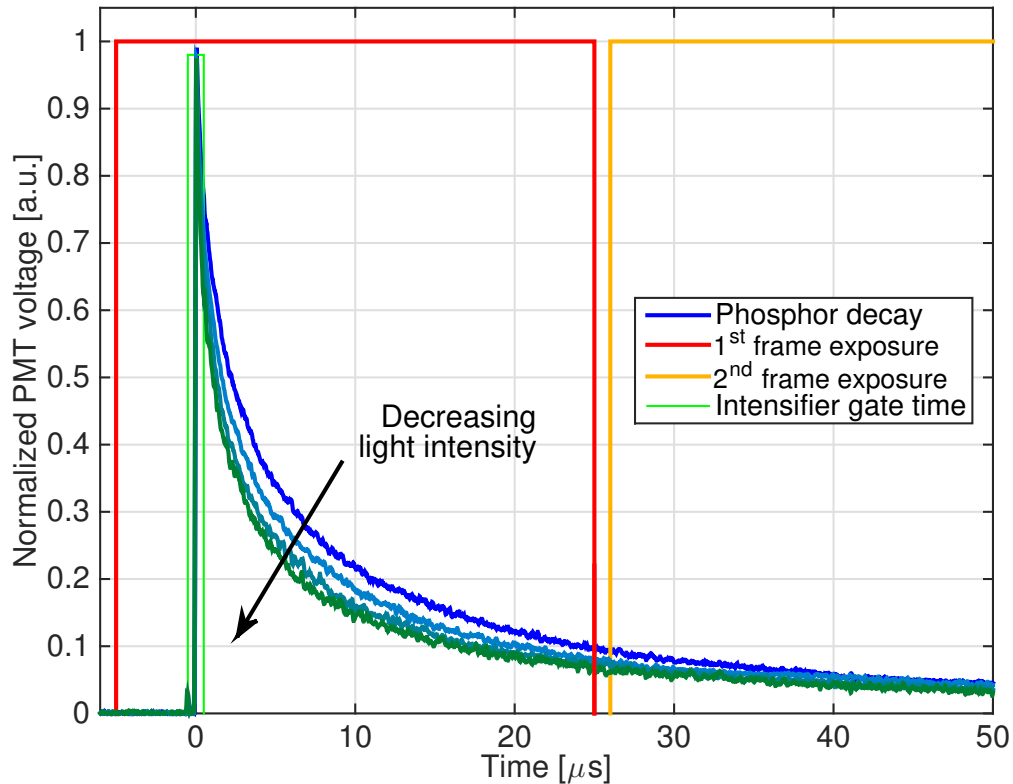


Figure 5.2: Normalized phosphor temporal decay, shown for decreasing light intensity, when compared to the image intensifier gate and Sensicam exposures.

In general, P20 phosphors are characterized by a non-exponential decay with two

distinct responses: an initial short-time behavior with a fast decay (which is the one shown in Fig. 5.2) followed by a long-time behavior, which has a much slower decay [90]. In this case, the characteristic time constant of the intensifier decay, as well as the CCD readout time, limited the measurements to repetition rates less than 20 Hz. The use of faster phosphors such as P46 or P47 [92], along with a detector capable of faster readout, would allow for higher repetition rates.

All steps of the acquisition process were controlled using the open source software OMA [50] and, regardless of the approach followed (conventional or averaged Rayleigh), each image was processed independently using Matlab. First, an offset subtraction (flame images taken with the laser off) was performed to account for fixed pattern camera noise and DC offset; the result was then normalized with a Rayleigh scattered image of air in order to account for laser sheet non-uniformities; both offset and air images were the result of an average over 10 shots. The Rayleigh intensity of areas with uniform temperature and gas composition are expected to be constant, so a final horizontal “stripe correction” was implemented to remove any remaining laser sheet non-uniformities: each column of the image was normalized with an array whose intensity was obtained by averaging, row by row, multiple columns in an area of the image where only air was present. Before applying the latter correction, each image was rotated by 1 degree in order to align the stripes horizontally and to account for the fact that the detector chip was not parallel to the laser sheet direction. This operation introduced additional pixels to the image, which was therefore clipped to 2.8 mm x 9.8 mm. Note that the rotation algorithm returned a slightly smoothed image as a result of the implemented bicubic interpolation, which in turn artificially decreased the original noise of the image.

### 5.1.2 Detector and image intensifier characterization

As in every quantitative imaging experiment, the meaningfulness of the data relies on the assumption that the detector is linear over its entire dynamic range. The linearity of the Sensicam used in this study was verified following the methodology presented in Chapter 4, where a pulsed LED was used as an illumination source and whose radiant energy was controlled by varying its gating time. The excellent linearity of the detector is shown by the green markers in Fig. 5.3a (the black line represents a perfect linear trend), where the solid and empty markers identify the response evaluated considering the first and second frames of the camera, respectively (when used in double-frame mode). The LED approach was not employed to verify the linearity of the image intensifier because of the relatively long LED exposures that could saturate and damage the intensifier itself. Instead, Rayleigh-scattered light of air was used as an illumination source and the phosphor-emitted light recorded using a Hamamatsu R928 photomultiplier connected to an Atten 100 MHz oscilloscope. The collected scattered light intensity was progressively decreased by means of neutral density filters, while both the photomultiplier and the image intensifier were operated at a fixed gain voltage (the intensifier gain was set to 7 V). Fig. 5.3b shows the integrated signal recorded by the PMT as function of the neutral density filter transmittance (blue markers). The linearity of the intensifier is seen to be excellent and the largest signal measured with the photomultiplier (case with no ND filter), which corresponds to the largest signal in the Rayleigh temperature measurement, was taken as a reference and the decay curve, similar to that shown in Fig. 5.2, was divided into two regions (with equal integrated voltages) to simulate the two sequential CCD exposures. The temporal splitting determined with the reference signal was maintained for all the remaining measurements and the resulting integrated voltages, for both “frames”, are shown in Fig. 5.3b (green and red markers).

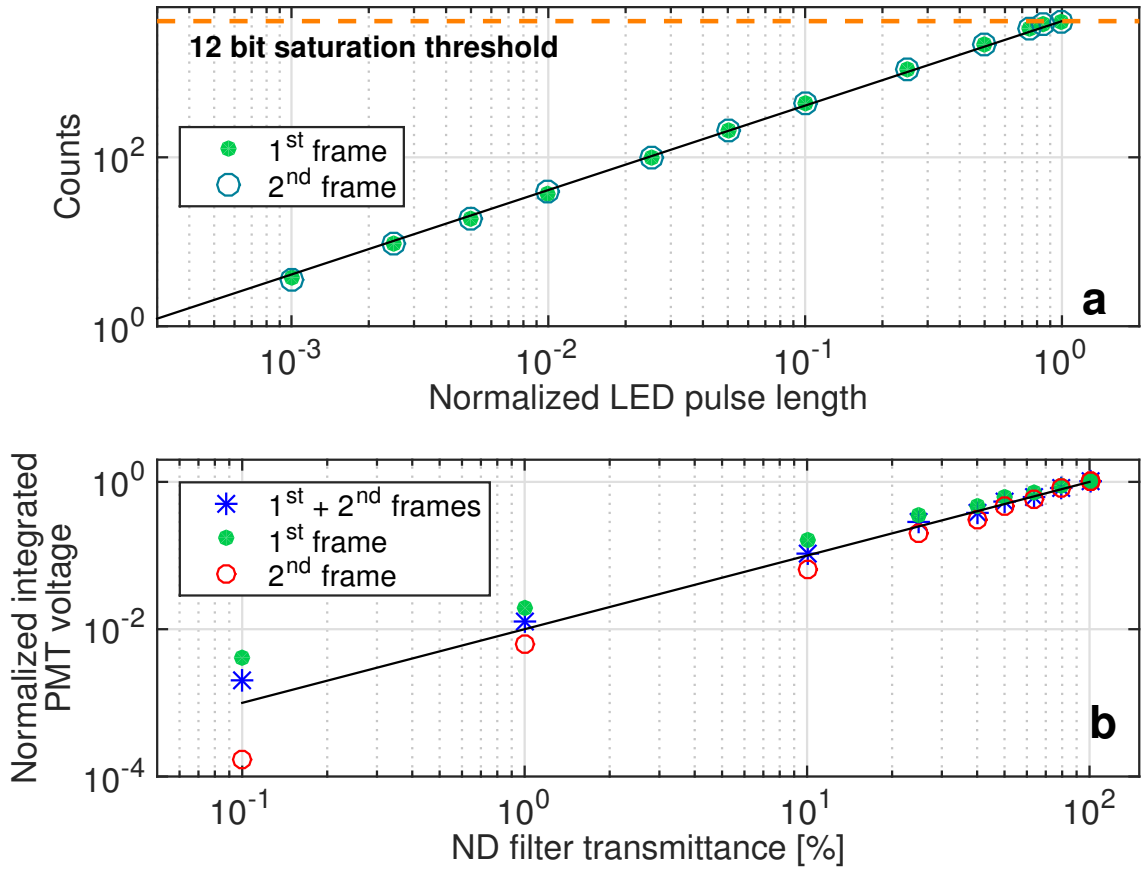


Figure 5.3: (a) Sensicam linearity as determined by LED measurements. Solid and empty markers identify the first and second frames of the interline-transfer CCD, respectively. (b) Image intensifier linearity as determined by photomultiplier measurements.

The small deviation of the individual frames that can be observed in Fig. 5.3b (as the neutral density filter transmittance is decreased) was attributed to the fact that the normalized shape of the phosphor decay changed depending on the intensity of the incoming light, as can be observed in Fig. 5.2. If the temporal splitting between the two regions was kept constant, the ratio between the two integrated voltages deviated from unity as the normalized decay shapes started deviating from the reference one. As a consequence it was seen that, if the camera exposures were set to equalize the high intensity counts, the low intensity ones could differ up to  $\sim 4\%$  of the detector full dynamic range. This discrepancy, however, did not affect the validity

of the quantitative result; when evaluating the average, the counts of the two frames were added and this, in turn, was equivalent to employing the conventional Rayleigh approach where all the light is recorded into a single frame (the subsequent division by 2 to obtain the average value is simply a normalization). The previous conclusion is true if the amount of light that is not recorded during the  $1 \mu\text{s}$  interframe separation is negligible. The photomultiplier results let us indeed verify that the light that was collected over the  $1 \mu\text{s}$  window accounted for less than 1% of the total integrated light.

The SNR of the image returned by the phosphor screen also depended on the gain level of the device itself [93]; typically, the SNR response of an intensifier is linear up to a certain gain value, above which the SNR level reaches a plateau. To evaluate the intensifier SNR characteristics, Rayleigh scattered images of dichlorodifluoromethane (which has a Rayleigh cross-section  $\sim 20$  times greater than that of air) were recorded as a function of the intensifier gain; the laser energy and the Sensicam exposure were kept constant, while the intensifier gain was varied in the range 6 V to 9 V. To decouple the influence of the SNR characteristics of the detector on the final result, the recorded counts, regardless of the chosen intensifier gain, were kept constant ( $\sim 2000$  counts) by means of neutral density filters. In Fig. 5.4a the solid markers represent the averaged counts of 10 images, divided by the neutral density filter transmittance, evaluated in an interrogation region where the recorded intensity was roughly constant, while the error bars identify the standard deviation.

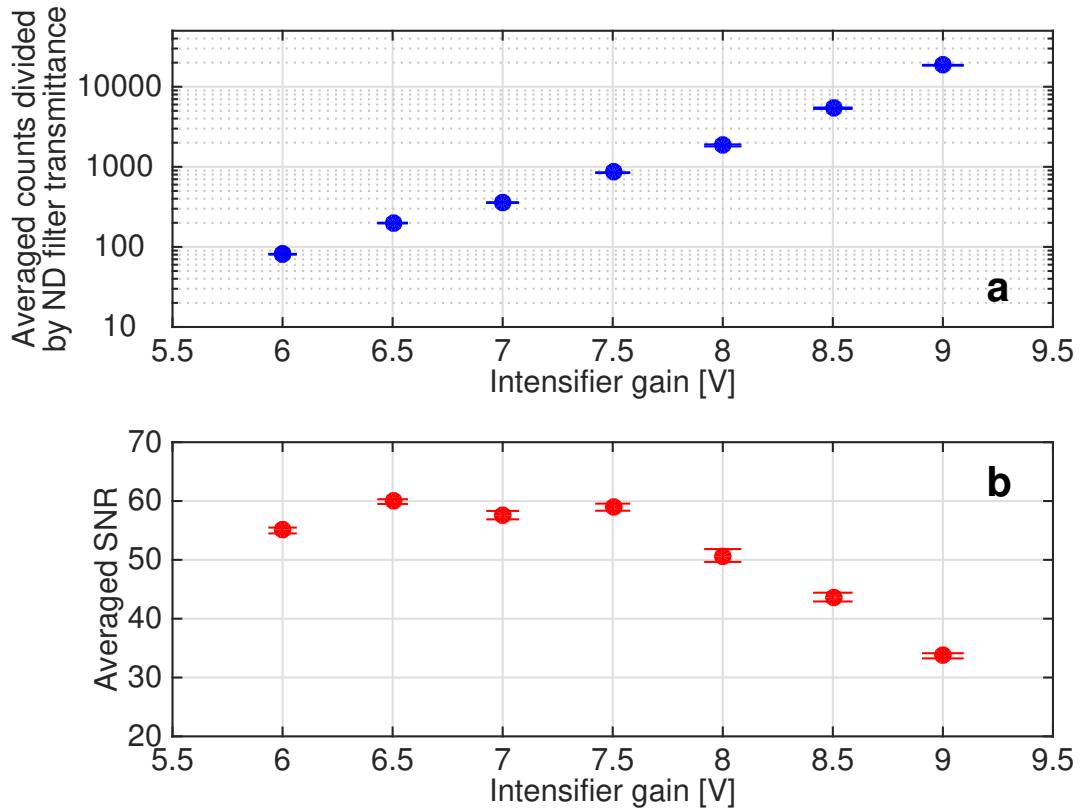


Figure 5.4: (a) Average counts evaluated from Rayleigh scattering images of dichlorodifluoromethane, divided by the neutral density filter transmittance, and (b) SNR of those images as function of the image intensifier gain. The error bars identify the standard deviation over 10 measurements.

The SNR of the image was evaluated according to the following procedure: an initial two-dimensional Gaussian smoothing was done to the image over an area with a  $1/e^2$  full width of 14 pixels; then, in a two-dimensional 9 by 9 pixels sub-interrogation region centered around each pixel (see blue square in Fig. 5.5a), the SNR was calculated by dividing the average value of the sub-interrogation region by the root mean square of the difference between the region intensity and the “average” surface obtained with the initial smoothing. Fig. 5.4b shows the average SNR of the 10 acquired images (solid marker) with the standard deviation identified by the error bars. Despite the recorded counts being kept constant, the SNR of the image remained unchanged only up to 7.5 V, above which the noise started increasing causing a drop in the overall

SNR. For this reason, the in-flame Rayleigh measurements were performed below the aforementioned threshold using a gain of 6.5 V and 7 V for the conventional and averaged approaches, respectively. As can be seen from Fig. 5.4a, increasing the gain from 6.5 V to 7 V doubled the light that was emitted by the intensifier (thus the counts recorded by the detector), which was necessary if the same detector dynamic range was used with the two approaches.

### 5.1.3 Results

As mentioned, the Rayleigh measurements were at first performed in a steady partially premixed methane/air flame to avoid the random variability of turbulent structures to affect the SNR evaluation. Figures 5.5a and 5.6a show the Rayleigh signal (corrected for laser sheet non-uniformities) recorded in the flame using the conventional and averaged approach, respectively. The high-signal-count region on the right identifies the air side at ambient temperature, and the blue square displayed in Fig. 5.5a shows the size of the interrogation region used for the SNR evaluation, as introduced in Section 5.1.2.

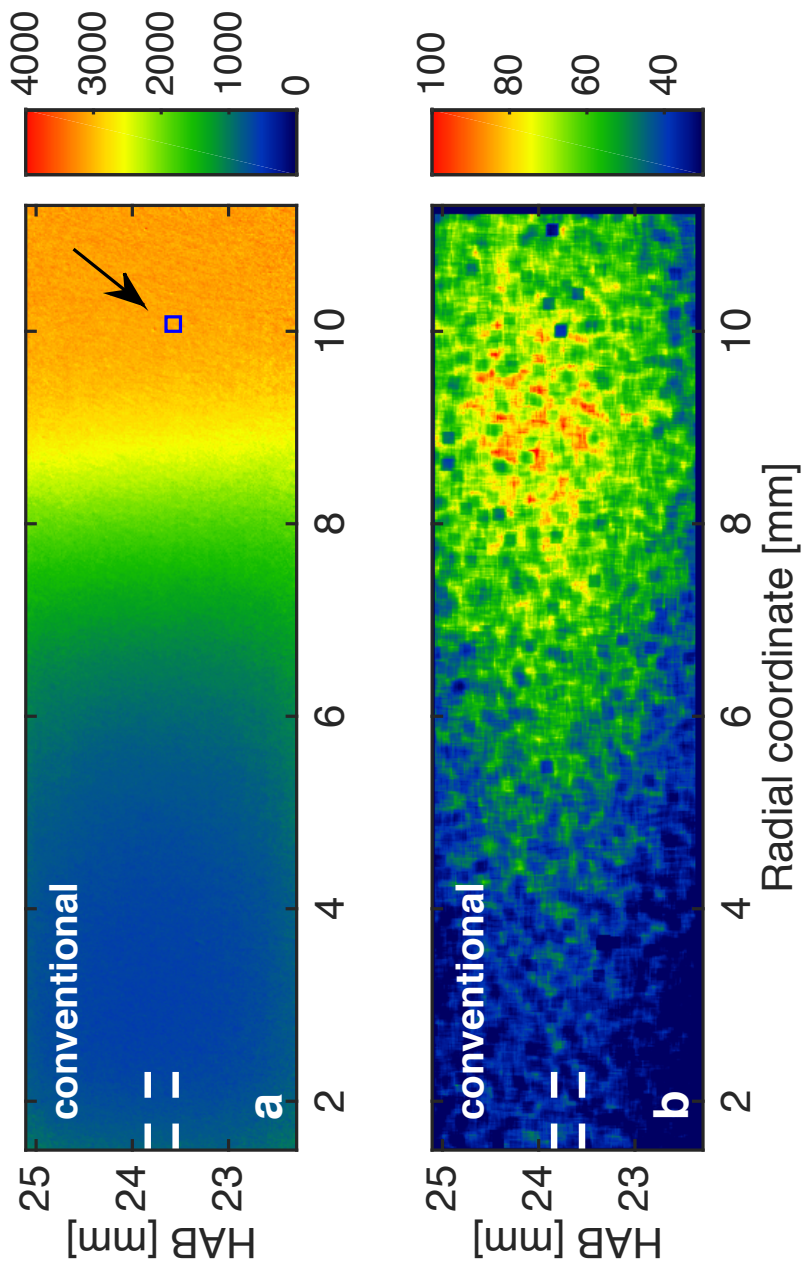


Figure 5.5: (a) Rayleigh signal, in arbitrary units and corrected for laser sheet non-uniformities, and (b) SNR distribution of the conventional Rayleigh image for the steady methane/air partially premixed flame. The dashed lines define a region over which axial averaging was performed to plot the curves shown in Fig. 5.7, while the blue square pointed by the arrow shows the size of the interrogation region used for the SNR evaluation, as explained in Section 5.1.2.

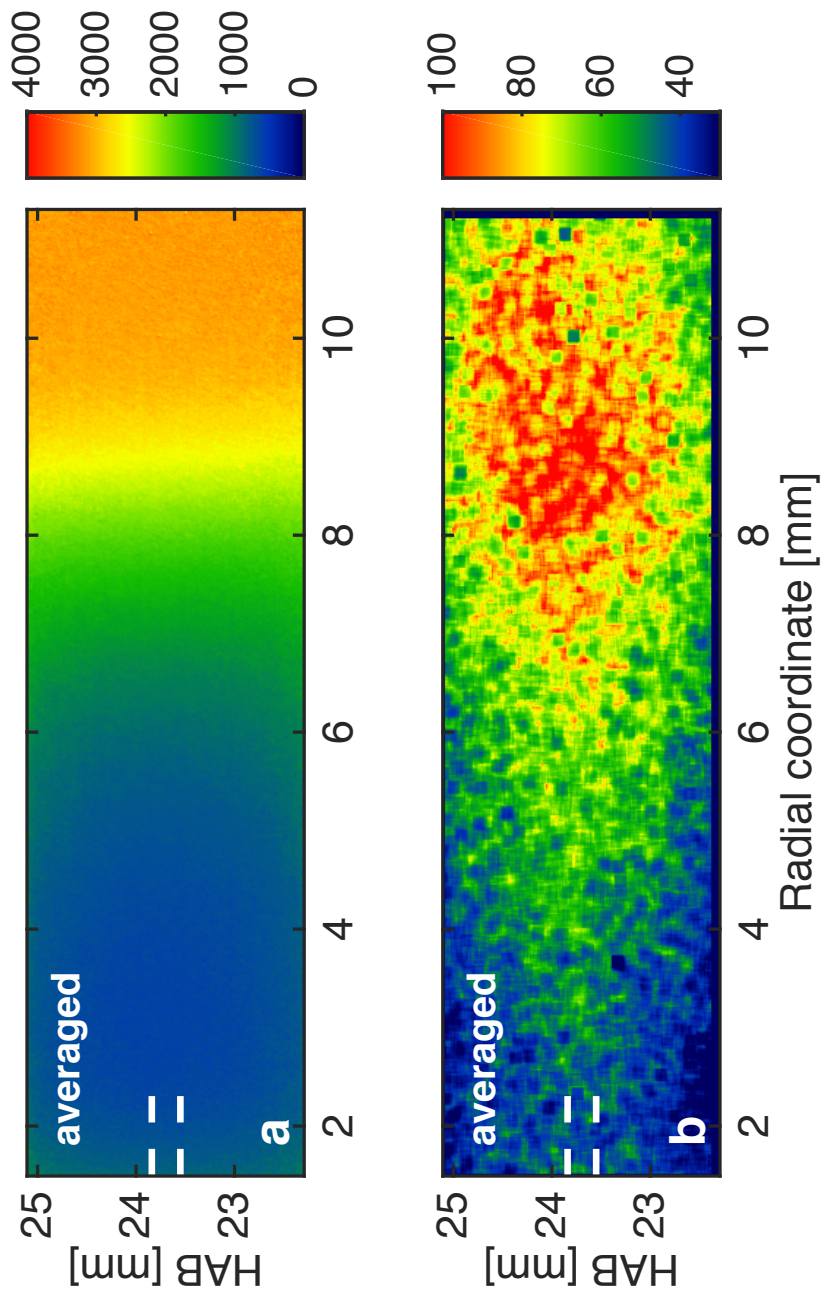


Figure 5.6: (a) Rayleigh signal, in arbitrary units and corrected for laser sheet non-uniformities, and (b) SNR distribution of the averaged Rayleigh image for the steady methane/air partially premixed flame. The dashed lines define a region over which axial averaging was performed to plot the curves shown in Fig. 5.7

Figures 5.5b and 5.6b show the SNR distribution of the Rayleigh images collected using the conventional and average approaches, respectively, evaluated according to the procedure described in Section 5.1.2. As expected, the SNR of the averaged image was higher than the one obtained with the conventional method, and the increase affected the whole image, regardless of the pixel value. Note that, in general, the SNR of an image tends to follow the signal intensity distribution before any correction is performed (shaped by the Gaussian energy distribution of the laser sheet along the image axial direction, as well as by image vignetting). Because of that, even though the corrected intensity of the Rayleigh scattered light was relatively constant in some regions, the SNR was not and, as can be seen in Figs. 5.5b and 5.6b, its value decreased towards the upper and lower, as well as towards the left and right edges of the image. Figure 5.7 shows a comparison similar to the one presented in Figs. 5.5 and 5.6 by plotting the axially averaged counts of the corrected Rayleigh images (Fig. 5.7a) and the axially integrated SNR values (Fig. 5.7b) over a region defined by the white dashed lines shown in Figs. 5.5 and 5.6. Given a comparable value of the recorded counts, for this particular example, the increase in SNR approached 30%. The green curve shows the axially averaged SNR value when considering just the first of the two frames of the image sequence with a result that is, predictably, equivalent to the conventional Rayleigh one.

The proposed approach was able to increase the overall SNR by exploiting the fact that noise is a random process having a zero mean; the averaging of multiple different images tended to even out the random noise fluctuations. The theoretical SNR improvement, if shot noise is the main noise contribution, would be proportional to  $\sqrt{2}$  (where two, in this case, is the number of images being averaged); however, in the current experiment, the large number of scattered photons collected by the detector meant that the combination of dark, intensifier, and readout noise was predominant over the shot noise leading to a SNR gain lower than the theoretical value.

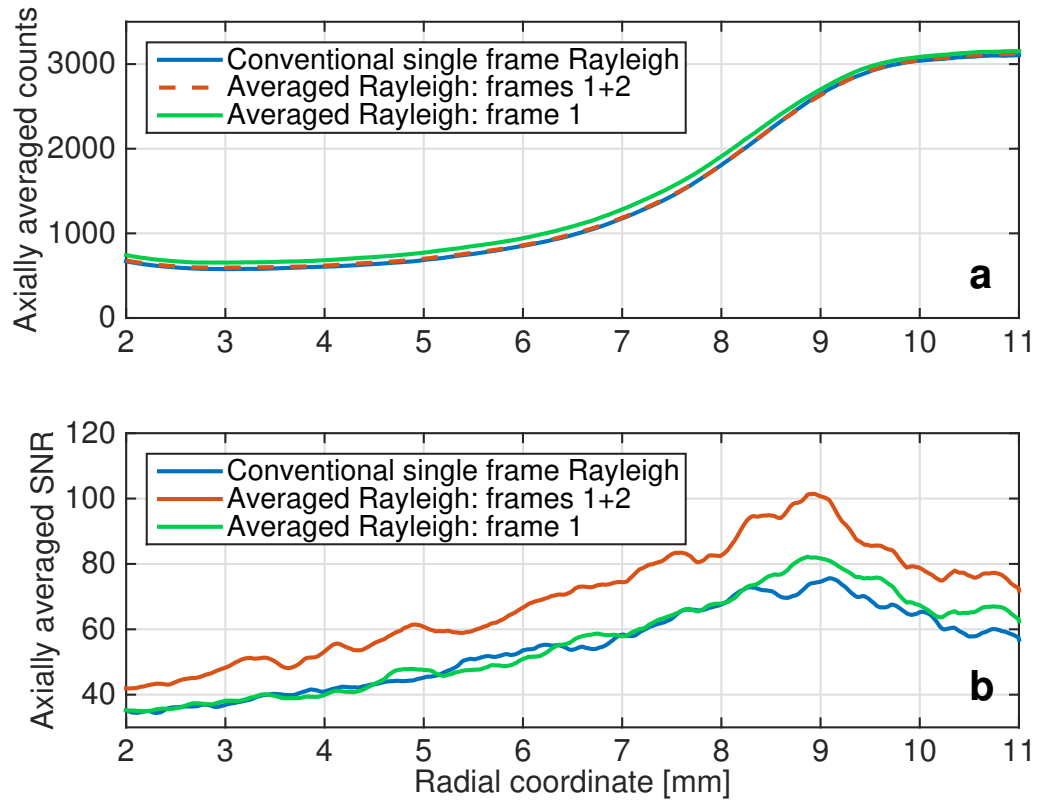


Figure 5.7: (a) Comparison between the axially averaged Rayleigh counts and (b) the axially averaged SNR, for the steady partially premixed methane/air flame.

Figures 5.8 and 5.9 show the result of the extension of the conventional and averaged Rayleigh imaging to the turbulent methane/air flame. Figures 5.8a and 5.9a display the Rayleigh signals (corrected for laser sheet non-uniformities), while Figs. 5.8b and 5.9b show the SNR distributions associated with the aforementioned Rayleigh images; the increase in SNR, for pixels that have a comparable count values, is again close to 30%.

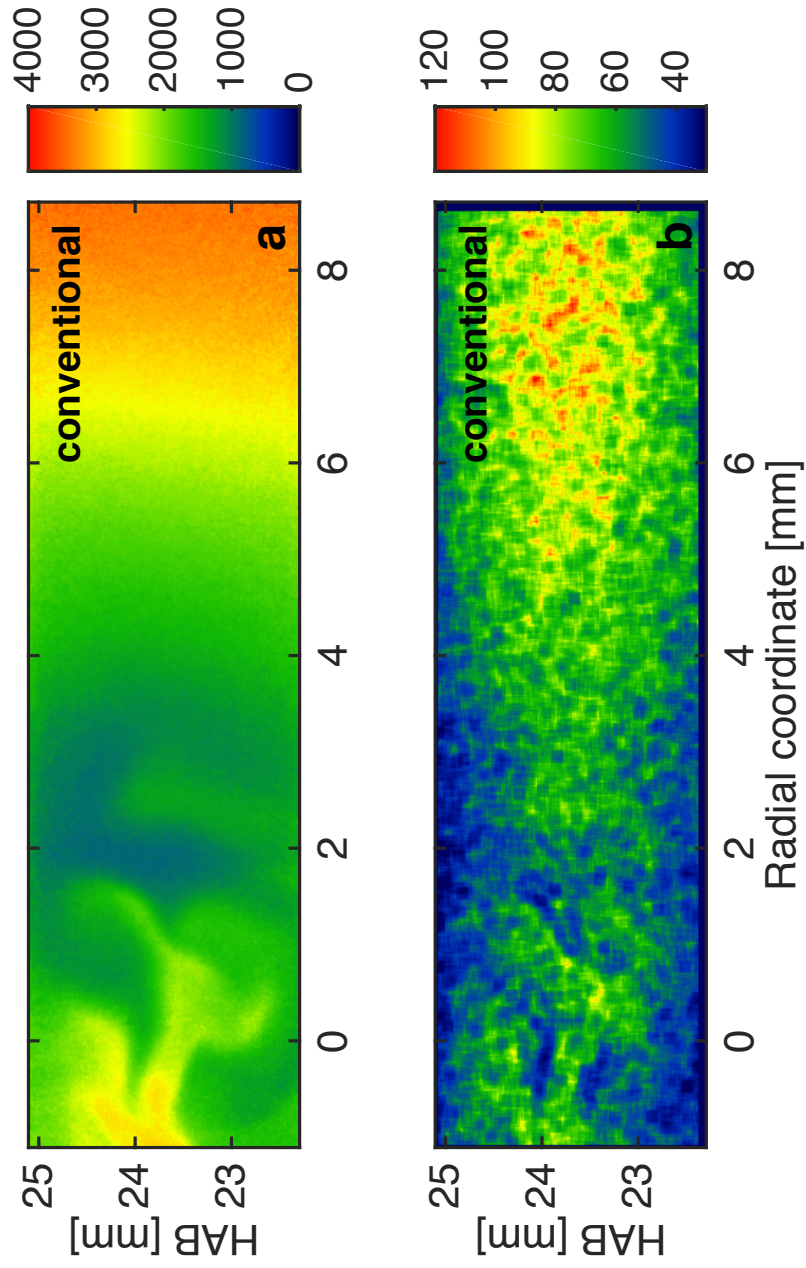


Figure 5.8: (a) Rayleigh signal, in arbitrary units and corrected for laser sheet non-uniformities, and (b) SNR distribution of the conventional Rayleigh images for the turbulent methane/air partially premixed flame ( $Re \sim 4000$ ).

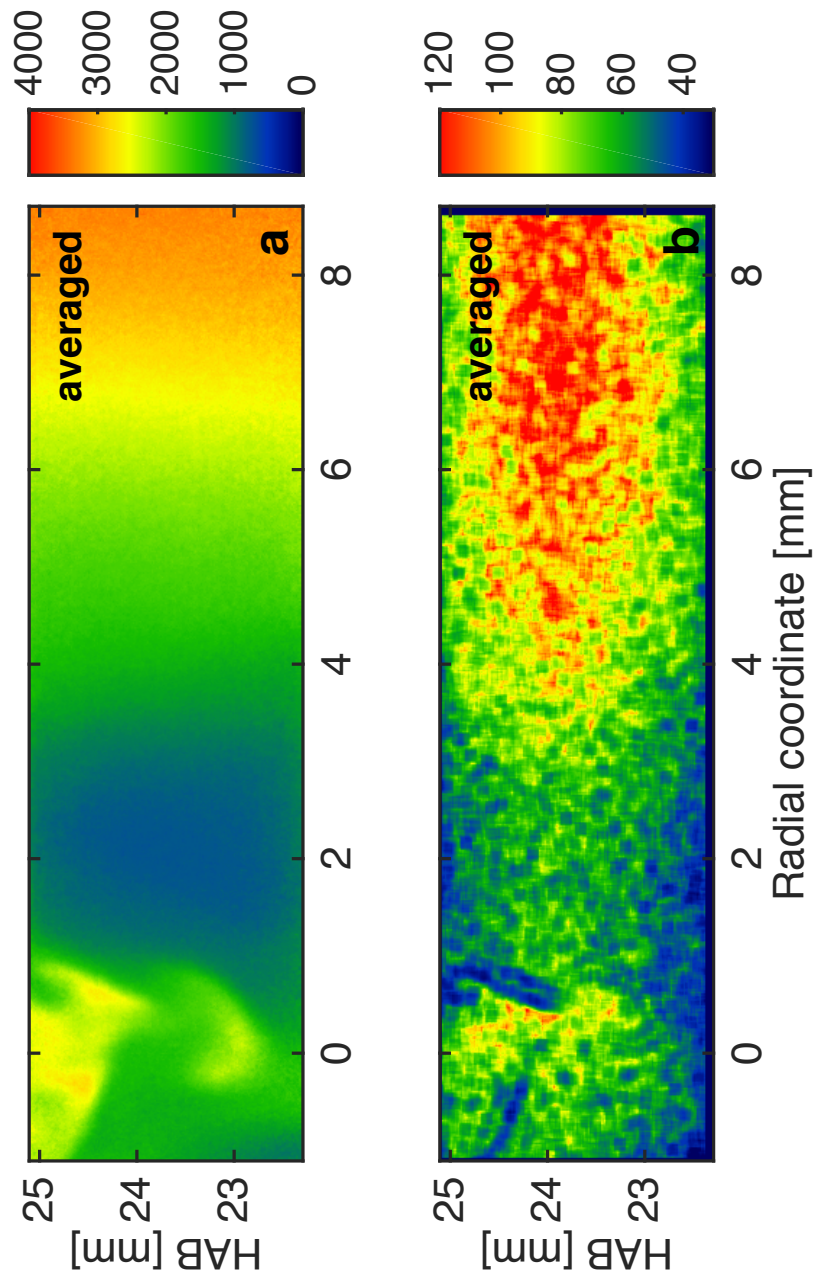


Figure 5.9: (a) Rayleigh signal, in arbitrary units and corrected for laser sheet non-uniformities, and (b) SNR distribution of the averaged Rayleigh images for the turbulent methane/air partially premixed flame ( $Re \sim 4000$ ).

## 5.2 High dynamic range imaging

In this section, an alternative method to enhance the image SNR, based on high dynamic range imaging, is demonstrated on a simplified unsteady flow of Freon-12 injected in air, and the SNR of the reconstructed HDR image compared to that of a conventionally averaged image. This section extends the approach introduced in Chapter 4, from steady combustion systems to unsteady ones, so that it can be implemented to increase the SNR in laser based imaging experiments (in which signals are large enough that image saturation becomes a limitation to the useful dynamic range). The method still relies on the combination of multiple partially saturated images into an unsaturated one [65,66] and experiments involving multiple synchronized lasers and detectors may be good candidates for this approach [94–99]. The flexibility of recently developed pulse burst laser systems [100–103] may also provide enough laser energy that limited detector dynamic range becomes the main experimental limitation. To test the applicability of the concept, planar Rayleigh imaging was taken again as a test case and used to acquire a two-frame sequence of a time-varying non-reacting flow injected in air, so that an HDR image could be computed.

When dealing with HDR imaging, it is important that two main assumptions are satisfied: first, the detector must display excellent linearity and reciprocity under both unsaturated and partially saturated conditions. Second, since multiple images have to be mathematically combined into a single one, the imaged phenomena must be the same, with little or no spatial variation between frames. If this condition is not satisfied, the resulting spatial mismatch will introduce unphysical features in the HDR image. In unsteady flows, the latter condition can be avoided by ensuring that the time separation between the first and last collected image of the HDR sequence is smaller than the characteristic time scale of the phenomenon under study. The linearity of the detector used in this study has already been shown in Section 5.1.2, and for the specific application of HDR imaging to techniques relying on pulsed lasers

for illumination, the camera reciprocity loses importance since each images recorded intensity is not determined by the camera exposure but by the energy of the laser pulse.

### 5.2.1 Experimental setup

The experimental configuration used to test the applicability of HDR imaging to unsteady flows is a variation of the one introduced in Section 5.1.1. It is shown in Fig. 5.10 where two illuminating sheets were generated by two different lasers and sent, from opposite directions, into the probe volume where Rayleigh-scattered light was collected and imaged onto an interline transfer CCD. Unlike the previous set of experiments, no image intensifier was used and the two images necessary for the HDR reconstruction were created by collecting the scattered light from the two separate laser shots.

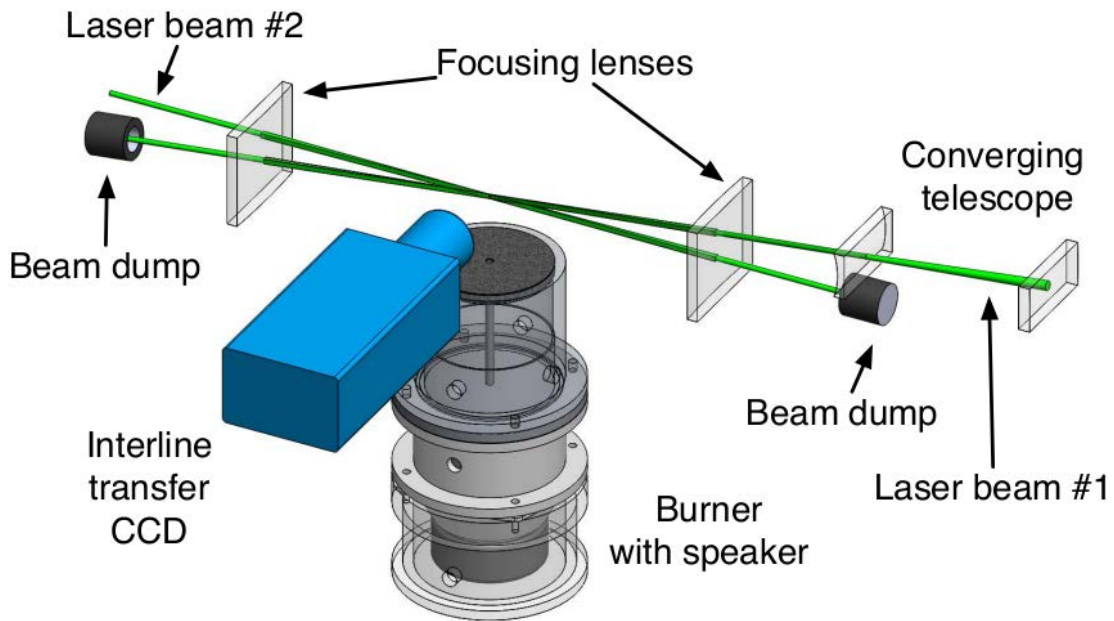


Figure 5.10: Schematic diagram of the experimental set-up used for the HDR planar Rayleigh scattering imaging.

The first image of the two-frame sequence was created by focusing the second harmonic of a Spectra Physics Pro 250 Nd-YAG laser into a sheet (3.3 mm height,  $\sim 35 \mu\text{m}$  FWHM beam waist thickness, 200 mJ/pulse) and sending it through a turbulent jet of dichlorodifluoromethane (Freon-12) injected into an air coflow (4 mm nozzle diameter, 75 mm coflow diameter). The relative Rayleigh cross sections of Freon-12 and air are 20.33 and 0.97, respectively. The average velocities of Freon and air were 22 cm/s and 27 cm/s, respectively and the flow unsteadiness was induced by a sinusoidal forcing generated with a speaker placed in the fuel plenum and driven at 30 Hz with a Stanford Research DS345 function generator (the forced flow was chosen over a turbulent one to allow for a comparison between HDR and conventionally-averaged results). The Rayleigh-scattered light was collected through a pair of Nikkor 50 mm lenses and imaged onto the chip of a Sensicam Interline Transfer CCD using one-to-one magnification. The second image of the sequence was created in a similar fashion with the use of a Continuum Powerlite Nd-YAG laser whose beam was focused into a sheet (6 mm height,  $\sim 140 \mu\text{m}$  FWHM beam waist thickness, 100 mJ/pulse) and sent through the same probe volume defined by the first laser sheet. For both beams, the final focusing was done with 300 mm focal length cylindrical lenses; in addition, the beam of the first laser was sent through a converging telescope to decrease the beam height and increase the fluence. The measurements were performed at a fixed height above the burner centered three diameters downstream; to prevent the laser beams from entering each other's cavities, the first beam was slightly tilted and crossed the probe volume with a 2.5-degree angle. Stanford Research DG535 pulse generators synchronized the lasers and camera. The camera chip was binned 2x2 pixels and the pulse energies were chosen so that the first image saturated the detector in some areas, while the second image used a significant portion of the camera dynamic range without any saturation. The interpulse separation was set to 2.5  $\mu\text{s}$ ; when compared to the average gas velocity, the spatial displacement of the flow structures between

the two collected frames was expected to be  $\sim 0.5 \mu\text{m}$ . This value, given the magnification of the collection optics, was well below the spatial resolution of the imaging system (the length projected onto a binned pixel was equal to  $13.5 \mu\text{m}$ ). While the velocity modulation induced by the speaker was not quantified, the large margin between spatial resolution and spatial shifting ensured that the two acquired frames sampled the same event.

The Rayleigh image post processing was similar to what already described in Section 5.1.1. The only difference involved the image “stripe correction”: before applying it, the first image was rotated by 2.5 degrees in order to align the stripes horizontally; after the correction was completed, the resulting image was rotated back to the initial orientation. Since the rotation algorithm returned a slightly smoothed image, for consistency across the data, the same rotations were applied to the second image as well.

When the image sequence comprises only two frames, as in this case, a simplified version of the algorithm for the computation of an HDR image can be employed. Equation 5.2 shows how the  $i^{\text{th}}$  pixel intensity of the reconstructed HDR image,  $H_i$ , was calculated:

$$H_i = \frac{h_i^L + \left(\frac{h_i^H}{R}\right)}{N_i}. \quad (5.2)$$

Here,  $h_i^L$  is the value of the  $i^{\text{th}}$  pixel in the unsaturated image (low pulse energy),  $h_i^H$  is the value of the partially saturated one (high pulse energy), and  $N_i$  is the number of frames in which the pixel is not saturated (either 1 or 2 in this two-image case). The factor  $R$  accounts for the difference in laser energy between the two frames. In order to be included in the HDR reconstruction,  $h_i^H$ , has to be lower than a certain threshold identifying the detector saturation; in this set of experiments the saturation threshold was chosen to be 80% of the detector full dynamic range to account for eventual pixel blooming effects. In other words, if neither one of the  $i^{\text{th}}$  pixels are saturated, a weighted average is taken; otherwise, only the value of

the unsaturated image is considered. In general, a lower threshold can be set as well to discard pixels whose intensity is close to the background noise and where the SNR is expected to be poor; since in Rayleigh scattering the signal never drops to zero, the lower threshold was not implemented. In conventional HDR imaging, the factor  $R$  is determined by the camera settings and exposure times; when dealing with systems in which the laser pulse is shorter than the minimum camera exposure, the collected luminosity becomes a function only of the laser pulse energy. The factor  $R$  was therefore determined by taking the ratio between average signals evaluated in an interrogation region in both the unsaturated and partially saturated images where the scattered signal was constant. Finally, to account for small shot-to-shot variations and non-uniformities between the two frames, the HDR result was normalized by an image resulting from a two-dimensional smoothing of the ratio between HDR and low dynamic range (LDR) results.

An alternative approach that exploited the capability of the Nd:Yag laser to generate a double pulse, instead of relying on two lasers, was tried with minor success: the implicit tradeoff between the pulses temporal separation and their energy did not allow for a proper implementation of the HDR concept; either the time separation between the turbulent features was too large, or the pulse energy was not enough to reach signal saturation.

### 5.2.2 Results

Figure 5.11a shows the resulting HDR image of the corrected Rayleigh signal with the contour plot highlighting the separation between unsaturated (right) and saturated regions (left) as determined from the raw uncorrected Rayleigh image. The signal-to-noise ratio of the images was evaluated according to the procedure described in Section 5.1.2 and Figs. 5.11b, 5.11c, 5.11d show the SNR distribution for the HDR image, the unsaturated LDR one, as well as that for a conventional two-shot average,

where neither of the two images were saturated.

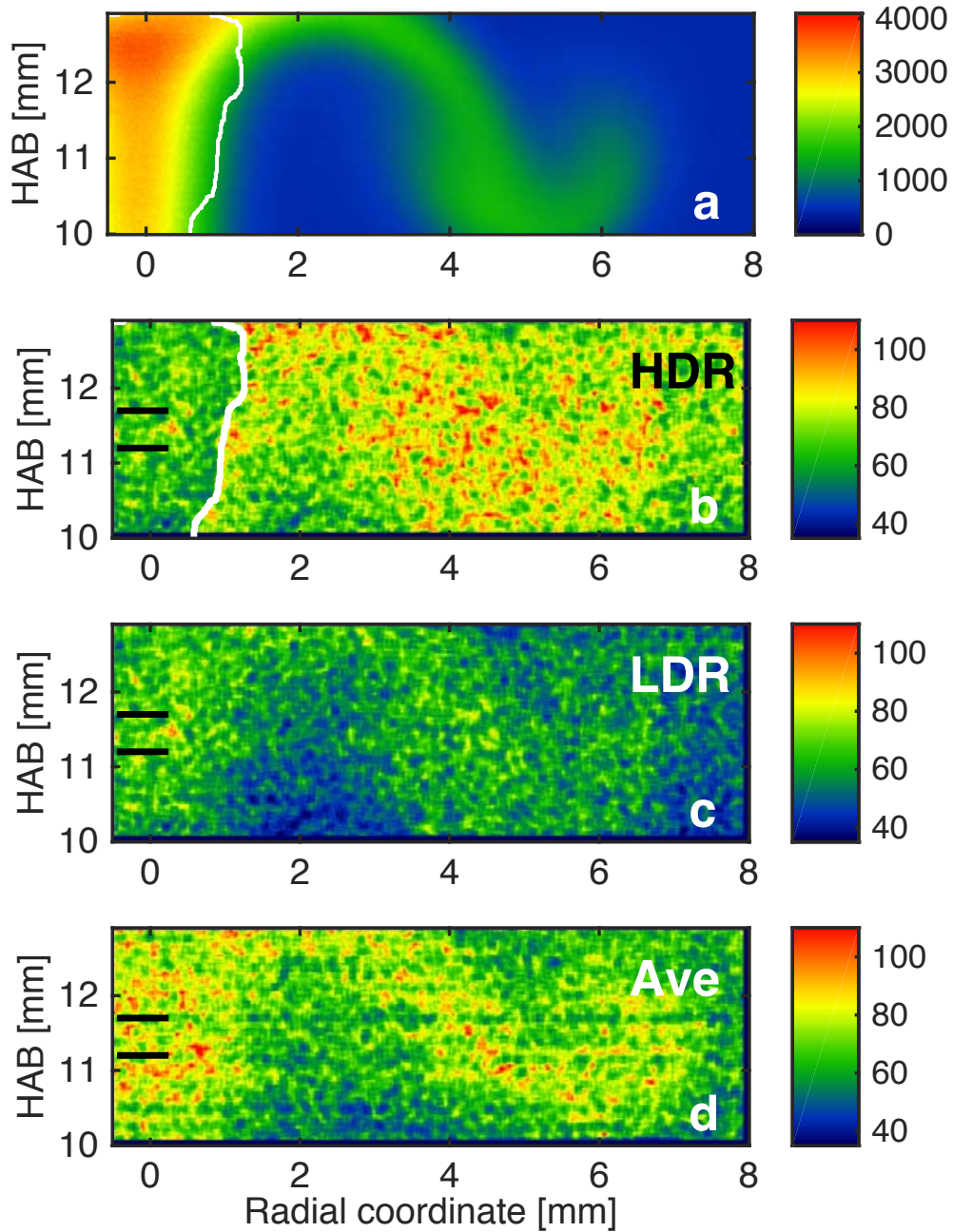


Figure 5.11: (a) HDR image of Rayleigh intensity, in arbitrary units, from a Freon-12 jet injected into air (corrected for laser sheet non uniformities); the white line identifies the separation between the saturated (left) and unsaturated (right) areas of the raw Freon-12 Rayleigh image. (b) SNR distributions for the HDR, (c) LDR, and (d) conventionally-averaged image. The solid black lines define a region over which the axial averaging was performed to plot the curves shown in Fig. 5.12b.

As expected, the SNR distribution of the LDR and conventionally-averaged images depended on the signal intensity, with higher SNR localized in the high pixel count regions. On the other hand, the HDR image returned an overall higher SNR in regions where both exposures contributed to the final image. Furthermore, when both exposures contributed to the HDR image, the SNR in the HDR image was seen to be as good as or better than that obtained with conventional averaging. Predictably, no improvement was possible in the saturated areas where information from just a single image was used. Figure 5.12 clarifies this conclusion by showing a radial plot of the axially averaged Rayleigh counts (Fig. 5.12a) and axially averaged SNR distribution (Fig. 5.12b) over a region defined by the black lines shown in Fig. 5.11. The increase in SNR of the unsaturated region was seen to be  $\sim 35\%$  and  $\sim 15\%$ , when compared to the LDR and conventionally averaged image, respectively.

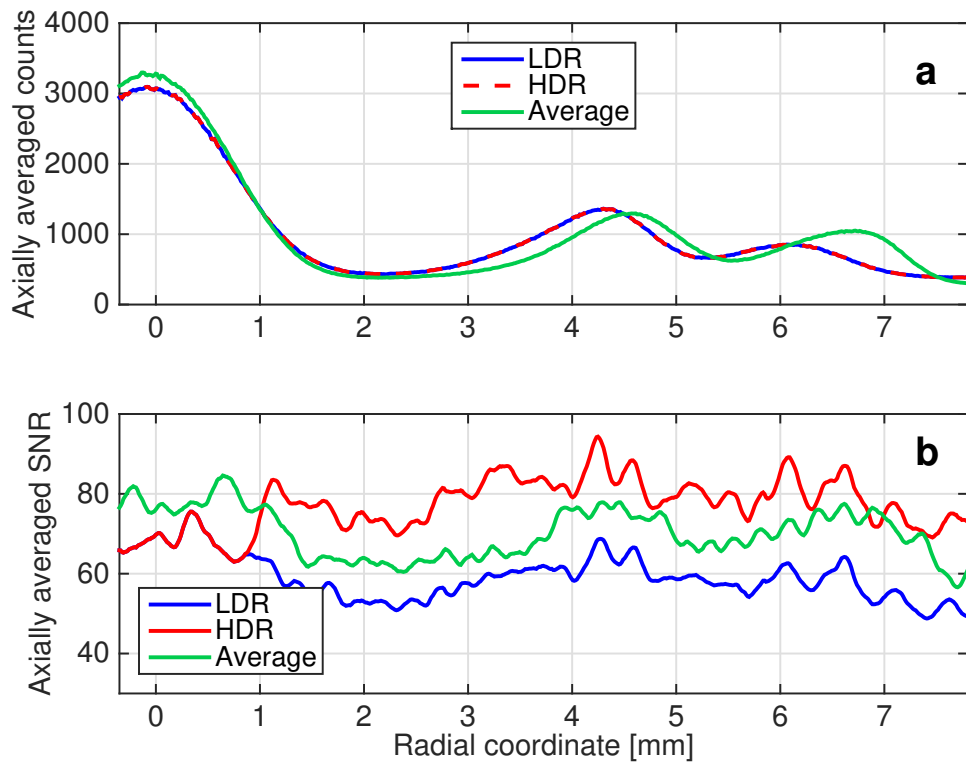


Figure 5.12: (a) Comparison between the axially averaged Rayleigh counts and (b) the axially averaged SNR.

Finally, the verification that the HDR image carried the same quantitative information of the unsaturated one was done by plotting and comparing, pixel by pixel, the HDR image pixels intensity (normalized to the detector full dynamic range) as function of the LDR one, as shown in Fig. 5.13. The result showed excellent agreement, with a linear relation that had an  $R^2$  value of 0.9999, giving confidence in the accuracy of the HDR reconstruction.

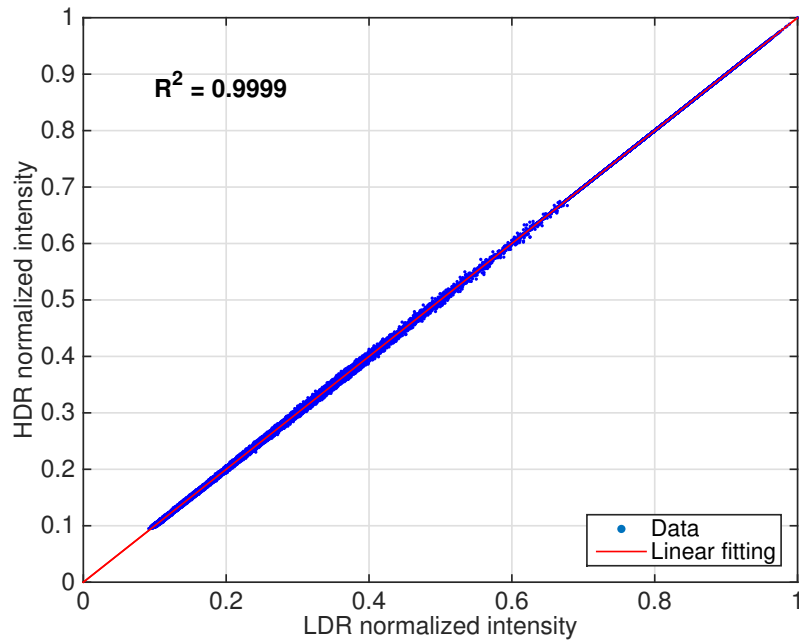


Figure 5.13: HDR normalized pixel intensity as function of the LDR one.

### 5.3 Conclusions

Two approaches to increase the SNR in laser-based turbulent imaging experiments were demonstrated in reactive and non-reactive flows with the acquisition of planar Rayleigh scattering images. First, the averaged Rayleigh method was tested on steady and turbulent partially premixed methane/air flames, and it was shown that, by suitably timing the double exposure of an interline transfer CCD camera with respect to the light emitted by the phosphor screen of an image intensifier, the intensifier

output light could be equally distributed over the two frames of the detector so that an averaged image could be calculated. A linearity analysis was performed on both detector and intensifier and no differences in response between the two frames could be observed when the camera was used in double-frame mode. For a given signal, the SNR fall-off of the intensifier occurred above 7.5 V and for this reason the measurements shown in this chapter were done with gains between 6.5 V and 7 V. To avoid uncertainties associated with the randomness of turbulent features, the approach was initially tested on a steady partially premixed methane/air flame: the comparison between conventional and averaged Rayleigh results showed that the SNR of the latter was 30% higher than the former. The extension of the technique to a turbulent flame confirmed the same SNR increase.

The second approach proposed the use of the high dynamic range imaging technique and it showed how HDR imaging could be extended and applied to time varying/unsteady systems. Planar Rayleigh scattering was used to acquire a two-frame sequence of an unsteady jet of Freon-12 injected in air so that an HDR image could be reconstructed. The results showed that the quantitative information carried by the HDR image was the same as the LDR one while providing a SNR  $\sim 15\%$  higher than the one obtained with conventional averaging.

The selection of one method over the other would depend mainly on the specific experimental set-up. The averaged Rayleigh approach could be quickly applied to imaging systems already equipped with intensifiers and interline transfer CCDs, after the verification of the linearity of both components. Despite its higher complexity (in terms of required equipment), the HDR approach could similarly be adapted to those systems already predisposed to accommodate its hardware requirements. Depending on the number of images used for the HDR reconstruction, as well as the level of partial saturation, SNR improvements higher than the ones presented here are likely to be expected.

# Chapter 6

## Measurements of $CH^*$ concentration in microgravity and normal gravity laminar coflow diffusion flames

In combustion systems, the prospect of using information from chemiluminescence of electronically excited species, such as  $OH$  or  $CH$  (denoted as  $OH^*$  and  $CH^*$ , respectively) has a great appeal because of the non-intrusiveness and the simplicity of their measurement. Among the relevant combustion quantities that can be monitored in flames, the heat release rate is recognized as critical, especially in modern turbulent combustors, given its relevance to the prediction of possible unsteady combustion behavior [104–106]. For this reason, several studies have investigated the capability of chemiluminescence of being an effective marker for the total and/or local flame heat release rate, particularly in turbulent flames. In such cases, the combustion systems are so complex that the spatial distribution of relevant quantities cannot be easily determined, and the possibility of extracting useful information from a total

integrated chemiluminescence becomes valuable.

A number of studies have focused on the ability of  $OH^*$  and  $CH^*$  chemiluminescent emissions (around 308 nm and 431 nm) to provide insight on the heat release in premixed turbulent flames [25–27, 107]; because of possible complications related to broadband soot emission and its interference with the radical spectral emission regions, steady diffusion flames have not been investigated as extensively [108]. Numerical studies of non-premixed strained flames have shown how  $OH^*$  and  $CH^*$  have the potential to be used as heat release rate markers [28]. A recent work by Hossain and Nakamura [29] extended the study on counterflow diffusion flames while providing an excellent summary of the major investigations done so far. The main conclusion of their review was that, for premixed flames, the results are contradictory, and there is no unique conclusion about the ability of either  $OH^*$  or  $CH^*$  to predict local or total flame heat release. Moreover, the limited examination of diffusion flames indicates that more study is required for these specific cases.

In this chapter, the study of chemiluminescence and its correlation with flame heat release rate was extended to the specific case of nitrogen-diluted methane laminar coflow diffusion flames under microgravity and normal gravity conditions. Specifically, the use of a commercial DSLR camera was investigated as a way to measure and quantify  $CH^*$  concentration, while numerical simulations of the considered diffusion flames allowed for an evaluation and comparison with the local and total flame heat release rates. The experimental data considered in this chapter is part of the NASA SLICE (Structure and Liftoff in Combustion Experiments) database, which comprises images of nitrogen-diluted laminar coflow diffusion flames collected during the campaign conducted on board the International Space Station (ISS) in 2012 [109], as well as their normal-gravity equivalents collected in a ground copy of the ISS flight hardware. The fact that micro- and normal gravity laminar coflow diffusion flames that share the same exit flow conditions behave quite differently allowed for a more

comprehensive study with diverse cases. The quantification of the two-dimensional  $CH^*$  concentration for both the microgravity and normal gravity diffusion flames, as well as its comparison with the numerical simulations, allowed us to conclude that the integrated absolute  $CH^*$  concentration in a cross section was a good indicator for the total flame heat release rate, and that the two-dimensional  $CH^*$  concentration distribution was a good marker to spatially identify the local heat release rate, albeit with differences in both intensity and gradients. Additionally, since the SLICE raw data has been recently available for the entire scientific community to study through the NASA Physical Sciences Informatics System [110], this chapter summarizes how to best process it and extract quantitative information regarding absolute  $CH^*$  concentration.

## 6.1 Experimental setup

Details regarding the experimental setup used for the acquisition of the SLICE flame images have been presented in [68]. A DSLR color camera (Nikon D300s , 4288 by 2848 pixels, capable of exporting 14-bit lossless raw data files) was used to acquire images of coflow laminar diffusion flames under various operating conditions (flow rates, fuel types, fuel nozzle sizes, gravity). A 2 mm blue-green color BG7 filter was added to the setup to balance the red, green, and blue (RGB) signals of the detector and account for the red-dominated emission from soot incandescence. A schematic of the SLICE coflow burner is shown in Fig. 6.1. The fuel tube was enclosed in a 76 mm by 76 mm square duct, which is 174 mm tall, allowing multiple fuel nozzles to be interchanged, with diameters varying from 0.4 mm to 3.2 mm I.D. The fuel flow rate was controlled using a mass flow controller, while the air coflow was induced by an electric fan placed at the bottom of the burner; a ceramic honeycomb and wire mesh were added to straighten the air velocity profile.

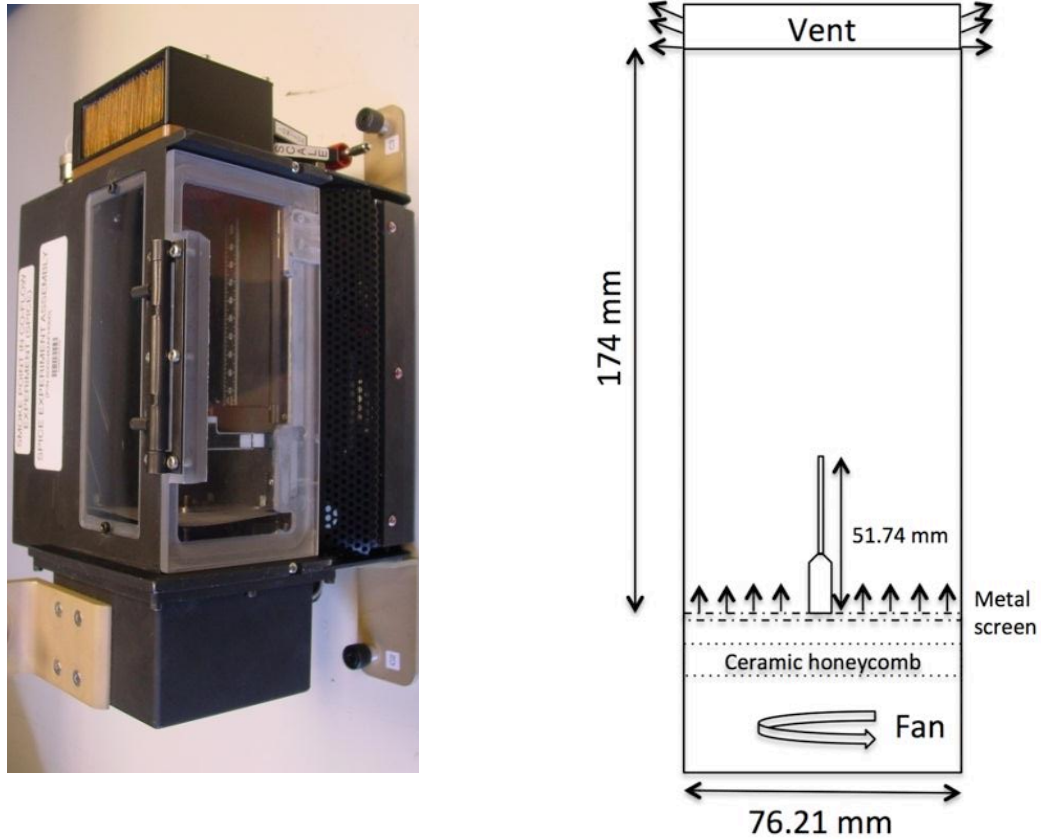


Figure 6.1: Photograph (left) and schematic representation (right) of the SLICE coflow burner.

The ground copy of the flight hardware was used to provide a calibration for both fuel and air velocities. However, despite being a close copy of the apparatus aboard the space station, minor differences in flow velocities between the microgravity and normal gravity units could not be ruled out. Although the microgravity database contains tests for a variety of fuels (methane, ethylene, propane, and ethane with varying nitrogen dilution), the results of this chapter focus on a subset of the nitrogen-diluted methane flames. The cases considered are summarized in Table 6.1.

Sequence	Fuel [by volume]	Nozzle [mm]	Fuel velocity [cm/s]	Coflow velocity [cm/s]	Exposure bracketing [s]	Lens <i>f</i> -number
A	40% $CH_4$ , 60% $N_2$	3.2	17-89	17	[1/15, 1/40, 1/25, 1/10, 1/6]	#2
B	70% $CH_4$ , 30% $N_2$	0.8	180-460	17	[1/40, 1/100, 1/60, 1/25, 1/15]	#2
C	70% $CH_4$ , 30% $N_2$	1.6	62	14-34	[1/10, 1/25, 1/15, 1/6, 1/4]	#4

Table 6.1: Summary of the flow conditions and camera settings of the normal gravity and microgravity image sequences considered in this chapter.

These configurations and velocity ranges were selected for several reasons. First, the flames are predominantly “blue”, with a faint sooty tip that develops only at the highest fuel velocity conditions. Second, numerical simulations of these flames are available, which contain relevant chemical species and temperature. Third, flow conditions are such that either the fuel or the coflow are varied. Finally, depending on the flow condition and gravity level, the flames show either an attached or lifted structure, and significantly vary in shape and structure.

As part of the SLICE acquisition procedure, flame images were taken employing bracketing sequences with varying exposure times to account for the fact that the optimal camera exposure time was unknown. This broad sampling was used to ensure that at least one of the images in the bracketing sequence was not saturated. The saturation problem was not encountered with the non-sooty flames analyzed in this work, but the reciprocity analysis performed on the detector (see Chapter 4 and [89]) allowed the use and the averaging of the information contained in each image of the bracketing sequence, thus enhancing the overall signal-to-noise ratio.

Both  $CH^*$  and  $OH^*$  are recognized chemiluminescent species for flame diagnostics. Unlike  $CH^*$ , however, the  $OH^*$  radical emits in the ultra-violet, and its measurement requires both a specific UV-sensitive detector and collection optics to isolate the emission peak around 308 nm. On the other hand,  $CH^*$  emits in the blue region, making its measurement simpler because of the larger availability of suitable detectors. The SLICE camera was sensitive in the visible range; therefore, only the collection of

$CH^*$  emission was possible and its quantification performed.

The Nikon D300s camera's CMOS detector was spectrally characterized, and it was seen that the signal collected by the blue channel was representative of the  $CH^*$  chemiluminescence around 431 nm. Experimentally, one of the most common procedures to isolate and collect the chemiluminescence of a radical species relies on the use of a narrowband interference filter. However, as seen in Fig. 6.2, a comparison between the normalized two-dimensional chemiluminescence collected through a Melles Griot interference filter (430 nm central wavelength, 10 nm FWHM) and the two-dimensional chemiluminescence recorded by the Nikon blue channel through the color BG filter showed how the two results matched reasonably well, both spatially and in intensity distribution.

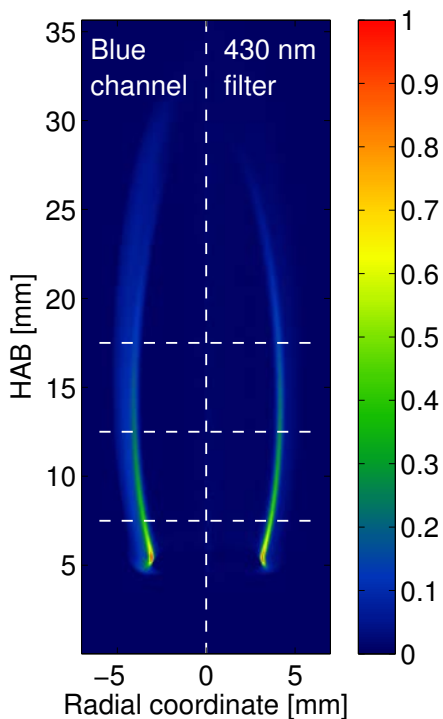


Figure 6.2: Two-dimensional chemiluminescence intensity comparison between Nikon D300s blue channel (left half) and 430 nm interference filter signal (right half). Each chemiluminescent signal was normalized with respect to its maximum. The horizontal dashed lines are axial locations that are the focus of analysis in Section 6.2.

For this comparison, one of the Yale target nitrogen-diluted laminar coflow methane flame was considered [111] (65%  $CH_4$ , 35%  $N_2$  by volume, velocity of 35 cm/s for both fuel and oxidizer, 4 mm I.D. fuel nozzle, and 50 mm I.D. coflow), and the two-dimensional chemiluminescence was obtained from the line-of-sight luminosity using an Abel deconvolution. The horizontal dashed lines identify specific axial locations that will be the focus of analysis in Section 6.2; the halo that can be seen on the oxidizer side in the blue channel chemiluminescence signal will be discussed in Section 6.2 as well. In Fig. 6.3, the normalized transmissivities of the blue and 430 nm interference filters are compared to the spectral location of relevant chemiluminescent species. The measured spectrum was obtained from the reference nitrogen-diluted 65% methane flame (at 7.5 mm above the burner and 4 mm from the centerline), while the simulated one was derived using the molecular software LIFBASE [31] assuming a temperature of 1900 K, as explained in Sections 6.2 and 6.4. Because of the relative position of the  $CH^*$  emission with respect to the blue channel's spectral response, the interference filter signal displayed in Fig. 6.2 was evaluated considering only the contribution from the blue pixels, too. The transmissivity curve of the camera's blue channel was obtained following a spectral characterization of the detector (as outlined in [12]), while the interference filter's transmissivity was measured with a Hitachi U-2001 spectrophotometer.

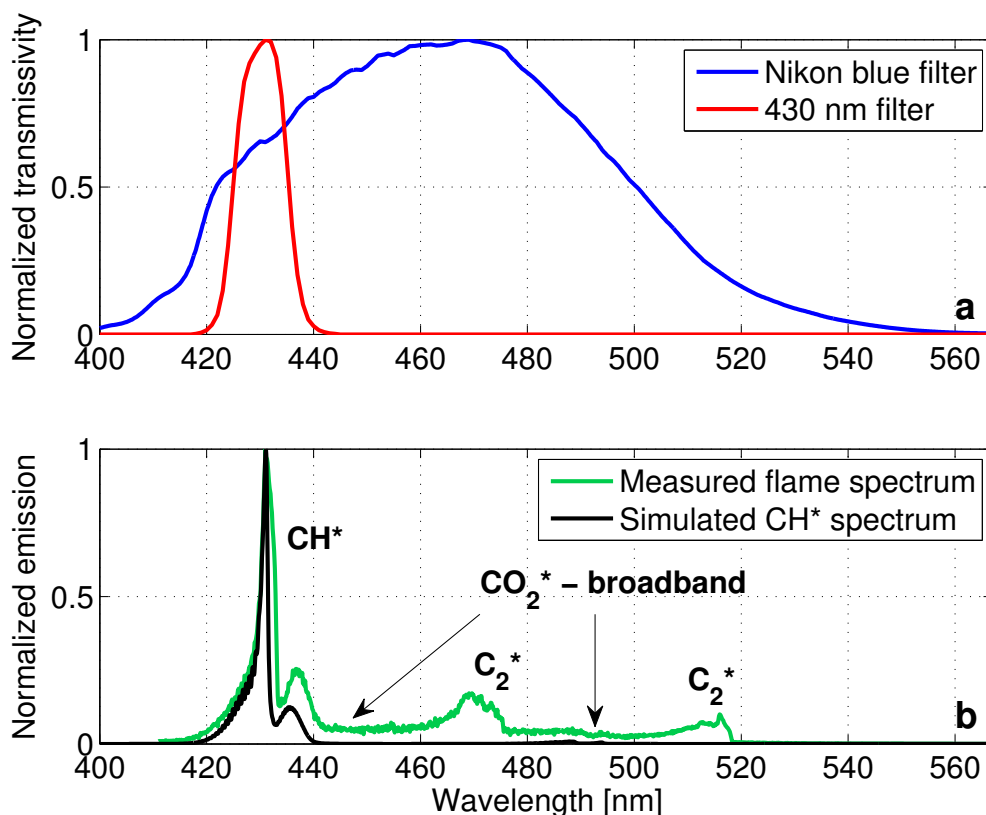


Figure 6.3: (a) Spectral transmissivity of the Nikon D300s blue channel and a 430 nm interference filter, each normalized with respect to its maximum. (b) Normalized flame and simulated  $CH^*$  spectrum showing the spectral location of relevant flame emitting species.

## 6.2 Imaging and spectral considerations

In flames that have an axisymmetric structure, such as the ones that were considered here, a two-dimensional intensity distribution is obtained from the line-of-sight emission through the implementation of an Abel deconvolution (Section 2.2.1). This operation relies on the assumption that the collected light rays are parallel. However, it was shown that, for a given distance between the light source and the collection optics, the smaller the lens  $f$ -number, the weaker the parallel ray hypothesis becomes [112]. As a consequence, the reconstructed two-dimensional intensity profile gets artificially broadened (radially), and the peak radial intensity is underestimated.

The sequence in Fig. 6.4 exemplifies the broadening by comparing the normalized two-dimensional chemiluminescence when obtained by Abel inverting images taken with varying  $f$ -numbers (of the reference nitrogen-diluted 65% methane flame). In order to maximize signal levels while minimizing exposure time (thus minimizing fuel consumption), the SLICE images were collected using a relatively open  $f$ -number of either 2 or 4. The effect of this choice will become apparent in Section 6.5 when comparing the experimental data (which were relatively broadened) and numerical results (which had high spatial resolution).

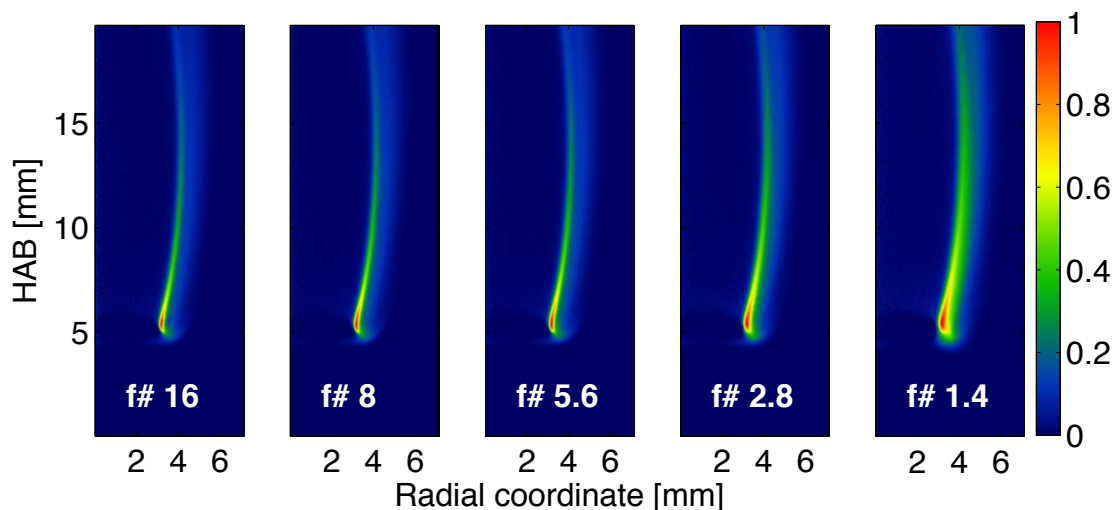


Figure 6.4: Influence of lens  $f$ -number on the Abel-inverted two-dimensional chemiluminescence of the reference nitrogen-diluted 65% methane flame. Each image was normalized with respect to its maximum value.

For the accuracy of the quantitative measurements, it is essential that the collected chemiluminescence was related only to the radical species of interest without any contribution from other emitting species. When a narrowband interference filter is used, this condition is typically satisfied. On the other hand, as shown in Fig. 6.3, the use of a broadband blue filter will likely collect light emitted from additional species such as  $C_2^*$  and broadband  $CO_2^*$  [113]. A spectroscopic measurement of the emission of the nitrogen-diluted flame introduced in Fig. 6.2 was therefore performed to assess

the presence and the contribution of these emitting species on the final collected signal. The flame chemiluminescence at three different heights above the burner (7.5, 12.5 and 17.5 mm - see the dashed lines in Fig. 6.2) was collected with the use of a Nikon 50 mm lens ( $f$ -number 16) and was focused on the entrance slit of a Jobin Yvon CP200 imaging spectrometer (100  $\mu\text{m}$  slit, 200 grooves/mm); the spectrum was then imaged on the chip of a cooled SBIG STF-8300M CCD camera (3 minutes exposure). The distance between flame and focusing lens was a compromise between a reasonable projected radial length (42 pixel/mm) and the satisfaction of the parallel rays collection assumption. To allow a comparison with the signal collected by the DSLR camera, the collected spectrum was corrected for the spectrometer spectral throughput and detector spectral sensitivity, as well as for the Nikon blue filter and BG color filter spectral transmissivities. Finally, an Abel inversion was performed to obtain a spectrally resolved radial distribution.

The result of the acquisition, at 7.5 mm above the burner, is shown in Fig. 6.5a. The horizontal axis refers to the radial coordinate (with 0 being the flame centerline), while the vertical axis refers to the emitted light's wavelength. The labels highlight the major emitting species that are present in the blue filter spectral range ( $CH^*$ ,  $C_2^*$ ,  $CO_2^*$ ). The measured spectrum shown in Fig. 6.3b was obtained by plotting a cross section of the two-dimensional spectrum of Fig. 6.5a at a radial distance of 4 mm. The white lines demarcate the FWHM spectral width of the 430 nm interference filter, while the Nikon blue filter covers the entire displayed spectral range, as seen in Fig. 6.3a.

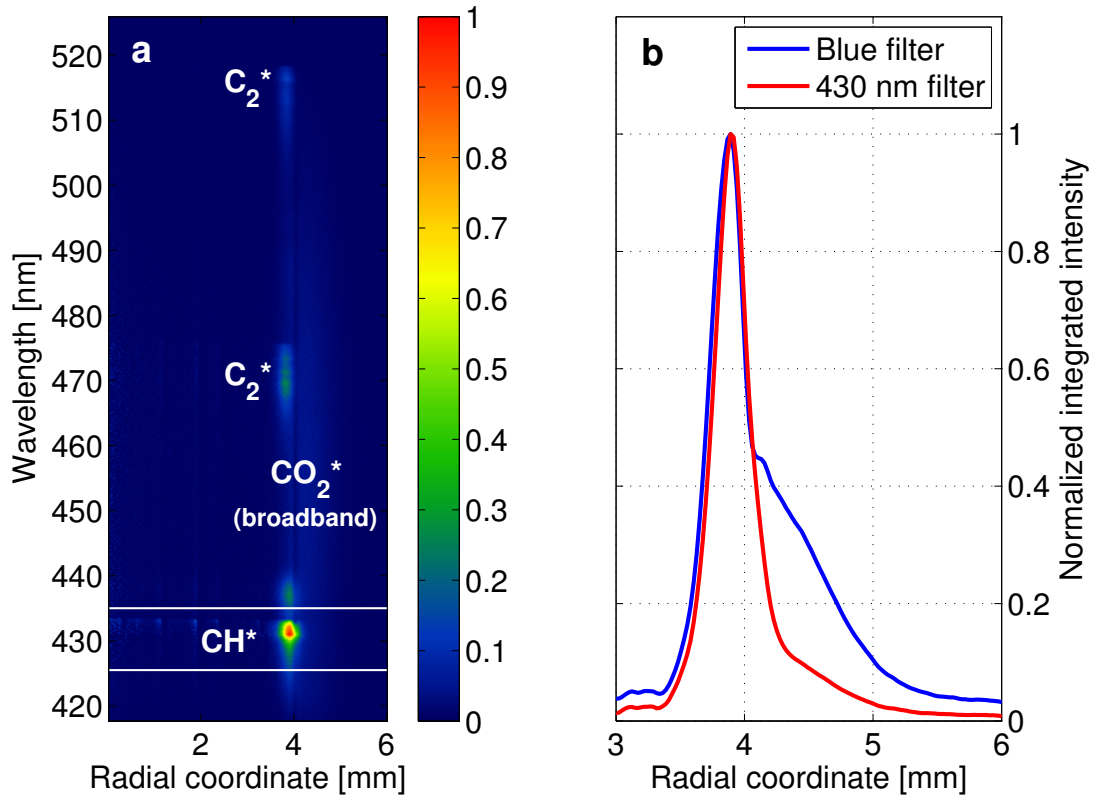


Figure 6.5: (a) Flame spectrum, normalized to the maximum, as a function of the radial coordinate (7.5 mm above the burner) for the reference nitrogen-diluted 65% methane flame introduced in Section 6.1. (b) Radial chemiluminescence profiles, normalized with respect to their maximum values, obtained by integrating over the spectral regions of the 430 nm and blue filters.

Figure 6.5b shows the normalized radial profile of the flame chemiluminescence (zoomed in around 4 mm from the flame centerline). The two curves, red and blue, were obtained by spectrally integrating over the 430 nm filter and blue filter spectral regions of Fig. 6.5a, respectively. It can be seen that the integration over the entire range, because of the contribution from  $C_2^*$  and  $CO_2^*$  (whose radial extension is wider than the  $CH^*$  one), yields a radial profile that broadens towards the oxidizer side. Therefore, the halo that can be observed in the chemiluminescence profile, when obtained from the blue channel (Fig. 6.2 left half), can be explained by the presence of the aforementioned emitting species. With the current spectroscopic imaging setup,

the radial displacement between  $C_2^*$  and  $CH^*$  peaks was measured to be 1 pixel ( $\sim 24 \mu\text{m}$ , given the system magnification), with  $CH^*$  positioned on the oxidizer side, with respect to  $C_2^*$ . When  $C_2^*$  is spectrally integrated with  $CH^*$ , as is the case of the blue channel acquisition, the radial distance of the peak  $CH^*$  from the centerline is expected to be underestimated. However, given the projected length of the SLICE imaging setup ( $\sim 17 \text{ pixel/mm}$ ), discerning the difference would require sub-pixel resolution, and the effect can be considered negligible.

When compared to just the  $CH^*$  emission, the additional light emitted by  $C_2^*$  and  $CO_2^*$  will increase the recorded counts causing, if not corrected, an overestimation of the actual  $CH^*$  signal. To evaluate the relative influence of  $C_2^*$  and  $CO_2^*$  emission on the  $CH^*$  signal, a comparison was done to show the differences in the peak recorded counts in the reconstructed radial profiles when the chemiluminescence was collected either through the Nikon blue channel or the 430 nm interference filter. Figure 6.6 shows such comparison for the three selected heights above the burner (HAB) highlighted in Fig. 6.2. Here the 430 nm filter signal was corrected to account for the partial transmissivity of the interference filter.

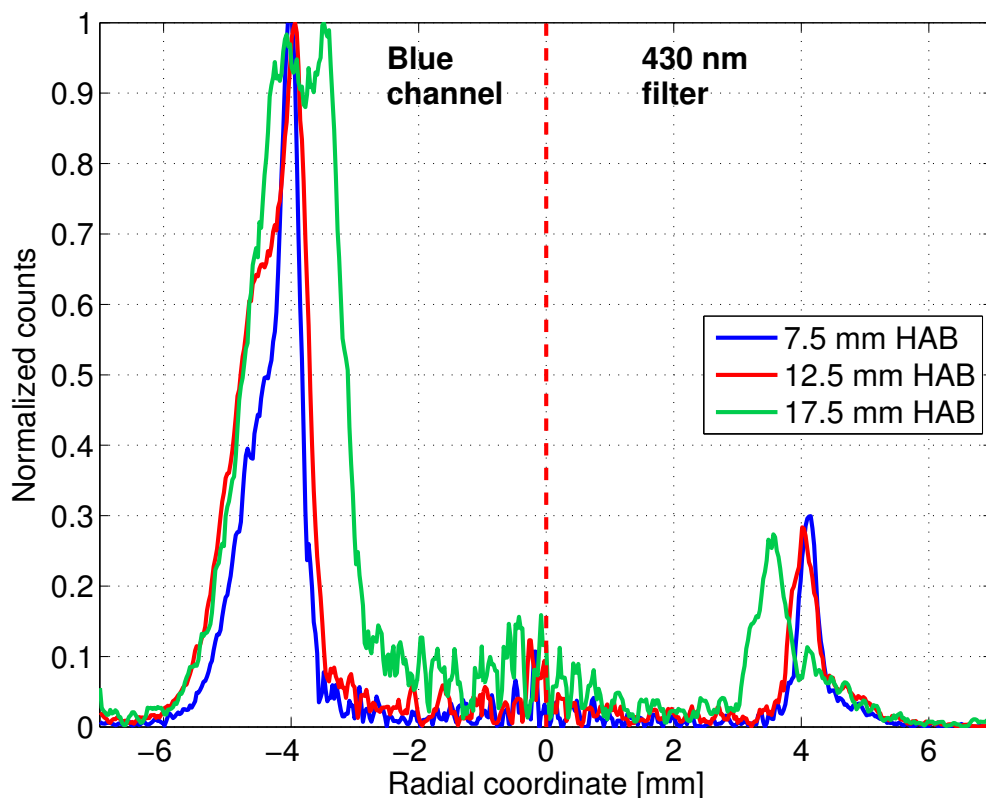


Figure 6.6: Comparison between the radial chemiluminescence, as collected by the blue channel (left half), and 430 nm interference filter (right half). The three curves identify the axial locations defined in Fig. 6.2, and each is normalized with respect to its maximum.

From Fig. 6.6 it can be seen that, for this specific flame, the  $CH^*$  peak intensity, when the signal was evaluated considering only the blue channel, could be overestimated by a factor of  $\sim 3.3$ . This difference seemed weakly dependent on the axial position. Therefore, in the following sections, where a quantification of the absolute  $CH^*$  concentration will be performed, this factor will be taken into account. Furthermore, the same correction will be applied to the SLICE nitrogen-diluted methane flames under the assumption that, because of the similarity of the chemistry involved, the flames have the same spectral characteristic displayed by the reference flame.

### 6.3 SLICE computational model

A description of the numerical simulations for SLICE nitrogen-diluted methane flames is presented in [68] and is based on the MC-Smooth vorticity-velocity formulation of the governing equations [114]. In the physical model, the chemically reactive mixture was treated as Newtonian with diffusion assumed as Fickian. The gas-phase chemistry was described with 42 species and 250 reactions, and it was based on the GRI 3.0 mechanism [115] with all the nitrogen-containing species removed, except  $N_2$ ; it included  $CH$ , but did not include the radical species  $CH^*$ . The axisymmetric structure of the flames allowed the implementation of a two-dimensional computational domain with boundary conditions chosen to match the experimental ones. The computational domain extended 4.29 cm in the radial direction and 12.20 cm in the axial direction, and it was spanned by a nonuniform tensor-product grid containing 167 x 289 points. The governing equations were discretized on this grid using a nine-point computational stencil. The resulting strongly coupled, highly nonlinear equations were solved simultaneously using a damped, modified Newtons method [116] with a nested Bi-CGSTAB linear solver [117].

### 6.4 $CH^*$ concentration diagnostics

The quantitative  $CH^*$  concentration measurements shown in this chapter have their basis in the approach presented in [111]. The  $CH^*$  chemiluminescence deriving from the  $A^2\Delta \rightarrow X^2\Pi$  transition was imaged onto the detector, and an Abel deconvolution of the blue signal was performed to obtain the two-dimensional  $CH^*$  emission from the line-of-sight flame luminosity. The  $CH^*$  emission  $S_{em}$  collected by the detector can be expressed as in Eq. 6.1, already introduced in Section 2.2.4 [30]:

$$S_{em} = \frac{1}{4\pi} A_{21} \tau V_{em} N^* K. \quad (6.1)$$

Here,  $A_{21}$  is the Einstein A coefficient ( $1.86 \cdot 10^6$  1/s),  $\tau$  is the detectors exposure time,  $V_{em}$  is the pixel volume,  $N^*$  is the number density of the excited species, and  $K$  is a constant that accounts for the solid collection angle and detector efficiency. For the determination of the calibration constant, the SLICE setup relied on a 100  $\mu\text{m}$  SiC fiber to be used as an absolute light calibration source; the fiber was heated with a non-sooty flame and its emitted radiation was imaged with the camera. The known fiber spectral emissivity, as well as the known camera spectral response, enabled the evaluation of the fiber temperature using the color ratio pyrometry approach [12]. In addition, the simulation of the fiber intensity of radiation collected by the blue channel at the measured fiber temperature,  $T$ , was obtained by employing Planck's law. The ratio between the measured signal and the simulated one provided a value for the intensity calibration, as shown in Eq. 6.2:

$$K = \frac{B}{\tau \int_{\lambda_1}^{\lambda_2} \eta_B(\lambda) \epsilon(\lambda) I_{BB}(\lambda, T) d\lambda} \cdot C \cdot \gamma_{CH}. \quad (6.2)$$

Here  $\eta_B$  accounts for the spectral transmissivity of the detectors blue channel as well as the color BG filter,  $\epsilon$  is the fiber emissivity (assumed to be constant = 0.88), and  $I_{BB}$  is the blackbody radiation at the measured temperature  $T$ . The quantities  $\lambda_1$  and  $\lambda_2$  identify the detectors detection wavelength range (400 to 700 nm), while  $B$  is the SiC fiber signal collected by the detector as obtained from a vertical addition and horizontal averaging of the blue pixel counts in a region where the axial fiber intensity can be considered constant. The constant  $C$  accounted for the fact that the recorded signal is not due to the  $CH^*$  emission alone, but other emitting species may contribute to the measured counts. Finally,  $\gamma_{CH}$  is the transmitted energy of a photon in the blue channel, as is defined in Eq. 6.3:

$$\gamma_{CH} = \int_{\lambda_1}^{\lambda_2} \eta_B(\lambda) \cdot \frac{hc}{\lambda} \cdot CH_{em}(\lambda) d\lambda. \quad (6.3)$$

Here  $h$  is Planck’s constant,  $c$  is the speed of light, and  $CH_{em}$  is the normalized  $CH^*$  spectral emission (see Fig. 6.3b). The latter was numerically obtained using the molecular software LIFBASE [31] while assuming a temperature of 1900 K (as suggested by the flame front temperature obtained from numerical simulations of the flames). Despite assuming a constant temperature for every pixel in which  $CH^*$  emission is present, a sensitivity analysis showed that the calibration constant was not sensitive to variations of  $CH^*$  emission spectra evaluated in a range of a few hundred Kelvins; as can be seen in Fig 6.7, the peak  $CH^*$  concentration varied less than  $\sim 0.05\%$  .

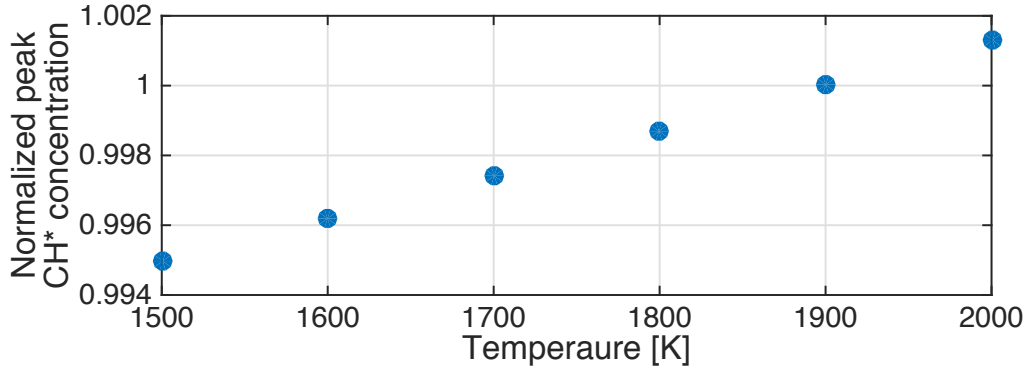


Figure 6.7: Variation of the normalized peak  $CH^*$  concentration when evaluating  $CH_{em}$  in the range 1500 K - 2000 K.

In cases where the flame tip becomes partially sooty, the blue channel will start collecting signal from soot incandescence. Despite being red-shifted, the soot emission overlaps with the blue channel, and its magnitude varies depending on the soot temperature. Because of the previous assumption that the blue channel is representative only of the  $CH^*$  chemiluminescence, the additional luminosity caused by soot will result in a corruption of the real  $CH^*$  signal. Figure 6.8a shows an example of the normalized blue channel of a partially sooty microgravity flame (Table 6.1, sequence A - 40%  $CH_4$ , 60%  $N_2$ , coflow velocity of 17 cm/s, fuel velocity of 89 cm/s),

in which the signal along the flame wing is due to  $CH^*$  chemiluminescence, while the tip luminosity is mainly due to soot emission.

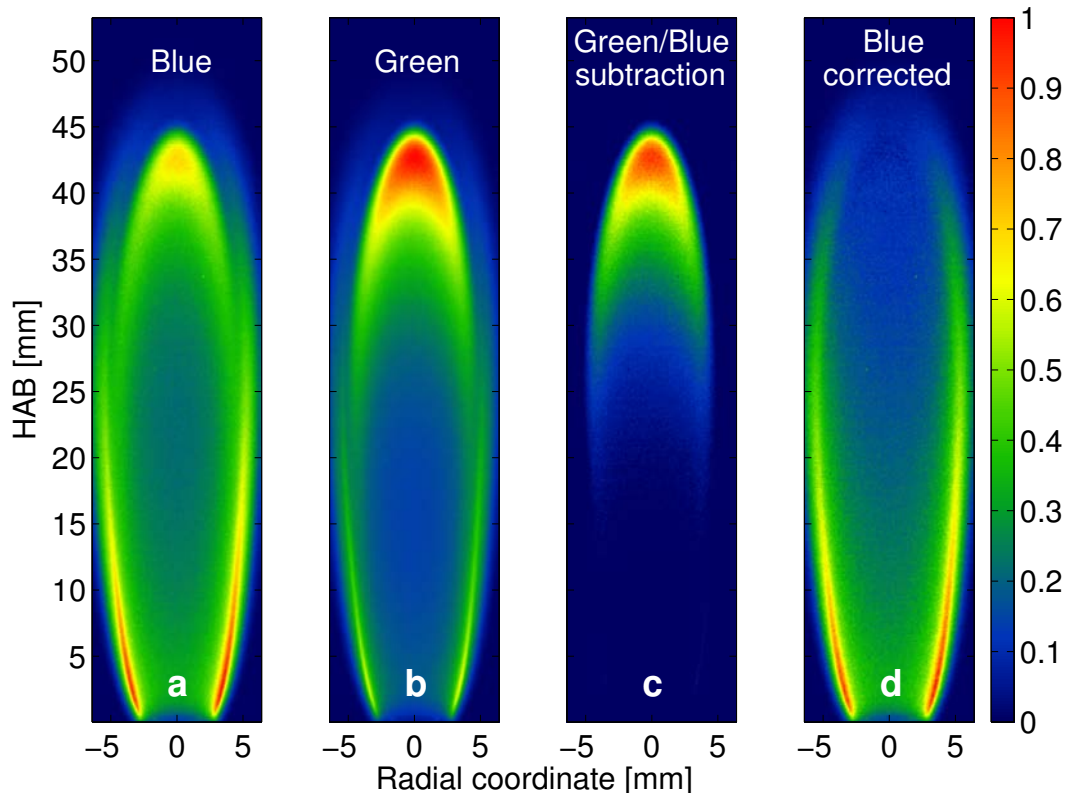


Figure 6.8: Line-of-sight luminosity of a representative microgravity partially sooty flame (40%  $CH_4$ , 60%  $N_2$ , 17 cm/s and 89 cm/s for coflow and fuel velocity, respectively) as collected by the (a) blue and (b) green channels. (c) Soot luminosity as determined by the subtraction between the green and blue channels. (d) Flames blue signal free of soot interference. Each image was normalized with respect to its maximum.

A method to perform a correction for the visualization of  $CH^*$  in sooty flames has previously been presented and relies on the combination of signals collected through multiple interference filters centered around 420, 430, and 440 nm [118]. The entirety of the SLICE data, however, was collected using just a DSLR camera coupled to a broadband color filter, without the use of any interference filters. An alternative approach was therefore implemented to deal with soot interference subtraction, a method that relied on information from just the blue and green channels.

1. The blue and green signals (Figs. 6.8a and 6.8b) were initially normalized with respect to their maximum value along the flame wings.
2. Since no soot is present along the wings, the two normalized images were subtracted to obtain one that had just the contribution from soot on the tip (Fig. 6.8c).
3. The resulting image was then scaled so that the peak value of the tip equaled the blue channel's tip peak value.
4. The scaled image was then subtracted from the original blue signal to obtain a "soot-free" blue image (Fig. 6.8d).

Among the SLICE flames analyzed in this chapter, the soot correction was applied to all the flames with the exception of the following non-sooty cases:

- Microgravity, sequence **A** from Table 6.1: 40%  $CH_4$ , 60%  $N_2$ , coflow velocity of 17 cm/s and fuel velocities of 17 cm/s and 25 cm/s.
- Normal gravity, sequence **A** from Table 6.1: 40%  $CH_4$ , 60%  $N_2$ , coflow velocity of 17 cm/s and fuel velocities of 17 cm/s, 25 cm/s, and 50 cm/s.

## 6.5 Results

The procedure to compute the absolute  $CH^*$  concentration was initially tested on the reference 65% methane flame. For that flame, the  $CH^*$  mole fraction has been previously evaluated using an approach similar to the one shown here. The approach relied on the use of a 430 nm interference filter and the absolute calibration, alternatively, was performed using Rayleigh scattering [111]. Figure 6.9 shows the comparison between the absolute two-dimensional  $CH^*$  concentration, in mole fraction, evaluated by [111] and the result obtained with the approach introduced in

this work. Since Eq. 6.1 returns a number density value, the mole fraction value was derived assuming a temperature of 1900 K.

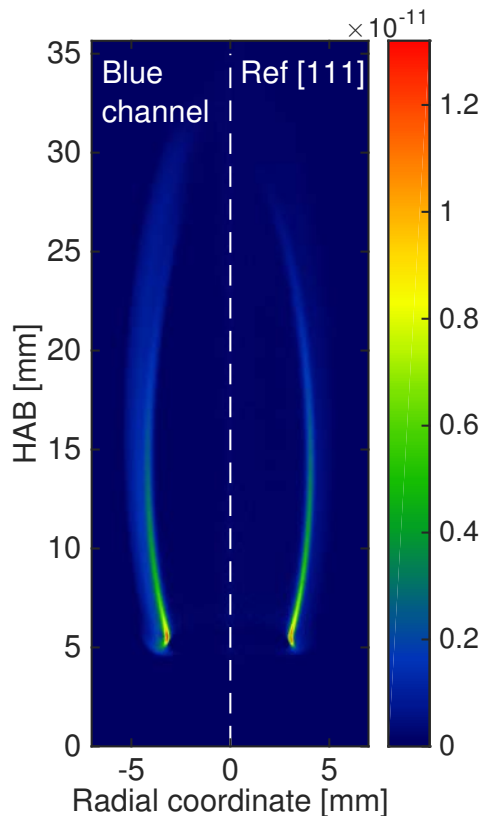


Figure 6.9: Two-dimensional  $CH^*$  mole fraction of the reference nitrogen-diluted 65% methane flame (left half) as compared to the result from [111] (right half).

When compared to previous results, the proposed approach was able to return comparable quantitative values; moreover, it confirmed that the Abel-inverted blue signal was a reasonable marker for the  $CH^*$  location in an axisymmetric flame, despite the presence of the halo on the oxidizer side. As introduced in Section 6.4, the calibration constant was derived using a heated SiC fiber as absolute light calibration (a 15  $\mu\text{m}$  diameter fiber was used for the reference flame calibration). The fiber temperature, inferred using the color ratio approach, has an uncertainty of  $\sim 30$  K [23]. This temperature uncertainty translated in an absolute peak  $CH^*$  concentration that, for this specific flame and measured fiber temperature, could vary up to  $\sim$

40% of the value determined considering the average fiber temperature. Calibrations performed using Rayleigh scattering, on the other hand, have been reported to return a  $CH^*$  concentration accuracy of  $\sim 25\%$  [111].

For the approach presented here, the uncertainty on the calibration constant was due to its high sensitivity to temperature. The denominator in Eq. 6.2, in fact, involves the integral of the intensity of radiation emitted by a blackbody, convolved with the color filter and the detector's blue spectral response. This integral, when evaluated in the visible wavelength range, is very sensitive to temperature variations, because of the blackbody emission temperature dependence. A better and more precise approach to perform the absolute light calibration would be based on the use of a thermocouple rather than a SiC fiber [7]. The lower uncertainty in the measured thermocouple temperature will translate into a smaller uncertainty for the calibration constant. Nonetheless, the SLICE data absolute light calibration relied on a SiC fiber and, to be consistent and to understand the limitations of such a technique, the same approach was used for the reference flame as well.

Focusing now the attention onto the SLICE dataset, Fig. 6.10 shows the calculated two-dimensional  $CH^*$  concentration for the sequence **A** of Table 6.1 (40%  $CH_4$ , 60%  $N_2$ , 3.2 mm I.D. nozzle, coflow velocity of 17 cm/s, fuel velocity ranging from 17 cm/s to 89 cm/s); the sequence is plotted as a function of the fuel velocity, for a fixed coflow velocity. The left half of each figure shows the microgravity result, while the right half shows the normal gravity one. Because of the lack of buoyancy effects, and for this particular fuel dilution and for these flow rates, the microgravity flames stayed attached to the burner, while the liftoff height of the normal gravity flames increased as the fuel velocity was increased.

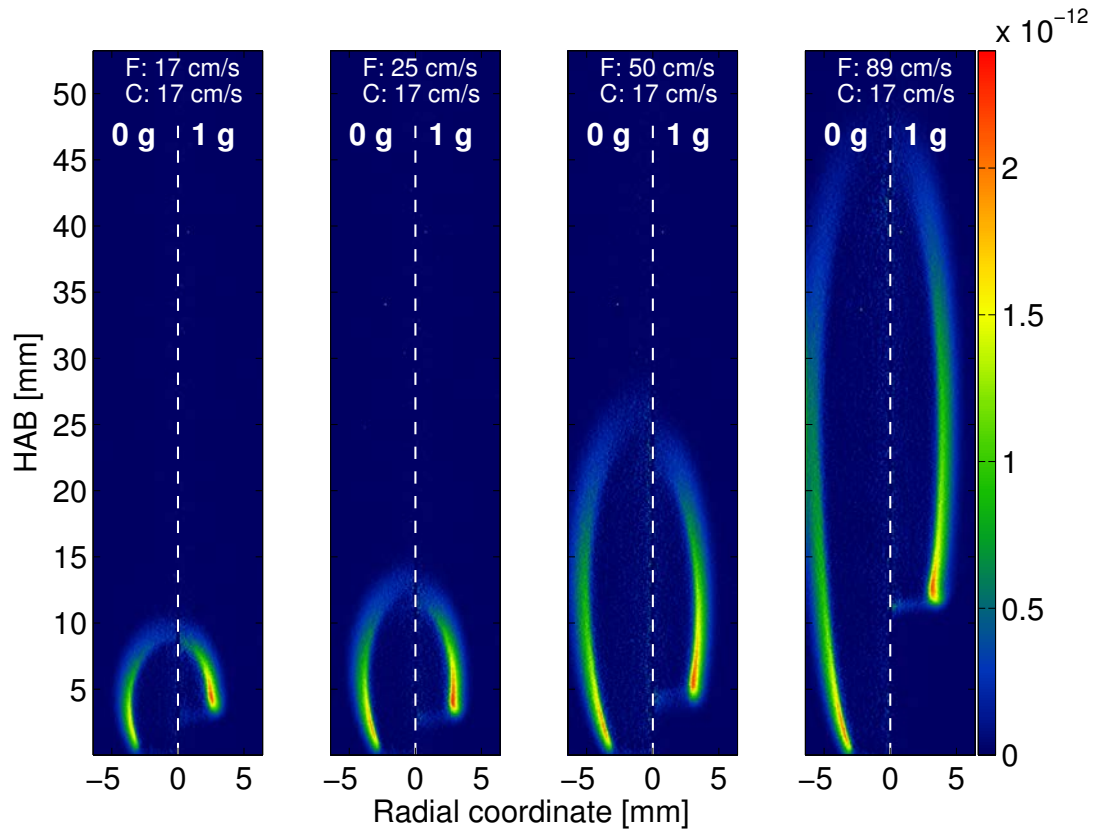


Figure 6.10: Two-dimensional  $CH^*$  mole fraction for the nitrogen-diluted methane flames from sequence **A** of Table 1 (40%  $CH_4$ , 60%  $N_2$ , coflow velocity, labeled C, of 17 cm/s, fuel velocities, labeled F, between 17 cm/s and 89 cm/s). The 0 g result is on the left half of each plot, and the 1 g result is on the right half.

For this specific configuration (sequence **A**), the peak  $CH^*$  concentration of the normal gravity flames was seen to be relatively insensitive to the fuel velocity and remained roughly constant as the flow conditions were changed. On the other hand, the microgravity flames displayed a small increase in peak concentration as the fuel velocity increased, as displayed in Fig 6.11. The less diluted 1 g flames of sequence **B** in Fig. 6.11 (70%  $CH_4$ , 30%  $N_2$ , coflow velocity of 17 cm/s, fuel velocity ranging from 180 to 460 cm/s) displayed a similar trend, with a 1 g peak  $CH^*$  concentration that seemed insensitive to the fuel velocity. Sequence **C** in Fig. 10 (70%  $CH_4$ , 30%  $N_2$ , fuel velocity of 62 cm/s, coflow velocity ranging from 14 to 34 cm/s) showed that both 0 g and 1 g peak  $CH^*$  concentrations increased with the coflow, instead. The

average peak  $CH^*$  concentrations of sequences **B** and **C**, which have a fuel mixture with 70% methane, were comparable to the one determined for the reference 65% methane flame (order of  $10^{-11}$ ); on the other hand, the more diluted 40% methane flame of sequence **A** displayed a lower average peak concentration (order of  $10^{-12}$ ).

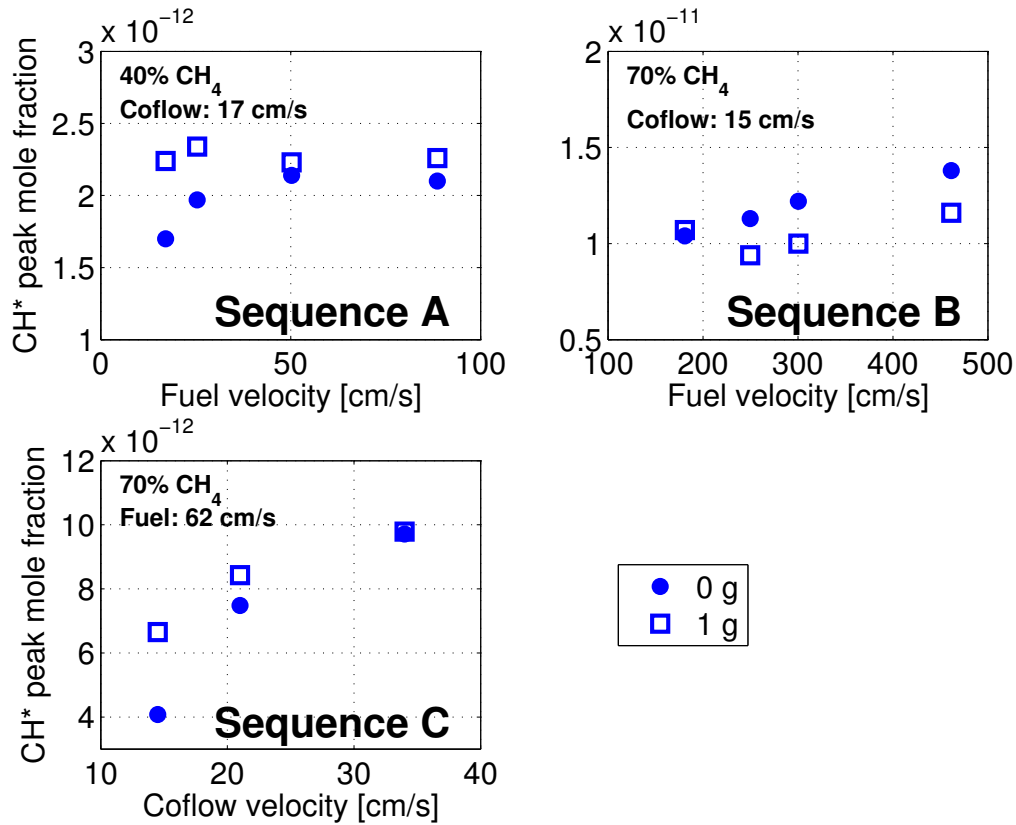


Figure 6.11: Variation of the peak  $CH^*$  concentration for the flame sequences **A**, **B**, and **C** of Table 6.1. The coflow and fuel velocities are summarized in each plot.

As stated in the Introduction, one of the objectives of this chapter was the verification of the correlation between  $CH^*$  chemiluminescence and flame heat release rate. In the following discussion, the integrated absolute  $CH^*$  concentration in a cross section will be considered as a possible marker for the total flame heat release rate. Figure 6.12 compares the normalized computed total heat release rate with the normalized integrated absolute  $CH^*$  concentration in a cross section, for the three flame sequences considered. The total heat release rate was evaluated by summing

the values of all the nonzero pixels in the two-dimensional numerical results, while the integrated absolute  $CH^*$  concentration was determined in a similar way but considering the experimental data. In Fig. 6.12, the solid circles refer to the microgravity results, while the empty squares refer to the normal gravity ones.

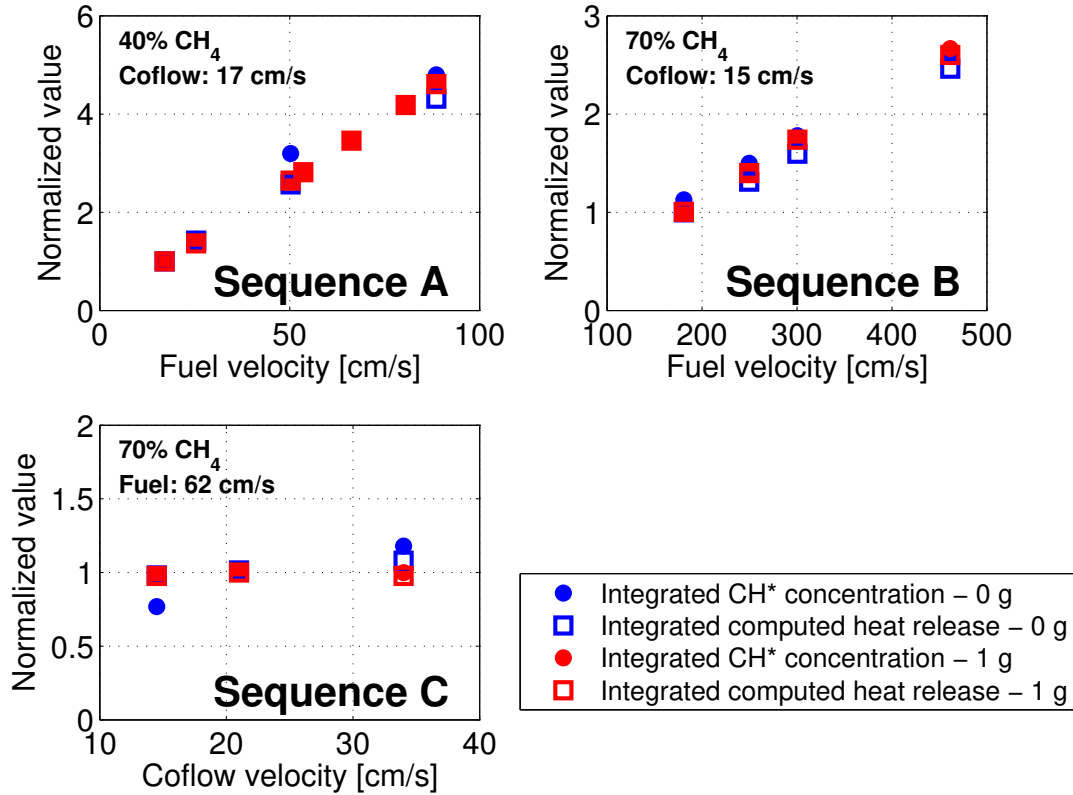


Figure 6.12: Integrated  $CH^*$  concentration in a cross section and integrated heat release rate (each normalized with respect to its minimum normal gravity value), for the flame sequences **A**, **B**, and **C** of Table 1. The coflow and fuel velocities are summarized in each plot.

The numerical simulations displayed little or no variation between the microgravity and normal gravity cases, while the experimental data generally showed lower integrated  $CH^*$  concentration for the normal gravity flames. These small differences may be attributed to two factors: first, the flow velocities of the microgravity and normal gravity cases, despite being comparable, were not exactly identical; second, the soot luminosity subtraction might play a role in all the cases in which it was

performed. Soot luminosity was accounted for in all the flames except for a few cases in sequence **A** (microgravity with fuel velocities of 17 cm/s, and 25 cm/s; normal gravity with fuel velocities of 17 cm/s, 25 cm/s, and 50 cm/s). Despite such distinctions, the correlation between total integrated heat release rate and integrated  $CH^*$  concentration was seen to be excellent. Moreover, the fact that the 1 g flames of sequence **A** become lifted has no influence on the linear relation between heat release rate and flow conditions. Being related to the amount of fuel in the system, the total heat release did not change when the fuel flow was fixed and the coflow was varied (sequence **C**).

In systems where a two-dimensional distribution of the  $CH^*$  concentration can be measured and a two-dimensional heat release rate can be computed, a comparison between the spatial distribution of the two quantities would indicate if any spatial correlation exists. Figure 6.13 shows the two-dimensional  $CH^*$  concentration distribution (left half of each image) and the computed two-dimensional heat release rate (right half) for two of the flames from sequence **A** (40%  $CH_4$ , 60%  $N_2$ , coflow velocity of 17 cm/s and fuel velocities of 25 and 50 cm/s). The two leftmost columns show the microgravity results, while the two rightmost columns show the normal gravity ones.

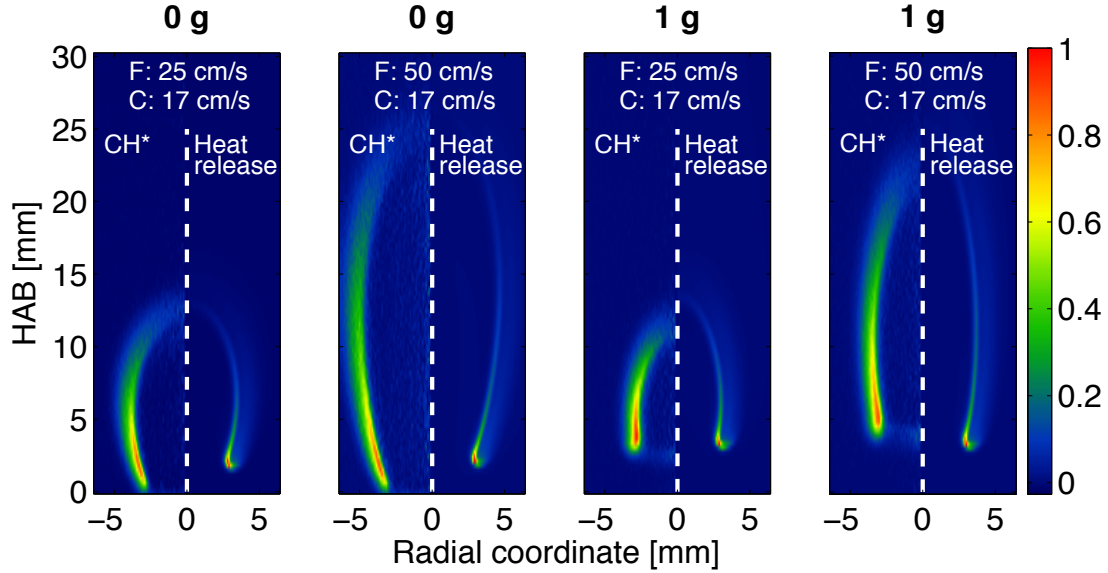


Figure 6.13: Comparison between normalized two-dimensional  $CH^*$  concentration (left half) and computed two-dimensional heat release rate (right half) for two of the flames from sequence **A** (40%  $CH_4$ , 60%  $N_2$ , coflow velocity of 17 cm/s and fuel velocities of 25 and 50 cm/s). Microgravity and normal gravity results are shown in the two leftmost and the two rightmost images, respectively.

Like the integrated quantities analyzed previously, the spatial correspondence between the  $CH^*$  distribution and heat release rate was seen to be satisfactory; despite minor differences in the flames liftoff heights and lengths, the  $CH^*$  and heat release rate spatial distributions were seen to be similar and both followed the position of the flame front. On the other hand, the gradients and intensity distributions of the two quantities did not match. Figure 6.14 plots the normalized radially integrated counts of the two aforementioned quantities as functions of an axial coordinate for a representative SLICE flame from sequence **A** (40%  $CH_4$ , 60%  $N_2$ , coflow velocity of 17 cm/s, fuel velocity of 25 cm/s.) The plotted profiles were axially shifted with respect to each other to account for the differences in liftoff heights using as a marker the peak values of the measured  $CH^*$  and the computed  $CH$ . Because of the shifting, the origin of the horizontal axis is no longer representative of the burner surface. The comparison between the axial distribution of  $CH^*$  (Fig. 6.14a) and heat release

rate (Fig. 6.14c) confirmed that the  $CH^*$  does not adequately reproduce the spatial gradients, at least in the upstream region close to the flame base.

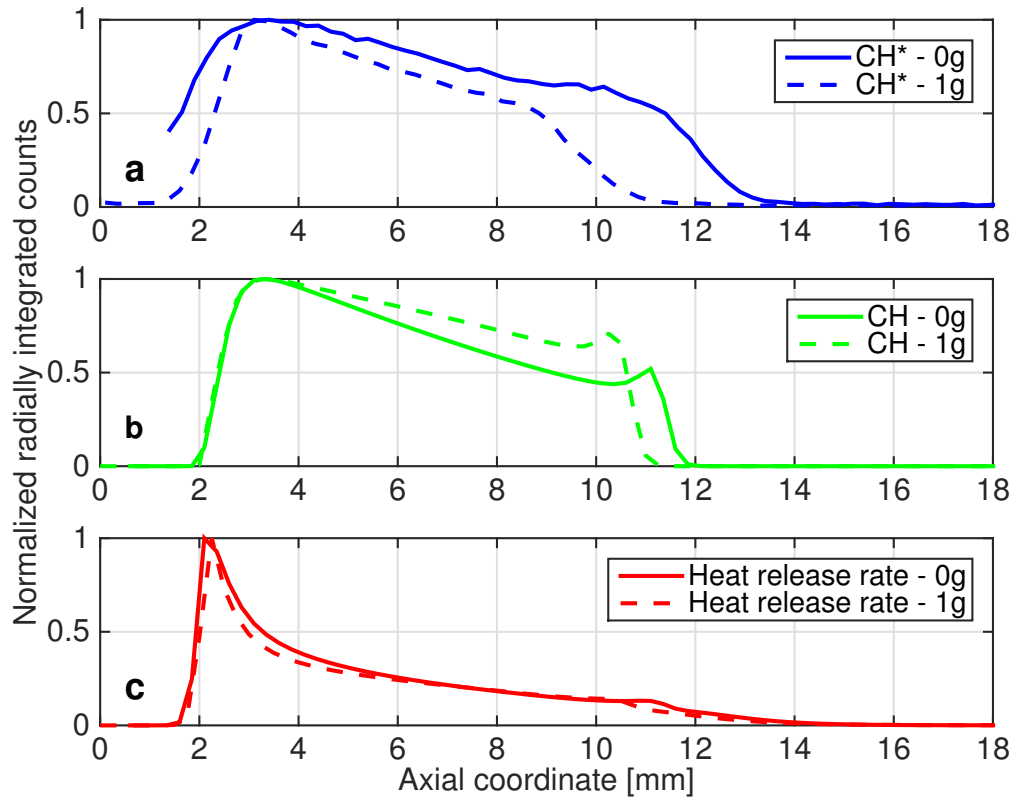


Figure 6.14: (a) Radially integrated  $CH^*$ , (b) radially integrated  $CH$ , and (c) radially integrated heat release rate of a representative SLICE flame from sequence **A** (40%  $CH_4$ , 60%  $N_2$ , coflow velocity of 17 cm/s, fuel velocity of 25 cm/s.) Solid lines identify microgravity results, while dashed lines identify normal gravity ones. Each curve is normalized with respect to its maximum.

Takahashi and Katta [119] suggested that the  $CH^*$  chemiluminescence would reproduce the heat release rate gradients if the contribution of the  $CH^*$ -related pathways remained the same throughout the flame zone. However, the flame structure in the peak reactivity spot at the flame base and in the trailing diffusion flame was different. In the former, the main contribution to the heat release rate came from enhanced formaldehyde production ( $CH_3 + O \rightarrow CH_2O + H$ ), because of the fuel-air premixing around the flame base.

Finally, Fig. 6.15 shows the peak values of the simulated two-dimensional heat release rate, for the three micro- and normal gravity flame sequences from Table 1.

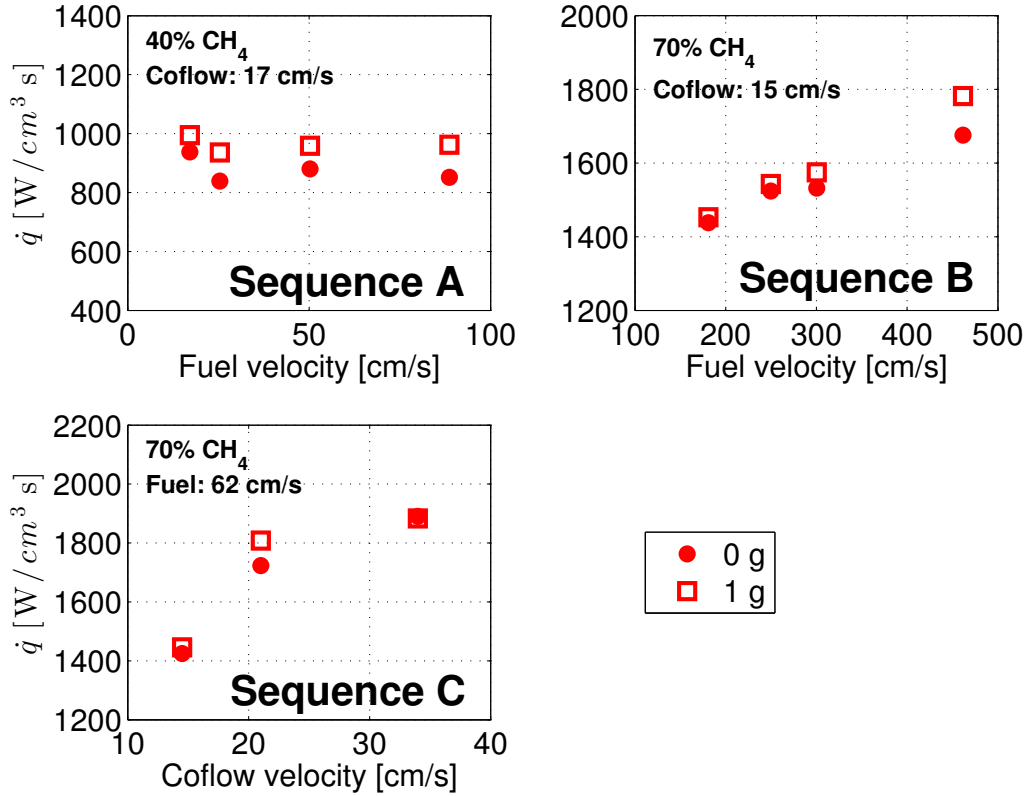


Figure 6.15: Variation of the computed peak heat release rate for the flame sequences **A**, **B**, and **C** of Table 6.1. The coflow and fuel velocities are summarized in each plot.

The similarities with the peak  $CH^*$  concentration plot of Fig. 10 are evident; the peak heat release rate of the highly diluted flames of sequence **A** seemed to be relatively insensitive to any variation of fuel velocity, while the less diluted flames of sequences **B** and **C** displayed peak values that are functions of fuel flow and coflow, respectively. Similar to what was observed between integrated  $CH^*$  concentration and integrated heat release rate, in laminar coflow diffusion flames, the peak  $CH^*$  concentration can be a marker for the variation of the peak heat release rate.

## 6.6 Conclusions

A simple diagnostic based on the use of a DSLR camera has been demonstrated to extract quantitative  $CH^*$  concentration information from the publicly available microgravity and normal gravity SLICE nitrogen-diluted methane laminar coflow diffusion flames, and the results have been compared with numerical simulations to investigate the correlation between  $CH^*$  chemiluminescence and flame heat release rate. The spectral characterization of the RGB camera's detector allowed the blue channel signal to be considered representative of the  $CH^*$  emission around 431 nm, while the analysis of the spectral emission of a reference nitrogen-diluted methane laminar coflow diffusion flame accounted for the contribution of chemiluminescence from emitting species other than  $CH^*$ . An Abel deconvolution was used to reconstruct the two-dimensional  $CH^*$  distribution from the line-of-sight emission, and a heated SiC fiber served as an absolute light calibration source. Previous quantitative  $CH^*$  measurements were used to verify the validity of the approach introduced in this work, and it was found that the uncertainty in the SiC fiber temperature evaluation could result in a  $\sim 40\%$   $CH^*$  concentration uncertainty.

The SLICE flames results showed that, if the contribution from soot emission is properly accounted for, the integrated absolute  $CH^*$  concentration in a cross section scales proportionally to the computed integrated flame heat release rate. For the flames considered here, and regardless of the gravity level, no major differences in peak  $CH^*$  concentration could be noted and the dependence of the peak  $CH^*$  concentration on the flow conditions was seen to mimic the behavior of the peak heat release rate. The two-dimensional  $CH^*$  concentration was shown to satisfactorily follow the computed heat release rates spatial distribution, but without reproducing the variation in spatial intensities and gradients, particularly close to the flame base.

# Chapter 7

## Nitrogen-diluted methane flames under moderate pressure

This chapter presents work done with nitrogen-diluted methane flames to study the influence that pressure, as well as fuel dilution, has on flame temperature and soot formation. Specifically, the experimental work shown here served as a complement and validation for numerical investigations performed in Professor Smooke's research lab. Numerical models, when applied to the simulation of diluted diffusion flames, still show some shortcomings, while the modeling of soot growth and evolution is still not fully understood. This combined experimental and numerical work, then, would provide experimental evidence and facilitate the refinement of numerical codes when applied to diluted and sooty flames [8].

Pressure plays a big role in affecting flame structure and flame chemistry, and an understanding of its influence can have positive implications in the design of practical combustion systems (which generally operate at pressures higher than ambient) [120–122]. Pressure influences combustion processes by favoring pressure-dependent third-body reactions and by modifying reaction rates that are weakly dependent on temperature. Additionally, higher pressure changes the gas density

and the diffusion coefficients, leading to variations in flame structure, flame length, and lift-off height [123,124]. Similar to pressure, variations in fuel dilution also affect diffusion flames. Adding an inert gas to the fuel mixture changes the flame temperature, concentrations and reaction rates of species. Typically, an increase in fuel dilution will result in a lower total heat release rate and a lower temperature which, in turn, will further change the velocity field, species concentration, flame structure, and sooting behavior of a flame [125,126]. In the following sections, the behavior and sooting characteristic of several nitrogen-diluted methane flames will be studied as a function of pressure and fuel dilution, and experimental observations will be compared with numerical predictions.

## 7.1 Experimental setup

The nitrogen-diluted diffusion methane flames considered in this chapter were lit on a coflow burner (4 mm I.D. for the fuel tube, 50 mm coflow diameter, with a 0.25" thick, 1/32" cell honeycomb on the burner outlet used as a flow straightener), placed in a 44.2 liters cylindrical pressure chamber. Four different fuel/nitrogen dilutions were considered for the fuel stream (50%, 55%, 60%, and 65% methane, by volume, with nitrogen balance); for each dilution, flame images were taken in the range of pressure from 1.0 to 2.7 atm, with 0.1 atm increments. Both coflow and fuel flow rates were controlled with mass flow controllers and set so that the fuel and oxidizer average velocities were equal to 35 cm/s, as measured at atmospheric pressure. The mass flow rates were kept constant but, because of the increase in pressure, the volumetric flow rates (thus the average flow velocity) decreased as a function of the pressure (see Fig. 7.1).

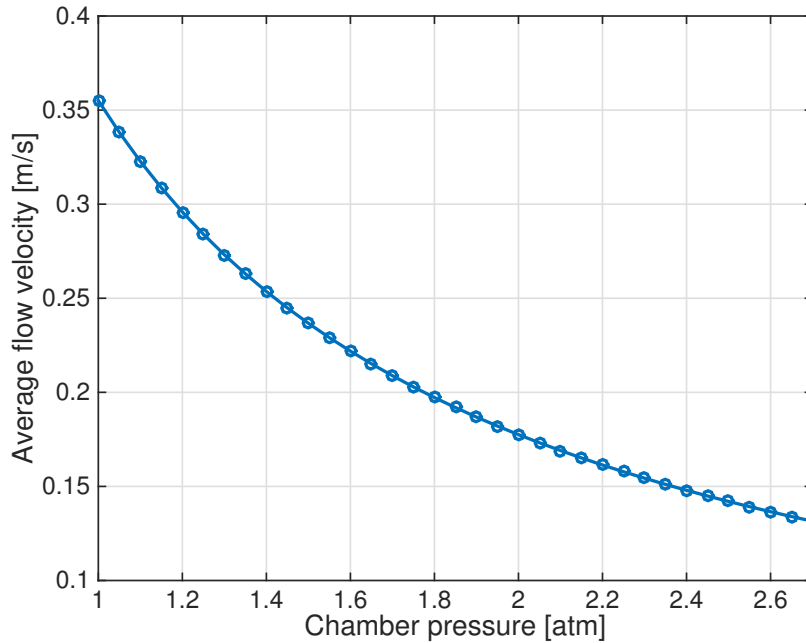


Figure 7.1: Decrease of average flow velocity as a function of increasing chamber pressure.

The variations in flame structure that could be observed as the pressure increased, and that are discussed in Section 7.2, were caused by a combination of pressure related changes and volumetric flow rate decrease. The pressure inside the chamber was monitored with an analog pressure transducer, while the pressure drop across the chamber exhaust was adjusted with a mechanical needle valve; the absolute pressure reading was believed to be accurate within  $\pm 0.01$  atm.

Flame images were taken with a DSLR Nikon D300s color camera paired with a 85 mm Nikkor lens ( $f$ -number 8) through one of the pressure chamber quartz optical accesses; a 1 mm thick Schott BG7 color filter was added to the optical setup to account for the red emission of soot and balance the RGB response of the detector. For each pressure value, a flame image was obtained by averaging five acquisitions, and the camera exposure was adjusted to optimize the use of the detector’s dynamic range. The camera’s raw data were decoded using algorithms from the open-source code dcraw [78]. For each RGB color channel of the image, the flame radial intensity profiles

were obtained using an Abel deconvolution and, thanks to a spectral characterization of the detector, the two-dimensional soot temperature was determined employing two-color ratio pyrometry (see Section 2.2.1). Finally, an S-type thermocouple was used as an absolute light calibration source for the evaluation of the soot volume fraction (see Section 2.2.5). Nitrogen-diluted methane flames are generally free of soot, especially for dilutions lower than 65%; however, at high pressure soot formation is favored and pyrometry techniques, that are generally relegated to heavily sooty ethylene flames, can be successfully applied to measure soot temperature.

## 7.2 Results and discussion

Figures 7.2 to 7.5 (top) show the line-of-sight flame luminosity (from the camera's green channel) for the four considered fuel dilutions, as a function of the chamber pressure. For each pressure value, only one half of the flame is displayed and their values are normalized with respect to each flame's maximum pixel count. The labels at the bottom of each flame identify the chamber's pressure value, in atm. Figures 7.2 to 7.5 (center) show the soot temperature pyrometry results, in Kelvin, as a function of the chamber pressure, while Figs. 7.2 to 7.5 (bottom) show the soot volume fraction results, as determined from the pyrometry temperature measurements and the absolute light calibration.

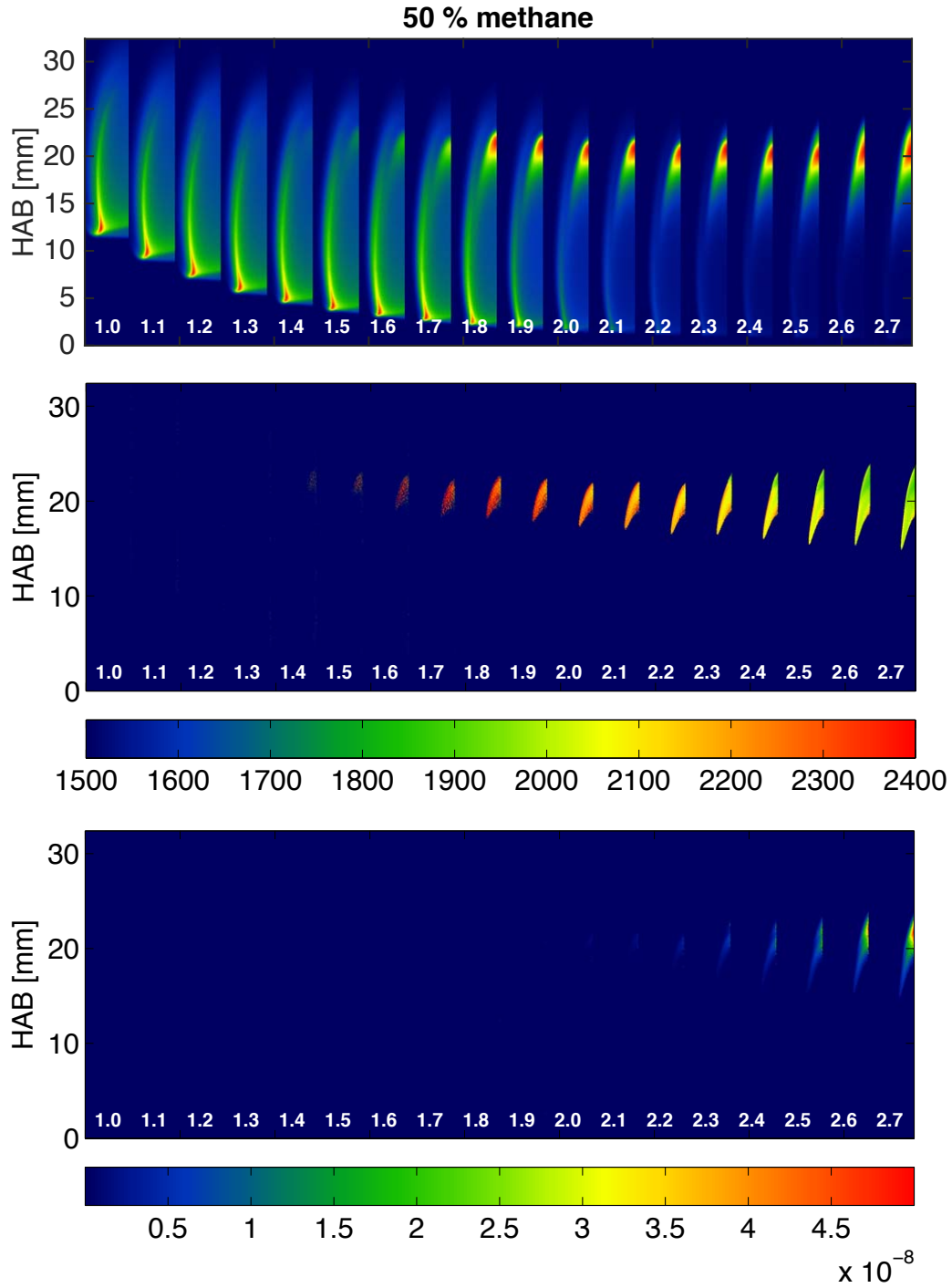


Figure 7.2: (Top) Normalized flame luminosity, (center) soot temperature, in Kelvin, and (bottom) soot volume fraction for the 50% methane flame as a function of pressure (in atm).

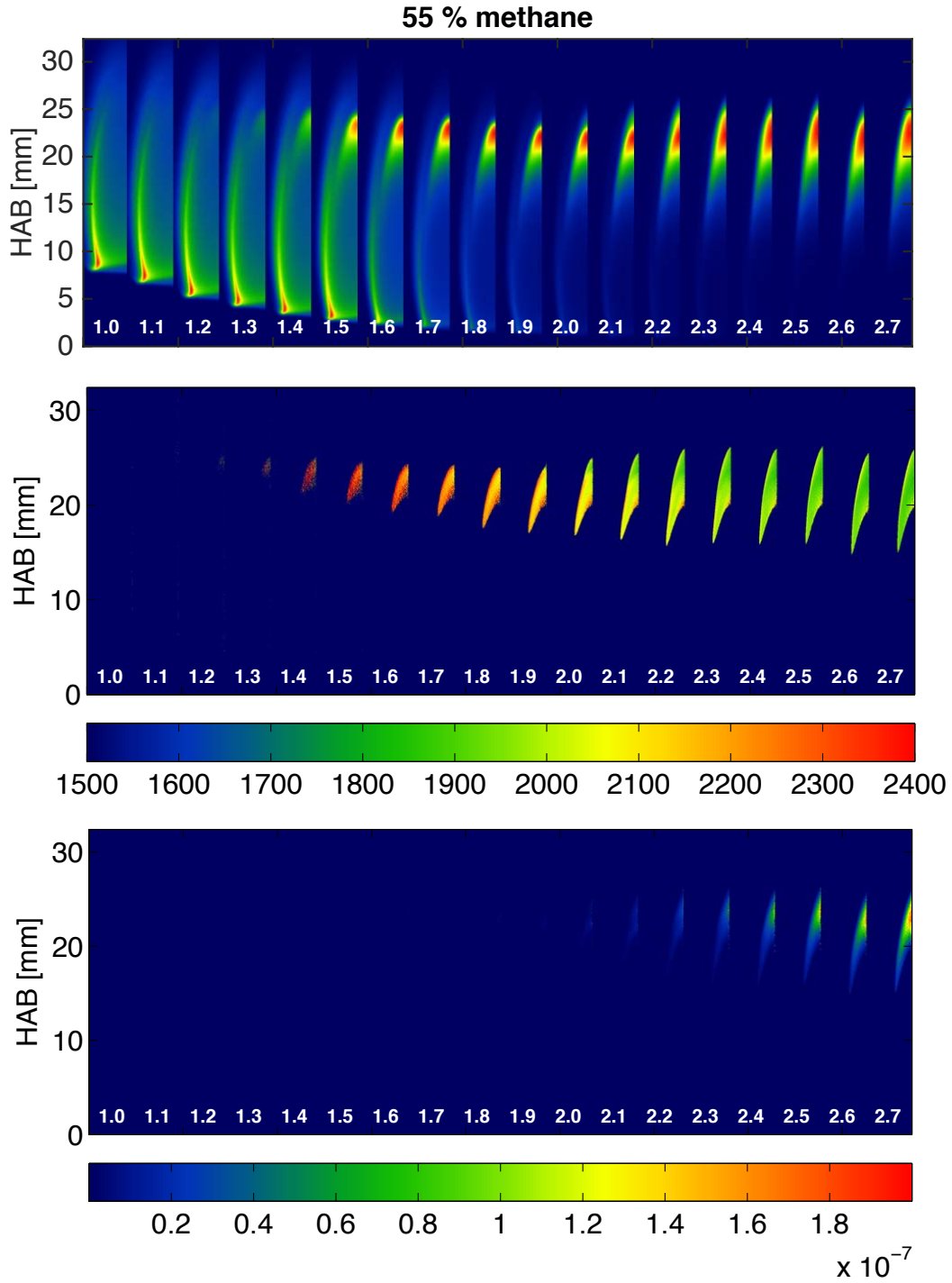


Figure 7.3: (Top) Normalized flame luminosity, (center) soot temperature, in Kelvin, and (bottom) soot volume fraction for the 55% methane flame as a function of pressure (in atm).

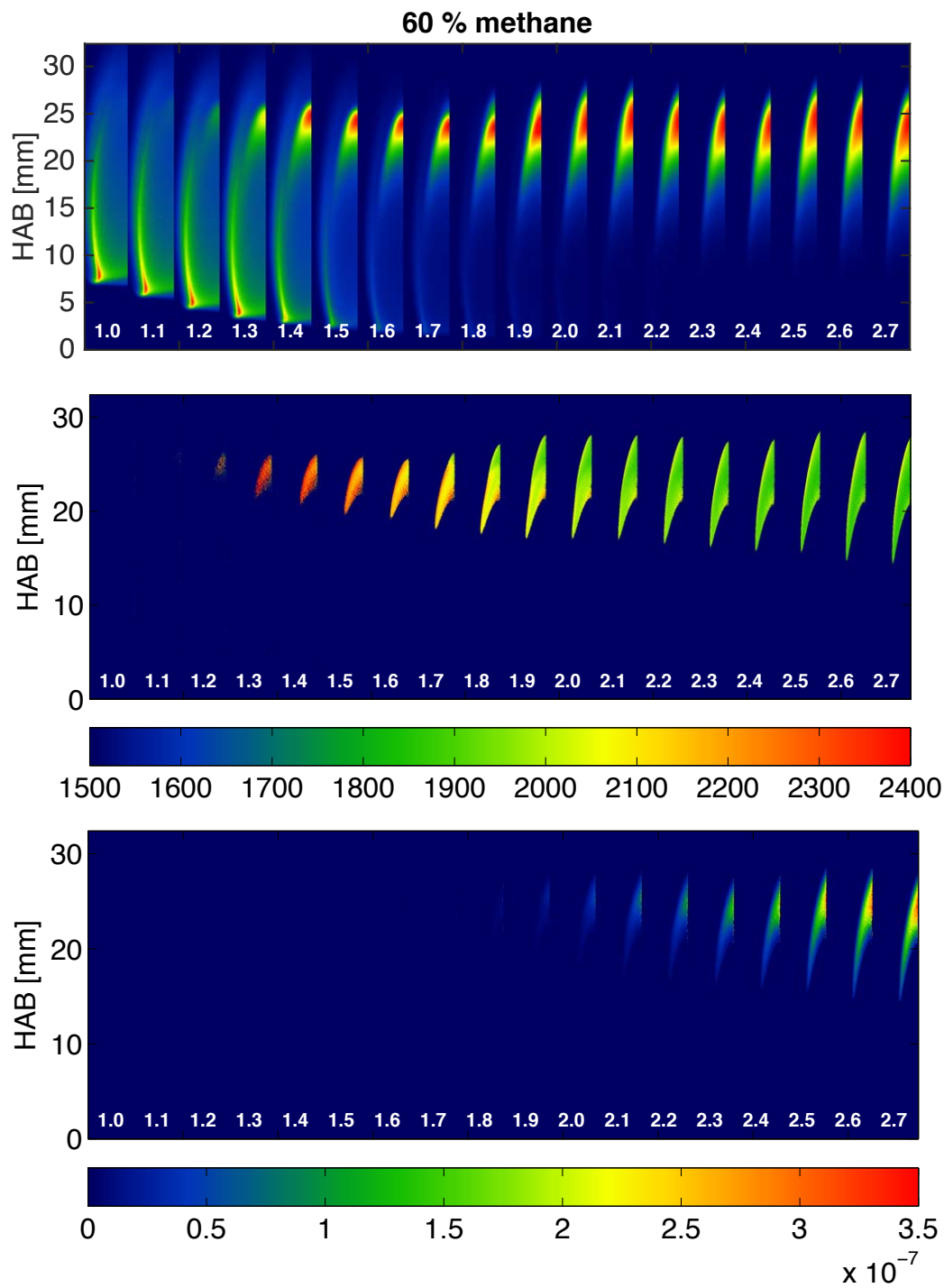


Figure 7.4: (Top) Normalized flame luminosity, (center) soot temperature, in Kelvin, and (bottom) soot volume fraction for the 60% methane flame as a function of pressure (in atm).

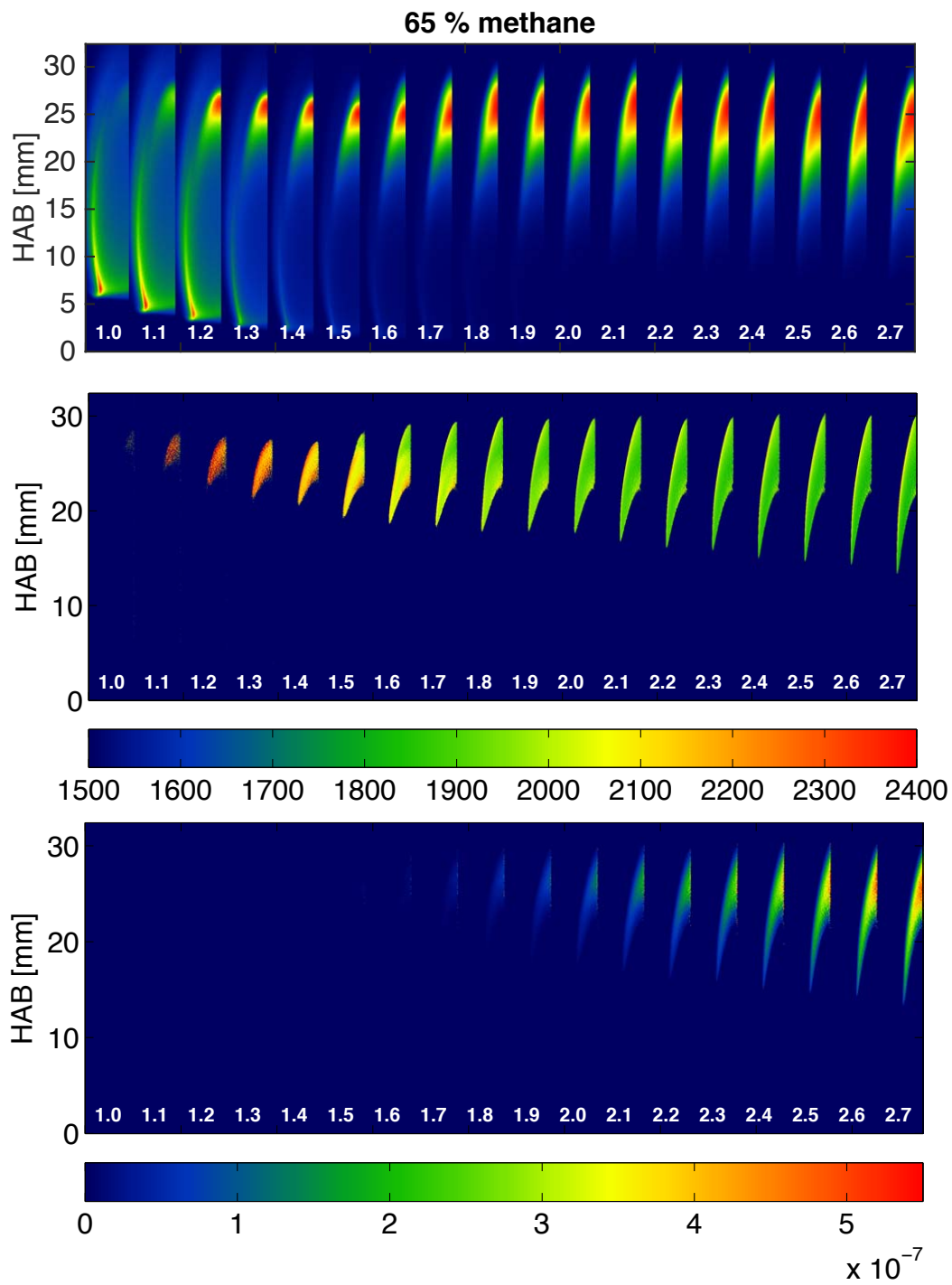


Figure 7.5: (Top) Normalized flame luminosity, (center) soot temperature, in Kelvin, and (bottom) soot volume fraction for the 65% methane flame as a function of pressure (in atm).

The soot pyrometry technique relies on the assumption that all the collected luminosity comes from soot emission; when the soot emission is faint, contributions from  $CH^*$  and  $CO_2$  chemiluminescence will introduce an unwanted background and therefore alter the color ratios. To try to account for this offset, a subtraction similar to the one introduced in Section 6.4 was applied to all the cases where the flame wing chemiluminescence intensity was greater than  $\sim 10\%$  of the maximum image counts (when considering the green channel); specifically, the red and green images were subtracted by a properly scaled blue image. The intensity of the blue channel, because of the spectral emission of  $CH^*$  and  $CO_2$ , and the characteristics of the blue filter transmissivity, was in fact considered a good marker for the chemiluminescence. The scaling factor was determined by dividing the maxima between red/blue and green/blue channels at the flame base, where it is known that all the luminosity comes from chemiluminescence since no soot is present. The subtraction was applied to the following cases:

- 50% flame: measurements at pressure lower than 2.4 atm.
- 55% flame: measurements at pressure lower than 2.1 atm.
- 60% flame: measurements at pressure lower than 1.8 atm.
- 65% flame: measurements at pressure lower than 1.6 atm.

Figures 7.6 to 7.9 show the updated soot temperature (top) and volume fraction results (bottom) after the chemiluminescence subtraction was implemented. The chemiluminescence subtraction had the effect of returning results with lower temperature and slightly higher volume fractions. Generally, in color ratio pyrometry the temperature is obtained by averaging the results from the three available color ratios; in this case, however, only the red/green pair was considered due to the applied correction.

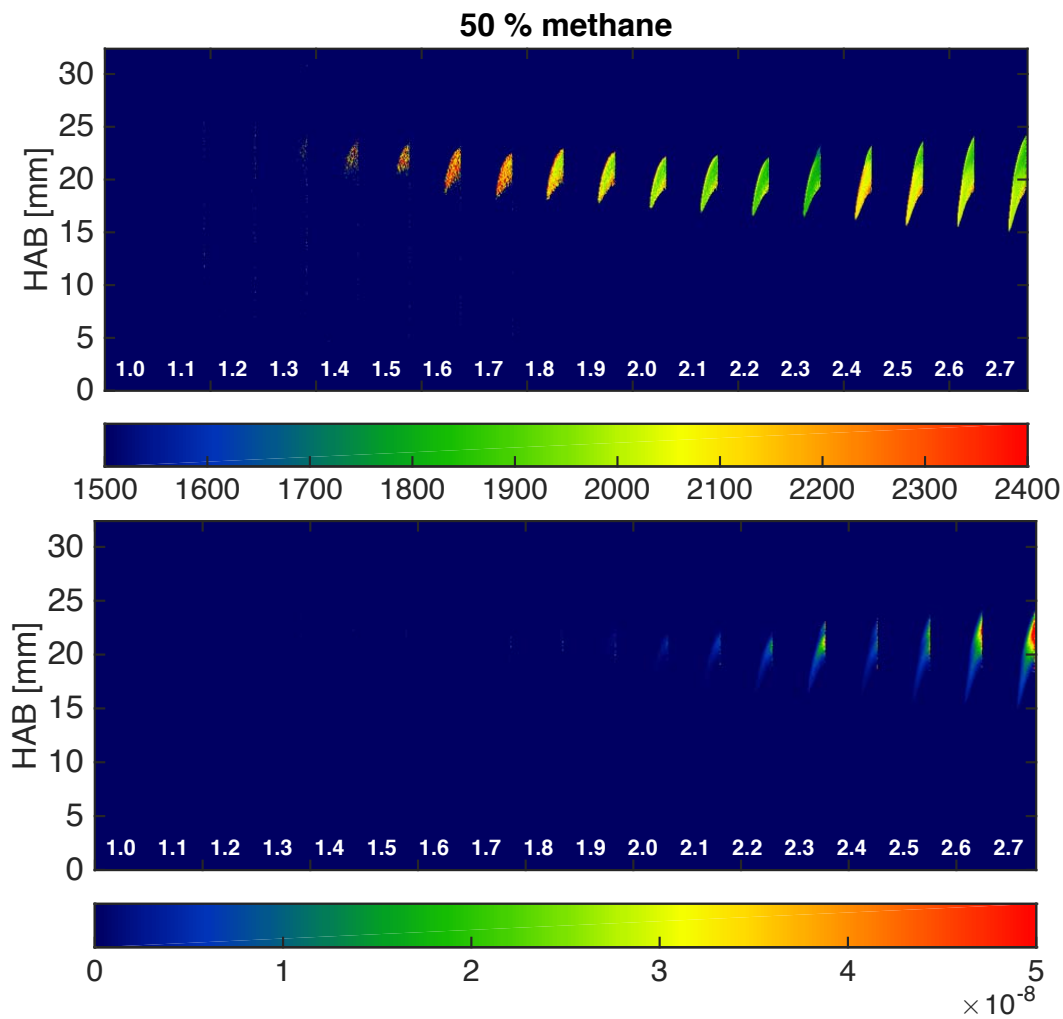


Figure 7.6: (Top) Soot temperature, in Kelvin, and (bottom) soot volume fraction for the  $CH^*$ -subtracted 50% methane flame as a function of pressure (in atm).

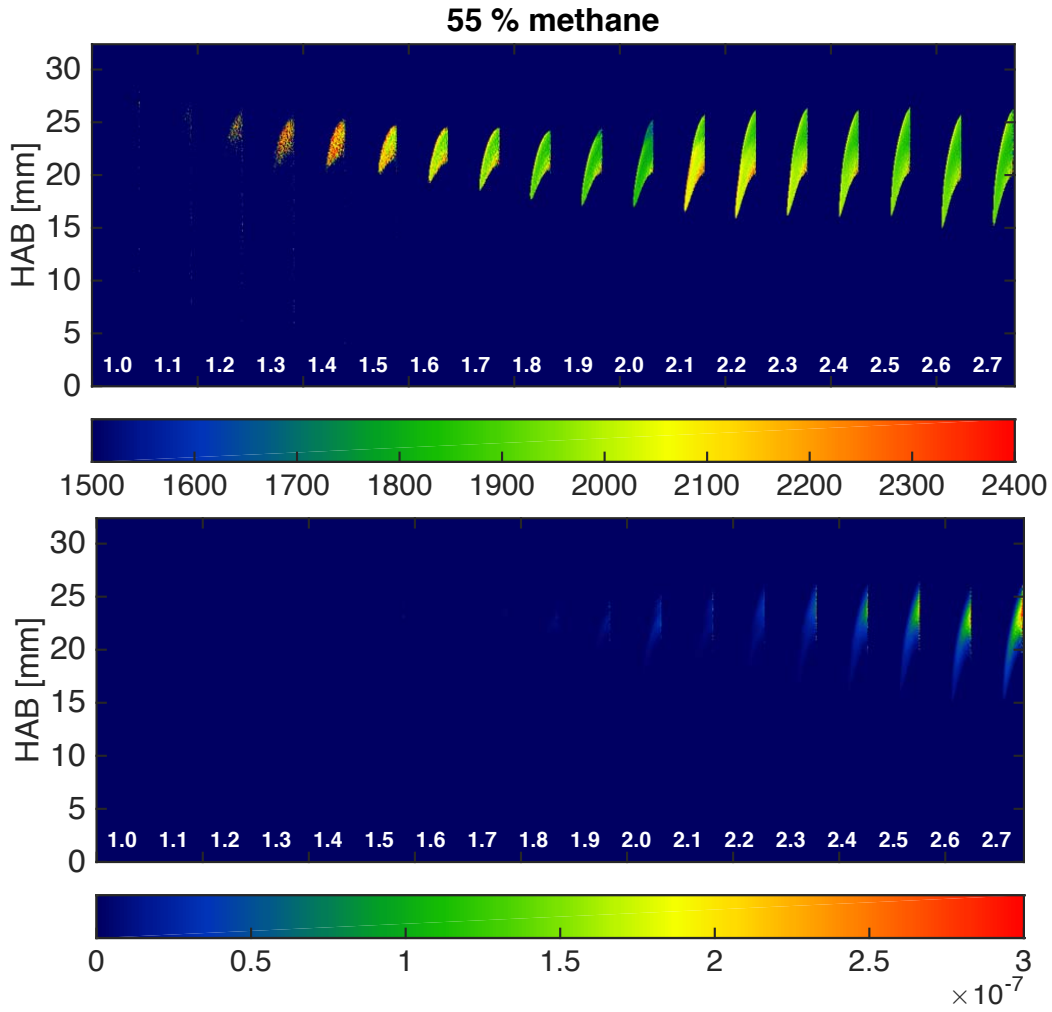


Figure 7.7: (Top) Soot temperature, in Kelvin, and (bottom) soot volume fraction for the  $CH^*$ -subtracted 55% methane flame as a function of pressure (in atm).

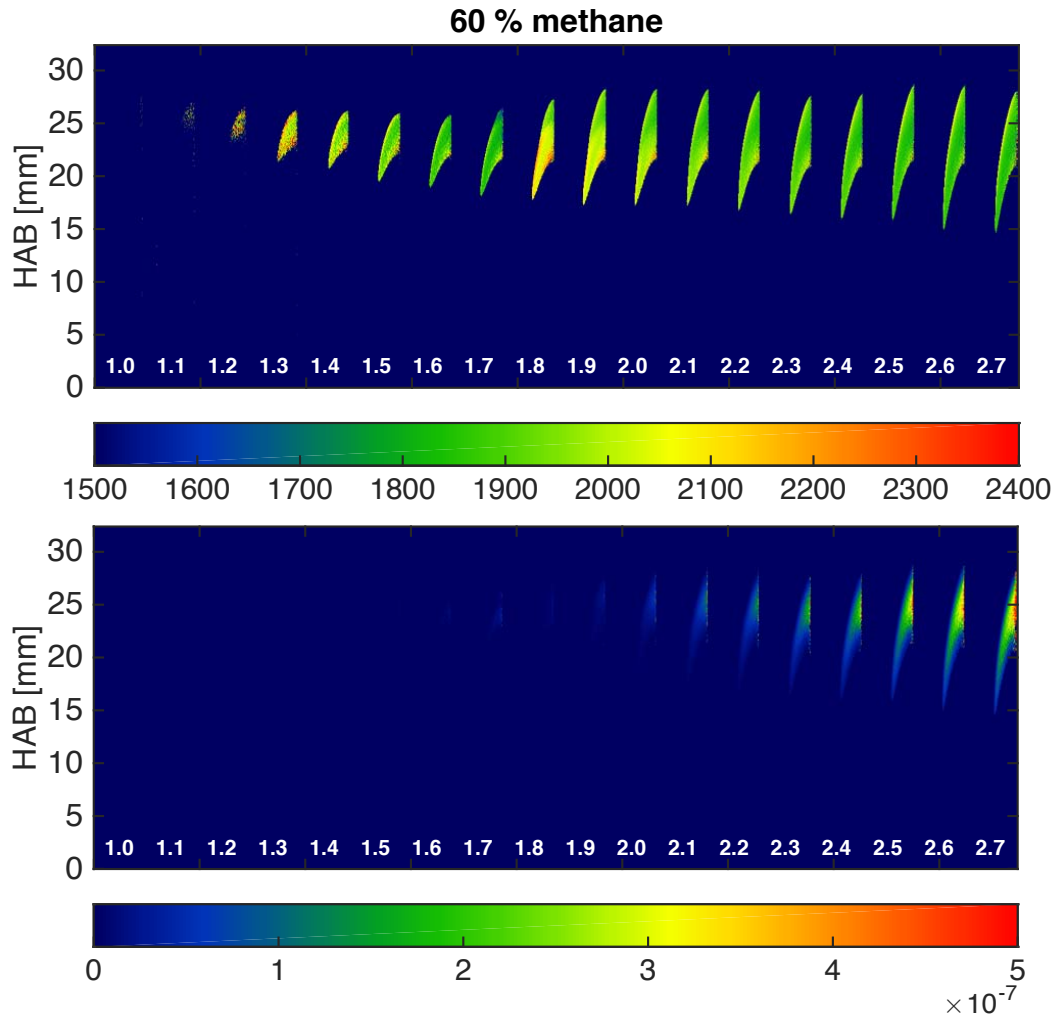


Figure 7.8: (Top) Soot temperature, in Kelvin, and (bottom) soot volume fraction for the  $CH^*$ -subtracted 60% methane flame as a function of pressure (in atm).

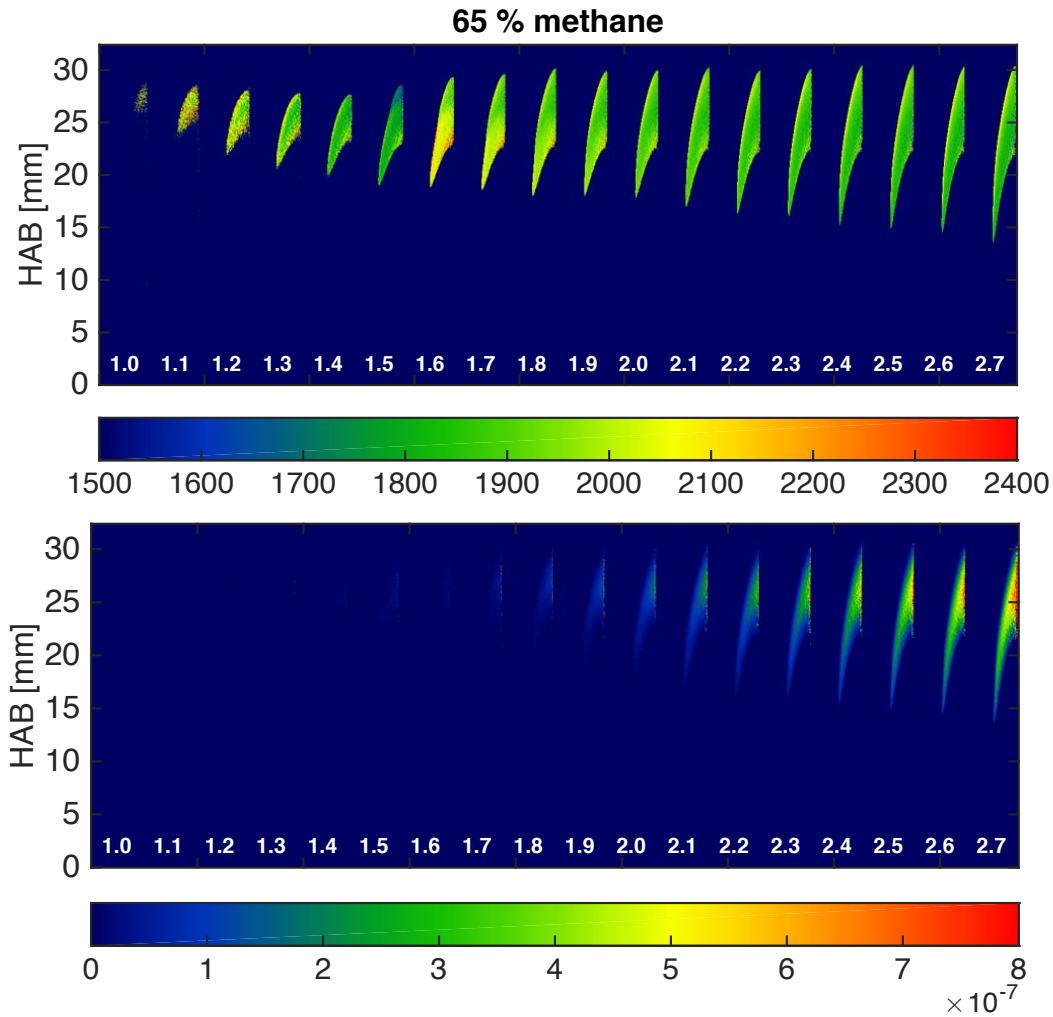


Figure 7.9: (Top) Soot temperature, in Kelvin, and (bottom) soot volume fraction for the  $CH^*$ -subtracted 65% methane flame as a function of pressure (in atm).

As discussed in the opening of this chapter, the influence that pressure has on the structure and characteristics of diffusion flames is clearly visible in the previous results. Specifically:

- Lift off height: the lift off height decreases with increasing pressure and decreasing velocity. The coflow and fuel flows are controlled with mass flow controllers, which keep the mass flow rate constant. Since  $\dot{m} = \rho v A$ , an increase in  $P$  (thus an increase in  $\rho$ ) will have the effect of decreasing the axial velocity  $v$ , in order to keep  $\dot{m}$  constant. The lift off height is also determined by a balance between

flow velocity (which is proportional to  $\propto P^{-1}$ ) and laminar flame speed (which is proportional to  $\propto P^{-0.4}$  [8]). When pressure is increased, the axial velocity will decrease faster than the flame speed, reducing therefore the lift off height.

- Flame length: after the flames become attached, the flame length remains relatively constant. The theoretical length of diffusion flames is proportional to  $\propto \frac{1}{\rho D}$  [127], where  $D$  is the diffusion coefficient. Since  $\rho \propto P$ , and  $D \propto P^{-1}$ , the net effect will be null. The flame length, being proportional to the flow rate, increases as the nitrogen concentration is reduced because the net  $CH_4$  flow rate increases.
- Peak centerline flame temperature: the peak centerline temperature decreases with the dilution, as a consequence of reduced flame reactivity, but it is relatively insensitive to pressure.
- Peak soot volume fraction: the peak soot volume fraction increases with the fuel concentration and with pressure. Since the axial velocity  $v$  is proportional to  $\propto P^{-1}$ , the increased residence times will favor soot growth.

Figures 7.10 and 7.11 summarize the peak centerline temperature and peak soot volume fraction, respectively, for the four considered flames (after the chemiluminescence contribution was subtracted). The experimental values were determined by averaging over an interrogation region close to the centerline, where the signals were relatively constant and where the artificial noise introduced by the Abel inversion was not too large. Figures 7.12 and 7.13 show, instead, the numerically-derived peak centerline flame temperature and soot volume fraction, respectively. The results were taken from [8] and are part of a numerical investigation focused on the study of the accuracy of simulations applied to nitrogen-diluted methane flames under pressure. In the temperature results of Fig. 7.12, the solid lines refer to numerical results that

include a soot model (that accounts for the formation and growth of soot as well as its radiative heat transfer), while the dashed lines refer to results that do not.

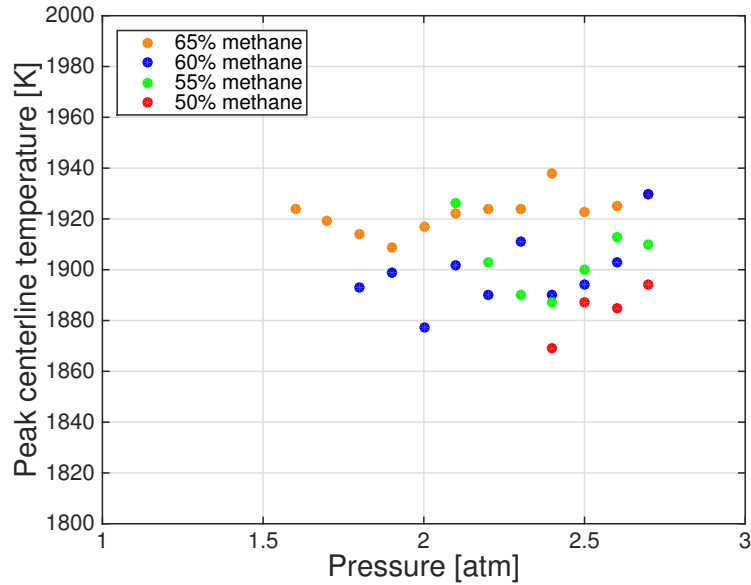


Figure 7.10: Peak centerline soot temperature, in Kelvin, for a subset of the four tested nitrogen-diluted methane flames as a function of pressure.

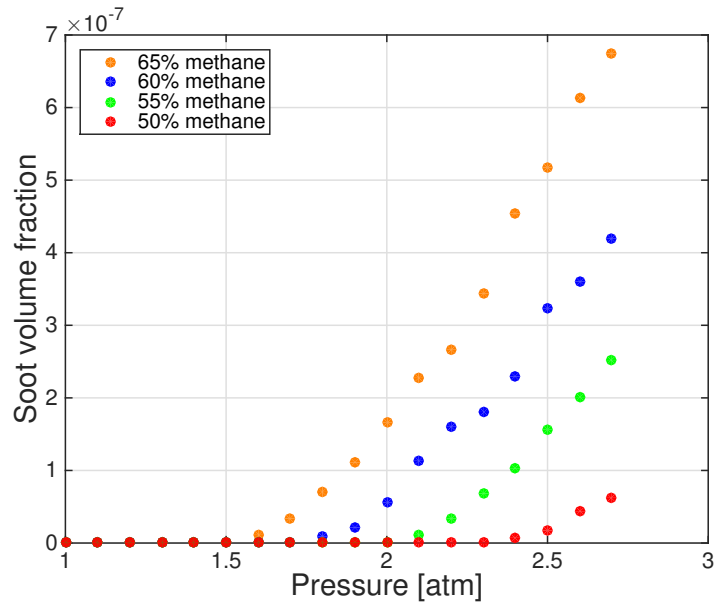


Figure 7.11: Peak centerline soot volume fraction for the four tested nitrogen-diluted methane flames as a function of pressure.

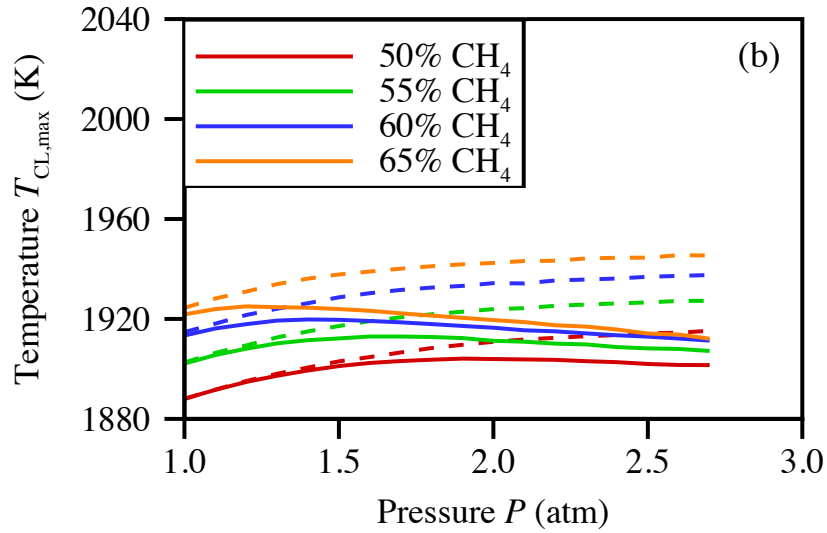


Figure 7.12: Computed peak centerline soot temperature, in Kelvin, for the four nitrogen-diluted methane flames as a function of pressure. Solid lines refer to results that include a soot model.

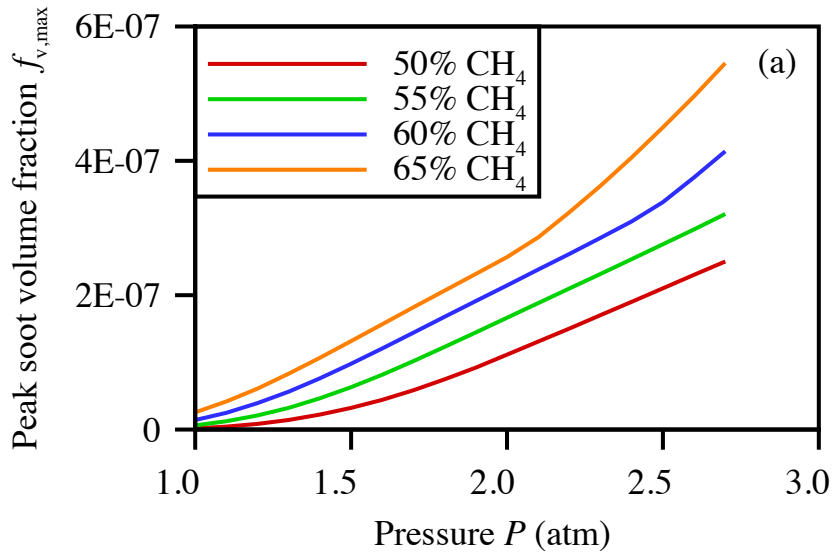


Figure 7.13: Computed peak centerline soot volume fraction for the four nitrogen-diluted methane flames as a function of pressure.

The predicted centerline temperature shown in Fig. 7.12 is relatively insensitive to pressure with values varying between  $\sim 1890$  and  $1920$  K. The measured results (Fig. 7.10) confirm the simulations and range, depending on the fuel dilution, between

$\sim 1880$  and  $1940$  K. The computed peak soot volume fractions (Fig. 7.13) agree reasonably well with the measurements (Fig. 7.11), both in the trends and absolute values. The numerical and experimental results obtained for the 65% methane flame are very close for pressure greater than 2 atm, but diverge at lower pressures where the optical techniques does not have enough sensitivity. Additionally, it is important to note that the temperature and soot volume fraction evaluations relied on assumptions regarding the soot spectral properties. The soot spectral emission was assumed to be proportional to  $\lambda^{-1.38}$  [13], a value that was shown to be not very accurate when applied to the “young” soot that characterizes the flames discussed in this chapter [14, 15]. For this same reason, during the evaluation of the peak centerline temperature, the value was estimated closer to the tip of the flame, rather than the base, since the higher temperature seen at the base is known to be a consequence of inaccurate soot properties [14, 15]. Moreover, in these flames the soot concentration is relatively low and temperature losses due to radiation can be considered negligible. The soot temperature is therefore expected to be relatively insensitive to the increasing pressure (i.e. soot load). Because of these considerations, in Fig. 7.10 only a subset of temperature values are plotted, since cases with negligible soot concentration were considered too inaccurate.

## Chapter 8

# Demosaicing algorithms for the improvement of spatial resolution and accuracy in color ratio pyrometry

Soot color ratio pyrometry is a quantitative diagnostic technique capable of measuring in-flame soot temperature that has found numerous applications in recent years due to its relative simplicity and the fact that inexpensive consumer color cameras can be used as imaging pyrometers [68]. Temperature information can be retrieved by measuring the incandescence from soot and, when the spectral responses of the red, green and blue (RGB) channels of a color filter array (CFA) are measured, and the spectral emissivity of the emitting bodies is known, signal ratios can be calculated as a function of the emitting body temperature (see [10–12, 128] and Section 2.2.1). Since the number of colors filters on a CFA is lower than the total number of pixels (as shown in Fig. 8.1), an interpolation can be implemented to evaluate the “missing” colors from the available ones; this process is know as demosaicing. In past

pyrometry works [12, 68], the raw images have always been separated into the three RGB channels without any demosaicing, thus halving the spatial resolution, and it was assumed that each color filter in every 2x2 RGGB pixel cluster sampled the same spatial location. This assumption holds as long as the detector’s pixel density, or the image magnification, is sufficiently high. However, during the characterization of the color camera selected for the NASA *Advanced Combustion via Microgravity Experiment* (ACME) campaign (see Chapter 9) it was seen that, due to the detector characteristics and relatively low image magnification, spatial gradients were not correctly reproduced yielding unrealistic soot temperature values in proximity of steep gradients. This chapter shows how the implementation of demosaicing algorithms, while maintaining the original image resolution, helps returning more accurate and realistic soot temperature values.

## 8.1 Demosaicing algorithms

As previously mentioned, a demosaicing algorithm interpolates a raw image to assign a RGB value to every pixel. The overall process is summarized in Fig. 8.1 where the image recorded through the Bayer-patterned CFA is decoded into the three colors, and then interpolated to obtain full-resolution RGB images.

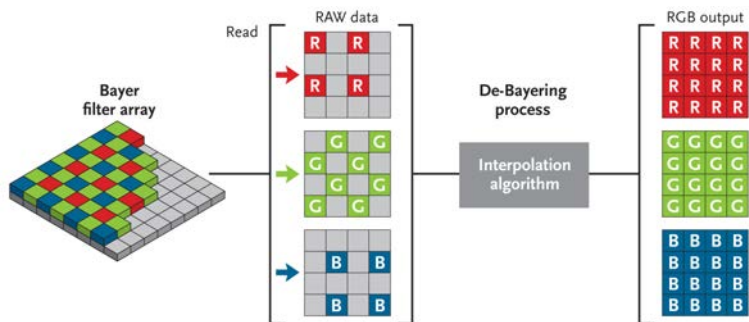


Figure 8.1: Sequence to convert a raw image into a demosaiced one (image courtesy of skyandtelescope.com).

Several algorithms and different strategies have been developed to deal with demosaicing: bilinear/cubic, hue-based, gradient-based, as well as adaptive/iterative interpolations [129–132]. In this chapter we focused and tested two approaches, namely the Bilinear interpolation [129] and the Malvar algorithm [133]. The former is the one with the simplest implementation; it spans at most a 4-pixel stencil, it is not computationally expensive, but can generate artifacts, especially along edges, or high-frequency structures. Figure 8.2 shows a general frame of reference to identify the spatial coordinates of pixels on a detector’s CCD and it is used to help formulating the algorithms behind demosaicing.

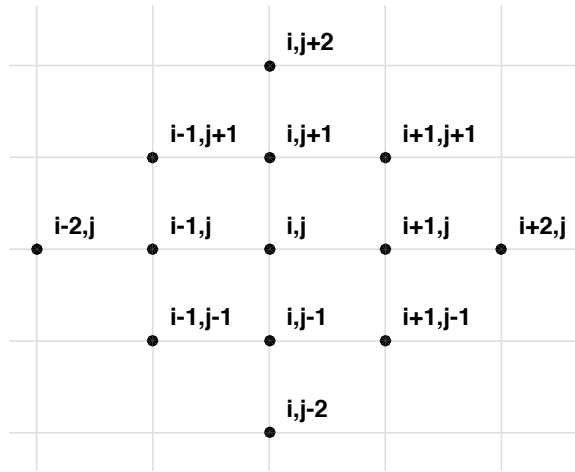


Figure 8.2: General pixel coordinates used for the formulation of demosaicing algorithms.

With reference to Fig. 8.2, at the location of a blue pixel with coordinate  $(i, j)$ , the green and red values  $G_{i,j}$  and  $R_{i,j}$  are computed in the bilinear interpolation as in Eqs. 8.1 and 8.2:

$$G_{i,j} = \frac{G_{i-1,j} + G_{i,j-1} + G_{i,j+1} + G_{i+1,j}}{4} \quad (8.1)$$

$$R_{i,j} = \frac{R_{i-1,j-1} + R_{i-1,j+1} + R_{i+1,j-1} + R_{i+1,j+1}}{4}. \quad (8.2)$$

When the location  $(i, j)$  falls on a green pixel (and on a row with alternating green and blue),  $R_{i,j}$  and  $B_{i,j}$  are reconstructed considering only the two neighboring pixels,

as in Eqs. 8.3 and 8.4.

$$R_{i,j} = \frac{R_{i,j-1} + R_{i,j+1}}{2} \quad (8.3)$$

$$B_{i,j} = \frac{B_{i-1,j} + B_{i+1,j}}{2}. \quad (8.4)$$

The Malvar algorithm operates over a larger 9 or 11-pixel stencil, it is a gradient-corrected approach and, unlike the previous method, it evaluates a pixel value considering information from all the available colors. With reference to Fig. 8.2, at the red and blue pixel locations with coordinate  $(i, j)$ ,  $G_{i,j}$  is computed using Eqs. 8.5 and 8.6, respectively:

$$G_{i,j} = G_{i,j}^{BL} + \alpha \Delta R_{i,j} = G_{i,j}^{BL} + \alpha \left( R_{i,j} - \frac{R_{i,j-2} + R_{i,j+2} + R_{i-2,j} + R_{i+2,j}}{4} \right) \quad (8.5)$$

$$G_{i,j} = G_{i,j}^{BL} + \gamma \Delta B_{i,j} = G_{i,j}^{BL} + \gamma \left( B_{i,j} - \frac{B_{i,j-2} + B_{i,j+2} + B_{i-2,j} + B_{i+2,j}}{4} \right). \quad (8.6)$$

Where the superscript  $BL$  means that the value  $G_{i,j}^{BL}$  is “predicted” with an initial bilinear interpolation.  $\Delta X_{i,j}$  is the gradient of color  $X$  at the location  $(i, j)$  that corrects the bilinear prediction, and  $\alpha$  and  $\gamma$  are “gain parameters” that control the intensity of the correction. For evaluating  $R_{i,j}$  at the location of a green and blue pixel, Eqs. 8.7 and 8.8 are used:

$$R_{i,j} = R_{i,j}^{BL} + \beta \Delta G_{i,j} \quad (8.7)$$

$$R_{i,j} = R_{i,j}^{BL} + \gamma \Delta B_{i,j}. \quad (8.8)$$

Here,  $\beta$  and  $\gamma$  are the gain parameters for the gradients  $\Delta G_{i,j}$  and  $\Delta B_{i,j}$ , respectively. The derivation of  $B_{i,j}$  uses similar formulas and the details of the spatial filters used for the 2D interpolations (i.e.  $\Delta G_{i,j}$ ,  $\Delta B_{i,j}$ , etc), as well as the values for the recommended gains  $\alpha$ ,  $\beta$ , and  $\gamma$ , can be found in [133].

## 8.2 Experimental setup

The effectiveness of demosaicing algorithms in improving ratio pyrometry results was tested in a sooty axisymmetric ethylene coflow diffusion flame (100%  $C_2H_4$ , 35 cm/s average velocity for the fuel mixture and coflow). To mimic conditions that will be encountered during the microgravity ACME campaign, the aforementioned reference flame was stabilized on the ACME coflow burner (fuel tube with a 2 mm I.D., coflow with a 25.4 mm I.D. - see Chapter 9), and images were acquired with the following two cameras:

- Nikon D300s, coupled to a 50 mm Nikkor lens: CMOS sensor, 4288 by 2848 pixels, 23.6 x 15.8 mm<sup>2</sup> sensor size, 14 bit A/D converter. Used in past pyrometry works [12, 22, 68].
- Prosilica GC1380-CH, coupled to a Navitar Zoom lens: CCD progressive sensor, 1360 x 1024 pixels, 8.77 x 6.60 mm<sup>2</sup> sensor size, 12 bit A/D converter. Selected for the ACME campaign [77].

The result obtained with the Nikon was considered here as a reference, and a high magnification was used for the raw image ( $\sim 128$  pixel/mm). Flame images were taken through a 1 mm thick BG7 Schott filter to mitigate the strong red emission of soot and balance the response of the three color channels. The Prosilica images were collected using the color filter and magnification that characterize the ACME imaging system (2 mm thick, coated BG7 Schott filter, raw image magnification of  $\sim 44$  pixel/mm). Each flame image was the result of an average over four acquisitions. The average raw image was decoded with no demosaicing into the three color channels using the image processing software OMA [50]. For the case of the Prosilica, an additional demosaicing using the bilinear interpolation and Malvar algorithm was done as well. The RGB images were finally Abel inverted to obtain the cross sectional intensities from the path-integrated luminosities, and pairs of color ratios were used with lookup

tables appropriate for each detection system to determine the soot temperature.

### 8.3 Results

Figure 8.3a shows the soot temperature of the reference ethylene flame evaluated with the Nikon camera; the spatial resolution of the result is reported at the base of the image, and the figure has been cropped to highlight only the sooty region, where temperature information is available (therefore the axial coordinate does not strictly represent the height above the burner). Figure 8.3b shows the normalized intensity of the Nikon Abel-inverted green channel's radial gradients. When the temperature is evaluated along the flame wings, where the steepest gradients are located, ratios taken between color pixels that belong to different columns, thus different radial locations, can return inaccurate results (note that the high gradient values close to the flame centerline are caused by the artificial noise introduced by the Abel inversion). To account for this, instead of decoding the green channel by averaging the values of the two diagonally-placed green pixels in each RGGB cluster, as it is generally done when no demosaicing is implemented, the reference temperature shown in Fig. 8.3a was computed using the  $B/G^*$  and  $G^+/R$  pairs, where the symbols  $*$  and  $+$  identify the green pixels located in a blue pixel column, and red pixel column, respectively. Due to the spectral transmissivity of the 2 mm BG filter, the Prosilica's red channel suffered of very poor signal-to-noise ratio, and the lookup table pertaining the  $G/R$  ratio flattened for temperatures larger than  $\sim 2500$  K. Even though soot never reaches those values, noise-induced fluctuations of the  $G/R$  ratio returned unrealistically high temperatures. For this reason, only the  $B/G$  ratio was considered for the temperature evaluation with the Prosilica.

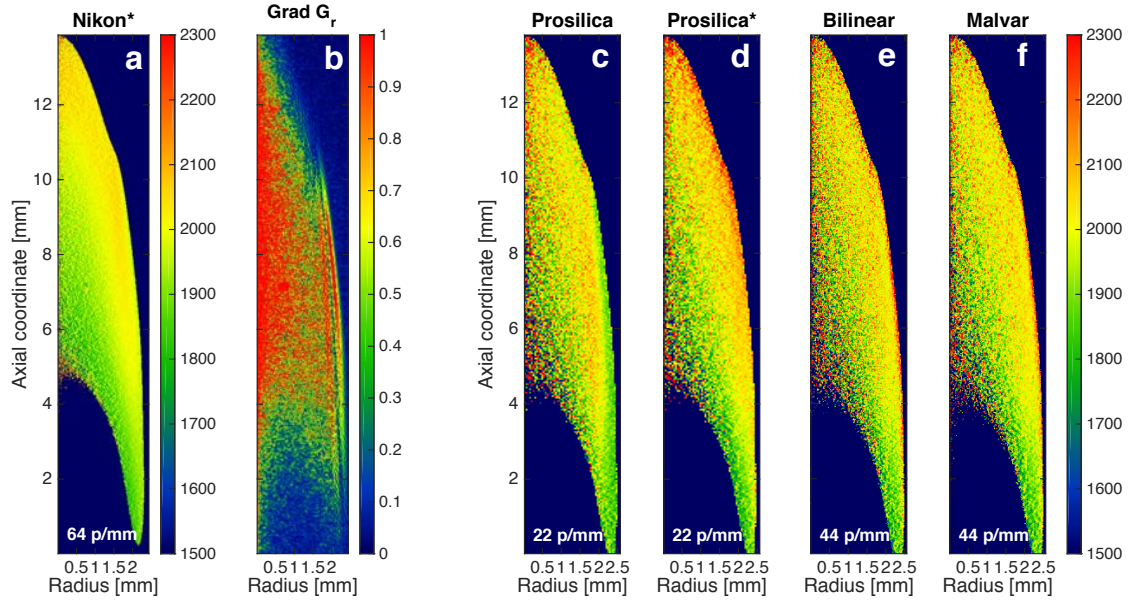


Figure 8.3: (a) Soot temperature, in Kelvin, for the reference  $C_2H_4$  flame evaluated with the Nikon D300s, and (b) normalized radial gradients intensity. Soot temperature evaluated considering the (c) B/G and (d) B/G\* ratios with the Prosilica. Soot temperature evaluated after implementation of (e) bilinear interpolation and (f) Malvar algorithm.

Figures 8.3c and 8.3d show the soot temperature maps for the reference ethylene flame measured using the Prosilica’s B/G ratio (where diagonally-placed green pixels are averaged) and B/G\* ratio (where only green pixels in blue columns are considered), respectively. The result obtained considering the B/G ratio showed an unrealistically low temperature region, close to the flame edge, that is not present in the reference result (Fig. 8.3a); the temperature is expected to increase towards the flame edge, where the flame front is located. The temperature obtained considering only the green values located on a blue column (Fig. 8.3d) returned a more realistic distribution that also mimicked more closely the distribution of the high-resolution reference result (Fig. 8.3a). The differences in absolute temperature, between the Nikon and Prosilica results, can be attributed to the implementation of different lookup tables (which are determined by the spectral responses of the detectors and transmissivities of the BG filters).

The alteration of the radial gradients that can happen when the green channel is decoded by averaging the two pixels of the RGGB cluster is larger if the image magnification is low. For these cases, considering pairs of colors by column, rather than by clusters, can improve the accuracy since no radial smoothing is introduced (as can be seen by comparing Fig. 8.3c and 8.3d).

Figures 8.3e and 8.3f show the temperature maps obtained from color channels that have been demosaiced with the bilinear interpolation and Malvar algorithm, respectively. The results obtained from the demosaiced data closely resemble both Fig. 8.3d and the reference temperature, with a distribution that does not show the unrealistic low temperature region along the flame wings.

As a way to assess the fidelity of the demosaiced data, Figs. 8.4a and 8.4b compare the ratios between the non-demosaiced Prosilica-derived temperature (Fig. 8.3d) and the bilinear and Malvar results, respectively. As seen in Eqs. 8.1 to 8.8, the interpolating algorithms span over several pixels, both axially and radially; despite this, the “demosaiced temperatures” agree reasonably well with the one obtained from the  $B/G^*$  ratio. In Figs. 8.4a and 8.4b, the white region identifies pixels where the difference is within  $\pm 2\%$ ; the main discrepancy is observed only along the very edge of the flame, where the difference approaches  $\sim 6\%$ . Given the test flame considered here and the imaging system’s characteristics, no significant differences in the evaluated temperature could be observed when implementing either the bilinear or Malvar algorithms.

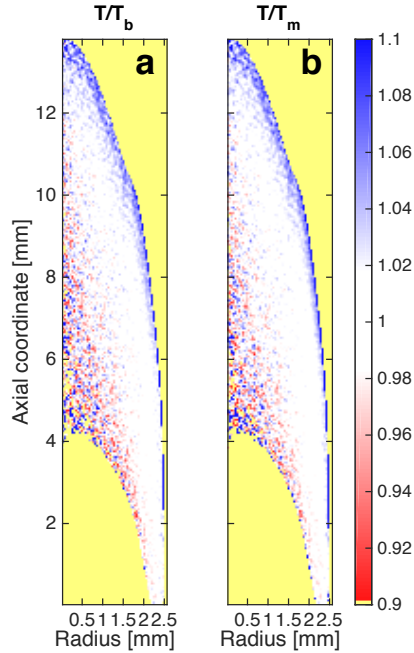


Figure 8.4: Ratios between non-desaiced and desaiced Prosilica temperature results: (a) bilinear interpolation and (b) Malvar algorithm.

The desaiced results, in addition to having a resolution equal to the raw image, were seen to have lower noise than for the non-desaiced case. Figures 8.5a, 8.5b, and 8.5c show the signal-to-noise ratio (SNR) maps of the temperature results presented in Figs. 8.3d, 8.3e, and 8.3f, respectively. The SNR has been evaluated according to the procedure introduced in Section 4.4: an initial two-dimensional Gaussian smoothing was done to the image over an area with a  $1/e^2$  full width of 10 pixels; then, in a two-dimensional 5 by 5 pixel sub-interrogation region centered around each pixel, the SNR was calculated by dividing the average value of the sub-interrogation region by the root mean square of the difference between the region intensity and the “average” surface obtained with the initial smoothing. The desaiced images’ SNR (Figs. 8.5b and 8.5c) was higher than the respective non-desaiced one (Fig. 8.5a); to reconstruct a color, the desaicing algorithms used averaged information from more than one pixel, smoothing out pixel-to-pixel noise. In the bilinear interpolation, a color is evaluated considering at least 2 neighboring pixels; the Malvar approach,

instead, interpolates a pixel considering at least 9 neighboring values, thus the higher SNR.

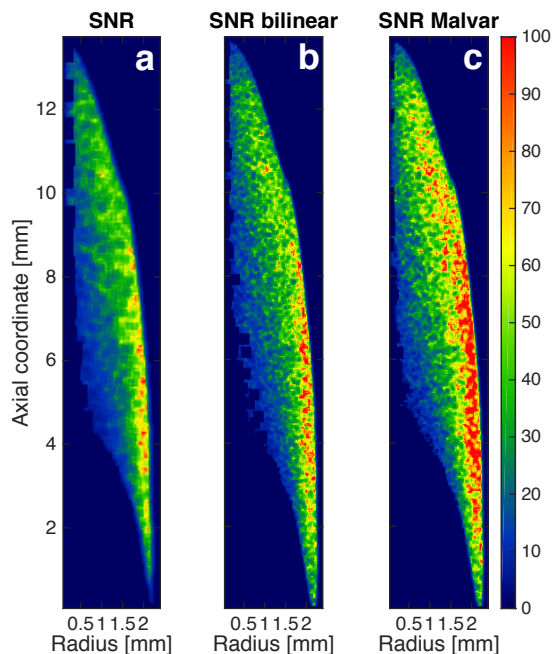


Figure 8.5: Temperature maps' SNR, calculated with the Prosilica. (a) non-demosaiced result, (b) bilinear interpolation, and (c) Malvar algorithm.

### Demosaicing applied to Abel-inverted blue images

The loss of spatial resolution that happens when no demosaicing is implemented can be detrimental when the features of interest are very narrow, as is the case with the Abel-inverted blue profiles that are used as marker for the  $CH^*$  chemiluminescence (see Chapter 6). Figures 8.6a, 8.7a, and 8.8a show the normalized Abel-inverted blue profiles from an ACME nitrogen-diluted methane flame (60%  $CH_4$ , 40%  $N_2$ , 30 cm/s for fuel mixture and coflow, lit on the ACME CLD flame burner), collected using increasingly smaller raw image magnifications (44, 34, and 20 pixel/mm). Since these highly-diluted flames are predominantly blue, and no soot is present, images were taken without the BG color filter. The maximum magnification of the ACME imaging system ( $\sim 44$  pixel/mm) is expected to be used for the majority of the flame

acquisitions; however, highly diluted cases, that are not sustained in normal gravity, may be lifted and may require different zoom settings (i.e. lower magnification).

As expected, the profiles tend to become noisier and less resolved as the magnification is lowered. Figures 8.6b, 8.7b, and 8.8b, and Figs. 8.6c, 8.7c, and 8.8c show the result of the implementation of the bilinear interpolation and Malvar algorithm, respectively. The white dashed line in Fig. 8.6a identifies the section chosen to plot the results displayed in Fig. 8.9.

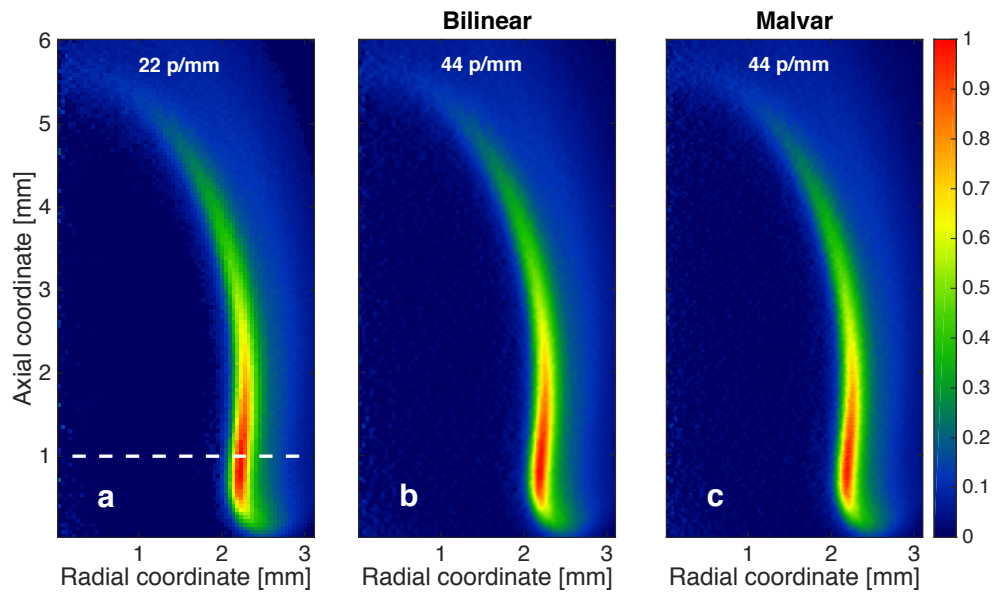


Figure 8.6: Abel-inverted blue profiles collected with the Prosilica and with a raw image magnification of 44 pixel/mm: (a) non demosaiced result, (b) bilinear interpolation, and (c) Malvar algorithm. The white dashed line identifies the section chosen to plot the results of Fig. 8.9.

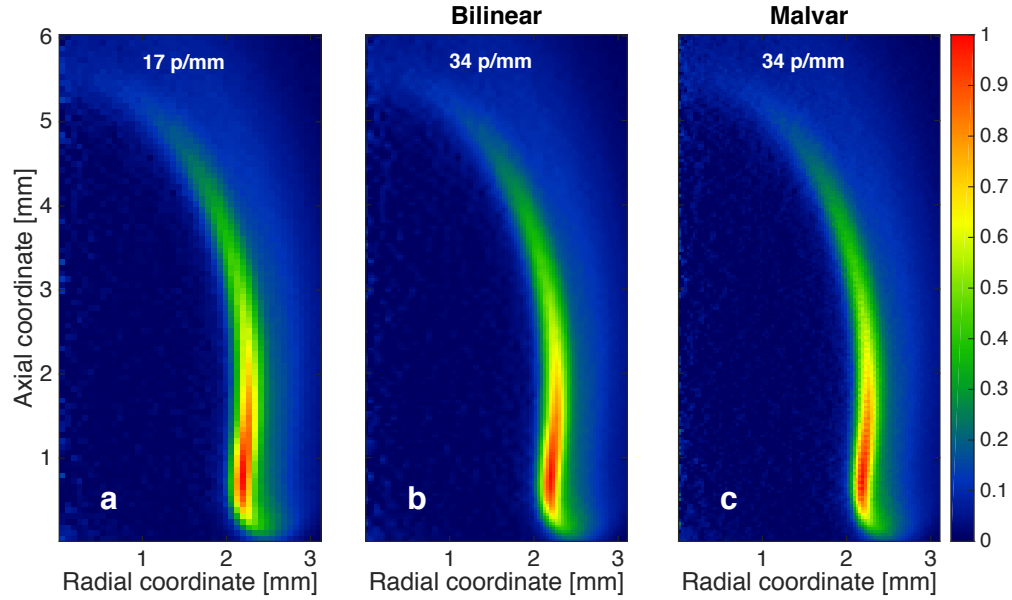


Figure 8.7: Abel-inverted blue profiles collected with the Prosilica and with a raw image magnification of 34 pixel/mm: (a) non demosaiced result, (b) bilinear interpolation, and (c) Malvar algorithm.

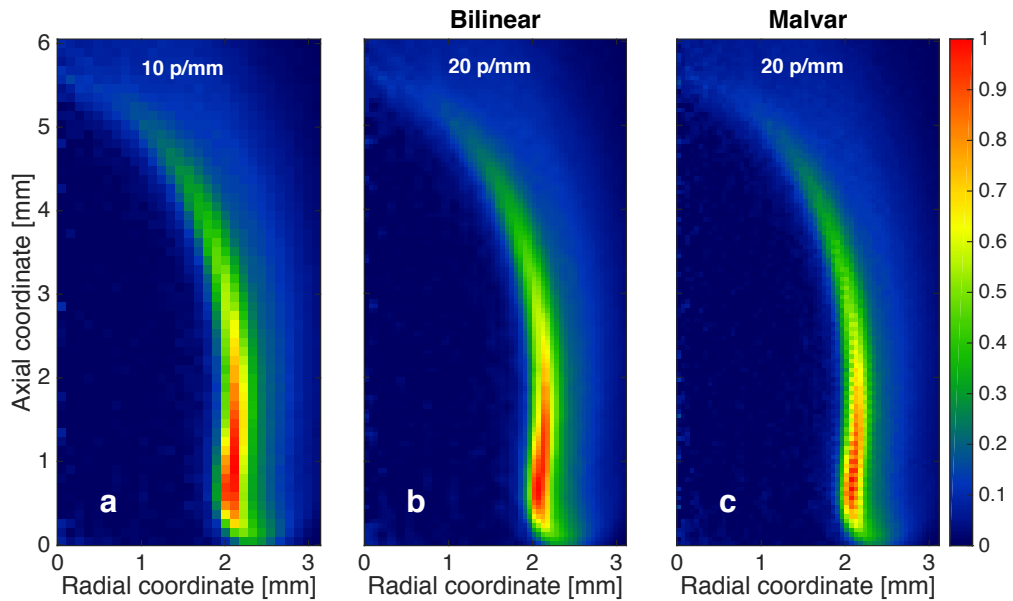


Figure 8.8: Abel-inverted blue profiles collected with the Prosilica and with a raw image magnification of 20 pixel/mm: (a) non demosaiced result, (b) bilinear interpolation, and (c) Malvar algorithm.

Naturally, the interpolated results were seen to improve the spatial resolution but, unlike the soot temperature measurements shown previously, the bilinear and Malvar interpolations displayed evident differences; in particular, the Malvar results were characterized by a striped pattern (clearly visible in Fig. 8.8c). Section 8.1 showed how, in order to reconstruct a blue pixel value, the Malvar algorithm uses information from the neighboring green and red pixels. In these kind of “blue” flames, however, the red channel intensity is roughly  $\sim 1/3$  of the blue one, and a more correct interpolation of the blue pixels would probably require different “gain parameters”.

Finally, Fig. 8.9 compares the normalized radial intensities, along the direction defined by the white dashed line of Fig. 8.6a. Fig. 8.9a refers to the results in Fig. 8.6; Fig. 8.9b refers to the results in Fig. 8.7; Fig. 8.9c refers to the results in Fig. 8.8. The non-desaiced profile with the highest resolution was taken as a reference, and its peak value used as a normalization parameter for all the other profiles.

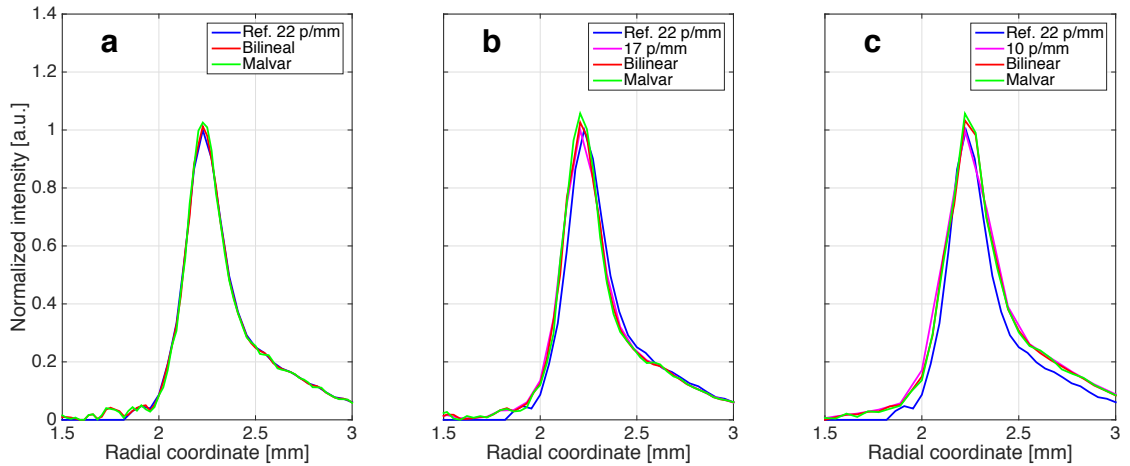


Figure 8.9: Normalized radial intensities, along the direction identified by the dashed line of Fig. 8.6a, of the Abel-inverted blue profiles shown in Figs. 8.6 to 8.8.

All the demosaiced data was seen to be consistent with the reference one. The higher pixel density, however, translated in better SNR, particularly for the bilinearly-interpolated results. The peak profile value returned by the bilinear interpolation was within  $\sim 3\%$  of the reference one, whereas the one returned by the Malvar algorithm

was within  $\sim 6\%$ .

## 8.4 Conclusions

The bilinear interpolation and the Malvar algorithm were tested as a way to maintain the spatial resolution and gradients when color images, collected through a Bayer-patterned CFA, are decoded into the RGB channels. Ratio techniques assume that pixels measuring different colors sample the same spatial location but, when the pixel density or the image magnification is low, this assumption is no longer valid and color ratios evaluated in proximity of steep gradients might not be correctly reproduced. An ethylene flame was taken as a test case and the soot temperature measured with color ratio pyrometry. A reference result was compared to a set that included both demosaiced and non-demosaiced data obtained with a Prosilica CCD (selected for the ACME experimental campaign). It was seen that by considering pairs of color ratios by columns, rather than by RGGB clusters, radial temperature gradients were reproduced more accurately; this approach was used to evaluate the reference temperature result. The demosaicing algorithms were found to be less sensitive to the presence of radial gradients and were able to return temperature distributions that agreed with the reference one. They retained the spatial resolution of the raw image while returning an improved SNR and, for the test case considered here, the maximum temperature discrepancy was close to 6%.

Additionally, the bilinear interpolation was seen to be beneficial in improving the spatial resolution and SNR when used for the evaluation of Abel-inverted blue profiles. The Malvar algorithm, on the other hand, returned noisier results as a consequence of a less-than-optimal interpolation gain parameter.

# Chapter 9

## ACME experiments

The scope of this chapter is to summarize the preliminary evaluation, characterization, and calibration work done on the NASA *Advanced Combustion via Microgravity Experiments* (ACME) coflow laminar diffusion (CLD) flame burner and detector for the upcoming combustion experiments to be performed on the International Space Station (ISS) in 2017 [77]. In the following sections, the word “*flight*” will refer to components that are going to be delivered and operated on the Space Station for the microgravity experiments, while the word “*ground*” will refer to copies that will be used for the normal gravity measurements.

### 9.1 Burner design

The ACME CLD burner was designed as an improvement over the previous SLICE one [109] in an attempt to correct for some of the limitations that affected the latter. In ACME, the coflow is controlled with a mass flow controller instead of an electric fan, providing a more stable and accurate coflow velocity. The coflow is limited to a co-annular region 25.4 mm in diameter with a flow straightener specifically designed to provide a flat and steady velocity profile. The burner will be operated in the *Combustion Integrated Rack* (CIR). The CIR is a sealed environment (volume of  $\sim$

80 liters) whose volume, depending on the result of preliminary tests, will be likely filled with nitrogen at the beginning of every test run (on the ISS, air is a life-supporting gas, therefore more valuable than nitrogen). Because of the initial inert environment, an electric fan like the one used in SLICE would not be adequate for providing oxidizer to the flame.

The first prototype of the ACME CLD burner designed at Yale, shown in Fig. 9.1, was a scaled-down version of the burner described in Section 2.1: the fuel tube had an inner diameter of 2.16 mm, an outer diameter of 2.41 mm, and the coflow had a inner diameter of 25.4 mm. The fuel tube length was such that the flow developed a parabolic profile, while the coflow was designed to have a plug flow profile.

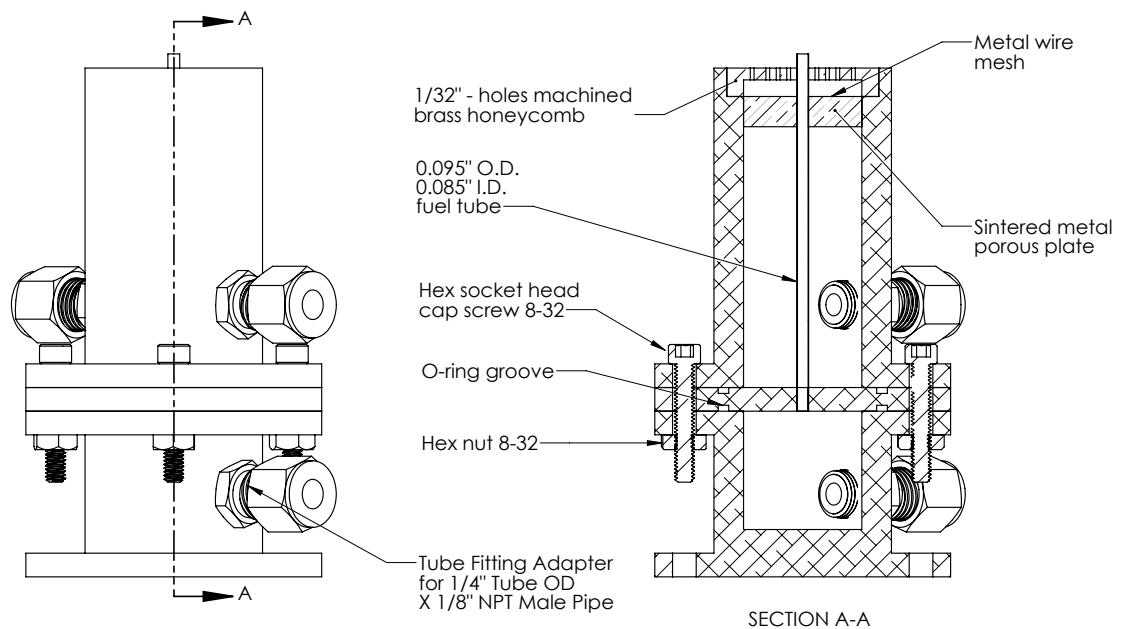


Figure 9.1: Yale prototype of the ACME CLD burner.

To ensure a symmetric and flat velocity profile, the commonly used 0.79 mm (1/32") cell hexagonal honeycomb that was implemented as a flow straightener for the coflow in the larger burner, was replaced by a 3.17 mm thick CNC machined brass plate with 0.79 mm holes placed in an axisymmetric arrangement (see Fig. 9.2). It was noticed that, with this smaller burner, the symmetry of lifted flames was very sensitive to

honeycomb imperfections and asymmetries. As a consequence of difficulties in cutting a hole that was perfectly centered with respect to a honeycomb cell (to accommodate the fuel tube), the machined plate option was tested and initially preferred over the more conventional hexagonal honeycomb. Additionally, a sintered metal porous plate was placed inside the coflow duct to introduce a pressure drop and obtain a velocity distribution as flat as possible.

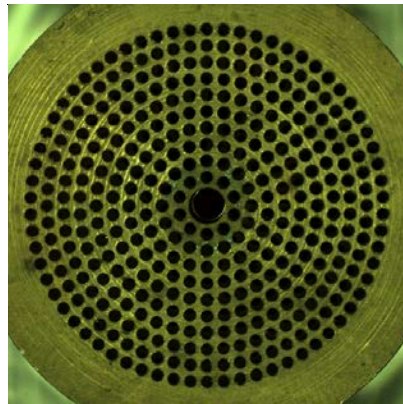


Figure 9.2: CNC-machined brass plate used to replace the conventional honeycomb in the 25.4 mm (1") coflow burner.

One drawback of the machined brass plate over the conventional honeycomb, was the reduced ratio open area; for a nominal coflow rate, the outlet radial velocity profile was characterized by small and discrete air jets that had a peak velocity higher than the nominal one. To allow for the radial diffusion to decrease the axial velocity and match the desired average flow velocity at the fuel tube outlet, the fuel tube itself was set to protrude 3 mm above the coflow surface. Fig. 9.3 shows velocity profiles measured at different heights above the coflow outlet, demonstrating how the coflow profile flattens for heights above the burner (HAB) equal or greater than 3 mm (given a nominal coflow velocity of 35 cm/s).

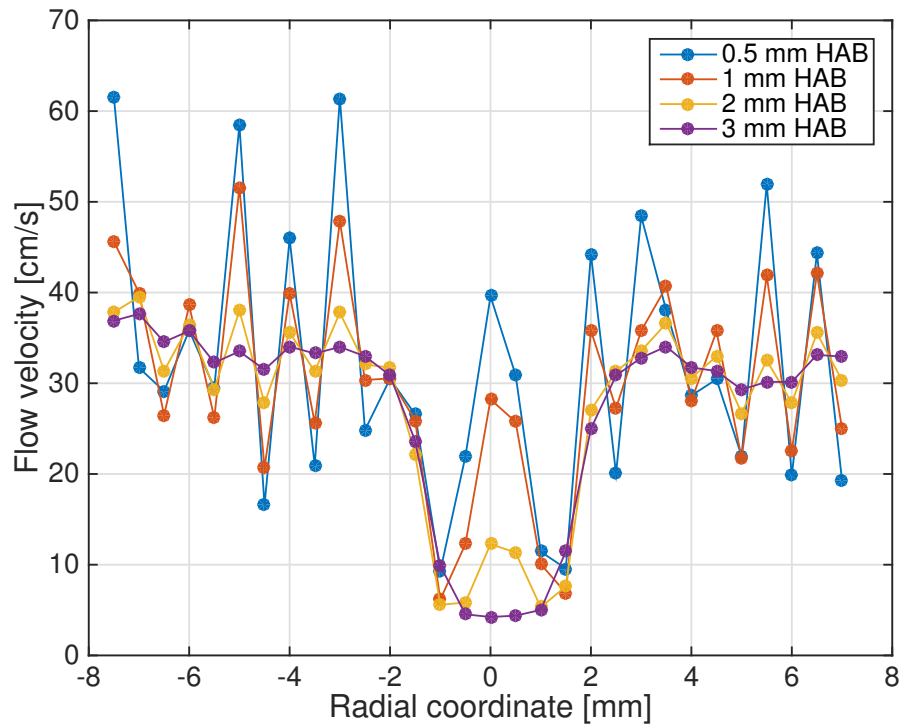


Figure 9.3: Comparison between velocity profiles measured at different HAB.

The version of the CLD burner built by the NASA contractor (ZIN Technologies Inc.) is shown in Fig. 9.4. Without considering the exterior appearance and dimensions, which are irrelevant to the flow characteristics, the following modifications were implemented with respect to the Yale prototype:

- Machined brass plate thickness reduced from 3.17 mm to 1.59 mm. Drilled holes placed in a non-axisymmetric arrangement.
- Coflow diameter reduced from 25.4 mm to 25.0 mm.
- Sintered metal porous plate replaced with a 3D printed ceramic flow straightener (for reasons related to material origin and certification).

Additionally, the flight and ground units were not exactly identical, because of minor damages of the ceramic flow straightener, which resulted in the two burners behaving differently (in terms of flow profiles and flames shapes).

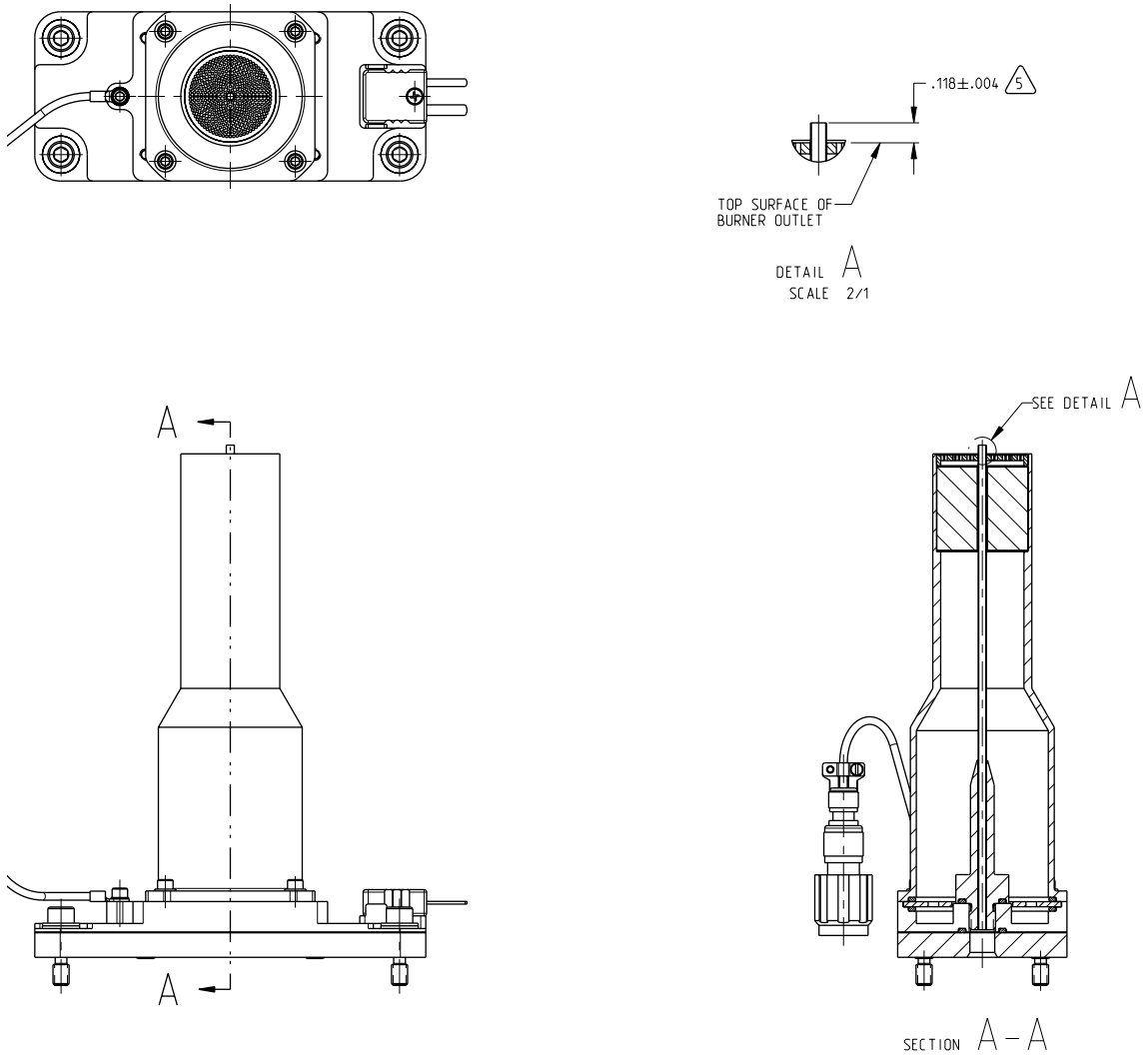


Figure 9.4: Version of the ACME CLD burner built by ZIN Technologies.

### Influence of chamber filling

As mentioned, nitrogen will likely be used to purge the sealed CIR and it will be the gas that will fill the chamber at the beginning of every test run; the oxidizer needed to sustain the flames will be provided by the coflow. To simulate the CIR closed environment, the ground experiments will be performed in a 44.2 liter cylindrical pressure chamber. To understand if the initial chamber filling gas had any effect on the flame structure, tests were done by placing the Yale prototype of the CLD burner in the pressure chamber, and by monitoring flames lit with the chamber initially filled

with either nitrogen or air. Specifically, images of a coflow ethylene flame (35 cm/s velocity, for fuel mixture and coflow) were taken with a Nikon D70 camera and the the peak flame luminosity, as well as the flame length, was measured as a function of time. Figure 9.5 shows the temporal evolution of the normalized peak flame luminosity (Fig. 9.5 top - considered here as the peak red value, given the sooty nature of the flames) and normalized flame length (Fig. 9.5 bottom) . The chamber had the needle valve used to seal it completely open, thus avoiding any pressure increase over the 8 minute acquisition time.

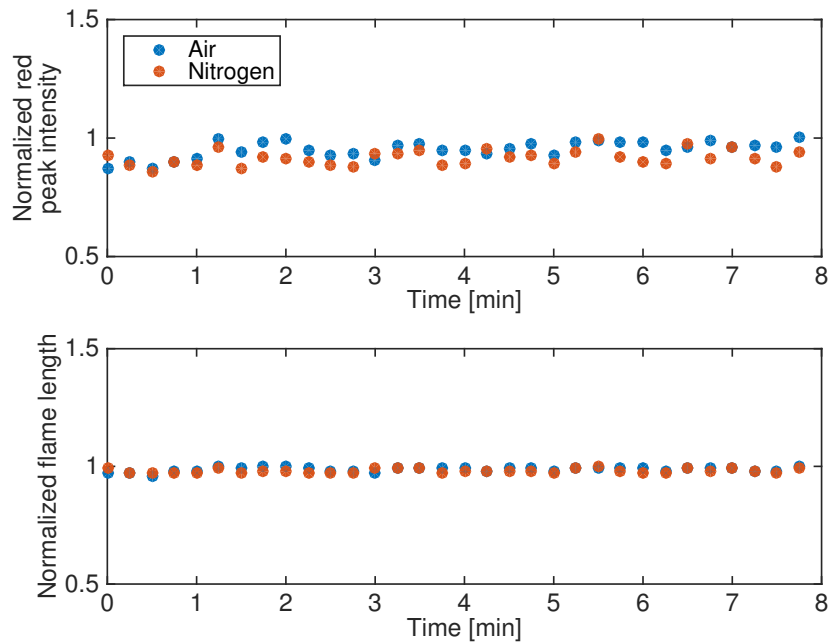


Figure 9.5: Comparison between peak flame luminosity (top), and flame length (bottom), for flames lit in an air-filled and nitrogen-filled pressure chamber.

By comparing the results obtained with the chamber initially filled with nitrogen or air no noticeable differences could be seen and it was concluded that the  $N_2$  entrainment induced by the coflow did not disrupt or modify the structure of the diffusion flame; therefore, the normal gravity experiments could be accurately performed in an air-based environment.

## 9.2 CLD burner flow velocity profiles

The flow velocity profiles of the ACME CLD burner had to be characterized so that they could meet the design specifications provided by the NASA *Integrated Science Requirement Document* (ISRD) [135], in terms of symmetry and uniformity. Hot wire anemometry was used to scan the burner and measure the flow profiles as a function of flow rates and height above the burner. Figure 9.6 shows a top view of the CLD burner with the colored arrows (blue, red, green, orange, defined as A, B, C, and D in the following sections, respectively) identifying the hot wire scanning directions. The teal arrow shows the ACME camera viewing direction.

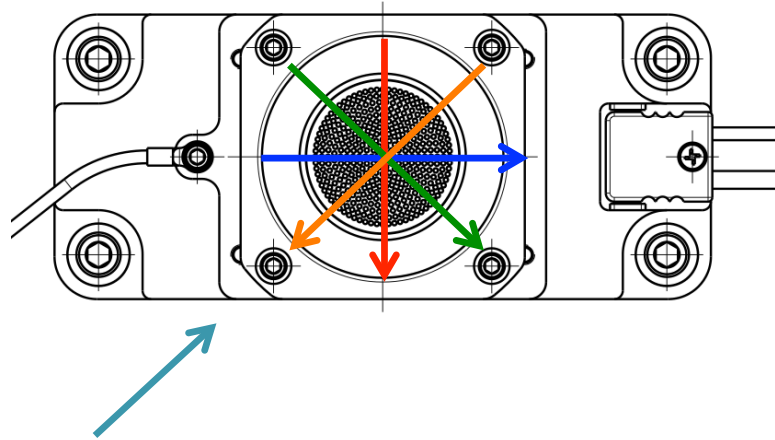


Figure 9.6: Top view of the ACME CLD burner with the hot wire scanning directions identified by the blue, red, green, and orange arrows. The teal arrow identifies the ACME camera viewing direction.

Among the requirements listed in the ISRD, the following were the ones that were subject of investigations and whose results are reported in this thesis:

- **1.4.9:** The burner shall have a uniform flow profile that is axisymmetric, i.e., where the velocity is independent of the angular position, especially (at radial positions) near the burner center. For the coflow burner, axisymmetric flow means that the variation in axial velocity with angular position (e.g., as measured in **1.4.11**) shall be less than 10% of the (mean) velocity, where this shall

hold for all radial positions from 0 to 10 mm.

The burner gas shall be ejected parallel to the chamber axis and without either swirl (i.e., helically rotating flow) or turbulence (i.e., eddies). To be without turbulence, the axial velocity at any position 0.5 mm downstream of the burner (e.g., as measured in 1.4.11) shall be constant with time within 3% (i.e., of the time-averaged value).

- **1.4.11:** The burners flow profile, across a plane orthogonal to the burner axis and within 0.5 mm downstream of the inner tube outlet, shall be well documented. The spatial uniformity shall be verified by 1g measurement of the velocity field using a cold flow (i.e., with no flame) simultaneously through both the annulus and the inner tube. The axial velocity shall be measured across a diameter of 30 mm at increments of no greater than 5 mm, especially within 5 mm of the burner axis where the increments shall be no greater than 1 mm. Unless otherwise specified, measurement across one diameter is sufficient.
- **1.4.11.1:** The flow profile shall be measured for a range of flow velocities in 10 cm/s increments from 20 to 50 cm/s where the inner tube and annulus velocities are matched.
- **1.4.11.2:** For the case of matched velocities at 10 cm/s, the flow profile shall be measured for at least four diameters (as just described) at increments of no greater than 45 degrees.
- **1.4.11.3:** The flow profile shall also be measured where the inner tube and annulus (i.e., outer tube) velocities are not matched for the following 11 velocity pairs: 0:10, 0:20, 0:30, 0:40, 0:50, 10:30, 10:50, 30:10, 30:50, 50:10, and 50:30 where each velocity pair is given as inner:outer and the values are in cm/s.

As a way to provide a more accurate set of measurements (considering that the measured velocity profiles will be used as boundary conditions for numerical simulations),

the following deviations from the ISRD were implemented:

- The hot wire scanning increments were set to 0.25 mm instead of the suggested minimum of 1 mm (1.4.11).
- Three heights above the burner were sampled (0.5, 5, and 10 mm) instead of the required 0.5 mm HAB (1.4.11).
- The four diameters were scanned for all the cases of matched flow velocity (1.4.11.2).

### 9.2.1 Hot wire setup and calibration

The burner velocity profiles were measured with a TSI hot wire system (TSI IFA-100 coupled to a TSI 1212-T.15 90° wire probe with a tungsten platinum coated filament - 3.8  $\mu\text{m}$  diameter and 1.27 mm sensitive length). A cold flow of air and nitrogen were used for the coflow and fuel tube, respectively, and set with a Sierra Instrument Smart Trak mass flow controller (maximum flow rate of 20 slpm of air, used for the coflow), and a Unit Instruments Inc. mass flow controller (maximum flow rate of 300 sccm of  $N_2$ , used for the fuel tube flow). The nitrogen controller was calibrated daily, before any measurement, with a manual bubble flow meter to correct for daily offset variations. The calibration of the air controller (which was known to be stable and repeatable) was verified twice, once before any measurement, and once at the end, with a mechanical flow meter calibrator. The flow rates were set based on a nominal coflow I.D. of 25.4 mm, and a fuel tube with I.D. of 2.16 mm and O.D. of 2.41 mm. The settings implemented for the hot wire system's electronics were:

- Cable resistance: 0.413 ohm
- Operative resistance: 10.56 ohm
- Bridge compensation: 35

- Gain: 20
- Offset: 1

The plot in Fig. 9.7 shows the result of the calibration performed on the hot wire probe (using a TSI 112700 calibrator), as well as the interpolating curve used to evaluate the flow velocity from the hot wire voltage readings.

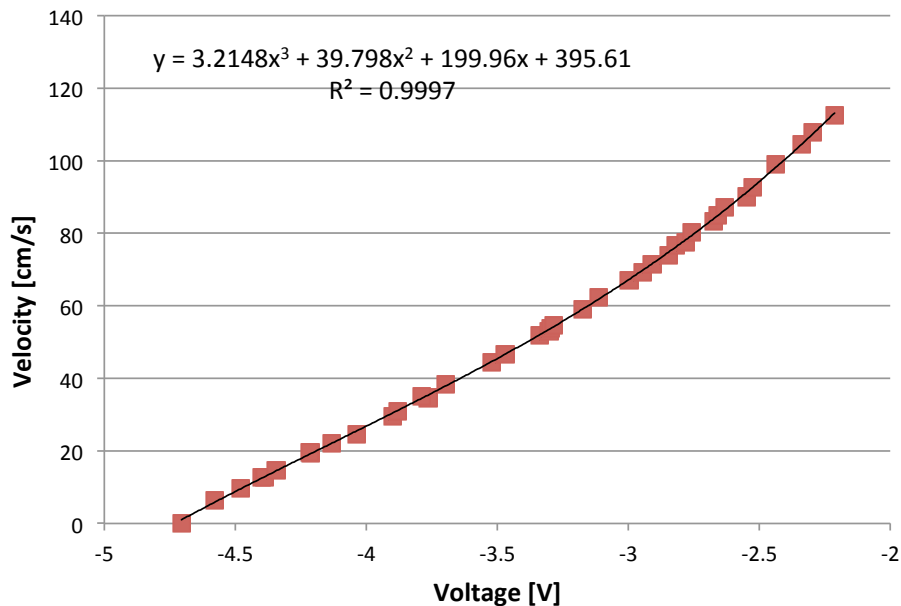


Figure 9.7: Calibration curve of the hot wire probe used for the measurements of the CLD burner flow profiles.

For the burner scan, the hot wire probe was mounted on a horizontal translation stage driven by a Velmex stepper motor; the height of the probe was varied with the help of a second manual translation stage. The software OMA was used to control the stepper motor and automate the acquisition process, as well as to record the hot wire voltage signals through a LabJack U12 (12 bit A/D converter, 4000 Hz sampling rate, 0.25 s acquisition time). The hot wire readings from radial positions between the fuel tube walls ( $r = \pm 1$  mm) were corrected to account for the fact the the flow hitting the sensitive part of the probe was not flat, but had a tridimensional paraboloid shape. It was assumed that the probe was invested by, and centered with

respect to, a parabolic velocity profile. For each chord, defined as the projection of the hot wire on the circular fuel tube, the correction factor was evaluated as in Eq. 9.1

$$K = \frac{3u_{max}^*}{2u_{max}^* + u_{min}^*}, \quad (9.1)$$

where  $u_{max}^*$  and  $u_{min}^*$  are the maximum and minimum velocities hitting the probe, respectively:

$$u_{max}^* = u_{max} \left( 1 - \frac{d^2}{R^2} \right) \quad (9.2)$$

$$u_{min}^* = u_{max}^* \left( 1 - \frac{w^2}{R_c^2} \right). \quad (9.3)$$

Here  $u_{max}$  is the peak velocity of the flow ( $= 2\bar{u}$ , as determined by the given volumetric flow rate),  $R$  is the inner radius of the fuel tube,  $d$  the distance of the chord from the fuel tube centerline,  $R_c$  the half length of the chord, and  $w$  the half length of the wire sensitive length. The correction described here was applied only to the measurements performed at 0.5 mm above the burner. At 5 and 10 mm above the burner the flow assumptions were not believed to be valid as a consequence of the mixing happening between fuel flow and coflow.

## 9.2.2 Results

The plots in Figs. 9.8, 9.9, and 9.10 show a subset of the required measurements defined earlier, when performed on the flight unit of the CLD burner shown in Fig. 9.4. The plots on the left display the velocity profiles, as a function of the radial coordinate, along four scanning directions; the plots on the right verify the flow symmetry by mirroring the left and right sides of each scan (red and green curves, respectively, with respect to the burner centerline) and comparing it to the average profile (blue curve). The blue shaded region represents the  $\pm 10\%$  variation with respect to the average velocity.

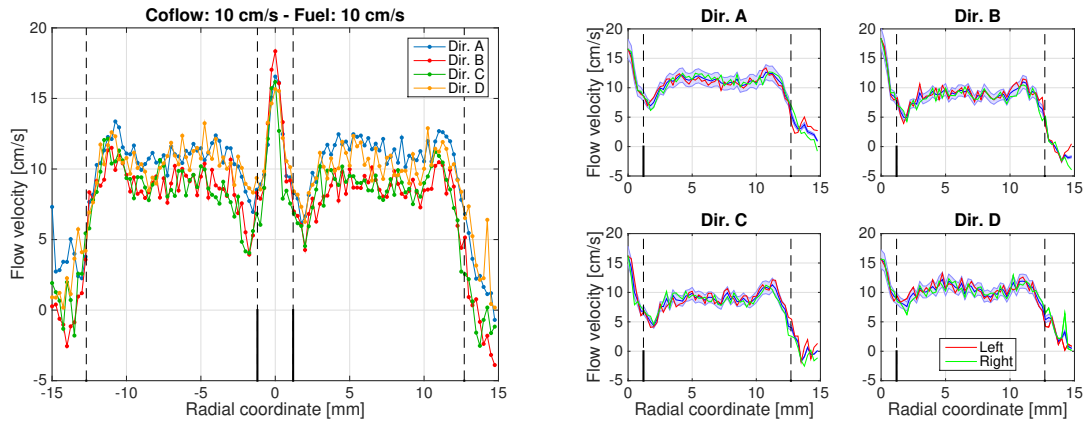


Figure 9.8: (Left) velocity profiles as determined from hot wire measurements and (right) symmetry plots - 10 cm/s matched flow velocities.

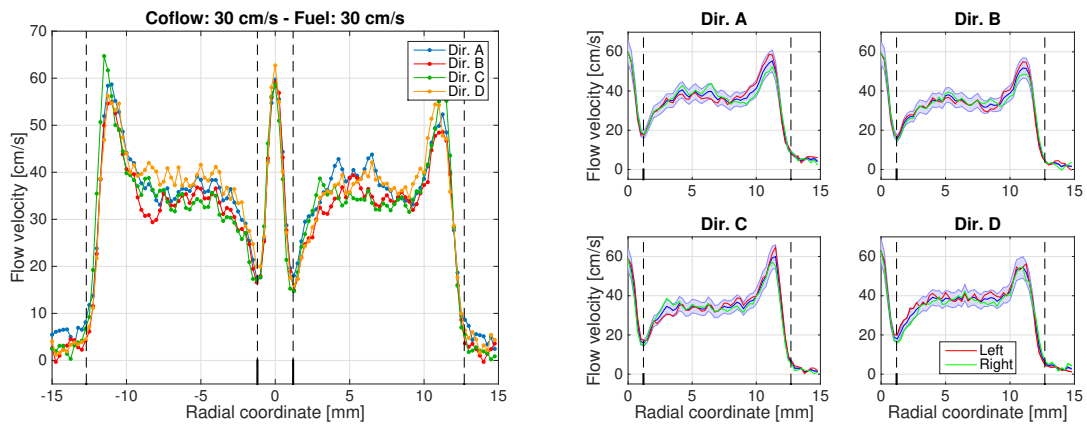


Figure 9.9: (Left) velocity profiles as determined from hot wire measurements and (right) symmetry plots - 30 cm/s matched flow velocities.

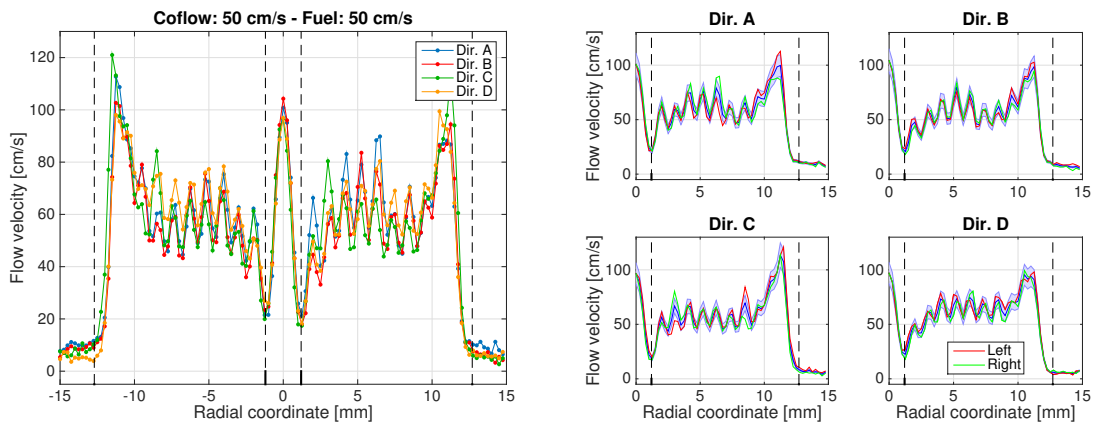


Figure 9.10: (Left) velocity profiles as determined from hot wire measurements and (right) symmetry plots - 50 cm/s matched flow velocities.

As it was clearly seen from the results in Figs. 9.8, 9.9, and 9.10, the performance of the flight burner was unacceptable since it did not satisfy the ISRD requirements. Even though the radial symmetry condition was satisfied (the radial profiles fell inside the  $\pm 10\%$  “blue shaded region”), the uniformity of the flow profiles was not. A similar behavior was observed with the ground unit of the burner, but those results are not shown here.

To improve flow symmetry and uniformity, the coflow internal components were replaced with a new set which allowed for satisfaction of the requirements (Fig. 9.11). The machined brass plate was replaced with a conventional 6.35 mm (1/4”) thick, 0.79 mm (1/32”) cell honeycomb (specifically selected from a pool of several honeycombs), while the ceramic flow straightener was replaced by a wire mesh sandwiched between two spacers. The height of the spacers, as well as the distance between wire mesh and honeycomb, was optimized in order to return flow profiles and flames as symmetric as possible.



Figure 9.11: Original (left) and final (right) CLD burner coflow internal components.

The new components were then implemented by NASA in revised versions of the flight and ground units of the CLD burner and underwent a second run of tests and characterization.

## Revised burner

The revised flight burner was characterized, once again, in terms of flow velocity profiles following the directives described in Section 9.2. Flow symmetry and uniformity were greatly improved and the results, due to the extent of the measurements, are not shown here but are reported in Appendix A (Figs. A.1 to A.16). It was also verified that the flow did not display any unsteadiness or turbulence (as in ISRD 1.4.9). Unlike the flow measurements described in Section 9.2, the ones done to verify the lack of turbulence were performed as follows:

- Each data point was evaluated as a one second average (sampling at 4000 Hz).
- Only one scanning direction was considered (blue arrow, or direction “A”).
- The scanning intervals were equal to 1 mm.
- With reference to Fig. A.17, the error bars in the “flow velocity” plots are equal to  $\pm \sigma$ .
- With reference to Fig. A.17, the “percent deviation” plots display the relative difference of the absolute value of  $\sigma$  with respect to the average velocity value.

The noise, and therefore the deviation from the time averaged value, was seen to be inherent to the measuring device, and not dependent on the flow (as can be seen from the “0 cm/s” measurement). Therefore it was concluded that the burner was able to provide a steady flow without unsteadiness or turbulence.

The flame symmetry was verified following ISRD 1.4.12:

- **1.4.12:** The coflow flame shall be axisymmetric over the full range of flow conditions. To be axisymmetric, (1) the variation in the radius of the visible flame edge with angular position shall be less than 10% of the (mean) radius for all axial positions from the flame base to tip, and (2) the plane of the

flames visible base shall be orthogonal to the burner axis such that the variation in axial distance from the visible flame base to the burner outlet (along the circumference of the base) is no more than 1 mm, especially for lifted flames, where the flame is detached and downstream from the burner outlet. [...] The axisymmetry of a 50/50  $CH_4/N_2$  flame shall be demonstrated in 1g for a range of flow velocities in 10 cm/s increments from 10 to 50 cm/s where the inner tube and annulus velocities are matched.

Figure 9.12 shows the result of this analysis displaying 5 different 50% methane flames with increasing flow velocities (shown as normalized line of sight luminosity). In the figure, the solid white lines identify the flame bases (evaluated, in the case of tilted flames, as the midpoint between the lower and upper base of the flame wings), while the dashed lines are the  $\pm 0.5$  mm variations with respect to the average value. The flow velocity values are labeled at the bottom of each case.

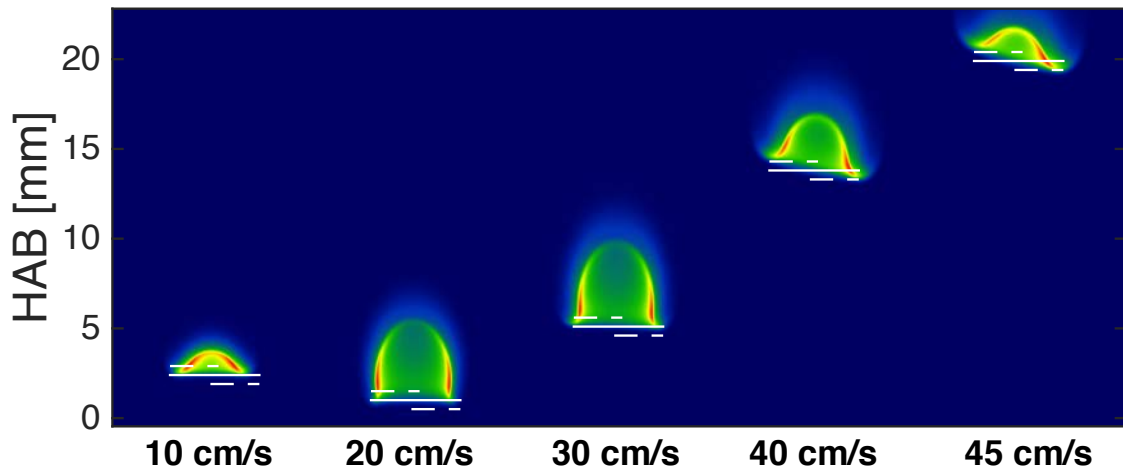


Figure 9.12: 50% methane flames selected for the verification of flame symmetry: the solid white lines identify the flame bases, while the dashed lines are the  $\pm 0.5$  mm variations. Flow velocity shown at the bottom of each flame.

The symmetry of the test flame was seen to be satisfactory for flow velocities up to or equal to 30 cm/s, above which the lift off became significant and the flames started tilting. The case at 40 cm/s barely satisfy the ISR requirements, and higher flow

rates produce flames that are even more tilted. As it will be clear from the flame image results introduced in Section 9.4, the flame tilting is closely related to the lift off and becomes significant for flames that are lifted more the  $\sim 10$  mm above the burner.

### 9.3 Detector characterization and calibration

As a detector aimed at the quantitative measurements of physical properties, the ACME color camera (Prosilica GC1380-CH, see Fig. 9.13) had to undergo characterization in order to evaluate its linearity characteristics and the spectral sensitivity of the RGB color channels.

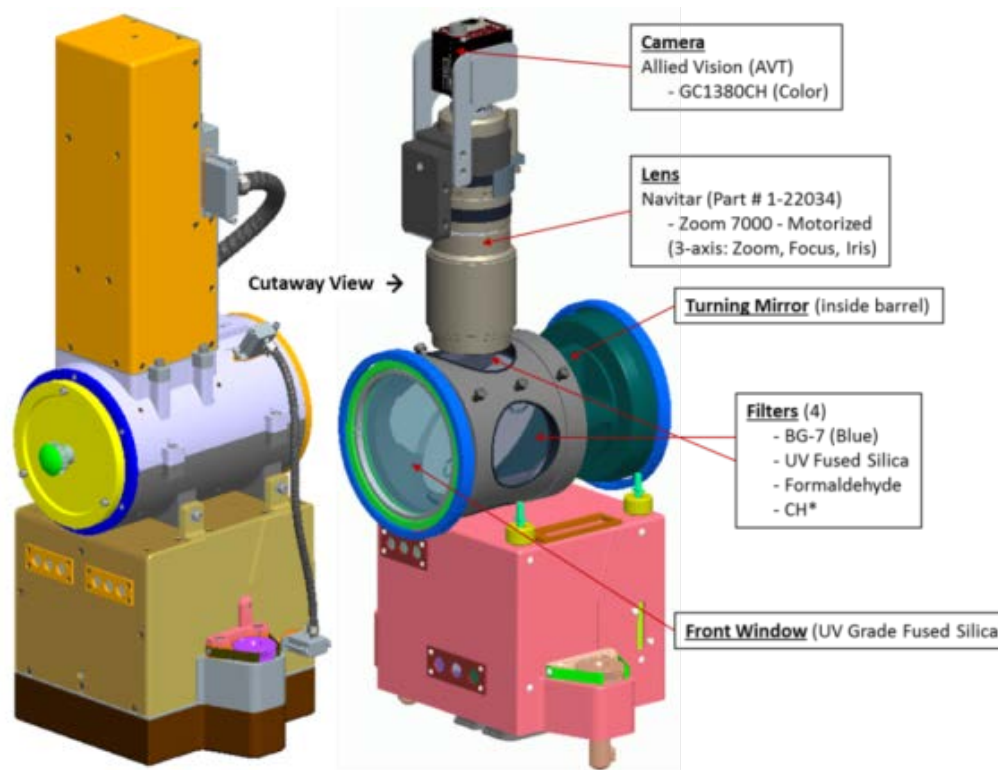


Figure 9.13: Drawing of the ACME imaging system, showing the camera, lens, and optical filter barrel.

The linearity analysis has already been shown in Section 4.2 whereas the spectral

response, shown in Fig. 9.14, was determined following the procedure outlined in [6]. For compactness reasons, the ACME imaging system is mounted vertically next to the chamber that houses the burner, and a turning mirror is used to reflect images from the chamber into the camera lens. Multiple optical filters are available for different measurements, and are mounted on a rotating filter barrel. The relative spectral transmissivity of the coated ACME 2 mm BG7 color filter (the one relevant to the CLD flame measurements) is shown in Fig. 9.14 as well, together with the transmissivity of the turning mirror.

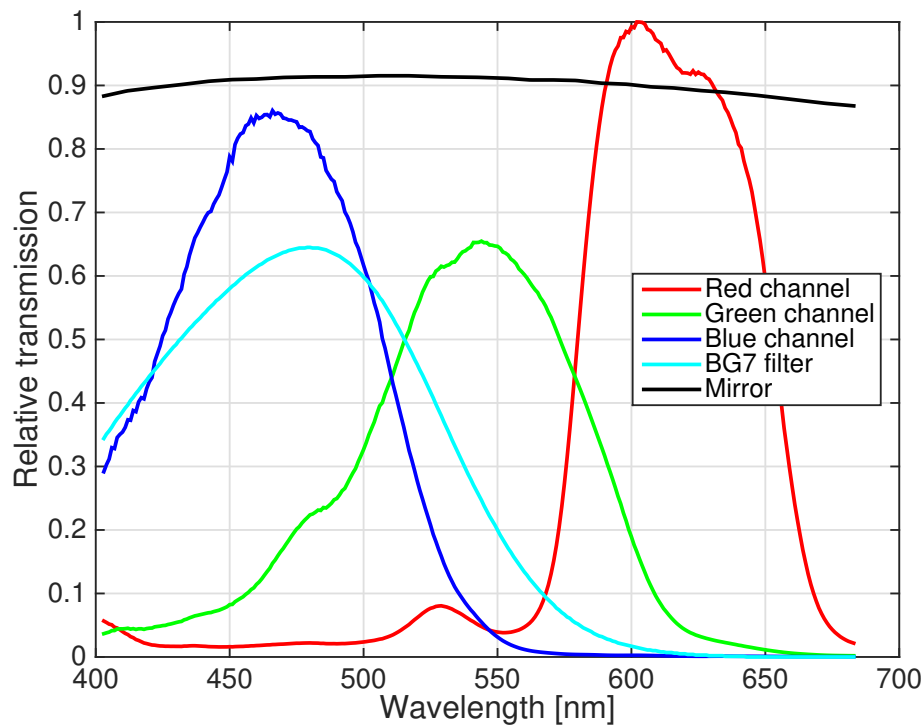


Figure 9.14: Spectral response of the Prosilica GC1380-CH, BG7 coated color filter, and turning mirror.

The absolute light intensity calibration that is required to quantify soot volume fraction and  $CH^*$  concentration (see Section 2.2.5) strongly depends on the specifics of the imaging system such as lens aperture, imaging collection angle, transmissivity of the components on the optical path, etc. To mimic conditions as realistic as possible,

the absolute light intensity calibration was performed off-site at ZIN Technologies using the actual flight detector and acquisition system. An S-type thermocouple (*Pt* wire, 200  $\mu\text{m}$  diameter, with a cylindrical junction) was placed at 253 mm from the “front window” (see Fig. 9.15), simulating the real distance between the center of the CIR (where the CLD burner will be positioned) and the detection system.

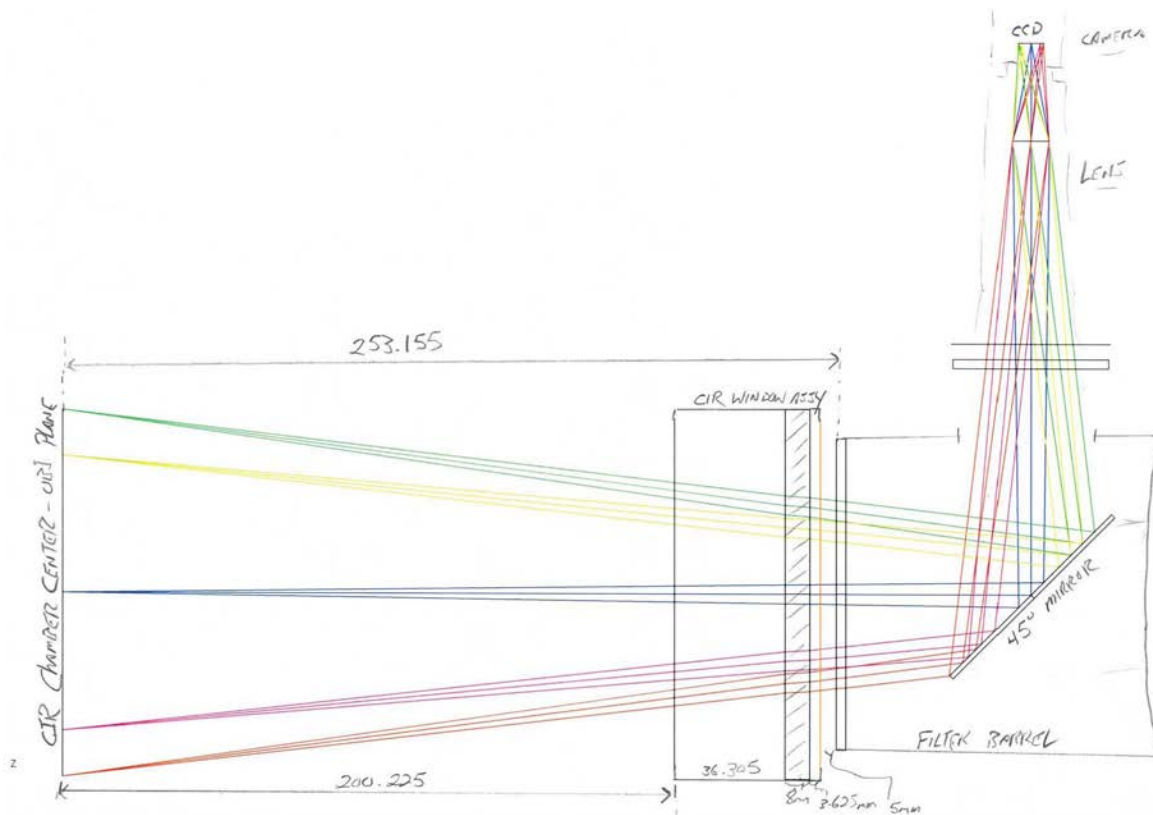


Figure 9.15: Geometry and optical path of the ACME color camera.

The thermocouple was heated with a premixed propane flame generated with a soldering torch; the fuel flow rate was kept stable and constant with the use of a mass flow controller. The thermocouple voltage was monitored with a National Instrument NI9211 through a Labview VI. The soldering torch was mounted onto a translation stage so that the thermocouple temperature could be varied by simply heating the junction with areas of the flame progressively distant from the flame front. Despite being positioned inside the flame, the thermocouple luminosity was larger than the

flame chemiluminescence and did not corrupt or modify the real thermocouple emission (as determined from the analysis of background images). Images of the heated thermocouple junction were taken with the Prosilica camera (1360x1024 pixels, 0 dB gain, white balance: 1/1, file format: BayerRG12) as a function of temperature and for several configurations of the optical system, obtained by varying the lens aperture and zoom. The thermocouple and background images were the result of the averaging over ten images, and each case had an exposure that used at least 75% of the detector's dynamic range, for a satisfactory signal-to-noise ratio. The test conditions are summarized in the following list:

- Thermocouple temperature: 1277, 1410, 1571, 1655, 1698, 1739, 1804, 1943 K.
- Zoom magnification: 44, 33, 25, 18 pixel/mm.
- Lens  $f$ -number: 2.5, 4, 5.6, 8, 11, 16.

The aforementioned thermocouple measurements were used to verify the  $Pt$  wire lookup tables and, in turn, to verify the accuracy of the flight camera spectral response and filter transmissivity. Figure 9.16 compares the experimental color ratios to the numerically-derived curves, when considering images taken with a magnification of 44 pixel/mm and a lens  $f$ -number of 2.5. In order to match the theoretical and experimental values, the camera's red and green curves were multiplied by a correction factor equal to 0.97 and 1.03, respectively. The other aperture and magnification settings that were investigated returned identical curves and are not shown here.

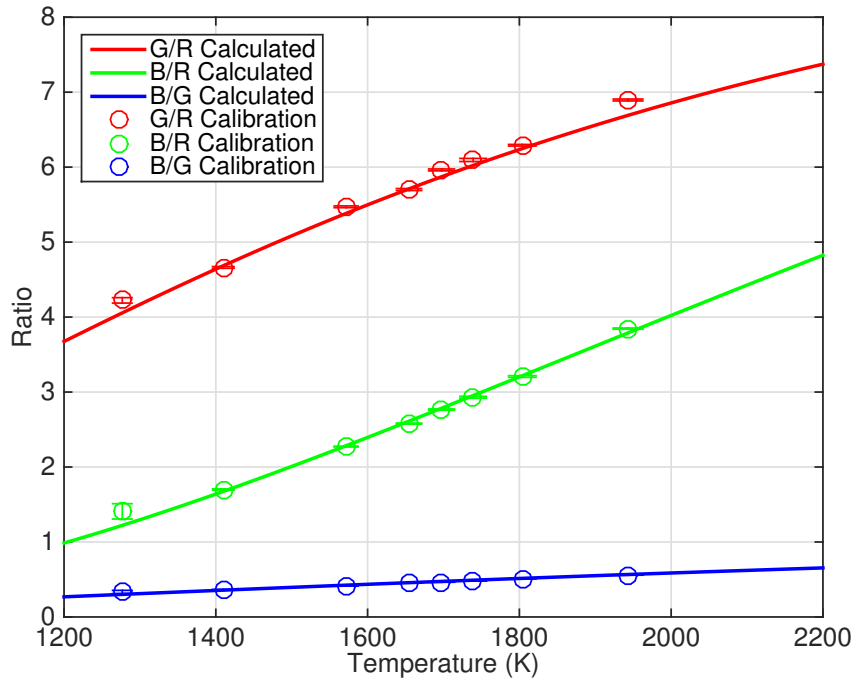


Figure 9.16: Pt thermocouple lookup table: comparison between experimental color ratios and numerically-derived curves. The error bars identify the standard deviation over 10 samples.

Figure 9.17 shows the result of the absolute light intensity calibration, with the calibration constants plotted as a function of the lens  $f$ -number and magnification. The constants were determined as explained in Section 2.2.5 by considering only the intensity from the camera’s green channel, the one with the highest signal-to-noise ratio. Each value was the average of results obtained considering eight different temperature values (as in the previous list), while the error bars identify the standard deviation. The flight unit’s lens aperture is controlled with a stepper motor, and the  $f$ -numbers were evaluated from the average intensity of calibration images taken at increasingly smaller aperture settings, along with Eq. 9.4.

$$f - number = 2.5 * \sqrt{\frac{I}{I_{2.5}}} \quad (9.4)$$

Here 2.5 is the  $f$ -number value of the reference largest aperture, while  $I$  and  $I_{2.5}$  are

the average intensities of the images taken with a generic aperture setting and with the reference one, respectively.

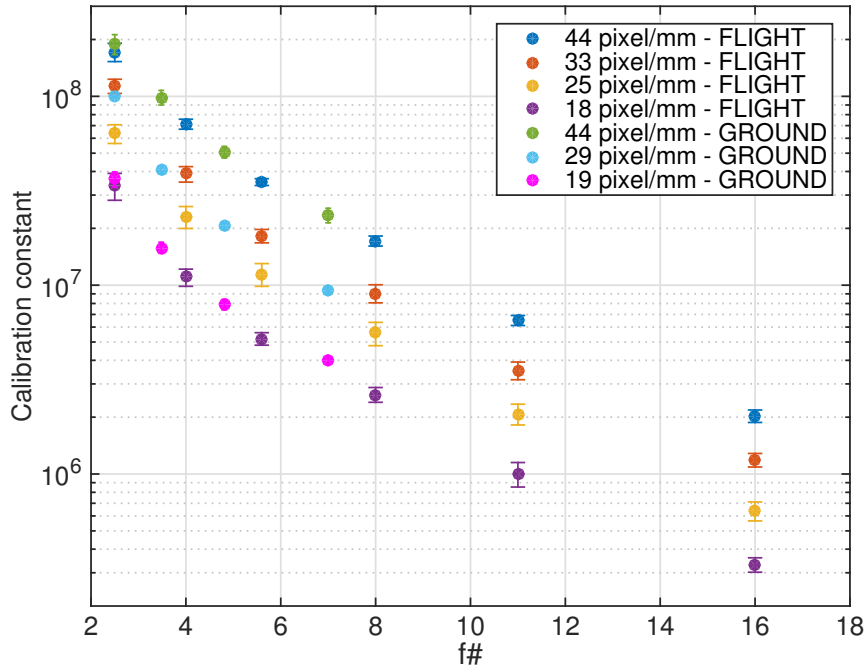


Figure 9.17: Calibration constants as determined from thermocouple measurements.

Figure 9.17 shows also the calibration constant results obtained with the ground imaging unit. A non sooty nitrogen-diluted methane flame was lit on the ACME CLD burner and used to heat the same *Pt* thermocouple used for the flight unit calibration. The test conditions were:

- Thermocouple temperature: 1300, 1440, 1510 K.
- Zoom magnification: 44, 29, 19 pixel/mm.
- Nominal lens *f*-number: 2.5, 4, 5.6, 8.

On the ground unit, the aperture was set based on the markings on the Navitar lens. However, to compare the flight and ground unit results, the “real” *f*-number was derived, once again, employing Eq. 9.4. As can be seen from Fig. 9.17, the nominal

$f$ -numbers overestimate the analytical values.

The comparison between the two results at  $f\#$  2.5 (magnification of 44 and 18 pixel/mm), showed that the flight unit throughput, in the green channel, is  $\sim 92\%$  of the ground unit system.

## 9.4 Normal gravity flames

During the time the flight unit of the ACME CLD burner was at Yale for the hot wire velocity measurements, images of nitrogen-diluted methane and ethylene flames were collected as well, to build a normal gravity image database to be used both as a reference (to match the performances of the ground unit burner) and comparison (with microgravity results subsequently taken on the ISS). The burner was placed inside the Yale pressure chamber and images of the flames, for several coflow and fuel flow rates, were collected as a function of the chamber pressure and fuel dilution. The chosen flow rates were such that, at ambient pressure, the average coflow and fuel velocities ranged between 10 and 50 cm/s. The coflow was controlled with a Smart Trak mass flow controller (maximum flow rate of 20 slpm of air), while a pair of Unit Instruments Inc. mass flow controllers were used for the nitrogen and fuel flows (maximum flow rate of 300 sccm of  $N_2$ ). Since the flow controllers operate by adjusting the mass flow rate, as the chamber pressure increases, the volumetric flow rate (and average flow velocity) is expected to decrease, as reported in Fig. 9.18.

The planned maximum burn time of each ACME test run is  $\sim 2$  minutes and, when the largest flow rates are used ( $\sim 15$  l/min), the CIR pressure is expected to increase no more than 0.37 atm. Figure 9.19 shows the relative pressure increase as a function of time, assuming a free CIR volume of 80 liters. The different curves refer to the different mass flow rates that, at ambient pressure, return the average flow velocities reported in the legend.

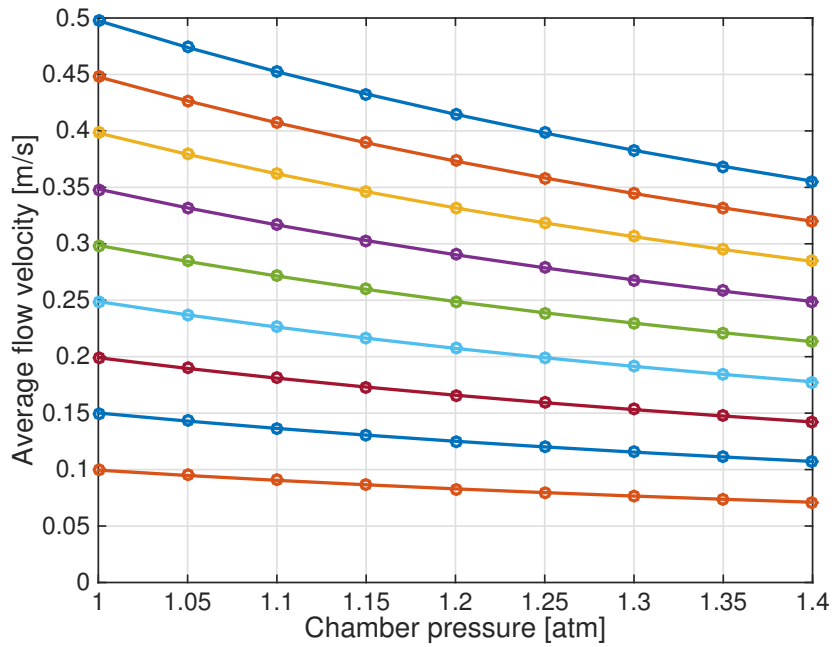


Figure 9.18: Expected decrease of the average flow velocity as a consequence of pressure increase.

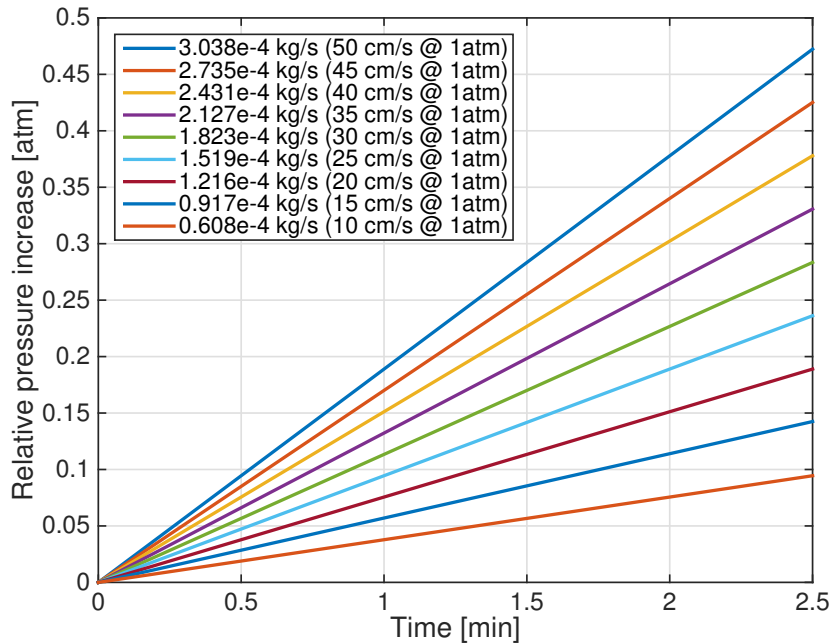


Figure 9.19: Expected CIR relative pressure increase as a function of time and flow rates.

Because of this upper threshold, the normal gravity images were recorded at equally spaced pressure values of 1.0, 1.1, 1.2, and 1.3 atm (1.0 to 1.2 atm for the ethylene flames, because of the 35 cm/s planned maximum velocity), even though the lowest flow rates will unlikely reach those values. The chamber pressure was monitored with a digital pressure transducer (Omega Engineering PX-213) and controlled with a needle valve driven by a stepper motor. Pressure transducer and valve stepper motor were interfaced through a National Instrument ER-8 relay connected to a Labview VI. The stepper motor controller was of the proportional-derivative type. The acquisition at constant pressure allowed for stable and steady flames, so that image averaging could be implemented. Note that, given the trends shown in Fig. 9.19, the nominal flow rate settings of the test runs performed on the ISS can be tested against the chamber pressure (known from real time pressure reading) and time. These, in turn, can be used to verify the real flow rates,  $\dot{m}$ , through the use of Eq. 9.5.

$$\dot{m} = \frac{PVm_{FLOW}}{tRT} \quad (9.5)$$

Where  $P$  is the chamber pressure reading,  $V$  the chamber volume,  $m_{FLOW}$  the molecular mass of the flow (coflow plus fuel mixture),  $t$  the time,  $R$  the universal gas constant, and  $T$  the temperature.

The normal gravity flame images were taken through a coated 2 mm BG7 color filter (provided by NASA) with a Prosilica GC1380-CH coupled to a Navitar 7000 zoom (models equivalent to the one equipping the flight hardware). The camera settings were:

- Frame size: 1360 x 1024 pixels.
- Gain: 0 dB.
- White balance: Red=100%, Blue=100%.

- File format: BayerRG12.

As per the flight hardware, the front lens of the Navitar Zoom was replaced with a Nikon 500D 52 mm close-up lens. The distance between burner axis and lens was set to 394.2 mm in order to replicate the CIR geometry (see Fig. 9.15) and obtaining, at the maximum zoom setting, a magnification of  $\sim 44$  pixel/mm. The lens  $f$ -number was set to an intermediate value of 5.6, to balance exposure times and imaging depth of field. For each condition (flow rate, fuel dilution, and pressure), four images with relative background were collected with an exposure that utilized at least 75% of the camera's dynamic range (but without exceeding 3 seconds, for flame stability reasons related to the semi-continuous adjustment of the chamber pressure valve). The raw images were, in the end, demosaiced using the bilinear interpolation (see Chapter 8).

Like in the CIR, the camera was mounted with a “landscape” orientation; it was placed vertically so that, at the maximum magnification, only the tip of the fuel tube was visible ( $\sim 0.5$  mm). Images were collected using the largest magnification that was compatible with each flame size, but that was also related to a marking on the lens (to ensure repeatability, since the lens' zoom adjustment is continuous).

The normalized line-of-sight luminosities of the methane flames (from the camera's green channel) are shown in the tables of Appendix B and are divided by flow rates. Tables B.1 to B.9 show the cases of matched fuel and coflow velocities (as a function of nitrogen dilution), while tables B.10 to B.15 show the cases of mismatched velocities (as a function of nitrogen dilution). Flow conditions are summarized in each table's label and, when a magnification differs from the standard one ( $\sim 44$  pixel/mm), the actual value is reported next to the specific case. Each sub-image displays a sequence of flames taken at the four considered pressures of 1.0, 1.1, 1.2, and 1.3 atm; only the very first sub-image is labelled with those values, while the others are missing for image clarity reasons. The average flow velocities that are reported in each label are the values evaluated at ambient pressure. For pressure values greater than one,

the real average velocity can be determined employing the graphs shown in Fig. 9.18. Tables B.16 to B.21 show the line of sight luminosity for the ethylene flames as a function of fuel dilution and chamber pressure. Once again, flow conditions are summarized in each table's label. The largest flow velocity displayed for the ethylene flames is 35 cm/s, as reported in the ISRD.

The whole methane flames set was acquired using the flight copy of the CLD flame burner, whereas the ethylene flames were collected partly on the flight unit (images at atmospheric pressure) and partly on the ground unit (cases with pressure of 1.1 and 1.2 atm). Being the ethylene flames rarely lifted, it was believed that minor differences between the flight and ground burners did not impact the flame structure.

### **Flame comparison between flight and ground burners**

Images of selected nitrogen-diluted methane flames were also taken on the ground copy of the CLD flame burner to additionally assess the similarities between the two units. The measurements of the flow velocity profiles showed that the behavior of the two burners is very similar (see plots in Appendix A), however, minor differences in the manufacturing, particularly for the honeycomb, can still impact the flow and affect highly lifted flames. Figure 9.20 shows the comparison between the line-of-sight luminosity (from the camera's green channel) of selected atmospheric nitrogen-diluted methane flames lit on the flight (top) and ground unit (bottom), as a function of fuel dilution and flow velocities. From left to right, the pair of images show the results at 50, 35, and 25 cm/s, while the percent values refer to the fuel concentration. These conditions were chosen because they show the behavior of lifted flames as they transition to attached ones.

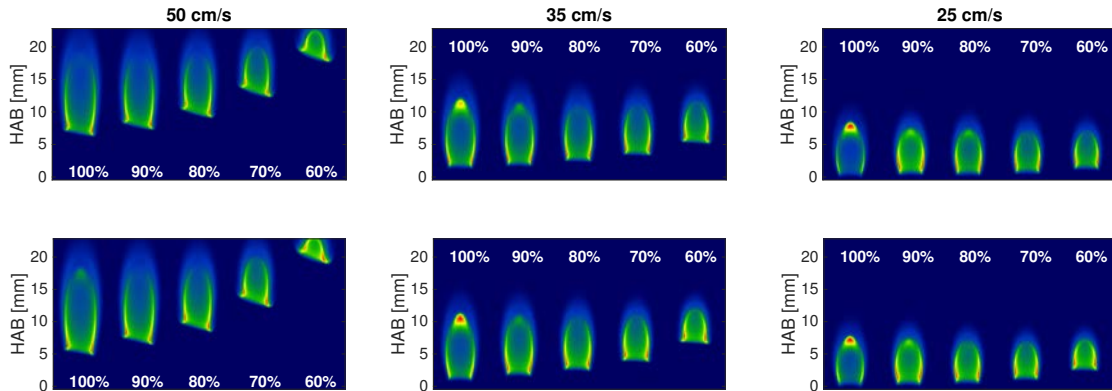


Figure 9.20: Normalized flame luminosity of nitrogen-diluted methane flames lit on the flight (top) and ground units of the CLD flame burner (bottom).

From Fig. 9.20 it is clear that the two burners behave very similarly, both in terms of flame structure and lift off. The only differences that can be noticed are the variation in soot luminosity (in relation to the flame wing chemiluminescence) of the 100% methane flames lit on the ground unit, as well as the smaller length of the lifted flames, again on the ground unit. These differences can be related to minor variations in the fuel and/or inert flows (rather than to burner geometry), which depend of the mass flow controller calibrations. Knowing about the similarity between the two units, and the sensitivity of the flames to minor flow variations (i.e. flow controller calibrations), will be useful during the comparisons between microgravity and normal gravity data.

#### 9.4.1 Examples of quantitative measurements applied to normal gravity ACME flames

This final section wants to demonstrate and show how quantitative information can effectively be extracted from the color images collected with the ACME camera. From the database reported in Appendix B, selected images of nitrogen-diluted ethylene and methane flames were processed to measure soot temperature, soot volume fraction, and  $CH^*$  concentration. Figure 9.21 shows the soot temperature evaluated

for two ethylene flames. The images on the left display a sequence, as a function of pressure, for a 100% ethylene flame with average flow velocity equal to 35 cm/s (as measured at atmospheric pressure); the images on the right display a sequence, as a function of pressure, for a 100% ethylene flame with average flow velocity equal to 20 cm/s (as measured at atmospheric pressure). The respective soot volume fraction values, determined as explained in Section 2.2.2, are shown in Fig. 9.22. Note that, because of the spectral transmissivity of the ACME BG filter, the camera's red channel suffered of very poor signal-to-noise ratio, and the lookup table pertaining the G/R ratio flattened for temperatures larger than 2500 K. Even though soot never reaches those values, noise-induced fluctuations of the G/R ratio returned unrealistic high temperatures. For this reasons, and to avoid additional noise, the color ratios involving the red channel were not considered in the temperature evaluation.

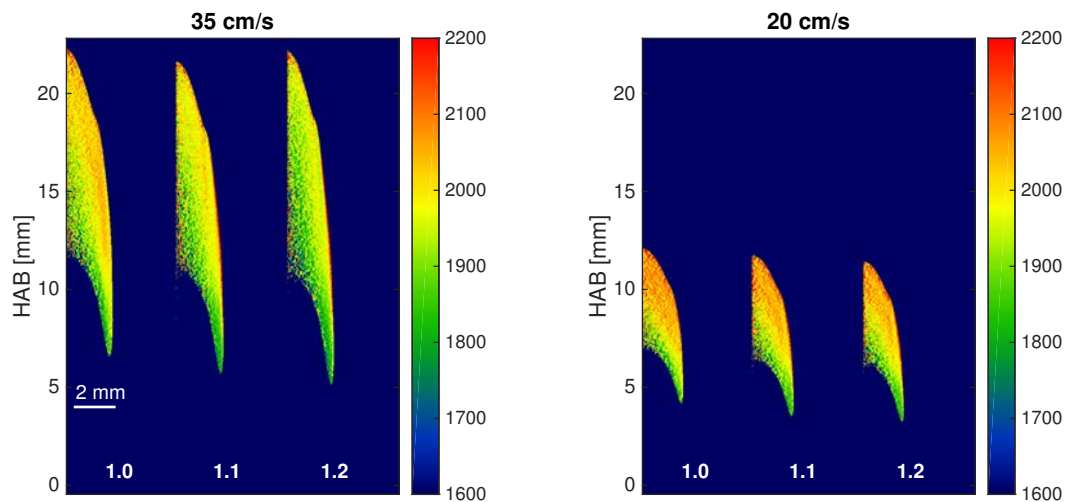


Figure 9.21: Soot temperature evaluated as a function of pressure for the 100% ethylene flames: 35 cm/s (left) and 20 cm/s average flow velocities (right), as measured at atmospheric pressure.

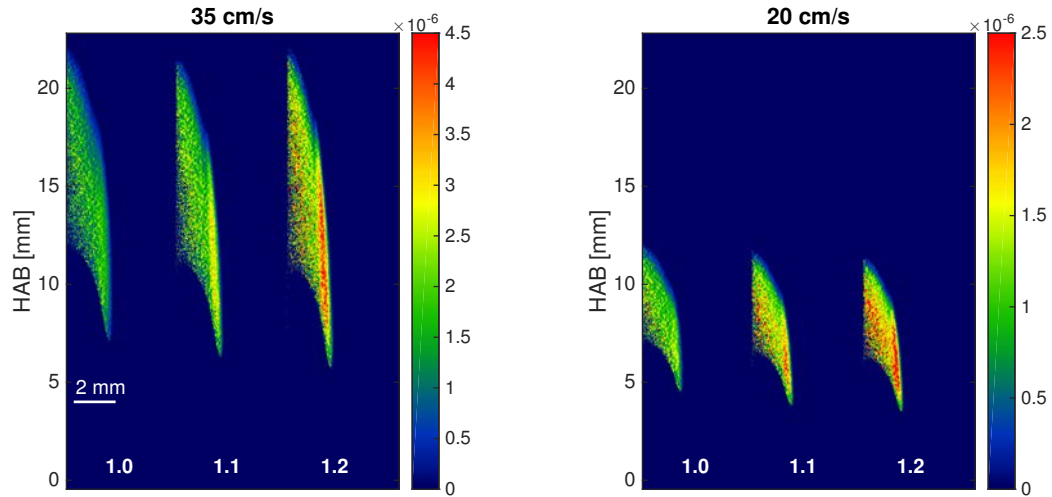


Figure 9.22: Soot volume fraction evaluated as a function of pressure for the 100% ethylene flames: 35 cm/s (left) and 20 cm/s average flow velocities (right), as measured at atmospheric pressure.

Despite the relatively noisy results, it can be seen how the soot temperature decreases as a function of pressure because of the enhanced radiation losses related to the increased soot load (especially when considering the case at 35 cm/s). Additionally, as the pressure increases, the peak soot volume fraction tends to shift towards the flame wings (from “inception-dominated” to “surface-growth-dominated” mode [136]).

Focusing now on the methane flames, Fig. 9.23 shows the  $CH^*$  concentration, in mole fraction, as a function of pressure for the 100%, 80%, and 50% methane flames with average flow velocity equal to 10 cm/s (as measured at atmospheric pressure). The  $CH^*$  concentration was derived from the camera’s blue channel in a way similar to the one explained in Chapter 6. Because of the specifics of the ACME optical setup and system throughput, however, the constant  $C$  in Eq. 6.2 had to be updated. From Fig. 9.23 it can be seen how, as the inert concentration is increased, the flame reactivity is reduced and the overall  $CH^*$  production is lowered.

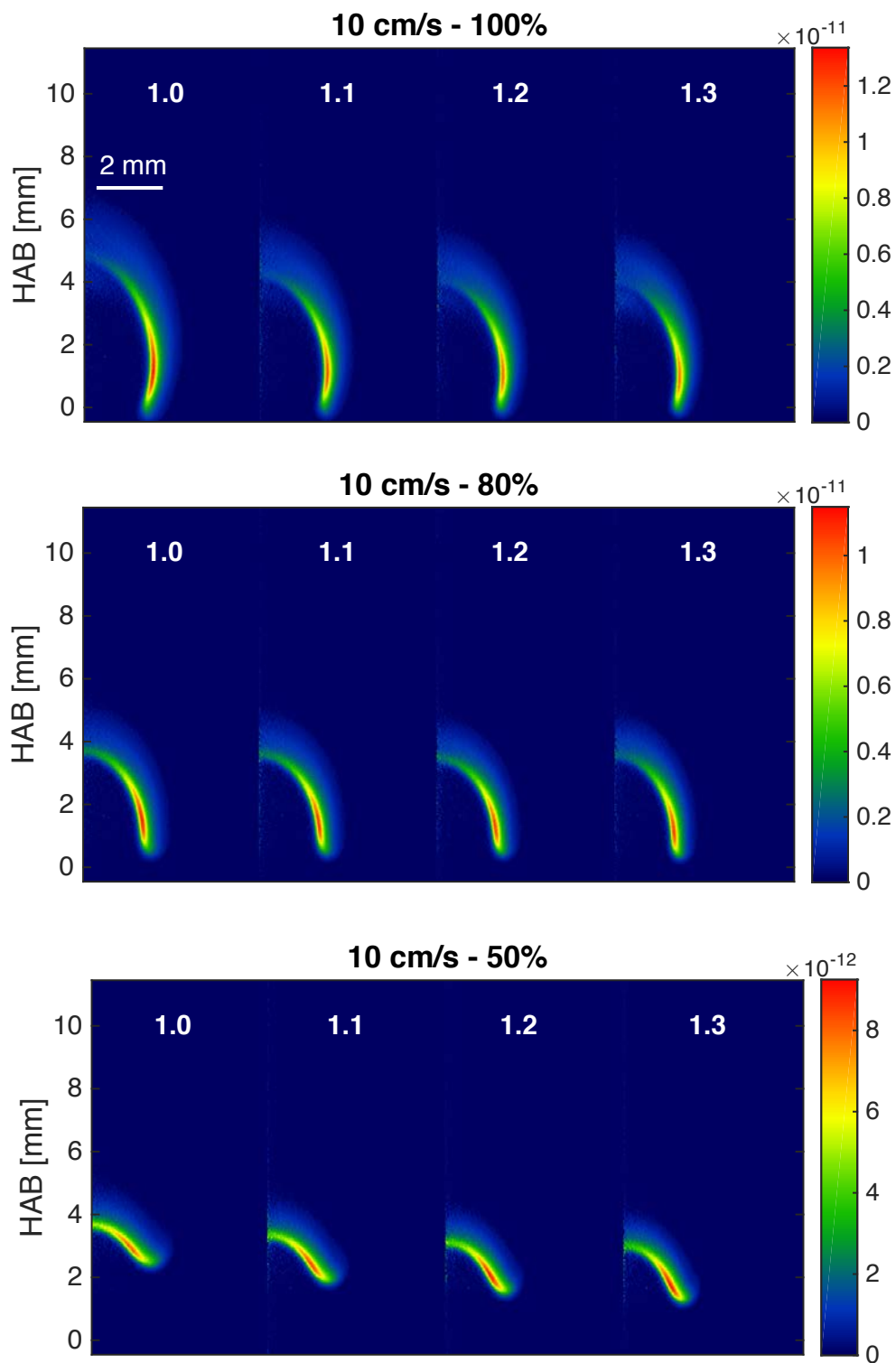


Figure 9.23:  $CH^*$  mole fraction, as a function of pressure, for a 100% (top), 80% (center), and 50% (bottom) nitrogen-diluted methane flame. Flow velocity equal to 10 cm/s, as measured at atmospheric pressure.

# Chapter 10

## Conclusions

In this dissertation, optical diagnostic techniques were applied to the quantitative characterization of coflow laminar diffusion flames in normal gravity and microgravity as a way to investigate and measure relevant physical properties. The work presented in the previous chapters can be summarized and categorized in three major areas:

- Measurements of minor species in steady and time-varying nitrogen-diluted coflow methane flames aimed at the extension of the Yale CLD flame chemical species database.
- Development of alternative approaches for the improvement of signal-to-noise ratio (SNR) in imaging of reactive and non-reactive flows (steady and unsteady).
- Application of simple diagnostics for the quantification of chemical species (i.e.  $CH^*$ ) in microgravity and normal gravity flames, and characterization/calibration of hardware designed for microgravity combustion experiments.

Specifically, minor species concentration measurements were performed in the steady and time-varying 65% methane flame using single and two-photon laser-induced fluorescence. The cross-sectional distributions of nitric oxide and carbon monoxide fluorescence were measured and, when possible, compared to numerical simulations.

A direct imaging approach was implemented instead of a spectrally resolved one: this had the effect of simplifying the experiments and returning better signal-to-noise ratios, due to the increased throughput of the imaging system. The *NO* measurements were extended from steady to time-varying cases and the results confirmed the importance of the Fenimore pathways in the formation of nitric oxide in the analyzed flames. *CO* measurements were performed in the photoionization regime making the quantification of the quenching rate unnecessary (species quenching cross-sections are not always known with sufficient accuracy, particularly at flame temperatures).

The concept of high dynamic range (HDR) imaging was investigated and applied to temperature measurements in steady non-sooty and sooty flames using thin filament and soot ratio pyrometry, respectively. The approach allowed for improved pyrometry sensitivity, and improved results' SNR. The increase of the latter, in the low pixel count regions, approached the factor of two. HDR imaging was then successfully extended to Rayleigh measurements of an unsteady jet of Freon injected in air thanks to the use of a dual laser system and an interline transfer CCD camera. It was seen that the reconstructed HDR result had a SNR  $\sim 15\%$  greater than the one obtained with a conventional image averaging. "Time-resolved averaging" was also envisioned and applied to the Rayleigh measurement of a partially-premixed turbulent methane flame thanks to the use of an interline transfer CCD camera coupled to an image intensifier. After proper timing of camera and intensifier, the temporal decay characteristics of the intensifier's phosphor screen allowed for a distribution of the phosphor's emitted light over the two-sequential frames of the detector, so that an average image could be reconstructed. The latter had a SNR  $\sim 30\%$  higher than the one of a conventional Rayleigh measurement.

A consumer Nikon D300s, used for the NASA SLICE microgravity experiments, was characterized and calibrated so that the camera's blue channel could be used to evaluate and quantify  $CH^*$  concentration in nitrogen-diluted coflow diffusion methane

flames in normal gravity and microgravity. The  $CH^*$  chemiluminescence was compared against complementary numerical results, and it was seen that the total flame chemiluminescence scaled proportionally to the total flame heat release rate.

In preparation for the upcoming NASA ACME experimental campaign, a series of related studies were undertaken. First, the effect that pressure and fuel dilution has on the structure and sooting behavior of coflow nitrogen-diluted methane flames was investigated. This was in part motivated by the fact that the ACME burner will be operated in a sealed environment, with pressure expected to raise over the duration of a test run. Color ratio pyrometry was used to evaluate soot temperature and volume fraction as a function of pressure, and the results compared to numerical simulations. Second, demosaicing algorithms were tested as a way to maintain the spatial resolution when color images are decoded into the RGB channels. Soot temperature measurements, as well as the analysis of Abel-inverted blue profiles, showed the ability of demosaicing algorithms in returning the correct quantitative information with an increased SNR. Third, the flight and ground units of the ACME CLD burner and imaging systems underwent a series of characterizations. The burners' flow velocity profiles were measured with hot wire anemometry to verify the flow symmetry, and they will serve as boundary conditions for the numerical simulations that will be performed. A heated  $Pt$  thermocouple was used for the absolute light intensity calibration of the imaging systems, and the measured spectral responses of the flight and ground cameras were verified. Nitrogen-diluted methane and ethylene flames were collected, and quantitative results were shown for selected cases (soot temperature, volume fraction,  $CH^*$  concentration).

The material presented in this dissertation had some of its basis in work previously done in our research lab, and it was aimed both at the better understanding of combustion processes, and at the application of improved optical imaging techniques. It is however possible to further build on what has been achieved so far, specifically:

- The accuracy and quality of the laser-induced fluorescence measurements could be improved with a two-dimensional imaging of a laser sheet rather than the imaging of a beam. This approach would speed up the whole acquisition process reducing any problems related to dye degradation and laser energy fluctuations. Reduced dye degradation would allow for a more accurate and consistent fluorescence signal calibration, since the same dye solution utilized for the measurements could be used for the calibration as well.
- High dynamic range imaging could be extended to measurements in reactive flows using various laser-based techniques. A Rayleigh scattering example has already been shown in Chapter 5, albeit in a non-reactive flow. Due to their resonant nature, fluorescence signals can be relatively strong and they could easily induce partial image saturation; by applying HDR imaging on those partially saturated acquisitions, the SNR of areas with low pixel counts could be improved.
- Data collected during the ACME campaign will be used for additional microgravity flames studies. Thanks to the well defined flows and boundary conditions, accurate comparisons with numerical simulations will be possible, facilitating validation of numerical models. Microgravity will in fact provide an environment in which to study flames at the very extremes of the fuel dilution, thus providing challenging conditions to test models. Thanks to some of the techniques used and developed in this thesis, images collected with the ACME color camera will be used to derive soot temperature, volume fraction, and  $CH^*$  concentration, while high dynamic range imaging will allow for a more complete use of the image database (without being limited by image saturation).

# Appendix A

## ACME CLD burner velocity profiles

The plots shown in the following pages summarize the hot wire measurement results performed on the flight and ground units of the ACME CLD burner. First, in Figs. A.1 to A.5, the flight unit cases of matched fuel and coflow velocities are presented (in the range 10 to 50 cm/s). Each figure displays two columns and three rows: the left column compares the velocity profiles along the four scanning directions, while the right column shows the symmetry plots. The three rows refer to the measurements performed at three heights above the burner (0.5, 5, and 10 mm HAB). In Figs. A.6 to A.16, the measurements are extended to the cases of mismatched velocities, where only one scanning direction (direction “A”), and one height above the burner (0.5 mm), are shown. Then, the results of the verification of non-turbulent flows is presented in Fig. A.17 (scanning direction “A”, 0.5 mm HAB).

Finally, in Figs. A.18 to A.22, the ground unit results are presented for the cases of matched fuel and coflow velocities (in the range 10 to 50 cm/s).

## A.1 Flight unit

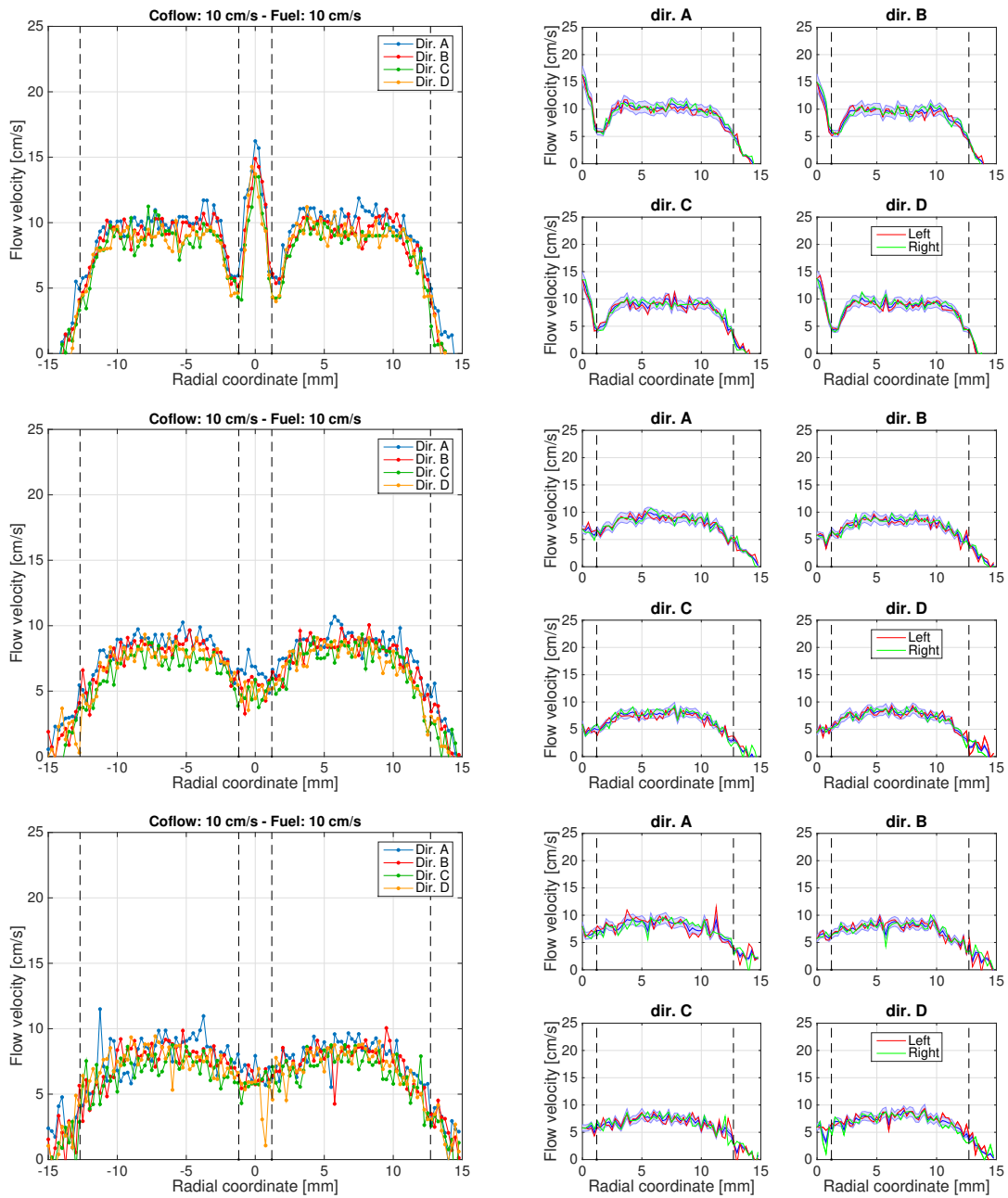


Figure A.1: (Left) velocity profiles as determined from hot wire measurements and (right) symmetry plots - 10 cm/s matched flow velocities. (Top) 0.5 mm, (middle) 5 mm, (bottom) 10 mm HAB.

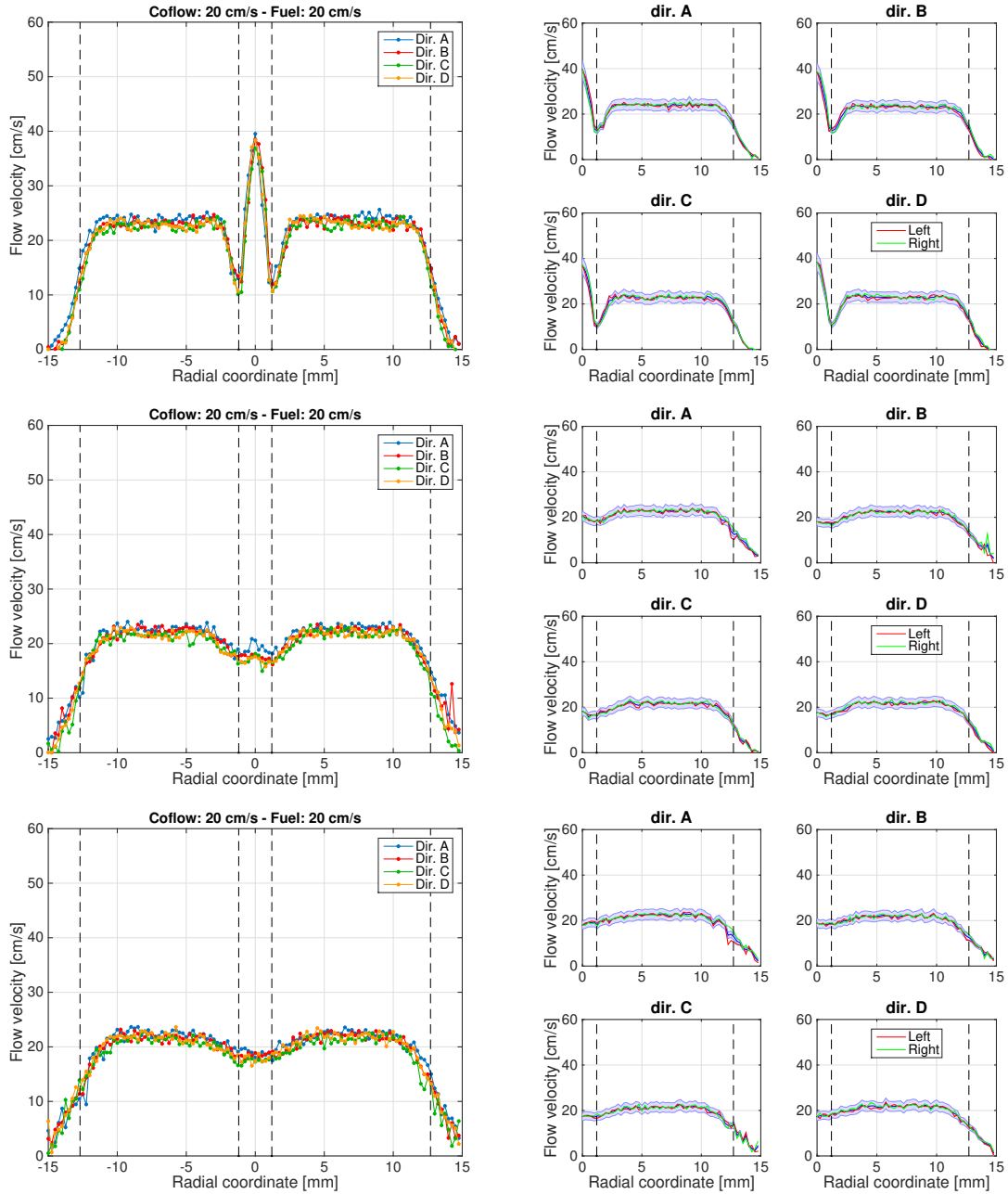


Figure A.2: (Left) velocity profiles as determined from hot wire measurements and (right) symmetry plots - 20 cm/s matched flow velocities. (Top) 0.5 mm, (middle) 5 mm, (bottom) 10 mm HAB.

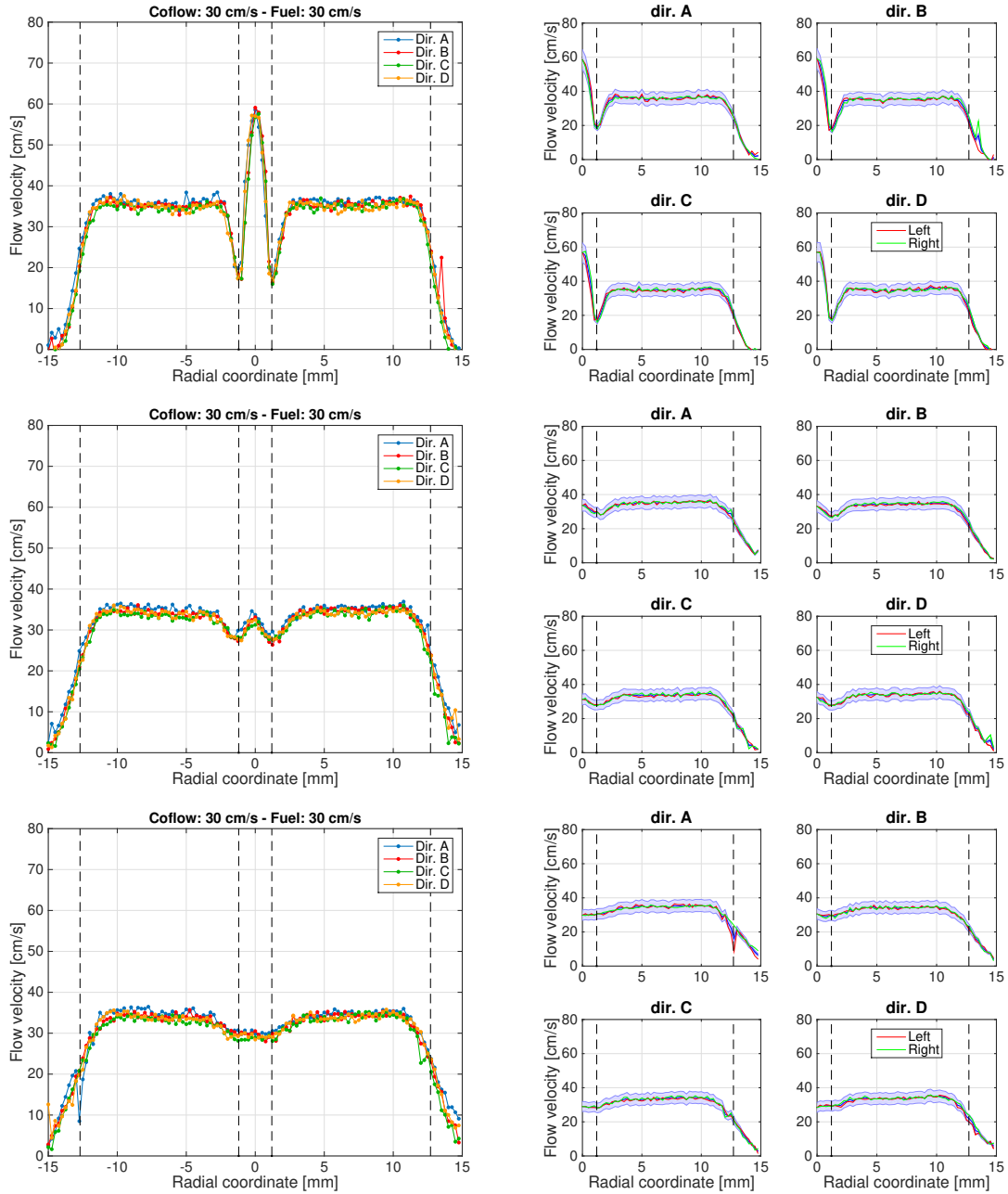


Figure A.3: (Left) velocity profiles as determined from hot wire measurements and (right) symmetry plots - 30 cm/s matched flow velocities. (Top) 0.5 mm, (middle) 5 mm, (bottom) 10 mm HAB.

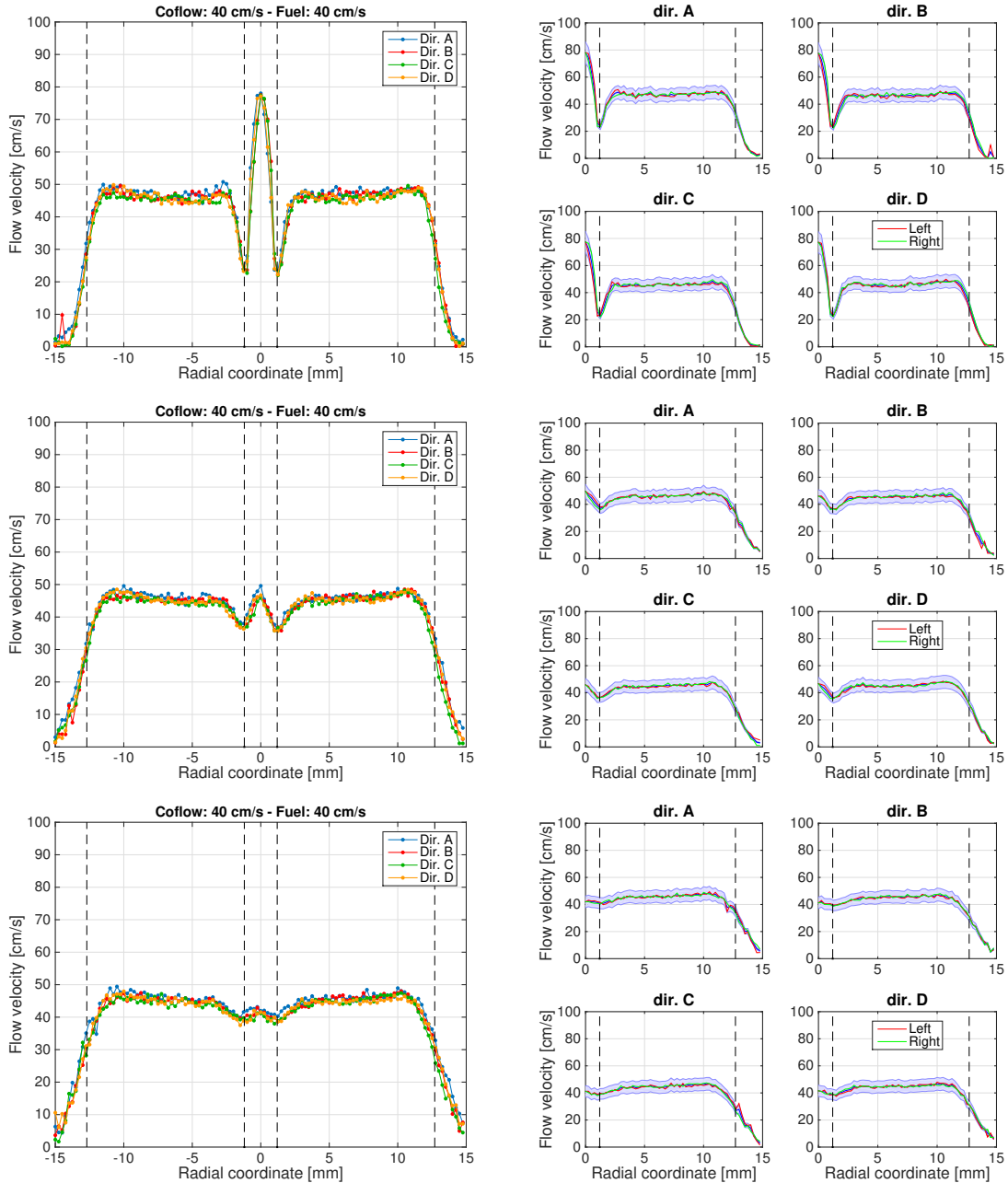


Figure A.4: (Left) velocity profiles as determined from hot wire measurements and (right) symmetry plots - 40 cm/s matched flow velocities. (Top) 0.5 mm, (middle) 5 mm, (bottom) 10 mm HAB.

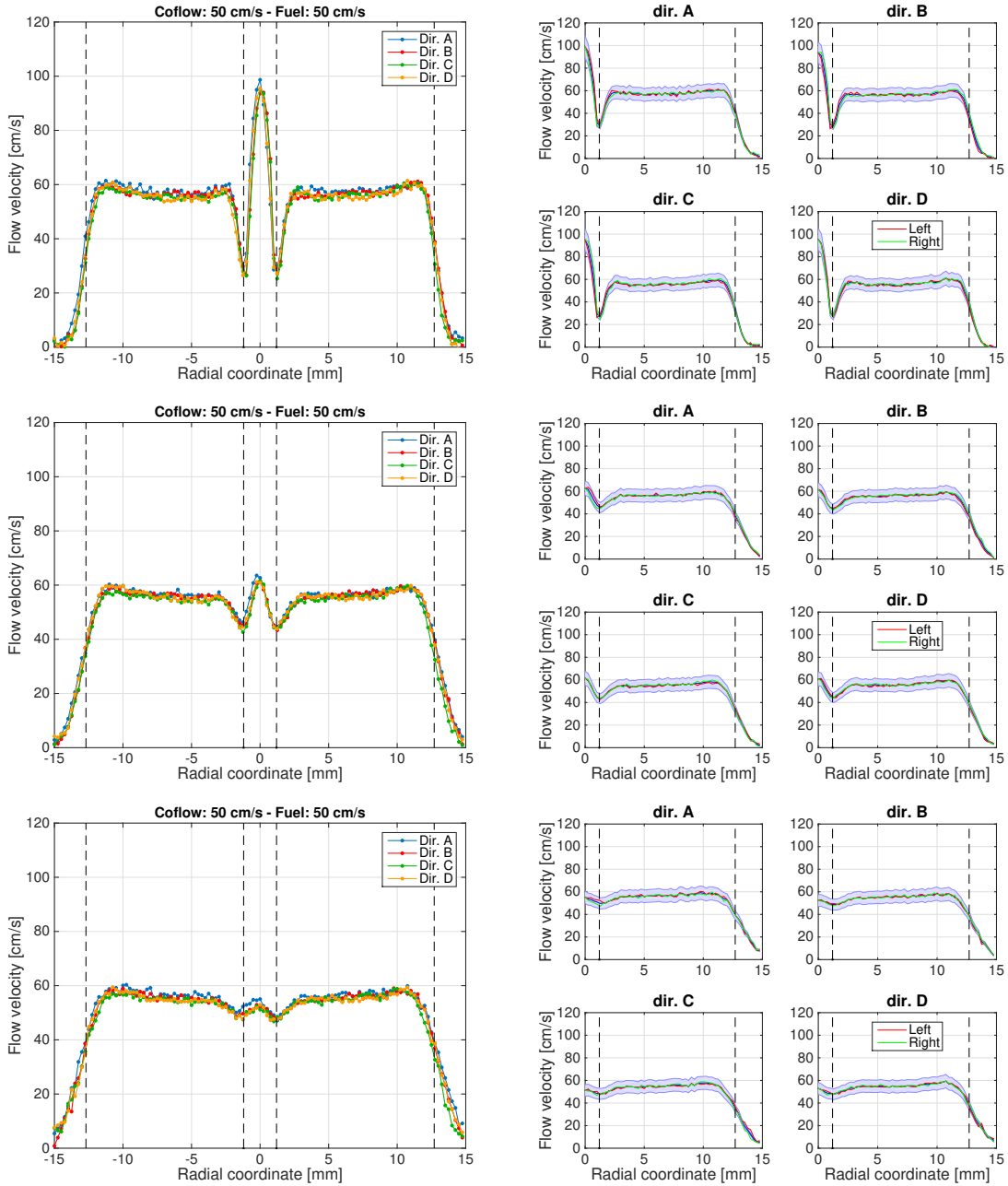


Figure A.5: (Left) velocity profiles as determined from hot wire measurements and (right) symmetry plots - 50 cm/s matched flow velocities. (Top) 0.5 mm, (middle) 5 mm, (bottom) 10 mm HAB.

## Mismatched velocities

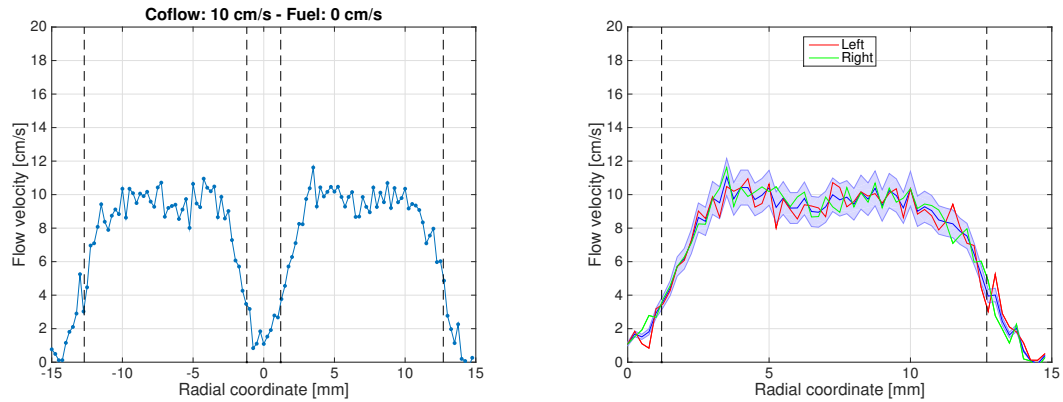


Figure A.6: (Left) velocity profiles as determined from hot wire measurements and (right) symmetry plots - 0 and 10 cm/s for fuel and coflow velocities, respectively.

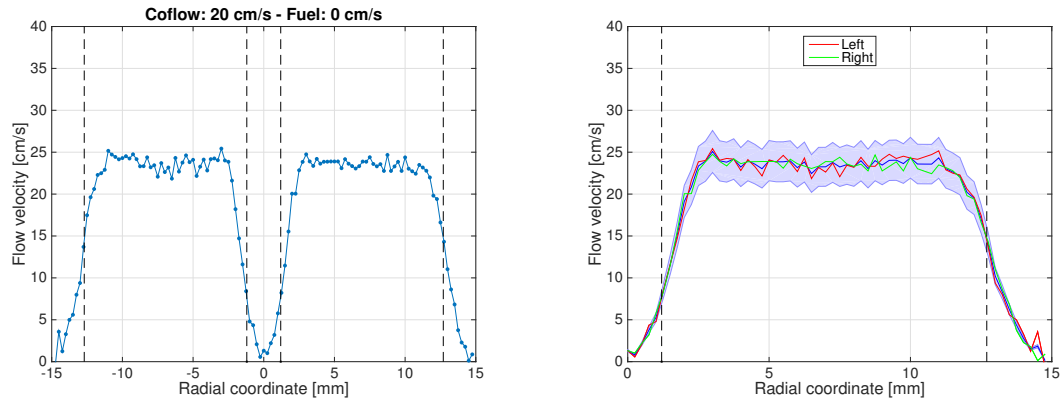


Figure A.7: (Left) velocity profiles as determined from hot wire measurements and (right) symmetry plots - 0 and 20 cm/s for fuel and coflow velocities, respectively.

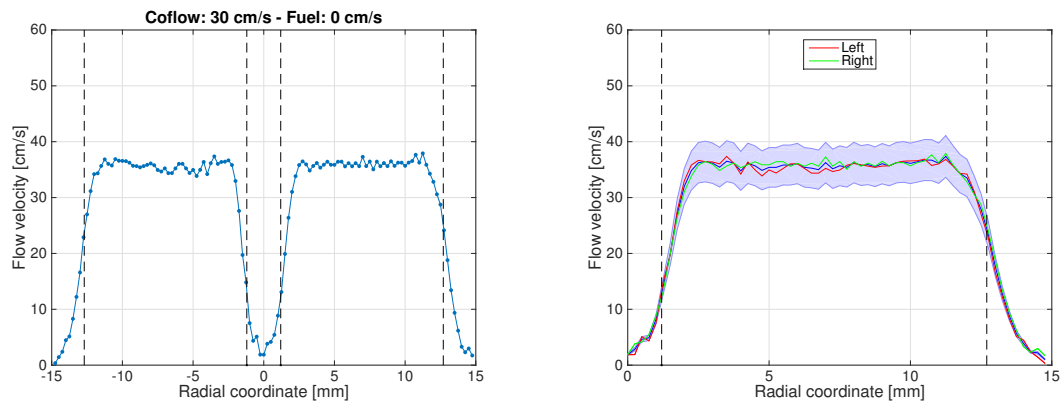


Figure A.8: (Left) velocity profiles as determined from hot wire measurements and (right) symmetry plots - 0 and 30 cm/s for fuel and coflow velocities, respectively.

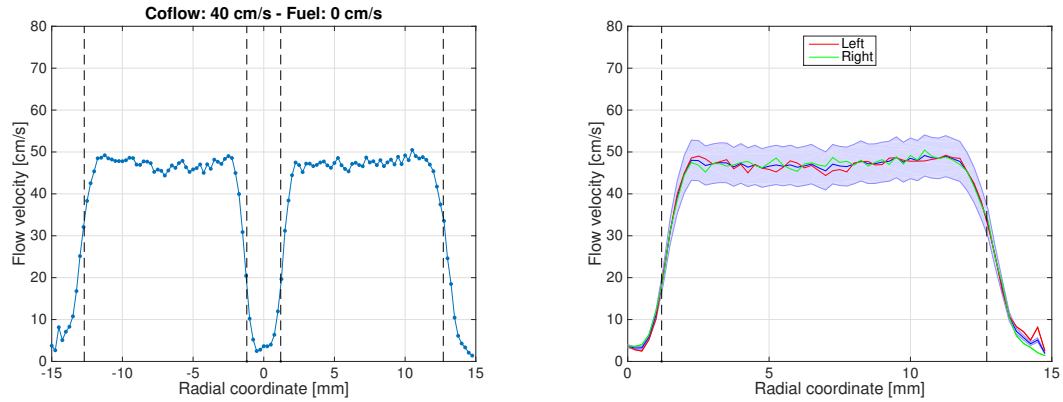


Figure A.9: (Left) velocity profiles as determined from hot wire measurements and (right) symmetry plots - 0 and 40 cm/s for fuel and coflow velocities, respectively.

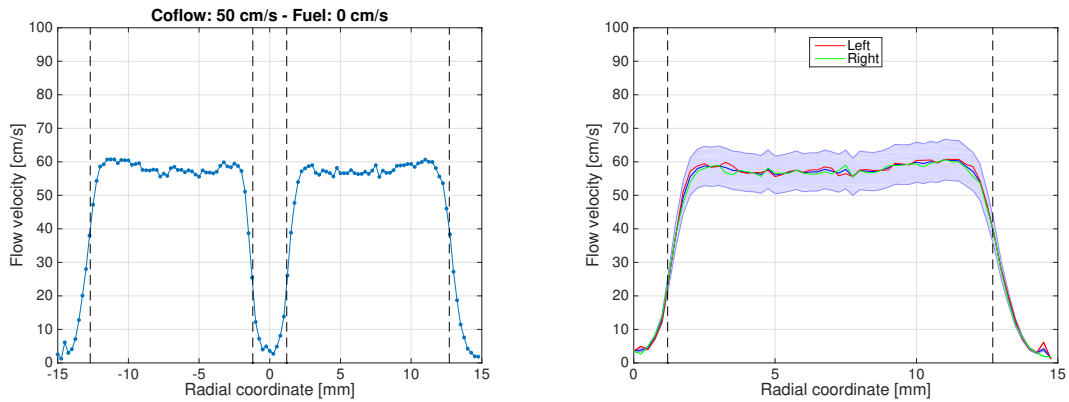


Figure A.10: (Left) velocity profiles as determined from hot wire measurements and (right) symmetry plots - 0 and 50 cm/s for fuel and coflow velocities, respectively.

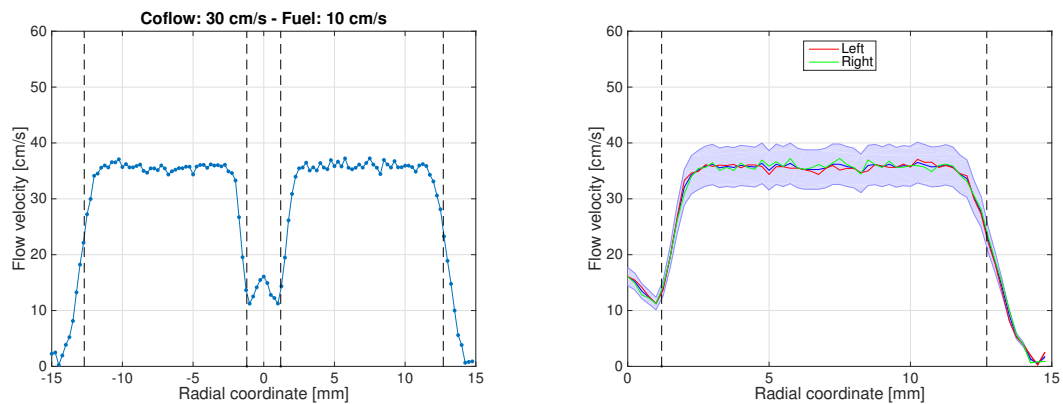


Figure A.11: (Left) velocity profiles as determined from hot wire measurements and (right) symmetry plots - 10 and 30 cm/s for fuel and coflow velocities, respectively.

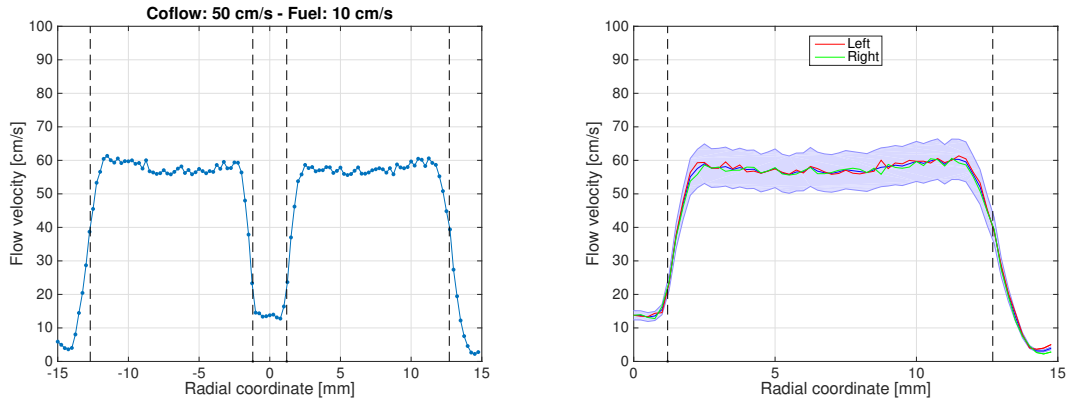


Figure A.12: (Left) velocity profiles as determined from hot wire measurements and (right) symmetry plots - 10 and 50 cm/s for fuel and coflow velocities, respectively.

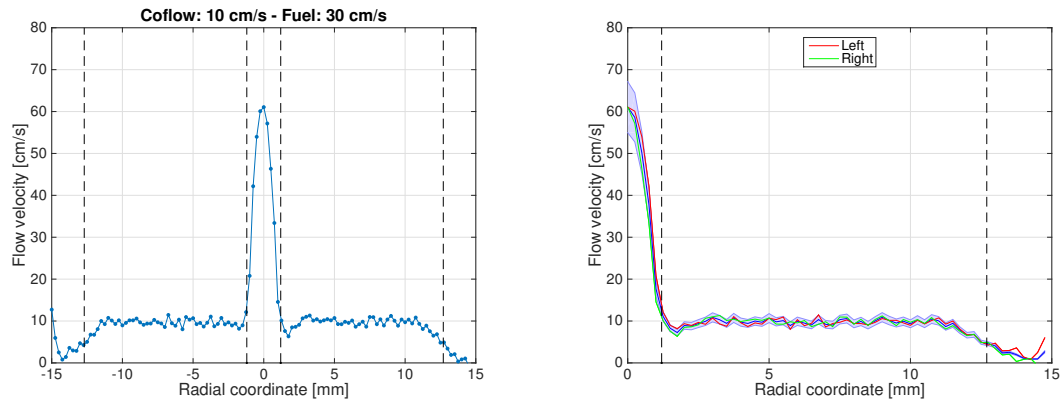


Figure A.13: (Left) velocity profiles as determined from hot wire measurements and (right) symmetry plots - 30 and 10 cm/s for fuel and coflow velocities, respectively.

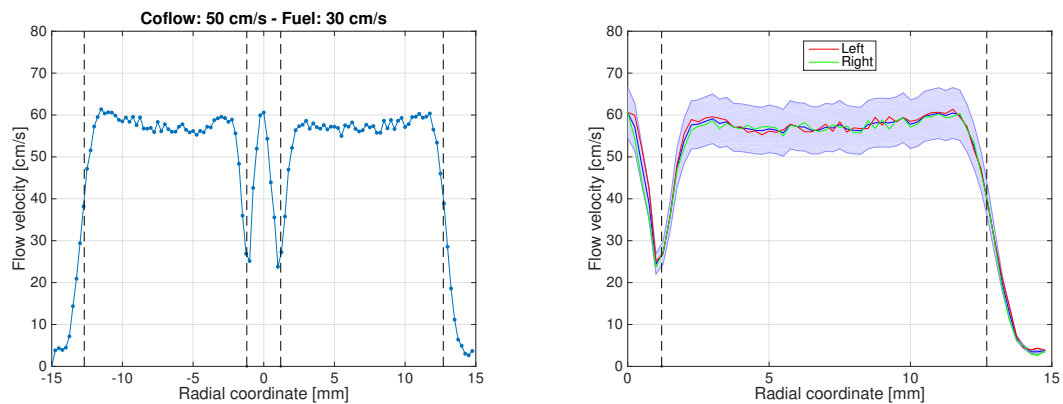


Figure A.14: (Left) velocity profiles as determined from hot wire measurements and (right) symmetry plots - 30 and 50 cm/s for fuel and coflow velocities, respectively.

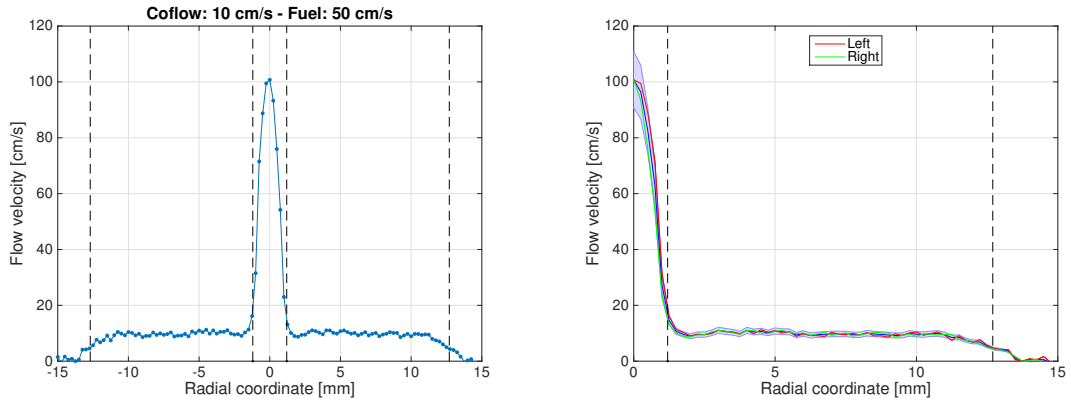


Figure A.15: (Left) velocity profiles as determined from hot wire measurements and (right) symmetry plots - 50 and 10 cm/s for fuel and coflow velocities, respectively.

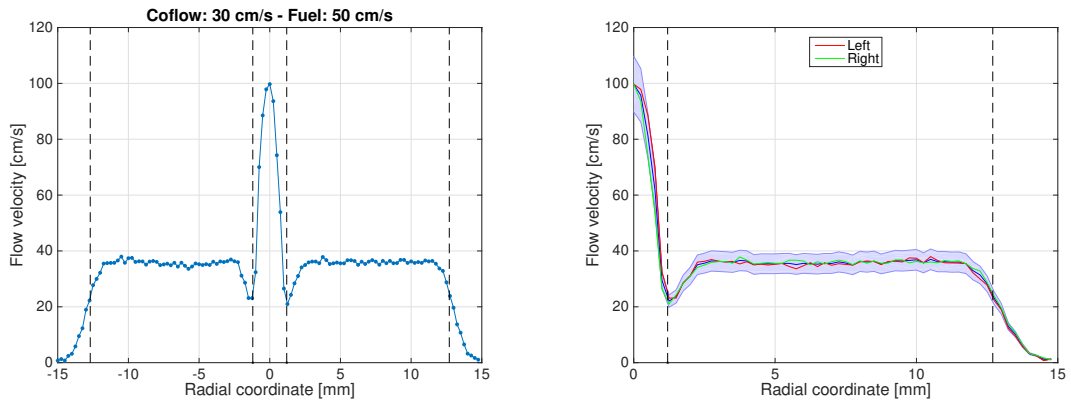


Figure A.16: (Left) velocity profiles as determined from hot wire measurements and (right) symmetry plots - 50 and 30 cm/s for fuel and coflow velocities, respectively.

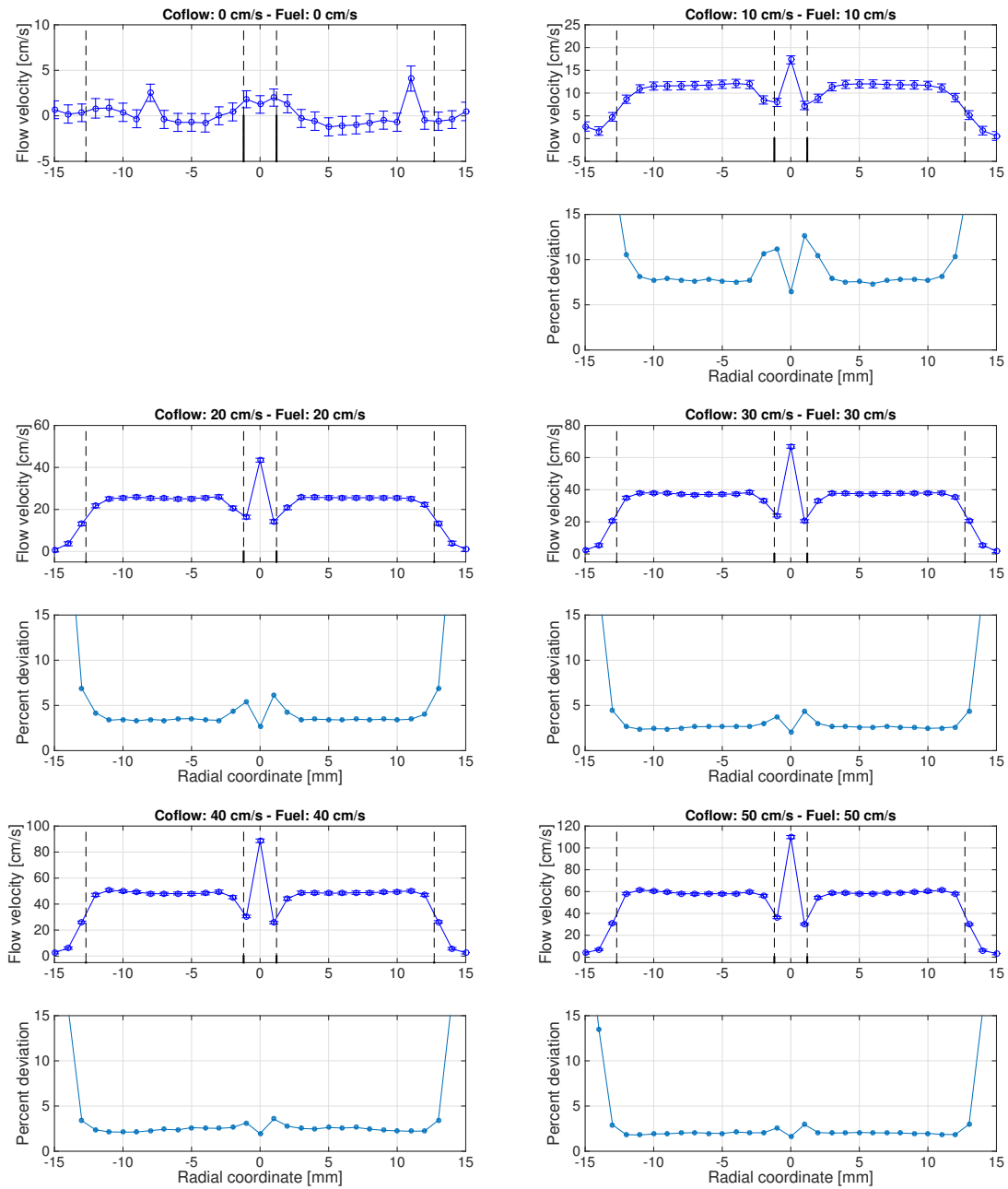


Figure A.17: Turbulence results. In each subplots, the top figure shows the flow velocity, while the bottom figure shows the maximum percent deviation with respect to the average velocity. The error bars are evaluated as  $\pm \sigma$ .

## A.2 Ground unit

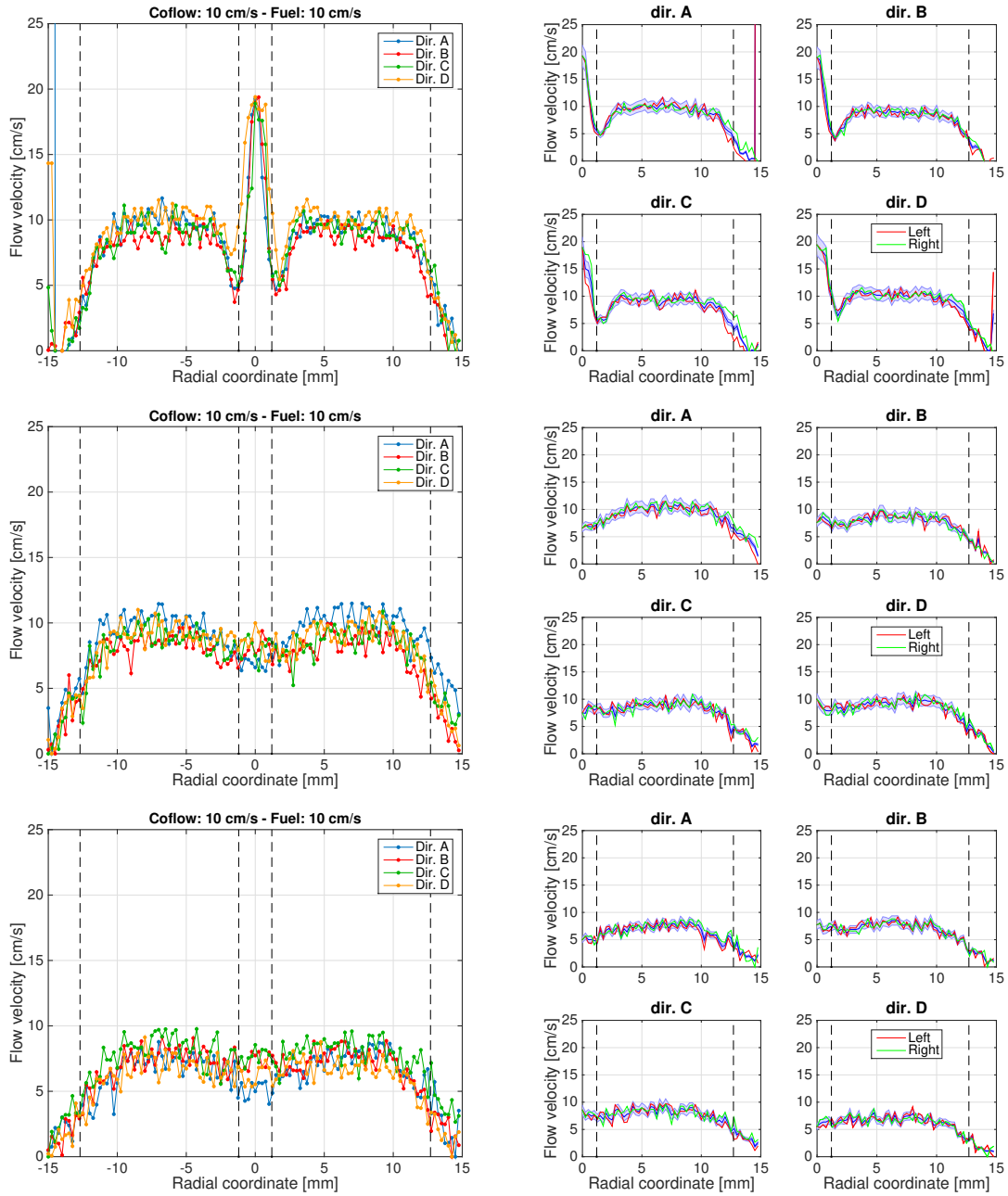


Figure A.18: (Left) velocity profiles as determined from hot wire measurements and (right) symmetry plots - 10 cm/s matched flow velocities. (Top) 0.5 mm, (middle) 5 mm, (bottom) 10 mm HAB.

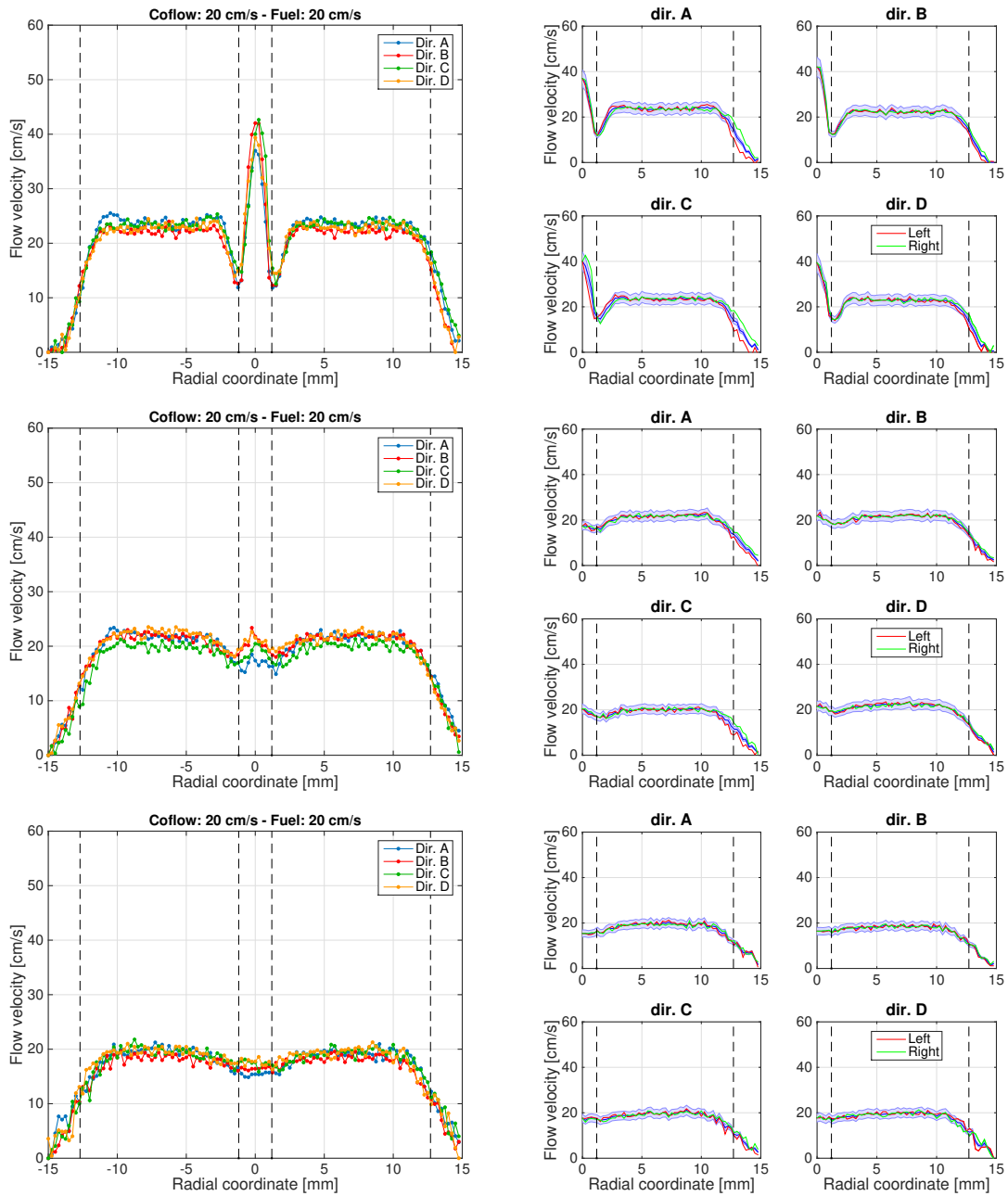


Figure A.19: (Left) velocity profiles as determined from hot wire measurements and (right) symmetry plots - 20 cm/s matched flow velocities. (Top) 0.5 mm, (middle) 5 mm, (bottom) 10 mm HAB.

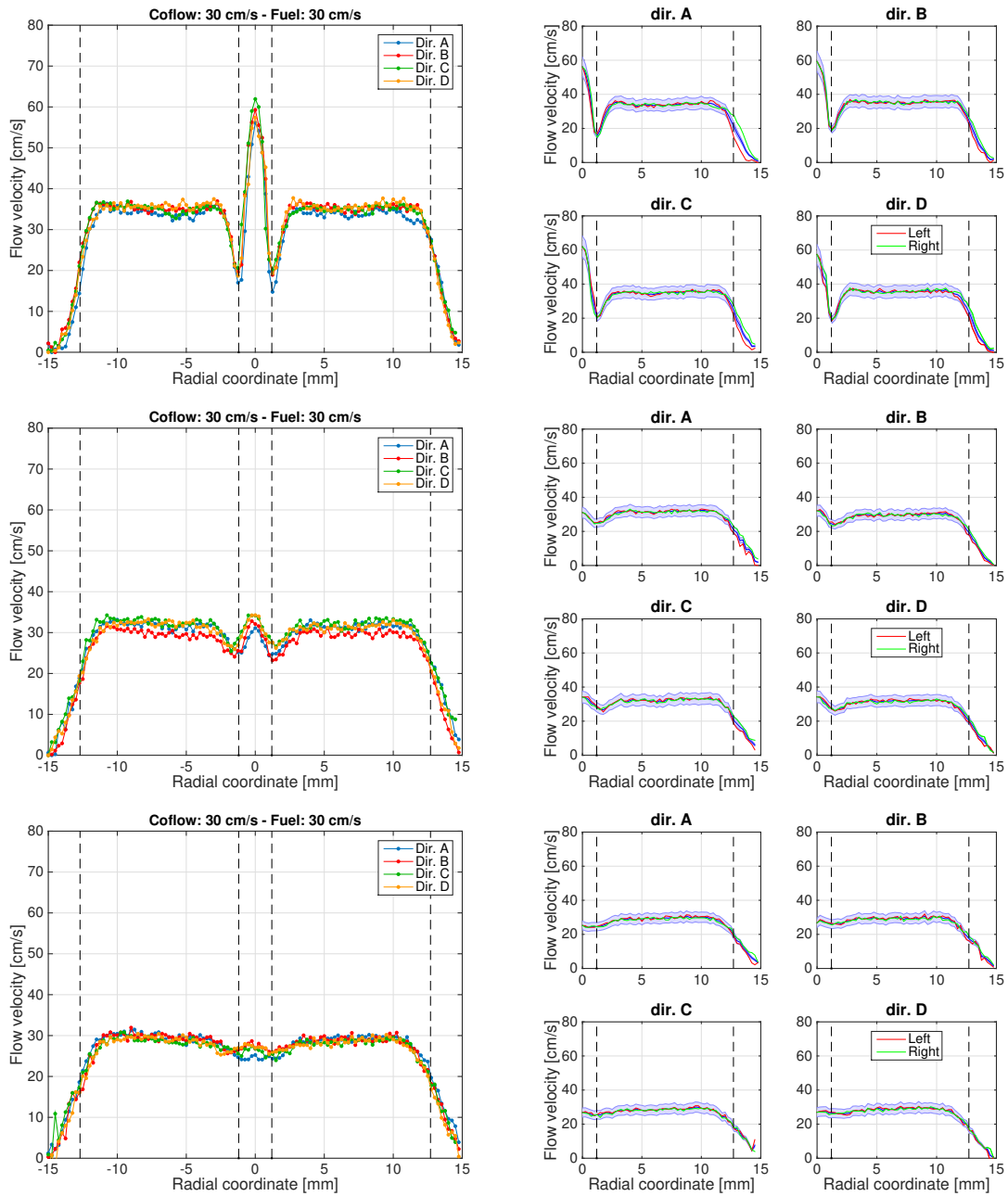


Figure A.20: (Left) velocity profiles as determined from hot wire measurements and (right) symmetry plots - 30 cm/s matched flow velocities. (Top) 0.5 mm, (middle) 5 mm, (bottom) 10 mm HAB.

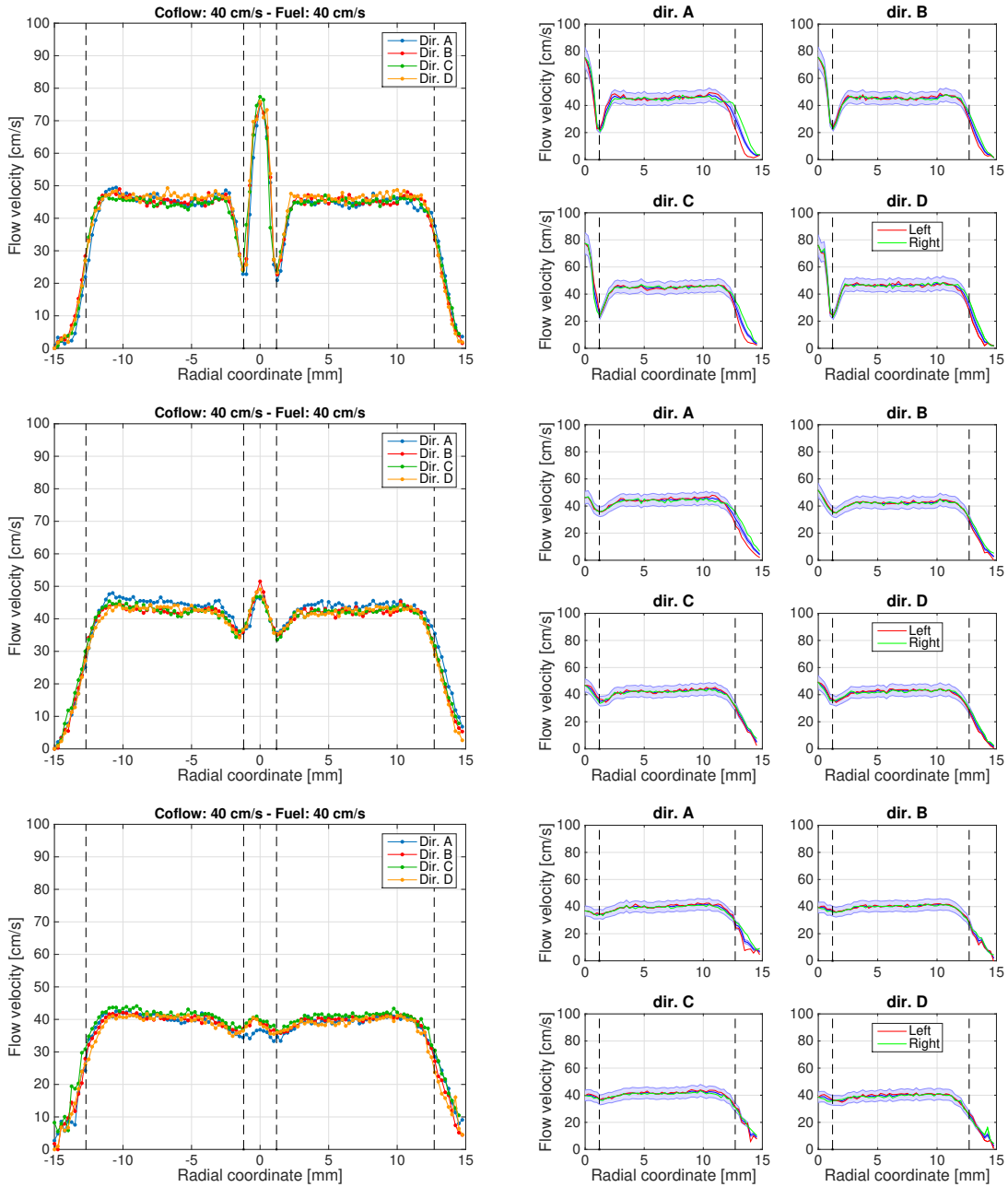


Figure A.21: (Left) velocity profiles as determined from hot wire measurements and (right) symmetry plots - 40 cm/s matched flow velocities. (Top) 0.5 mm, (middle) 5 mm, (bottom) 10 mm HAB.

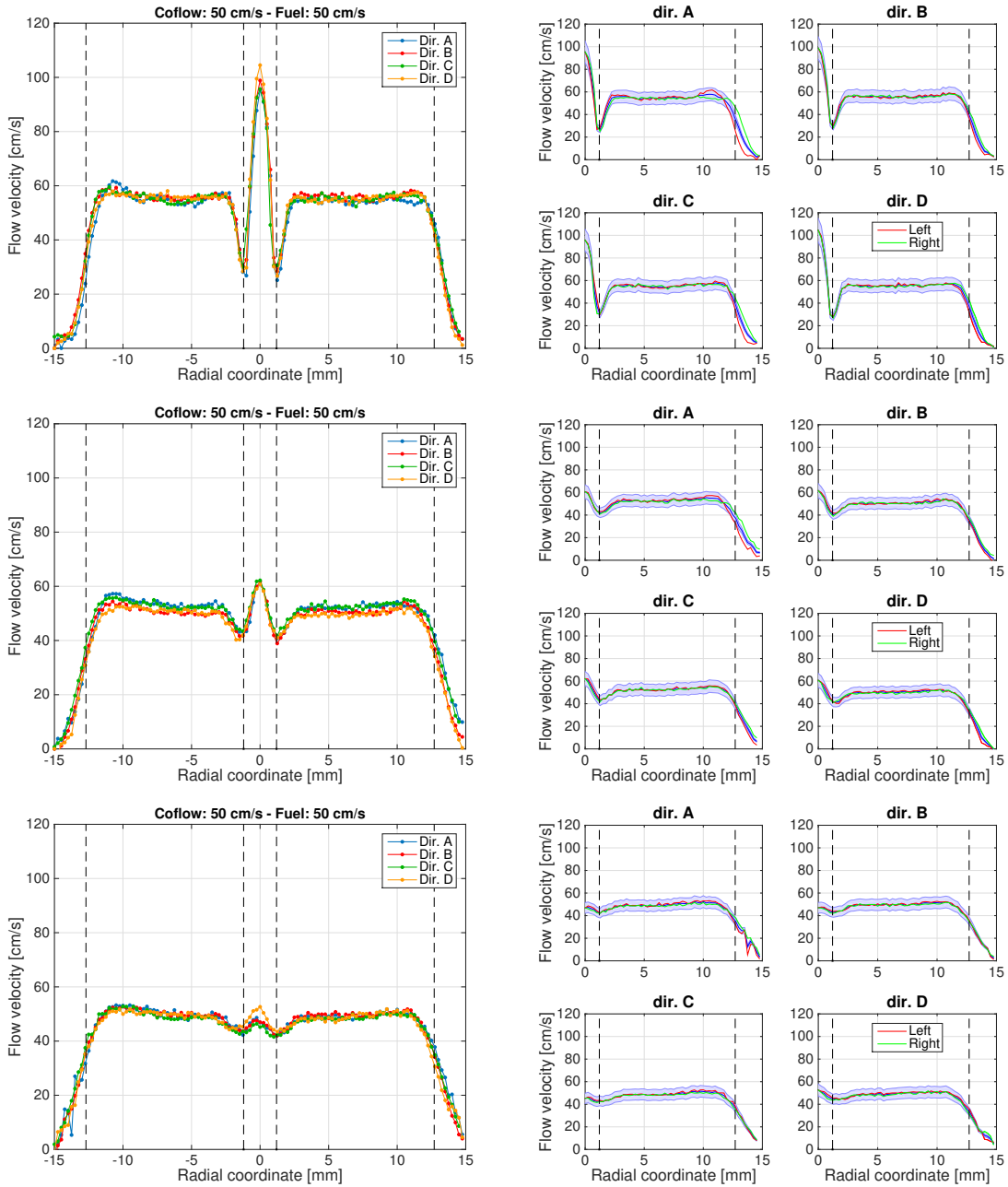


Figure A.22: (Left) velocity profiles as determined from hot wire measurements and (right) symmetry plots - 50 cm/s matched flow velocities. (Top) 0.5 mm, (middle) 5 mm, (bottom) 10 mm HAB.

# Appendix B

## ACME CLD flames

The tables reported in Appendix B summarize the results of the normal gravity flame images collected with the flight unit of the ACME CLD burner. Tables B.1 to B.9 show the nitrogen-diluted methane flames collected with matching fuel and coflow velocities, while Tables B.10 to B.15 show the results of mismatched velocities. In each table, the results are divided by fuel concentration (the percent values) and are plotted as a function of the chamber pressure (see the labels 1.0, 1.1, 1.2, and 1.3 atm in the first image of Table B.1). The nominal flow velocities reported in the figures' captions are values determined at atmospheric pressure; the average velocities, for pressures different from atmospheric, can be determined from Fig. 9.18.

In general, image magnification is equal to  $\sim 44$  pixel/mm; when a different magnification value is displayed, that value is reported next to the fuel concentration level.

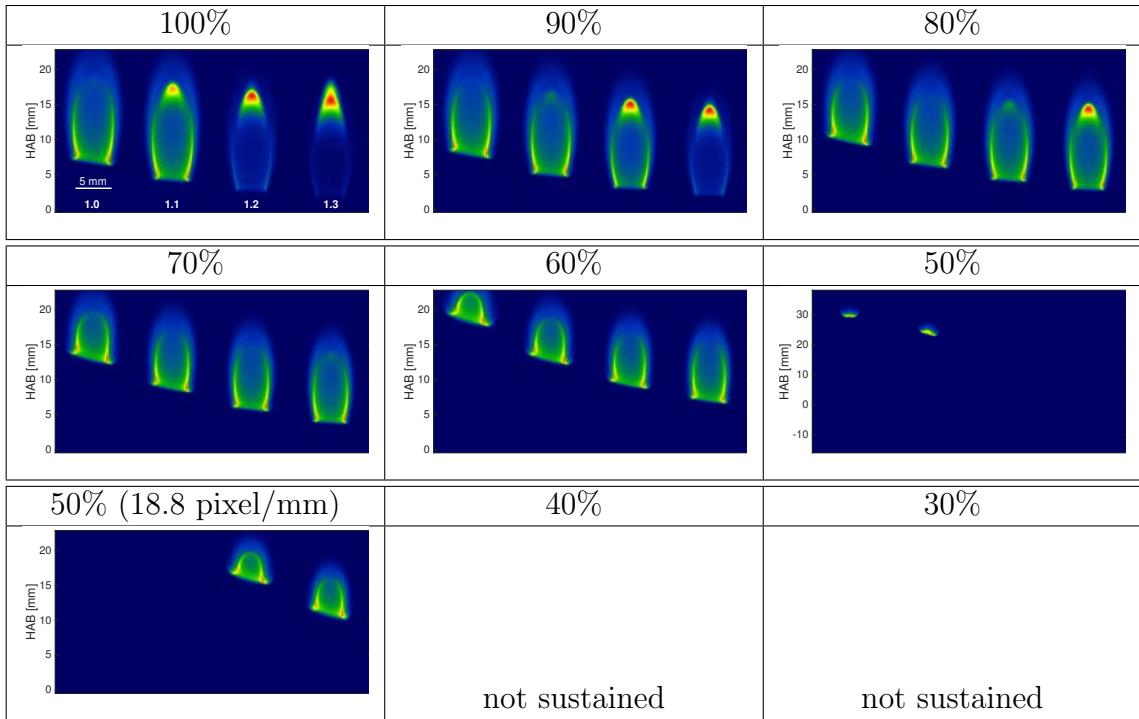


Table B.1: Nitrogen-diluted ACME  $CH_4$  flames: 50 cm/s flow velocities.

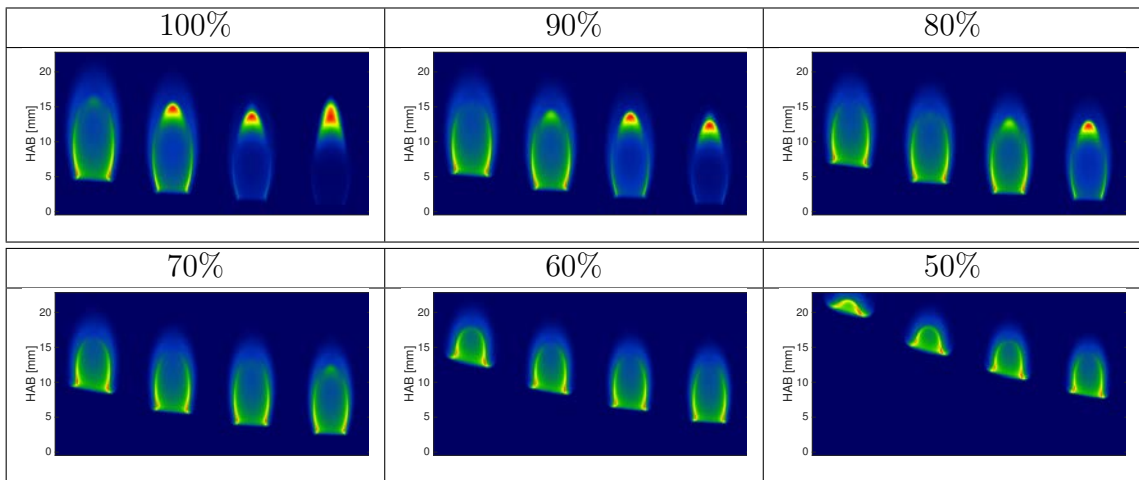


Table B.2: Nitrogen-diluted ACME  $CH_4$  flames: 45 cm/s flow velocities.

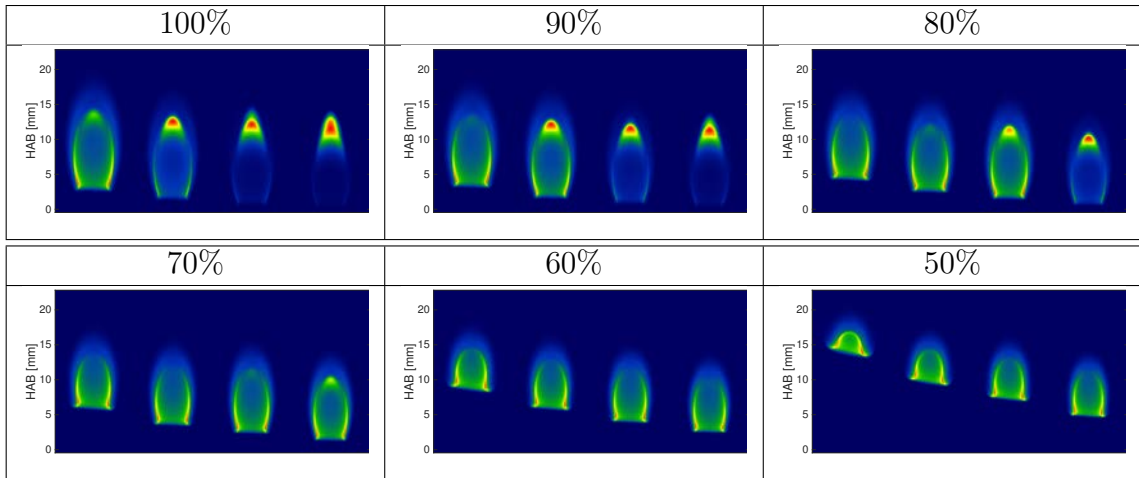


Table B.3: Nitrogen-diluted ACME  $CH_4$  flames: 40 cm/s flow velocities.

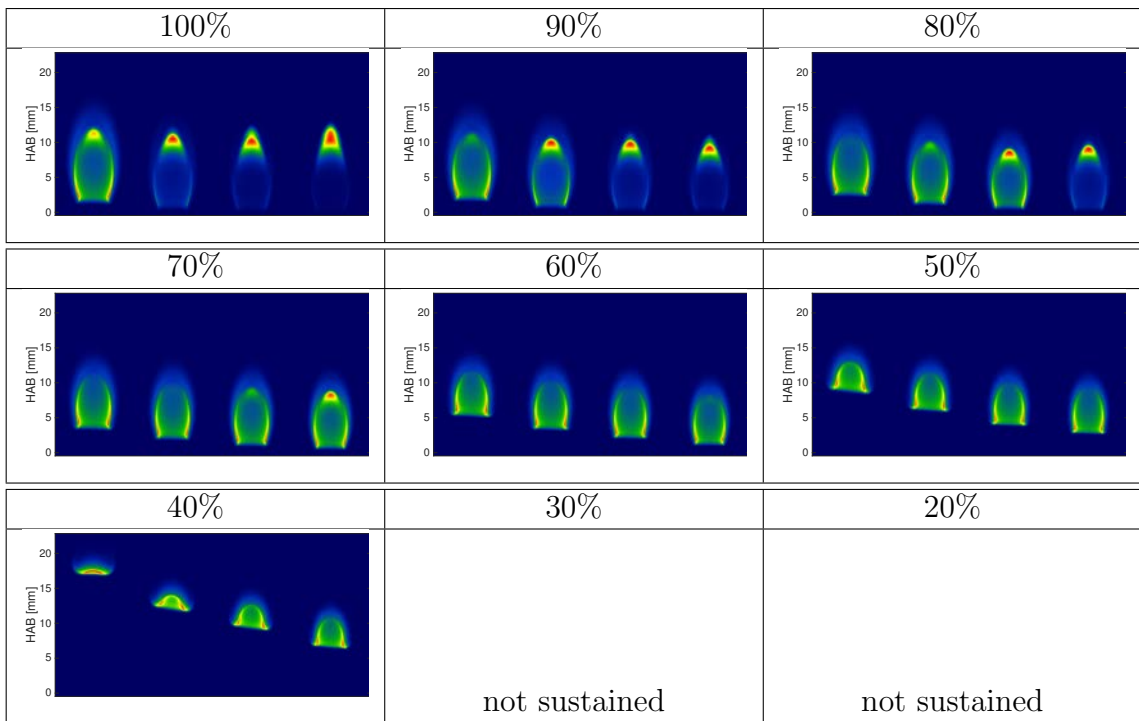


Table B.4: Nitrogen-diluted ACME  $CH_4$  flames: 35 cm/s flow velocities.

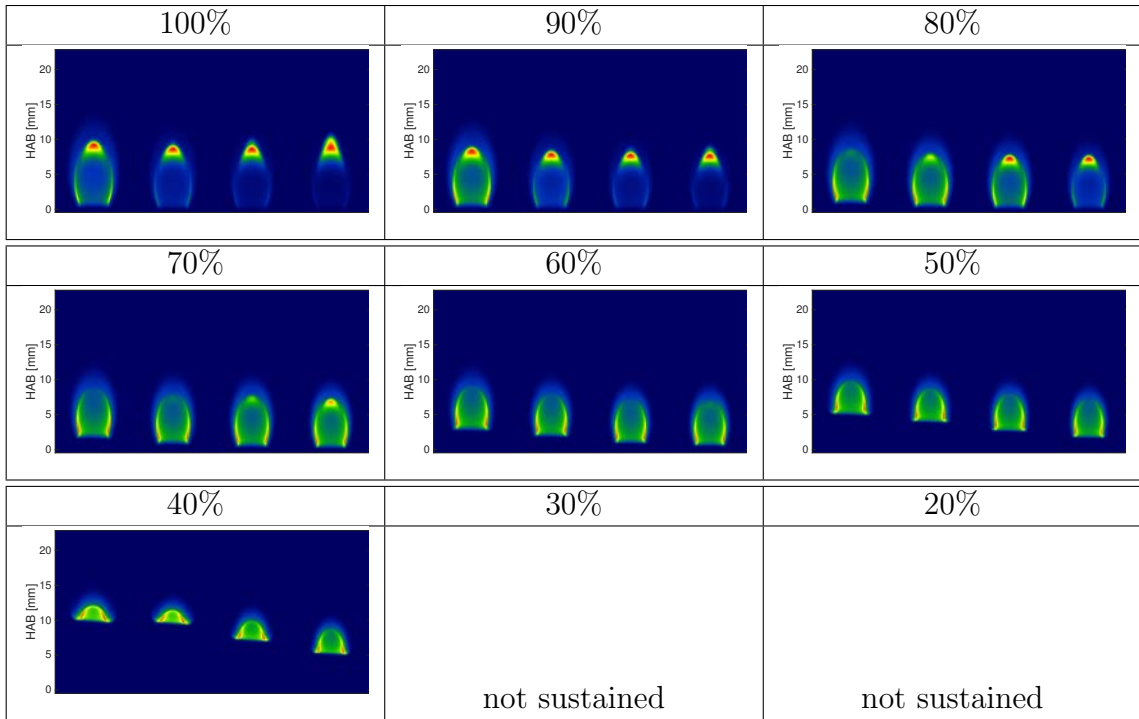


Table B.5: Nitrogen-diluted ACME  $CH_4$  flames: 30 cm/s flow velocities.

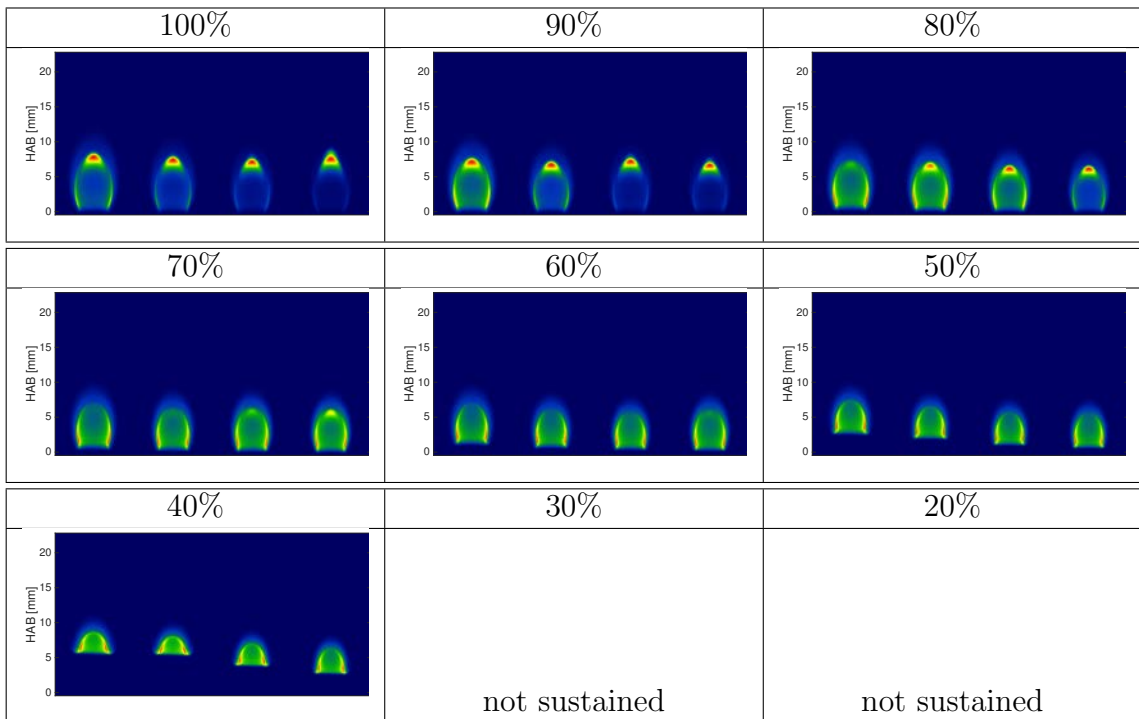


Table B.6: Nitrogen-diluted ACME  $CH_4$  flames: 25 cm/s flow velocities.

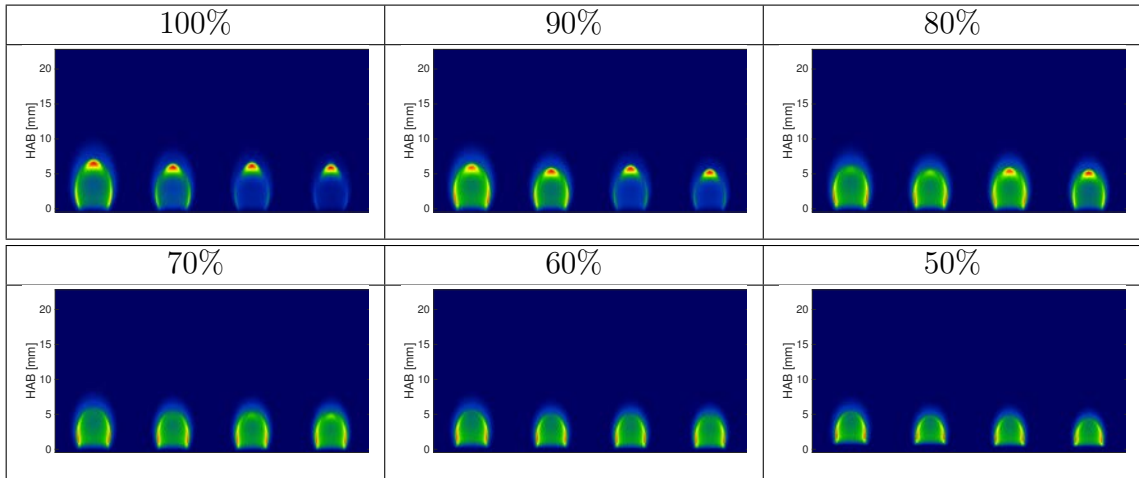


Table B.7: Nitrogen-diluted ACME  $CH_4$  flames: 20 cm/s flow velocities.

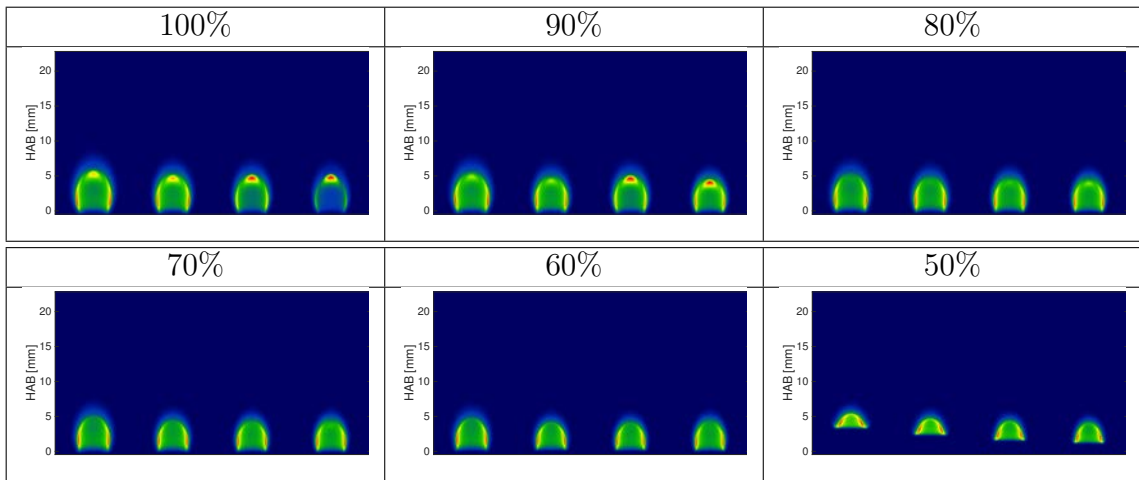


Table B.8: Nitrogen-diluted ACME  $CH_4$  flames: 15 cm/s flow velocities.

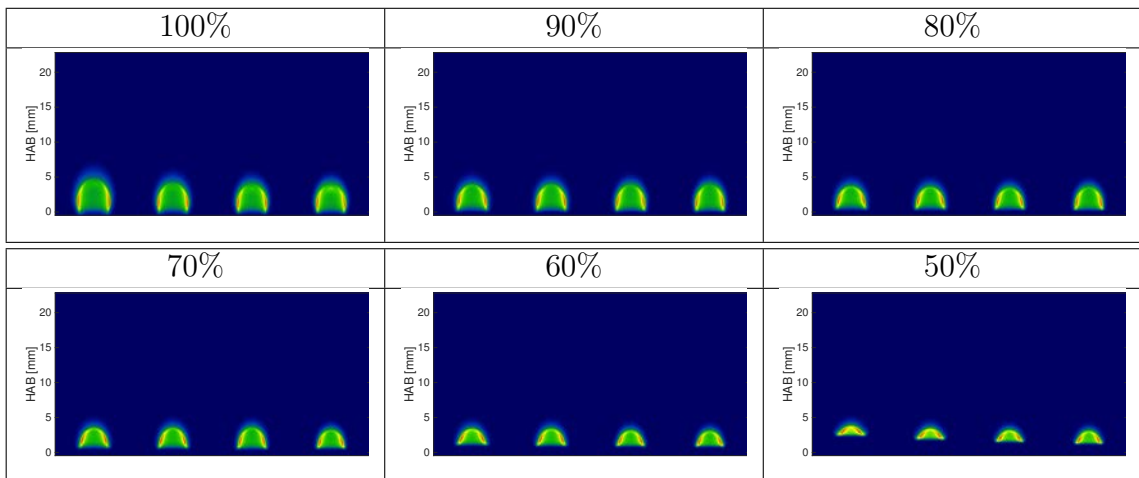


Table B.9: Nitrogen-diluted ACME  $CH_4$  flames: 10 cm/s flow velocities.

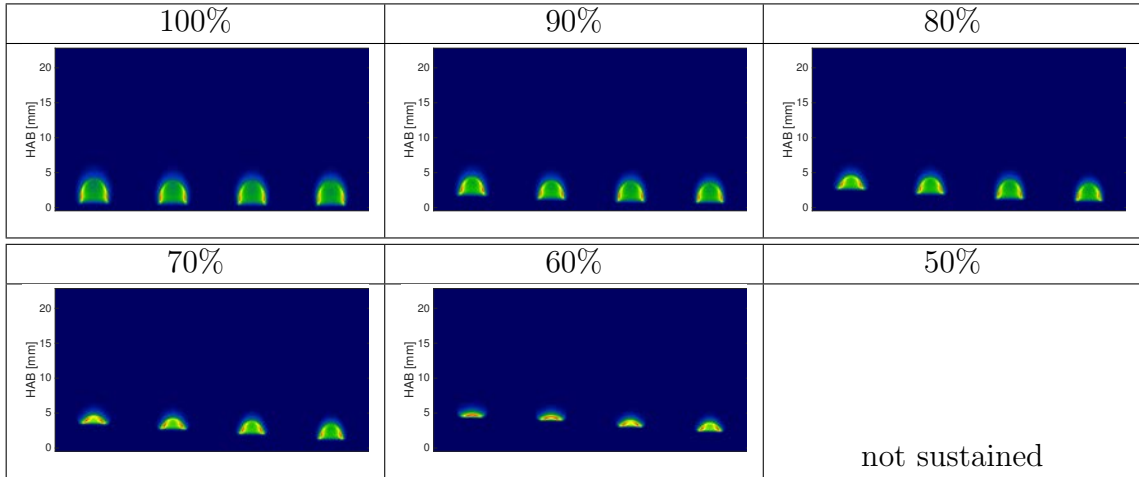


Table B.10: Nitrogen-diluted ACME  $CH_4$  flames: 10 cm/s and 30 cm/s fuel and coflow velocities, respectively.

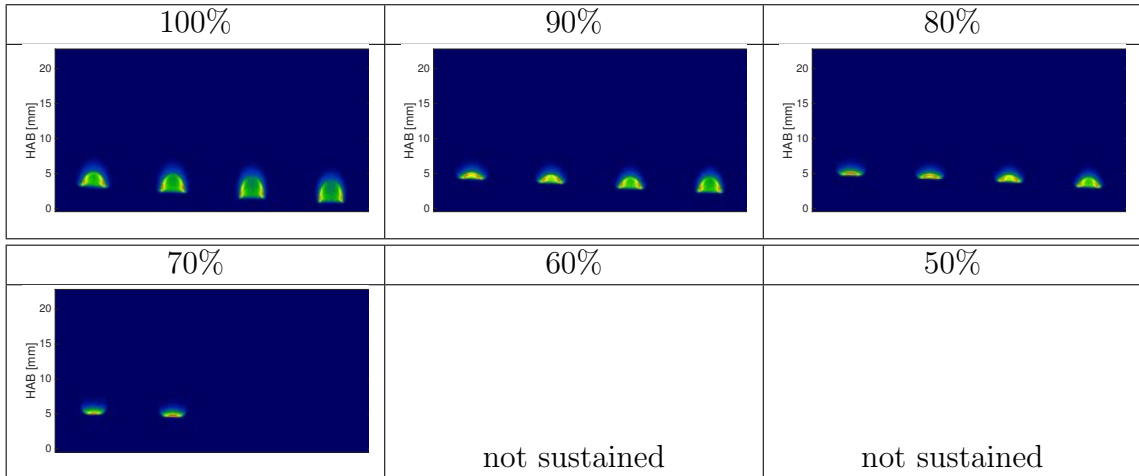


Table B.11: Nitrogen-diluted ACME  $CH_4$  flames: 10 cm/s and 50 cm/s fuel and coflow velocities, respectively.

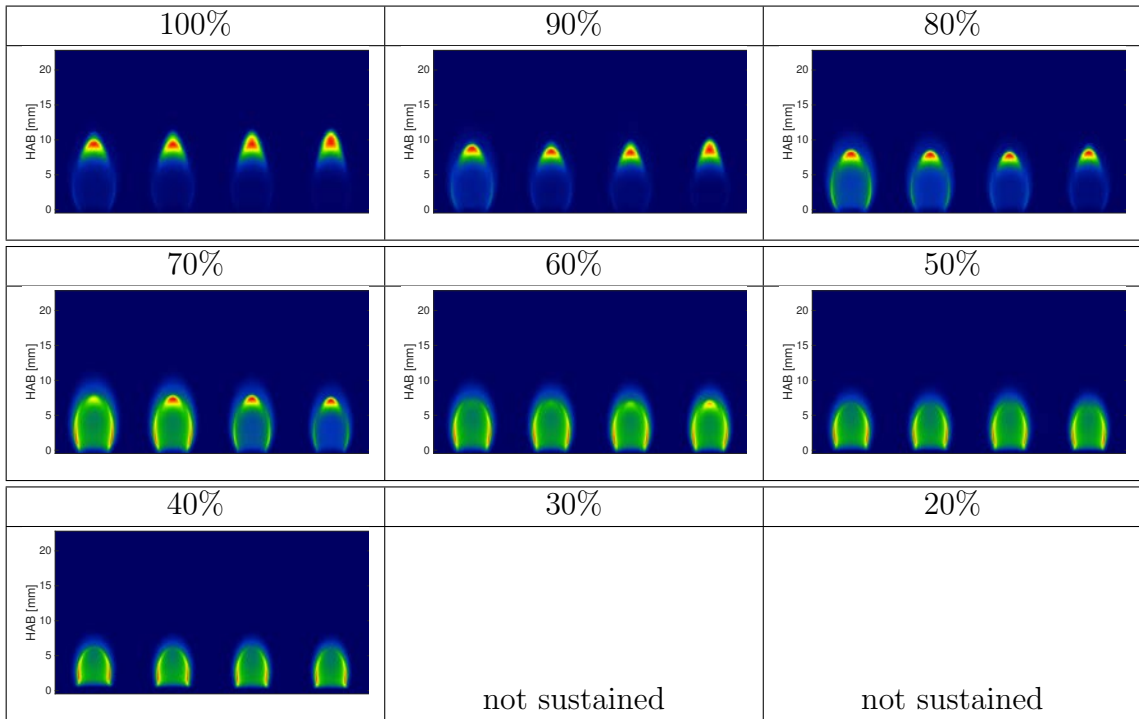


Table B.12: Nitrogen-diluted ACME  $CH_4$  flames: 30 cm/s and 10 cm/s fuel and coflow velocities, respectively.

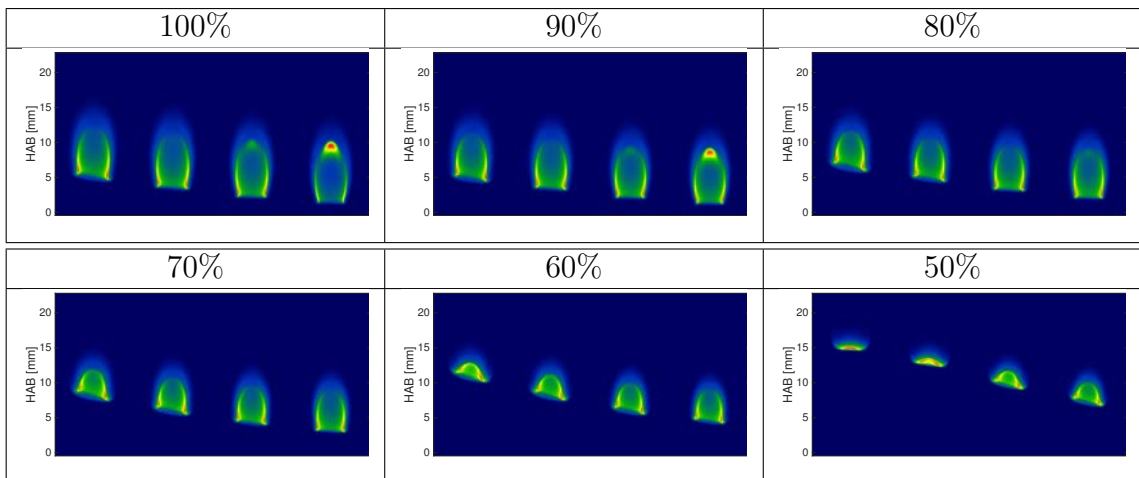


Table B.13: Nitrogen-diluted ACME  $CH_4$  flames: 30 cm/s and 50 cm/s fuel and coflow velocities, respectively.

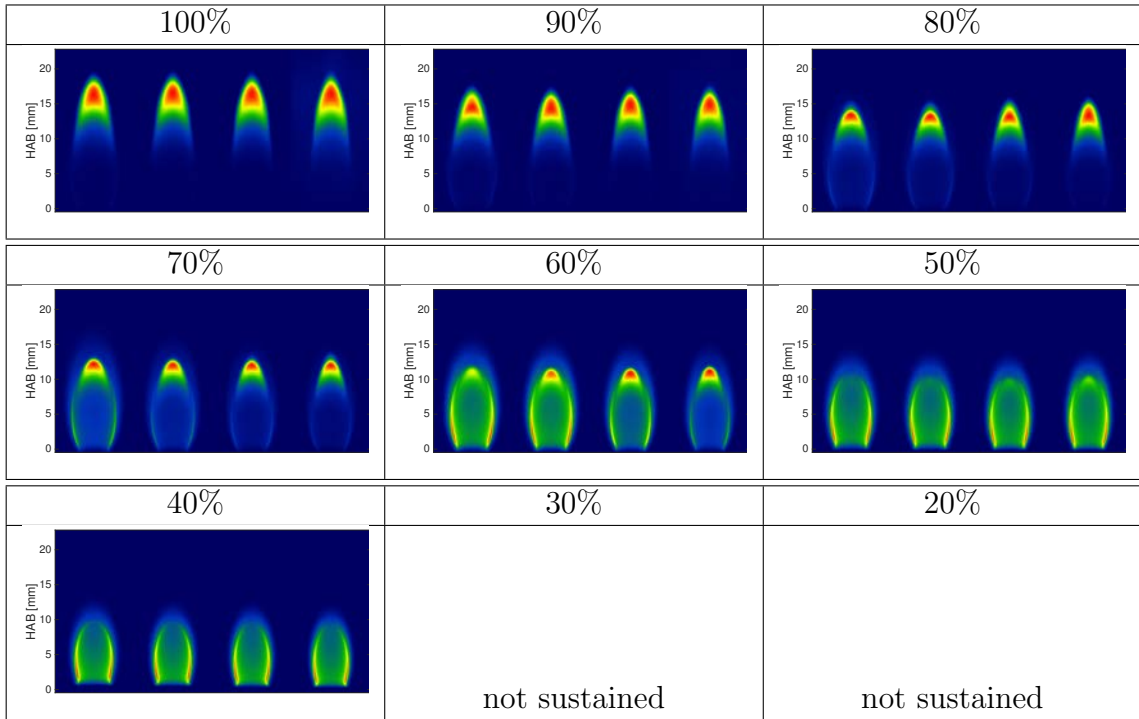


Table B.14: Nitrogen-diluted ACME  $CH_4$  flames: 50 cm/s and 10 cm/s fuel and coflow velocities, respectively.

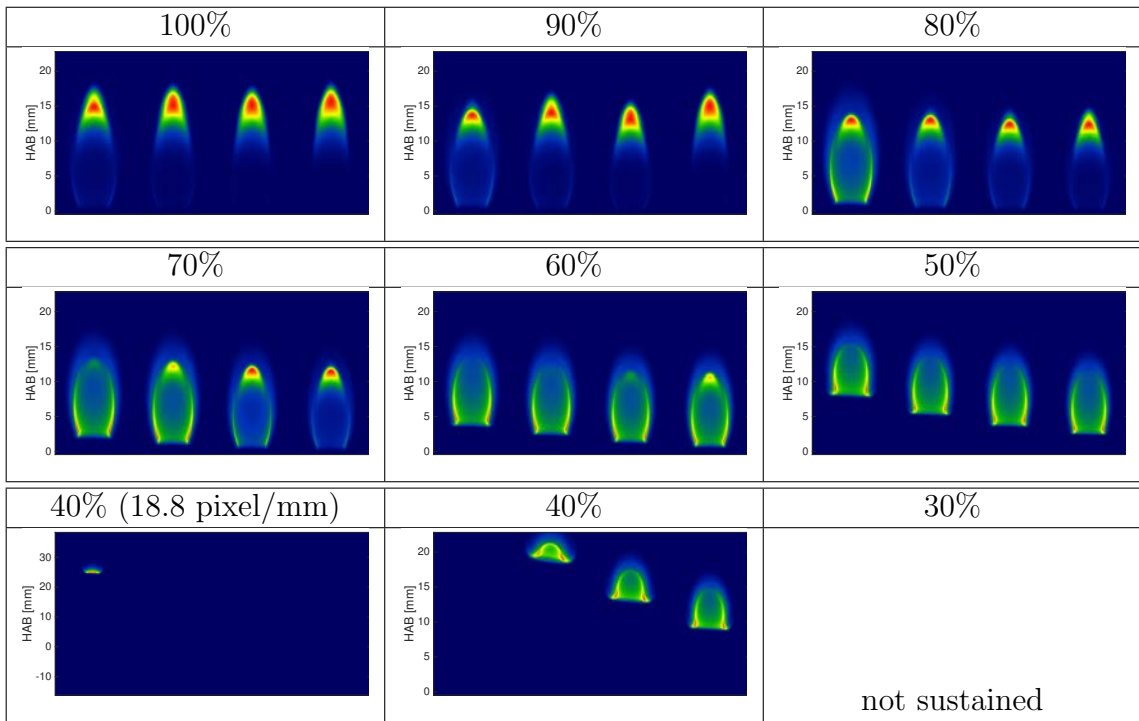


Table B.15: Nitrogen-diluted ACME  $CH_4$  flames: 50 cm/s and 30 cm/s fuel and coflow velocities, respectively.

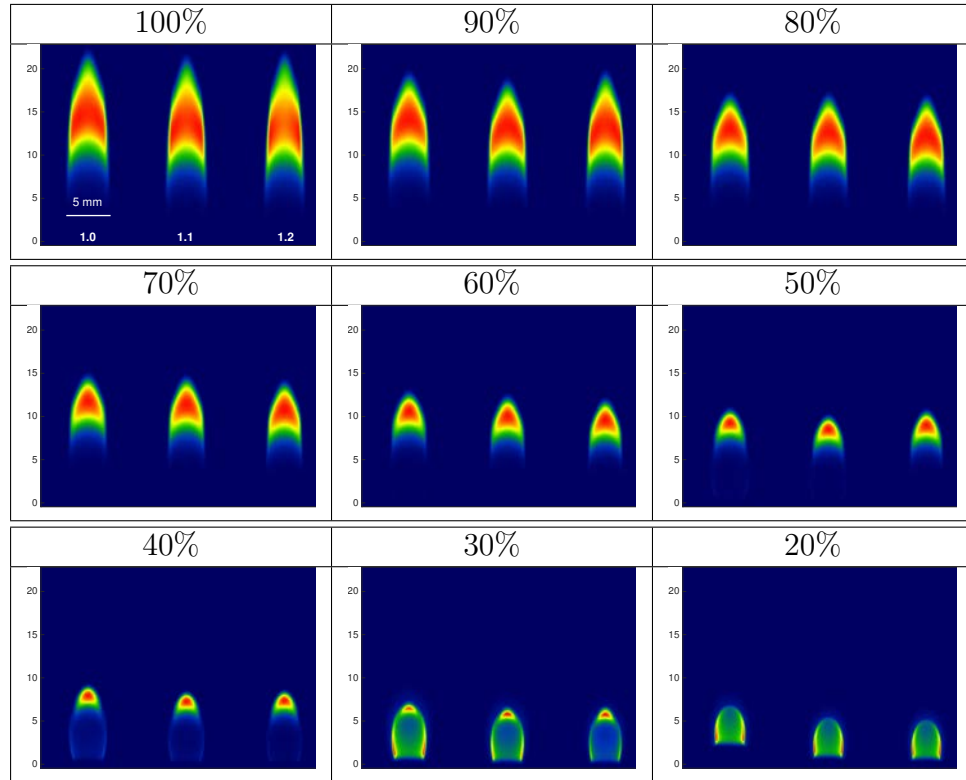


Table B.16: Nitrogen-diluted ACME  $C_2H_4$  flames: 35 cm/s flow velocities.

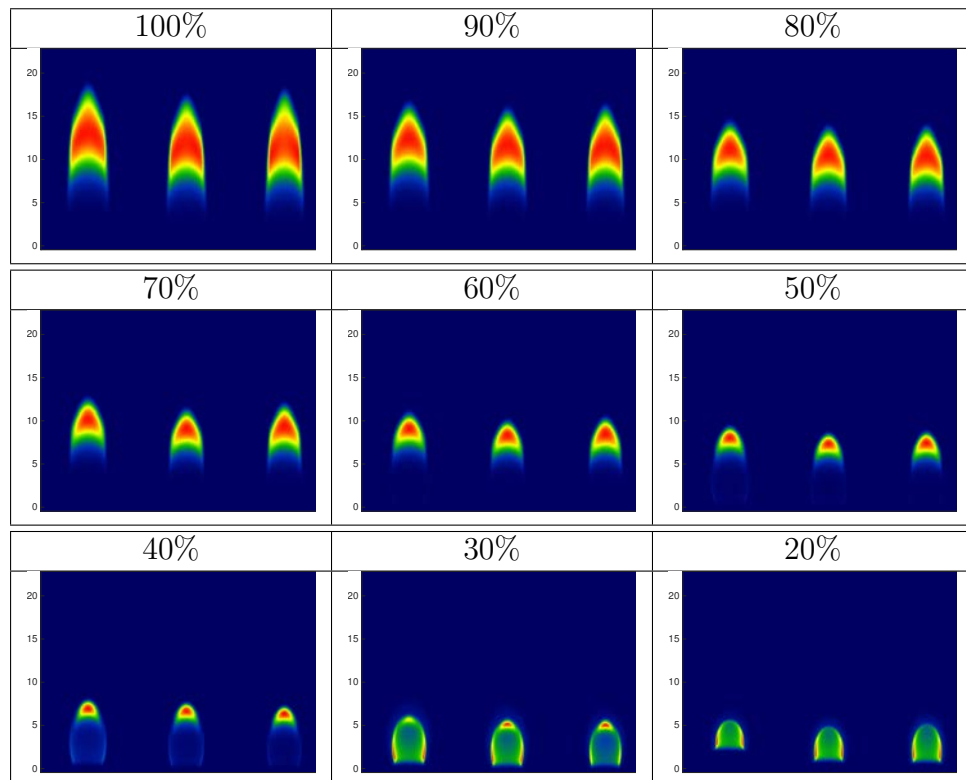


Table B.17: Nitrogen-diluted ACME  $C_2H_4$  flames: 30 cm/s flow velocities.

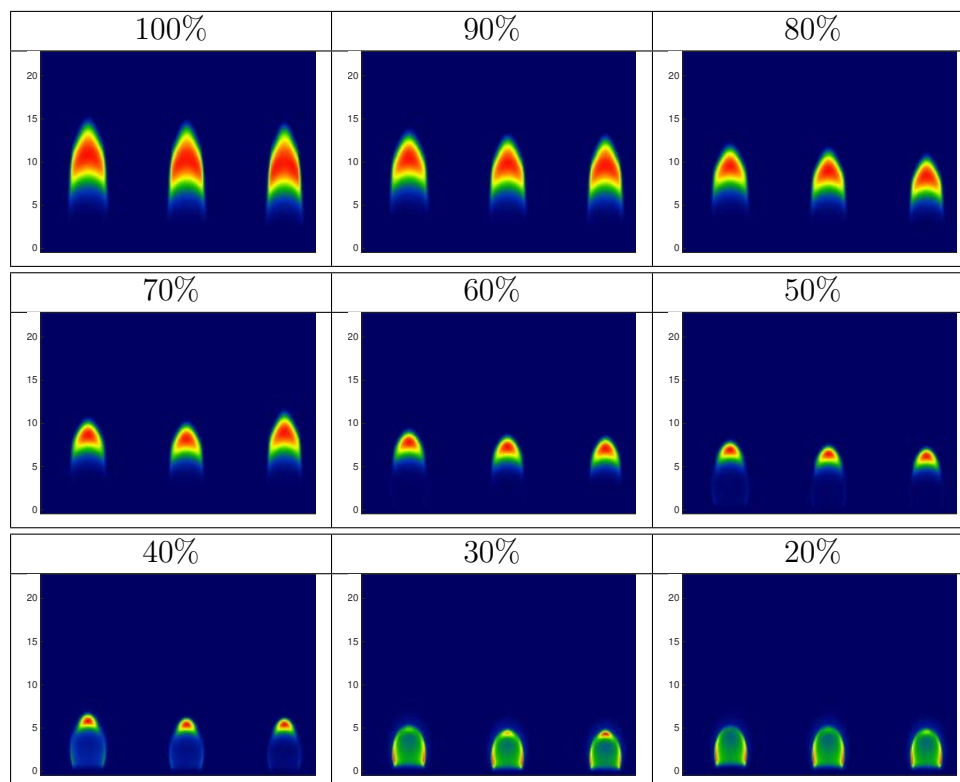


Table B.18: Nitrogen-diluted ACME  $C_2H_4$  flames: 25 cm/s flow velocities.

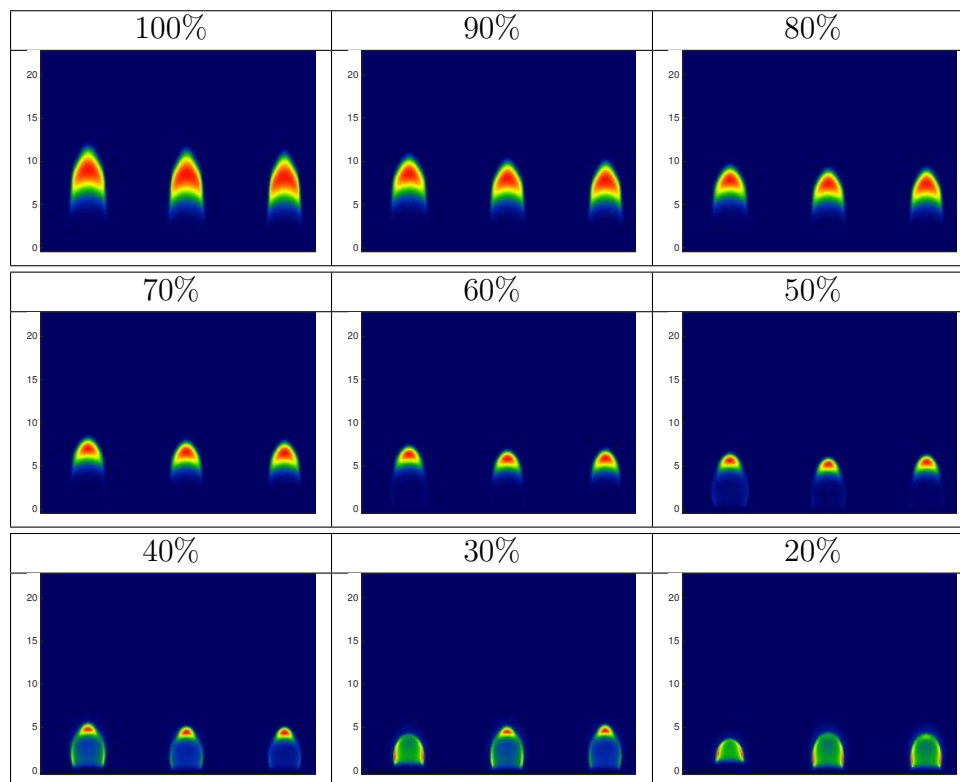


Table B.19: Nitrogen-diluted ACME  $C_2H_4$  flames: 20 cm/s flow velocities.

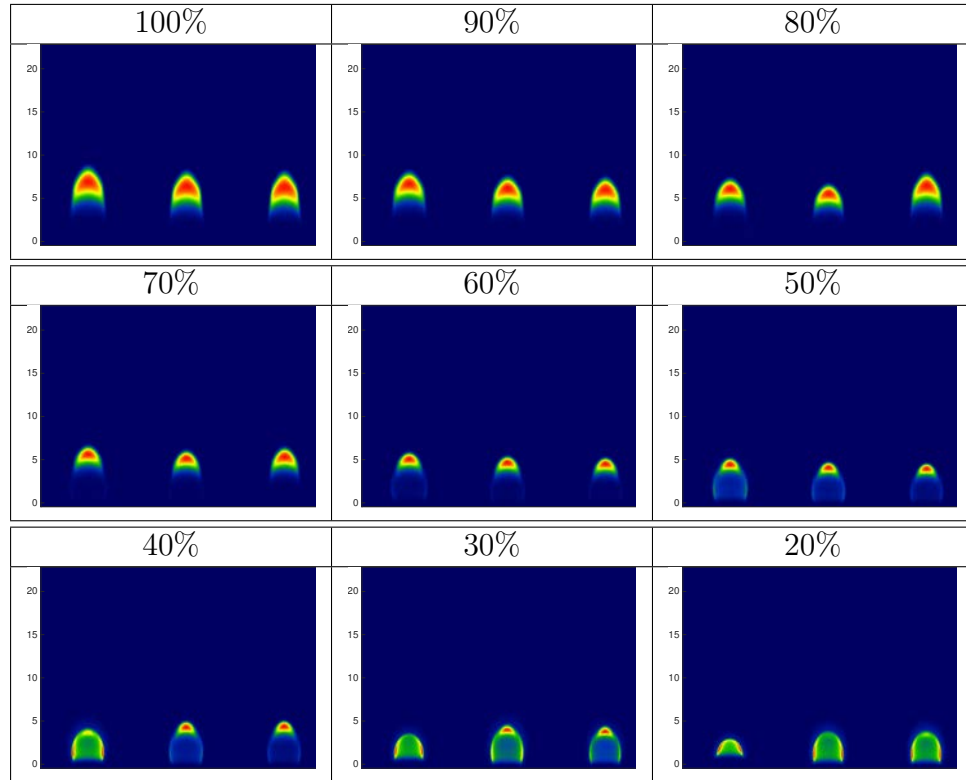


Table B.20: Nitrogen-diluted ACME  $C_2H_4$  flames: 15 cm/s flow velocities.

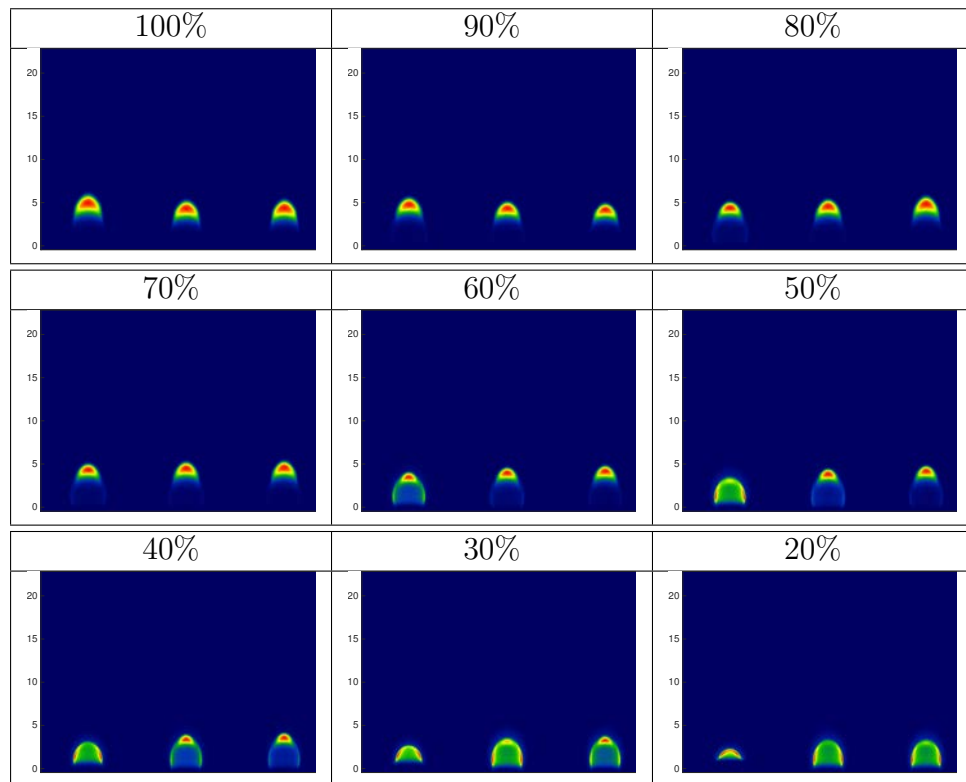


Table B.21: Nitrogen-diluted ACME  $C_2H_4$  flames: 10 cm/s flow velocities.

# Bibliography

- [1] U.S.E.I. Administration, "Annual Energy Outlook 2017," (2017).
- [2] D. Marran, "Quantitative two-dimensional laser diagnostics in idealized and practical combustion system, PhD Thesis, Yale University, (1997).
- [3] A. Shaffer, "Quantitative characterization of species, temperature, and particles in steady and time-varying laminar flames by optical methods," PhD Thesis, Yale University, (2001).
- [4] B.C. Connelly, "Quantitative characterization of steady and time-varying, soot-ing, laminar diffusion flames using optical techniques," PhD Thesis, Yale University (2009).
- [5] K. T. Walsh, "Quantitative characterizations of coflow laminar diffusion flames in a normal gravity and microgravity environment," PhD Thesis, Yale University (2000).
- [6] B. Ma, "Development of quantitative optical techniques for microgravity combustion and sooty flame characterization", PhD Thesis, Yale University (2013).
- [7] B. Ma and M.B. Long, "Absolute light calibration using S-type thermocouples," Proceedings of the Combustion Institute 34:3531-3539 (2013).
- [8] S. Cao, "Development of a mass-conserving, smooth vorticity-velocity formulation for chemically reacting flow simulations", PhD Thesis, Yale University, (2015).
- [9] N.J. Kempema and M.B. Long, "Boundary condition thermometry using a thermographic-phosphor-coated thin filament," Applied Optics 55, 4691-4698 (2016).
- [10] Y.A. Lavendis, K.R. Estrada, and H.C. Hottel, "Development of multicolor pyrometers to monitor the transient-response of burning carbonaceous particles," Review of Scientific Instruments 63(7): 3608-3622 (1992).
- [11] F. Cignoli, S. De Iuliis, V. Manta, and G. Zizak, "Two-dimensional two-wavelength emission technique for soot diagnostics," Applied Optics 40(30): 5370-5378 (2001).

- [12] P.B. Kuhn, B. Ma, B.C. Connelly, M.D. Smooke, and M.B. Long, "Soot and thin-filament pyrometry using a color digital camera," *Proceedings of the Combustion Institute*. 33, 743-750 (2011).
- [13] H. Chang and T.T. Charalampopoulos, "Determination of the wavelength dependence of refractive-indexes of flame soot," *Proceedings of the Royal Society of London Series a-Mathematical Physical and Engineering Science* 430(1880):577-591 (1990).
- [14] B. Ma and M.B. Long, "Combined soot optical characterization using 2-D multi-angle light scattering and spectrally resolved line-of-sight attenuation and its implication on soot color-ratio pyrometry," *Applied Physics B*, 117: 287-303 (2014).
- [15] N.J. Kempema and M.B. Long, "Combined optical and TEM investigations for a detailed characterization of soot aggregate properties in a laminar coflow diffusion flame," *Combustion and Flame*, 164: 373-385 (2016).
- [16] A.M. Cormack, "Computed tomography: some history and recent developments," *Computed Tomography, Proceedings of Symposia in Applied Mathematics*, 27: 35-42 (1982).
- [17] C.J. Dasch, "One dimensional tomography: a comparison of Abel, onion-peeling, and filtered back projection methods," *Applied Optics* 31(8): 1146-1152 (1992).
- [18] K.J. Daun, K.A. Thomson, F.S. Liu, and G.J. Smallwood, "Deconvolution of axisymmetric flame properties using Tikhonov regularization," *Applied Optics*, 45(19): 4638-4646 (2006).
- [19] S. De Iuliis, M. Barbini, S. Benecchi, F. Cignoli, and G. Zizak, "Determination of the soot volume fraction in an ethylene diffusion flame by multiwavelength analysis of soot radiation," *Combustion and Flame* 115(1-2): 253-261 (1998).
- [20] S.S. Krishnan, K.C. Lin, and G.M. Faeth, "Optical properties in the visible of overfire soot in large buoyant turbulent diffusion flames," *Journal of Heat Transfer* 122(3): 517-524 (2000).
- [21] J.D. Maun, P.B. Sunderland, and D.L. Urban, "Thin filament pyrometry with a digital still camera," *Applied Optics* 46(4): 483-488 (2007).
- [22] B. Ma, "Development of quantitative optical techniques for microgravity combustion and sooty flame characterization," PhD Thesis, Yale University (2013).
- [23] B. Ma, G. Wang, G. Magnotti, R.S. Barlow, and M.B. Long, "Intensity-ratio and color-ratio thin-filament pyrometry: uncertainties and accuracy," *Combustion and Flame* 161:908-916 (2014).
- [24] W.M. Rohsenow, J.P. Harnett, and Y.I. Cho, "Handbook of heat transfer," McGraw-Hill New York, (1988).

- [25] Y. Hardalupas, and M. Orain, “Local measurements of the time-dependent heat release rate and equivalence ratio using chemiluminescent emission from a flame,” *Combustion and Flame* 139, 188-207 (2004).
- [26] L. C. Haber, U. Vandesburger, W. R. Saunders, and V. K. Khanna., “An examination of the relationship between chemiluminescent light emissions and heat release rate under non-adiabatic conditions,” *ASME Turbo Expo 2000: Power for Land, Sea, and Air*, pp. V002T02A041. American Society of Mechanical Engineers (2000).
- [27] M. Lauer, and T. Sattelmayer, “On the Adequacy of Chemiluminescence as a Measure for Heat Release in Turbulent Flames With Mixture Gradients,” *J. Eng. Gas Turb. Power* 132 (2010).
- [28] C.S. Panoutsos, Y. Hardalupas, and A. M. K. P. Taylor, “Numerical evaluation of equivalence ratio measurement using  $OH^*$  and  $CH^*$  chemiluminescence in premixed and non-premixed methane-air flames,” *Combustion and Flame* 156, 273-291 (2009).
- [29] A. Hossain, and Y. Nakamura, “A numerical study on the ability to predict the heat release rate using  $CH^*$  chemiluminescence in non-sooting counterflow diffusion flames,” *Combustion and Flame* 161, 162-172 (2014).
- [30] H.M. Hertz, and G.W. Faris, “Emission tomography of flame radicals,” *Optics Letters* 13, 351-353 (1988).
- [31] J. Luque and D.R. Crosley, “LIFBASE: Database and spectral simulation (version 1.5)”, SRI International Report MP 99-009 (1999).
- [32] A.C. Eckbreth, “Laser diagnostics for combustion temperature and species,” 2nd ed., Gordon and Breach Publishers, Amsterdam, (1996).
- [33] J.E.M. Goldsmith and N.M. Laurendeau, “Two-photon-excited fluorescence measurements of  $OH$  concentration in a hydrogen-oxygen flame,” *Applied Optics*, 25:276-283 (1986).
- [34] T.B. Settersten, J.H. Frank, and R.L. Farrow, “Modeling two-photon LIF detection of  $CO$ ,” Personal communication, (2005).
- [35] M.D. Di Rosa and R.L. Farrow, “Cross sections of photoionization and ac Stark shift measured from Doppler-free  $B \leftarrow X(0, 0)$  excitation spectra of  $CO$ ,” *Journal of the Optical Society of America B*, 16:861-870 (1999).
- [36] G. Herzberg, “Molecular spectra and molecular structure I. Spectra of diatomic molecules,” New York, Prentice-Hall, (1989).
- [37] T.B. Settersten, B.D. Patterson, and J.A. Gray, “Temperature and species dependent quenching of  $NO$  probed by two-photon laser-induced fluorescence using picosecond laser,” *Journal of Chemical Physics* 124(24) (2006).

- [38] T.B. Settersten, A. Dreizler, and R.L. Farrow, "Temperature- and species-dependent quenching of  $CO$  probed by two-photon laser-induced fluorescence using a picosecond laser," *Journal of Chemical Physics*, 117:3173-3179 (2002).
- [39] F.Q. Zhao and H. Hiroyasu, "The application of laser Rayleigh-scattering to combustion diagnostics," *Progress in Energy and Combustion Science* 19:447-485 (1993).
- [40] C. Law, "Combustion Physics," Cambridge University Press (2010).
- [41] I. Glassman, R.A. Yetter, and N.G. Glumac, "Combustion," 5th ed. (2014)
- [42] Y.B. Zeldovich, *Acta Physicochim USSR*, 21:557 (1946).
- [43] C.T. Bowman and D.V. Seery, "Emission from continous combustion systems," New York, Plenum Press (1972).
- [44] J. Blauwens, B. Smets, and J. Peeters, "Mechanism of "prompt"  $NO$  formation in hydrocarbon flames," 16th International Symposium on Combustion 1055 (1977)
- [45] <http://guilford.eng.yale.edu/YaleCoflowFlames/> (1/2017).
- [46] R.K. Mohammed, M.A. Tanoff, M.D. Smooke, A.M. Shaffer, and M.B. Long, *Proceedings of the Combustion Institute*, 27 693-702 (1998)
- [47] C.S. McEnally, L.D. Pfefferle, A.M. Schaffer, M.B. Long, R.K. Mohammed, M.D. Smooke, and M.B. Colket, "Characterization of a coflowing methane/air non-premixed flame with computer modeling, Rayleigh-Raman imaging, and on-line spectrometry," *Proceedings of the Combustion Institute*, 28:2063-2070 (2000).
- [48] S.B. Dworkin, B.C. Connelly, A.M. Schaffer, B.A.V. Bennett, M.B. Long, M.D. Smooke, M.P. Puccio, B. McAndrews, and J.H. Miller, "Computational and experimental study of a forced, time-dependent, methane-air coflow diffusion flame," *Proceedings of the Combustion Institute*, 31:971-978 (2007).
- [49] B.C. Connelly, B.A.V. Bennett, M.D. Smooke, M.B. Long, "A paradigm shift in the interaction of experiments and computations in combustion research," *Proceedings of the Combustion Institute*, 32:879-886 (2009).
- [50] P.A.M. Kalt and M.B. Long, "OMA - Image processing for Mac OS X". <http://www.oma-x.org> (1/2017).
- [51] B.A.V. Bennett, Z. Cheng, R.W. Pitz, and M.D. Smooke, "Computational and experimental study of oxygen-enhanced axisymmetric laminar methane flames," *Combustion Theory and Modelling*, 12:497-527 (2008).
- [52] Q.V. Nguyen, R.W. Dibble, and R.S. Barlow, "Raman-LIF measurements of temperature, major species,  $OH$ , and  $NO$  in a methane-air bunsen flame," *Combustion and Flame* 105(4):499-510 (1996).

- [53] J.R. Reisel, C.D. Carter, N.M. Laurendeau, and M.C. Drake, "Laser-saturated fluorescence measurement of nitric oxide in laminar, flat, C<sub>2</sub>H<sub>6</sub>/O<sub>2</sub>/N<sub>2</sub> flames at atmospheric pressure," *Combustion Science and Technology*, 91:271-295 (1993).
- [54] M. Alden, S. Wallin, and W. Wendt, "Application of two-photon absorption for detection of CO in combustion gases," *Applied Physics B: Lasers and Optics* 33:205-212 (1984).
- [55] J.M. Seitzman, J. Haumann, and R.K. Hanson, "Quantitative two-photon LIF imaging of carbon monoxide in combustion gases," *Applied Optics*, 26:2892-2899 (1987).
- [56] G.W. Loge, J.J. Tiee, and F.B. Wampler, "Multiphoton induced fluorescence and ionization of carbon monoxide," *Journal of Chemical Physics*, 79:196-202 (1983).
- [57] F. Fuest, R.S. Barlow, J.Y. Chen, and A. Dreizler, "Raman/Rayleigh scattering and CO-LIF measurements in laminar and turbulent jet flames of dimethyl ether," *Combustion and Flame*, 159:2533-2562 (2012).
- [58] D.A. Everest, C.R. Shaddix, and K.C. Smyth, "Quantitative two-photon LIF imaging of CO in flickering CH<sub>4</sub>/Air diffusion flames," *Twenty-Sixth Symposium (International) on Combustion*, Vols 1 and 2:1161-1169 (1996).
- [59] S. Linow, A. Dreizler, J. Janicka, and E.P. Hassel, "Comparison of two-photon detection schemes for CO detection in flames," *Applied Physics B: Lasers and Optics*, 71:689-696 (2000).
- [60] B.J. Kirby, and R.K. Hanson, "Imaging of CO and CO<sub>2</sub> using infrared planar laser-induced fluorescence," *Proceedings of the Combustion Institute*, 28:253-259 (2000).
- [61] P.J.H. Tjossem and K.C. Smyth, "Multiphoton excitation spectroscopy of the  $B^1\Sigma^+$  and  $C^1\Sigma^+$  Rydberg states of CO," *Journal of Chemical Physics*, 91:2041-2048 (1989).
- [62] M. Eidelsberg, J.Y. Roncin, A. Le Floch, F. Launay, C. Letzelter, and J. Rostas, "Reinvestigation of the vacuum ultraviolet spectrum of CO and isotropic species: the  $B^1\Sigma^+ \leftarrow X^1\Sigma^+$  transition," *Journal of Molecular Spectroscopy*, 121:309-336 (1987).
- [63] R. T. Birge, "The band spectra of carbon monoxide," *Physical Review*, 28:1157-1181 (1926).
- [64] F. Di Teodoro, J.E. Rehm, R.L. Farrow, and P.H. Paul, "Collisional quenching of CO  $B^1\Sigma^+$  ( $V'=0$ ) probed by two-photon laser-induced fluorescence using a picosecond laser," *Journal of Chemical Physics*, 113:3046-3054 (2000).

- [65] E. Reinhard, W. Heidrich, P. Debevec, S. Pattanaik, G. Ward, and K. Myszkowski, "High Dynamic Range Imaging," Second ed. (Morgan Kaufmann, 2010).
- [66] B.C. Madden, "Extended Intensity Range Imaging," (1993).
- [67] S. Battiato, A. Castorina, and M. Mancuso, "High dynamic range imaging for digital still camera: an overview," *J Electron Imaging* 12, 459-469 (2003).
- [68] B. Ma, S. Cao, D. Giassi, D.P. Stocker, F. Takahashi, B.A.V. Bennett, M.D. Smooke, and M.B. Long, "An experimental and computational study of soot formation in a coflow jet flame under microgravity and normal gravity," *Proceedings of the Combustion Institute* (2014), <http://dx.doi.org/10.1016/j.proci.2014.05.064>.
- [69] P. Debevec and J. Malik, "Recovering High Dynamic Range Radiance Maps from Photographs," *ACM SIGGRAPH* (2008).
- [70] M.D. Grossberg and S.K. Nayar, "Determining the camera response from images: What is knowable?," *Ieee T Pattern Anal* 25, 1455-1467 (2003).
- [71] C.V. Singh and K. Nallaperumal, "Application of HDR Imaging Techniques for Sonar Images," *2012 Ieee International Conference on Computational Intelligence and Computing Research (Iccic)*, 694-698 (2012).
- [72] P. Fei, Z.L. Yu, X. Wang, P.J. Lu, Y.S. Fu, Z. He, J. W. Xiong, and Y.Y. Huang, "High dynamic range optical projection tomography (HDR-OPT)," *Opt Express* 20, 8824-8836 (2012).
- [73] L. Bellia, M. Musto, and G. Spada, "Illuminance measurements through HDR imaging photometry in scholastic environment," *Energy Buildings* 43, 2843-2849 (2011).
- [74] D.B. Kim, M.K. Seo, K.Y. Kim, and K.H. Lee, "Developing a multi-spectral HDR imaging module for a BRDF measurement system," *Reflection, Scattering, and Diffraction from Surfaces Ii* 7792 (2010).
- [75] A.A. Bell, D. Meyer-Ebrecht, A. Bocking, and T. Aach, "HDR-microscopy of cell specimens: Imaging and image analysis," *Conference Record of the Forty-First Asilomar Conference on Signals, Systems & Computers, Vols 1-5*, 1303-1307 (2007).
- [76] T.J. Park, and I.K. Park, "High dynamic range image acquisition using multiple images with different apertures," *Optical Engineering* 51 (2012).
- [77] <http://spaceflight systems.grc.nasa.gov/SOPO/ICHO/IRP/FCF/Investigations/ACME/>.
- [78] D. Coffin, <http://www.cybercom.net/~dcoffin/dcraw/> (1/2010).

- [79] G. Agranov, V. Berezin, and R. H. Tsai, "Crosstalk and microlens study in a color CMOS image sensor," *Ieee Transactions on Electronic Devices* 50, 4-11 (2003).
- [80] I. Shcherback, T. Danov, and O. Yadid-Pecht, "A comprehensive CMOS APS crosstalk study: Photoresponse model, technology, and design trends," *Ieee Transactions on Electronic Devices* 51, 2033-2041 (2004).
- [81] W. Yang, C. Philip, and R. Howard, "Decoupling photo collection efficiency and color crosstalk from the quantum efficiency spectrum for cmos image sensor pixel development," *Proceeding SPIE 7250, Digital Photography V*, (2009).
- [82] J. Vaillant, C. Mornet, T. Decroux, D. Herault, and I. Schanen, "Characterization of pixel crosstalk and impact of Bayer patterning by quantum efficiency measurement," *Digital Photography Vii 7876* (2011).
- [83] C.F. Kaminski and M.B. Long, "Multidimensional Diagnostics in Space and Time. In: Kohse-Hoinghaus K and Jeffries J B (eds) *Applied Combustion Diagnostics*," Taylor and Francis, London, pp. 224-251 (2002).
- [84] R. Miles and W. Lempert, "Two-dimensional measurement of density, velocity, and temperature in turbulent high-speed air flows by UV Rayleigh scattering," *Applied Physics B* 51:1-7 Doi 10.1007/BF00332317 (1990).
- [85] J.R. Janesick, "Scientific charged-coupled devices," Bellingham: SPIE press, Washington (2001).
- [86] L. Shao, R. Yan, X. Li, and Y. Liu, "From heuristic optimization to dictionary learning: a review and comprehensive comparison of image denoising algorithm," *IEEE Transaction on Cybernetics* 44:1001-1013 Doi 10.1109/T-CYB.2013.2278548 (2014).
- [87] A. Jain, M.S. Kerhalkar, M.M. Ahmed, T.A. Shaikh, M.R. Prabhu, U.T. Sasikala, S.K. Majumder, P. Guha, U.M. Uche, and O.H. Christian, "Review on denoising technique for the AWGN signal introduced in a stationary image," *International Journal of Engineering Science Invention* 3:01-10 (2014).
- [88] I. Irum, M.A. Shahid, M. Sharif, M. Raza, "A review of image denoising methods," *Journal of Engineering Science and Technology Review* 5:41-48 (2015).
- [89] D. Giassi, B. Liu, and M.B. Long, "Use of high dynamic range imaging for quantitative combustion diagnostics," *Applied Optics* 54:4580-4588 (2015).
- [90] P. Hoess and F. Karlheinz, "Time-integrated phosphor behavior in gated image intensifier tubes," *International Symposium on Optical Science and Technology. International Society for Optics and Photonics* 23-28 (2000).
- [91] Product datasheet, Proxitronic Funk GmbH & Co.KG, Bensheim, Germany (1998).

- [92] P. Hoess and F. Karlheinz, "Response of very-fast-decay phosphors in image intensifier tubes for CCD readout devices," 24th International Congress on High-Speed Photography and Photonics. International Society for Optics and Photonics 127-132 (2001).
- [93] J. Zhou, Y. Qiu, and X. Wu, "Relation between signal-to-noise ratio of UV image intensifiers and voltage of MCP," Image Processing and Photonics for Agricultural Engineering, Proceedings SPIE 8761 (2013).
- [94] R.S. Barlow, G.H. Wang, P. Anselmo, M.S. Sweeney, and S. Hochgreb, "Application of Raman/Rayleigh/LIF diagnostics in turbulent stratified flames," Proceedings of the Combustion Institute 32:945-953 Doi:10.1016/J.Proci.2008.06.070 (2009).
- [95] J.H. Frank, S.A. Kaiser, and M.B. Long, "Multiscalar imaging in partially premixed jet flames with argon dilution," Combustion and Flame 143:507-523 (2005).
- [96] F. Fuest, R.S. Barlow, J.Y. Chen, and A. Dreizler, "Raman/Rayleigh scattering and CO-LIF measurements in laminar and turbulent jet flames of dimethyl ether," Combustion and Flame 159:2533-2562 (2012).
- [97] F. Fuest, R.S. Barlow, G. Magnotti, A. Dreizler, I.W. Ekoto, and J.A. Sutton, "Quantitative acetylene measurements in laminar and turbulent flames using 1D Raman/Rayleigh scattering," Combustion and Flame 162:2248-2255 (2015).
- [98] A.N. Karpetsis and R.S. Barlow, "Measurements of scalar dissipation in a turbulent piloted methane/air jet flame," Proceedings of the Combustion Institute 29:1929-1936 Doi 10.1016/S1540-7489(02)80234-6 (2002).
- [99] S.A. Kaiser and J.H. Frank, "Spatial scales of extinction and dissipation in the near field of non-premixed turbulent jet flames," Proceedings of the Combustion Institute 32:1639-1646 (2009).
- [100] F. Fuest, M.J. Papageorge, W.R. Lempert, and J.A. Sutton, "Ultrahigh laser pulse energy and power generation at 10 kHz," Optics Letters 37:3231-3233 (2012).
- [101] M.J. Papageorge, T.A. McManus, F. Fuest, and J.A. Sutton, "Recent advances in high-speed planar Rayleigh scattering in turbulent jets and flames: increased record lengths, acquisition rates, and image quality," Applied Physics B:197-213 (2014).
- [102] R.A. Patton, K.N. Gabet, N. Jiang, W.R. Lempert, and J.A. Sutton, "Multi-kHz mixture fraction imaging in turbulent jets using planar Rayleigh scattering," Applied Physics B Lasers Opt 106:457-471 (2012).

- [103] R.A. Patton, K.N. Gabet, N. Jiang, W.R. Lempert, and J.A. Sutton, “Multi-kHz temperature imaging in turbulent non-premixed flames using planar Rayleigh scattering,” *Applied Physics B-Lasers Opt* 108:377-392 (2012).
- [104] J. G. Lee, K. Kim, and D. A. Santavicca, “Measurement of equivalence ratio fluctuation and its effect on heat release during unstable combustion,” *Proceedings of the Combustion Institute* 28, 415-421 (2000).
- [105] S. Kato, T. Fujimori, A. P. Dowling, and H. Kobayashi, “Effect of heat release distribution on combustion oscillation,” *Proceedings of the Combustion Institute* 30, 1799-1806 (2005).
- [106] S. Hemchandra, N. Peters, and T. Liewen, “Heat release response of acoustically forced turbulent premixed flames - role of kinematic restoration,” *Proceedings of the Combustion Institute* 33,1609-1617 (2011).
- [107] Y. Hardalupas, C. S. Panoutsos, and A. M. K. P. Taylor, “Spatial resolution of a chemiluminescence sensor for local heat-release rate and equivalence ratio measurements in a model gas turbine combustor,” *Experiments in Fluids* 49, 883-909 (2010).
- [108] S. A. Farhat, W. B. Ng, and Y. Zhang, “Chemiluminescent emission measurement of a diffusion flame jet in a loudspeaker induced standing wave,” *Fuel* 84, 1760-1767 (2005).
- [109] <https://spaceflight systems.grc.nasa.gov/sopo/i hho/psrp/msg/slice/> (2015).
- [110] <http://psi.nasa.gov/index.html> (2016).
- [111] K. T. Walsh, J. Fielding, M. D. Smooke, M. B. Long, and A. Lian, “A comparison of computational and experimental lift-off heights of coflow laminar diffusion flames,” *Proceedings of the Combustion Institute* 30, 357-365 (2005).
- [112] K. T. Walsh, J. Fielding, and M. B. Long, “Effect of light-collection geometry on reconstruction errors in Abel inversions,” *Opt. Lett.* 25, 457-459 (2000).
- [113] A. G. Gaydon, “The spectroscopy of flames,” 2nd. Edition, Chapman and Hall, London (1974).
- [114] S. Cao, B. A. V. Bennett, and M. D. Smooke, “MC-Smooth: A mass-conserving, smooth vorticity-velocity formulation for multi-dimensional flows,” *Combustion Theory and Modelling*, 19, 657-695 (2015).
- [115] G. P. Smith, D. M. Golden, M. Frenklach, N. W. Moriarty, B. Eite-  
neer, M. Goldenberg, C. T. Bowman, R. K. Hanson, S. Song, W. C. Gar-  
diner, Jr., V. V. Lissianski, and Z. Qin, “GRI Mech. version 3.0,” *http* :  
*//www.me.berkeley.edu/gri\_mech/* (2015).

- [116] P. Deuffhard, "A modified Newton method for the solution of ill-conditioned systems of nonlinear equations with application to multiple shooting," *Numerische Mathematik* 22, 289-315 (1974).
- [117] H. A. Van der Vorst, "Bi-CGSTAB: A Fast and Smoothly Converging Variant of Bi-CG for the Solution of Nonsymmetric Linear Systems," *SIAM Journal on Scientific and Statistical Computing* 13, 631-644 (1992).
- [118] S. Karnani and D. Dunn-Rankin, "Visualizing CH\* chemiluminescence in sooting flames," *Combustion and Flame* 160, 2275-2278 (2013).
- [119] F. Takahashi and V. R. Katta, "Reaction kernel structure and stabilizing mechanisms of jet diffusion flames in microgravity," *Proceedings of the Combustion Institute* 29, 2509-2518 (2002).
- [120] I. Glassman, "Sooting laminar diffusion flames: effect of dilution, additives, pressure, and microgravity," *Proceedings of the Combustion Institute*, 27:1589-1596 (1998).
- [121] F. Liu, K.A. Thompson, H.S. Guo, and G.J. Smallwood, "Numerical and experimental study of an axisymmetric coflow laminar methane-air diffusion flame at pressure between 5 and 40 atmospheres," *Combustion and Flame* 146:456-471 (2006).
- [122] M.R.J. Charest, C.P.T. Groth, and O.L. Gulder, "Effects of gravity and pressure on a laminar coflow methane-air diffusion flames at pressures from 1 to 60 atmospheres," *Combustion and Flame*, 158, 860-875 (2011).
- [123] M.R.J. Charest, C.P.T. Groth, and O.L. Gulder, "A numerical study on the effects of pressure and gravity in laminar ethylene diffusion flames," *Combustion and Flame*, 158, 1933-1945 (2011).
- [124] F.S. Liu, K.A. Thomson, H.S. Guo, G.J. Smallwood, "Numerical and experimental study of an axisymmetric coflow laminar methane-air diffusion flame at pressures between 5 and 40 atmospheres," *Combustion and Flame*, 146, 456-471 (2006).
- [125] B.J. Lee, J.S. Kim, and S.H. Chung, "Effect of fuel dilution on the liftoff of non-premixed jet flames," *Proceedings of the Combustion Institute*, 25:1175-1181 (1994).
- [126] H.K. Chelliah, C.K. Law, T. Ueda, M.D. Smooke, and F.A. Williams, "An experimental and theoretical investigation of the dilution, pressure and flow-field effects on the extinction condition of methane-air-nitrogen diffusion flames," *Proceedings of the Combustion Institute* 23:503:511 (1991).
- [127] F.G. Roper, "The prediction of laminar jet diffusion flame sizes: part I. theoretical model," *Combustion and Flame*, 29: 219-226 (1977).

- [128] T. Panagiotou, Y. Lavendis, and M. Delichatsios, "Measurement of particle flame temperature using three-color optical pyrometry," *Combustion and Flame* 104(3):272-287 (1996).
- [129] R. Ramanath, W.E. Snyder, G.L. Bilbro, and W.A. Sander, "Demosaicking methods for Bayer color arrays," *Journal of Electronic Imaging*, 11(3), 306-315 (2002).
- [130] R. Kimmel, "Demosaicing: image reconstruction from color CCD samples," *IEEE Transactions on Image Processing*, 8: 1221-1228 (1999).
- [131] X. Li, "Demosaicing by successive approximation," *IEEE Transactions on Image Processing*, 14: 370-379 (2005).
- [132] K. Hirakawa and T.W. Parks, "Joint demosaicing and denoising," *IEEE Transactions on Image Processing*, 15: 2146-2156 (2006).
- [133] H.S. Malvar, L. He, and R. Cutler, "High-quality linear interpolation for demosaicing of Bayer-patterned color images," *ICASSP III*, 485-488 (2004).
- [134] N.J. Kempema and M.B. Long, "Quantitative Rayleigh thermometry for high background scattering applications with structured laser illumination planar imaging," *Applied Optics* 53, 6688-6697 (2014).
- [135] [https://spaceflight systems.grc.nasa.gov/wp-content/uploads/ACME\\_ISRD\\_revB.20130930\\_signed.pdf](https://spaceflight systems.grc.nasa.gov/wp-content/uploads/ACME_ISRD_revB.20130930_signed.pdf)
- [136] M.D. Smooke, M.B. Long, B.C. Connelly, M.B. Colket, and R.J. Hall, "Soot formation in laminar diffusion flames," *Combustion and Flame* 143(4): 613-628 (2005).
- [137] Y.C. Chien, D. Escofet-Martin, and D. Dunn-Rankin, "CO emission from an impinging non-premixed flame," *Combustion and Flame*, 174:16-24 (2016).